Multi-dimensional materials design for advanced zinc-ion batteries

Fangjia Zhao

A thesis presented for the degree of Doctor of Philosophy

Supervised by

Professor Ivan P. Parkin

Doctor Guanjie He

Department of Chemistry

Mathematical and Physical Sciences Faculty

University College London

July 2024

Declaration

I, Fangjia Zhao, declare that this thesis and the work presented in it are my own and have been generated by me as the result of my original research.

I confirm that:

1.Results derived from others' published work are cited, as well as figures are reproduced with permission from the original publishers.

2.Parts of this thesis have been published in:

(1) F. Zhao, J, Li. A. Chutia, L. Liu, L. Kang, F. Lai, H. Dong, X. Gao, Y. Tan, T. Liu, I. Parkin*, G. He*, Highly stable manganese oxide cathode material enabled by Grotthuss topochemistry for aqueous zinc ion batteries, *Energy Environ. Sci.*, 2024, 17, 1497-1508. DOI: 10.1039/D3EE04161A.

(2) **F. Zhao**, J. Feng, H. Dong, R. Chen, T. Munshi, I. Scowen, S. Guan, Y. Miao, T. Liu, I. P. Parkin*, G. He*, Ultrathin protection layer via rapid plasma strategy for stable aqueous zinc ion batteries, *Adv. Funct. Mater.*, **2024**, 202409400.

(3) **F. Zhao**, Z. Jing, X. Guo, J. Li, H. Dong, Y. Tan, L. Liu, Y. Zhou, R. Owen, P. Shearing, D. Brett, G. He*, I. P. Parkin*, Trace amounts of fluorinated surfactant additives enable high performance zinc-ion batteries, *Energy Storage Mater.*, **2022**, 53, 638-645. DOI: 10.1016/j.ensm.2022.10.001.

Figures, tables and texts in these parts are adapted with permission from *Energy Storage Materials* (Copyright @ 2022 Elsevier B.V.), Advanced Functional Materials (Copyright @ 2024 John Wiley and Sons) and *Energy & Environmental Science* (Copyright @ 2024 Royal Society of Chemistry). These three publications listed above are open access.

3.All the main sources of help for this thesis have been acknowledged.

Signature:

Abstract

Zinc-ion batteries have drawn intensive research interest due to their ease of fabrication and less-flammable electrolyte. However, the discovery of the unique properties of the aqueous environment of aqueous zinc-ion batteries remains a challenge. For example, the most significant obstacle for zinc-ion batteries is water-related side reactions. An advantage of zinc-ion batteries is that the aqueous environment provides an additional charge carrier: hydronium ions. To fully exploit the differences in zinc-ion batteries, it is essential to address these interconnected challenges from the fundamental aspect of aqueous zinc-ion batteries: water.

The unregulated zinc deposition process can lead to zinc dendrite formation due to the 'tip effect'. These dendrites can penetrate the separator and cause micro short-circuits. To protect the zinc anode from dendrite issues and water-related side reactions, a carbon layer doped with nitrogen and oxygen was investigated using a rapid sputtering method. This method increased the zinc nuclei density and achieved a uniform zinc deposition process.

Water-related side reactions were further mitigated using perfluorooctanoic acid as an electrolyte additive. This fluorinated surfactant has low surface energy, forming an adsorption protection layer with fluorinated tails to limit the amount of water molecules near the interface, thus reducing side reactions. It also reduces the surface tension of the electrolyte, leading to enhanced wettability on both the anode and cathode, which improves rate performance due to sufficient mass transfer.

To further understand the positive aspects of aqueous zinc-ion batteries, a series of manganese oxides were synthesised, and the synergistic collaboration between vacancies, lattice water, and nickel ions, which enhances hydrated proton hopping *via* the Grotthuss mechanism, was studied. Protons preferentially bond with O²⁻ ions in the Mn-O layer, and proton transfer is favoured in the presence of vacancies. The Grotthuss mechanism enables efficient proton charge transfer without the long-distance movement of the molecule, leading to high ionic conductivity and high specific capacity.

This thesis emphasises the significant role of water molecules and their impact on the overall performance of aqueous zinc-ion batteries. It demonstrates that water-related side reactions in aqueous zinc-ion batteries can be mitigated using practical strategies, such as a minute amount

of PFOA additive and the rapid sputtering process, both of which require minimal raw materials. More importantly, it shows that aqueous zinc-ion batteries can be further enhanced *via* the Grotthuss-like mechanism by utilising hydronium as a charge carrier in the aqueous electrolyte. These strategies and the Grotthuss mechanism can be further applied to other aqueous systems to enhance the energy density and lifespan.

Impact statement

The pursuit of sufficient energy supply is consistent throughout human history. The past decades have experienced an explosive development of secondary energy storage technologies, which provide general energy support ranging from universe exploration to daily life in modern civilisation. Further development relies on the investigation of more affordable and sustainable energy storage technologies. Aqueous zinc ion batteries have advantages on safety, abundant mineral resource and rate performance. This Ph.D. project aims to provide a fundamental understanding of the mechanisms related to the water molecules in the AZIBs system and to explore the interconnection between the cathode, anode and electrolyte regarding water-related reactions. This project uncovers both sides of the aqueous system and provides relevant solutions. The drawbacks of the aqueous environment are addressed by designing an anode protection layer combined with designing aqueous electrolyte additives. The advantages of the aqueous environment are investigated, focusing mainly on the unique charge transfer mechanism of hydronium hopping in the aqueous system: the Grotthuss mechanism, which distinguishes of AZIBs from general none-aqueous systems. The highlights of the project are as follows:

- 1. An ultrathin and ultra rapid zinc electrode sputtering strategy is demonstrated to regulate the water-related side reactions in zinc ion battery. This modification method provides one of the thinnest and shortest solutions for zinc anode protection. The prepared sputtering layer shows controllable oxygen and nitrogen dopants for highly reversible zinc deposition.
- 2. The further investigation of balancing the anode performance and cathode performance in one solution was achieved *via* minute amount electrolyte additive design. PFOA additive has two roles: 1, participating in the solvation structure of Zn²⁺-H₂O system, which promotes charge transfer in the electrolyte; 2, the PFOA molecule absorption layer also acts as a zincophilic layer, regulating the free water molecules at the interface, thereby enlarging the working window of the electrolyte.
- 3. Further understanding of water molecule transfer is achieved through the exploration of hydronium ion hopping. The prepared NiMn₃O₇·3H₂O cathode material shows a specific capacity close to its theoretical value and exhibits excellent stability. The main finding is the identification of the synergistic collaboration between manganese vacancies, the lattice water and nickel ions in facilitating the Grotthuss mechanism.
- 4. The utilisation of advanced characterisation methods combined with *in-situ* experiments reveals the charge transfer mechanism and the electrochemical process at the atomic level and

through direct monitoring. The further exploration of theoretical simulation on molecular dynamics and density functional theory matches well with the experimental data. The combination of multiple technologies provides an understanding of water-related reactions and transfer mechanisms from a broad perspective.

Apart from the above academic outcomes, this Ph.D. project has also inspired subsequent research, including the surface plasma modification, nano materials defect engineering, ammonium ion transfer mechanisms in coin cell and pouch cell level, and scaling up within a broader research network.

UCL Research Paper Declaration Form

referencing the doctoral candidate's own published work(s)

Please use this form to declare if parts of your thesis are already available in another format, e.g. if data, text, or figures:

- have been uploaded to a preprint server
- · are in submission to a peer-reviewed publication
- have been published in a peer-reviewed publication, e.g. journal, textbook.

This form should be completed as many times as necessary. For instance, if you have seven thesis chapters, two of which containing material that has already been published, you would complete this form twice.

- 1. For a research manuscript that has already been published (if not yet published, please skip to section 2)
 - a) What is the title of the manuscript?

Ultrathin protection layer via rapid sputtering strategy for stable aqueous zinc ion batteries

b) Please include a link to or doi for the work

https://doi.org/10.1002/adfm.202409400

c) Where was the work published?

Advanced Functional Materials

d) Who published the work? (e.g. OUP)

Wiley

e) When was the work published?

2024/07/08

f) List the manuscript's authors in the order they appear on the publication

Fangjia Zhao, Jianrui Feng, Haobo Dong, Ruwei Chen, Tasnim Munshi, Ian Scowen, Shaoliang Guan, Yue-E Miao, Tianxi Liu, Ivan P. Parkin*, Guanjie He*

g) Was the work peer reviewed?

Yes

h) Have you retained the copyright?

No

i) Was an earlier form of the manuscript uploaded to a preprint server? (e.g. medRxiv). If 'Yes', please give a link or doi)

Νc

If 'No', please seek permission from the relevant publisher and check the box next to the below statement:

X

I acknowledge permission of the publisher named under **1d** to include in this thesis portions of the publication named as included in **1c**.

- 2. For a research manuscript prepared for publication but that has not yet been published (if already published, please skip to section 3)
 - a) What is the current title of the manuscript?

b) Has the manuscript been uploaded to a preprint server? (e.g. medRxiv; if 'Yes', please give a link or doi)

Click or tap here to enter text.

c) Where is the work intended to be published? (e.g. journal names)

Click or tap here to enter text.

d) List the manuscript's authors in the intended authorship order

Click or tap here to enter text.

e) Stage of publication (e.g. in submission)

Click or tap here to enter text.

3. For multi-authored work, please give a statement of contribution covering all authors (if single-author, please skip to section 4)

F.Z.: conceptualisation, methodology, software, data acquisition, data curation, formal analysis, investigation, validation, visualisation, writing – original draft, and writing – review and editing. F.J.: conceptualisation, data acquisition, software.

H.D., R.C., T.M. data acquisition, software, formal analysis.

I.S., S.G, Y.M., T.L.: data curation, review.

I.P.: funding acquisition, supervision, and writing – review and editing.

G.H.: conceptualisation, methodology, funding acquisition, supervision, and writing – review and editing.

4. In which chapter(s) of your thesis can this material be found?

Chapter 3

5. e-Signatures confirming that the information above is accurate (this form should be co-signed by the supervisor/ senior author unless this is not appropriate, e.g. if the paper was a single-author work)

Candidate

Supervisor/ Senior Author (where appropriate)

Click or tap here to enter text.

Date

UCL Research Paper Declaration Form

referencing the doctoral candidate's own published work(s)

Please use this form to declare if parts of your thesis are already available in another format, e.g. if data, text, or figures:

- have been uploaded to a preprint server
- are in submission to a peer-reviewed publication
- have been published in a peer-reviewed publication, e.g. journal, textbook.

This form should be completed as many times as necessary. For instance, if you have seven thesis chapters, two of which containing material that has already been published, you would complete this form twice.

- **6.** For a research manuscript that has already been published (if not yet published, please skip to section 2)
 - j) What is the title of the manuscript?

Trace amounts of fluorinated surfactant additives enable high performance zinc-ion batteries

k) Please include a link to or doi for the work

https://doi.org/10.1016/j.ensm.2022.10.001

I) Where was the work published?

Energy Storage Materials

m) Who published the work? (e.g. OUP)

Elsevier

n) When was the work published?

December 2022

o) List the manuscript's authors in the order they appear on the publication

Fangjia Zhao, Zhuanfang Jing, Xiaoxia Guo, Jianwei Li, Haobo Dong, Yeshu Tan, Longxiang Liu, Yongquan Zhou, Rhodri Owen, Paul R. Shearing, Dan J.L. Brett, Guanjie He, Ivan P. Parkin

p) Was the work peer reviewed?

Yes

q) Have you retained the copyright?

Νo

r) Was an earlier form of the manuscript uploaded to a preprint server? (e.g. medRxiv). If 'Yes', please give a link or doi)

No

If 'No', please seek permission from the relevant publisher and check the box next to the below statement:

X

I acknowledge permission of the publisher named under **1d** to include in this thesis portions of the publication named as included in **1c**.

- 7. For a research manuscript prepared for publication but that has not yet been published (if already published, please skip to section 3)
 - f) What is the current title of the manuscript?

g) Has the manuscript been uploaded to a preprint server? (e.g. medRxiv; if 'Yes', please give a link or doi)

Click or tap here to enter text.

h) Where is the work intended to be published? (e.g. journal names)

Click or tap here to enter text.

i) List the manuscript's authors in the intended authorship order

Click or tap here to enter text.

j) Stage of publication (e.g. in submission)

Click or tap here to enter text.

8. For multi-authored work, please give a statement of contribution covering all authors (if single-author, please skip to section 4)

Fangjia Zhao: Conceptualisation, Formal analysis, Investigation, Writing – original draft. Zhuanfang Jing: Formal analysis, Writing – original draft. Xiaoxia Guo: Investigation. Jianwei Li: Investigation, Data curation. Haobo Dong: Investigation. Yeshu Tan: Investigation. Longxiang Liu: Investigation. Yongquan Zhou: Data curation. Rhodri Owen: Investigation. Paul R. Shearing: Funding acquisition. Dan J.L. Brett: Funding acquisition. Guanjie He: Conceptualisation, Funding acquisition, Supervision, Writing – review & editing. Ivan P. Parkin: Funding acquisition, Supervision, Writing – review & editing.

9. In which chapter(s) of your thesis can this material be found?

Chapter 4

10. e-Signatures confirming that the information above is accurate (this form should be co-signed by the supervisor/ senior author unless this is not appropriate, e.g. if the paper was a single-author work)

Candidate

Supervisor/ Senior Author (where appropriate)

Click or tap here to enter text.

Date

UCL Research Paper Declaration Form

referencing the doctoral candidate's own published work(s)

Please use this form to declare if parts of your thesis are already available in another format, e.g. if data, text, or figures:

- have been uploaded to a preprint server
- are in submission to a peer-reviewed publication
- have been published in a peer-reviewed publication, e.g. journal, textbook.

This form should be completed as many times as necessary. For instance, if you have seven thesis chapters, two of which containing material that has already been published, you would complete this form twice.

- 11. For a research manuscript that has already been published (if not yet published, please skip to section 2)
 - s) What is the title of the manuscript?

Highly stable manganese oxide cathode material enabled by Grotthuss topochemistry for aqueous zinc ion batteries

t) Please include a link to or doi for the work

DOI: 10.1039/D3EE04161A

u) Where was the work published?

Energy & Environmental Science

v) Who published the work? (e.g. OUP)

Royal Society of Chemistry

w) When was the work published?

16/01/2024

x) List the manuscript's authors in the order they appear on the publication

Fangjia Zhao, Jianwei Li, Arunabhiram Chutia, Longxiang Liu, Liqun Kang, Feili Lai, Haobo Dong, Xuan Gao, Yeshu Tan, Tianxi Liu, Ivan P. Parkin, Guanjie He

y) Was the work peer reviewed?

Yes

z) Have you retained the copyright?

aa) Was an earlier form of the manuscript uploaded to a preprint server? (e.g. medRxiv). If

'Yes', please give a link or doi)

If 'No', please seek permission from the relevant publisher and check the box next to the below statement:

X

I acknowledge permission of the publisher named under 1d to include in this thesis portions of the publication named as included in 1c.

- 12. For a research manuscript prepared for publication but that has not yet been published (if already published, please skip to section 3)
 - k) What is the current title of the manuscript?

I) Has the manuscript been uploaded to a preprint server? (e.g. medRxiv; if 'Yes', please give a link or doi)

Click or tap here to enter text.

m) Where is the work intended to be published? (e.g. journal names)

Click or tap here to enter text.

n) List the manuscript's authors in the intended authorship order

Click or tap here to enter text.

o) Stage of publication (e.g. in submission)

Click or tap here to enter text.

- 13. For multi-authored work, please give a statement of contribution covering all authors (if single-author, please skip to section 4)
 - F. Z.: conceptualisation, methodology, software, data acquisition, data curation, formal analysis, investigation, validation, visualisation, writing original draft, and writing review and editing. J. L.: conceptualisation, methodology, formal analysis, and writing review and editing. A. C.: conceptualisation, data acquisition, formal analysis, software, and writing review and editing. L. L., L. K., H. D., X. G., and Y. T.: data acquisition, software, formal analysis. F. L., T. L.: methodology, data acquisition, and writing review and editing. I. P.: funding acquisition, supervision, and writing review and editing. G. H.: conceptualisation, methodology, funding acquisition, supervision, and writing review and editing.
- 14. In which chapter(s) of your thesis can this material be found?

Chapter 5

15. e-Signatures confirming that the information above is accurate (this form should be co-signed by the supervisor/ senior author unless this is not appropriate, e.g. if the paper was a single-author work)

Candidate

Supervisor/ Senior Author (where appropriate)

Click or tap here to enter text.

Date

Acknowledgements

First and foremost, I would like to express my deep appreciation to my principal supervisor, Professor Ivan P. Parkin. He opened my academic career and guided me through my PhD with professional suggestions and always timely support, which impressed me a lot. His positive mindsets are worth my deepest appreciation and set me a good example on professional behaviour both in and beyond academia life.

I would like to specially thank Dr. Guanjie He, who guided me to start the search in zinc-ion batteries, helped me with the research project demonstration, and paper publishing. His passion for research and academic knowledge motivates me to provide high-quality research output. I could not reach my current achievements in research without him. Moreover, I would like to thank Dr. Jianwei Li, who helped me establish essential knowledge about cathode material synthesis and characterisation. I would like to thank Dr. Haobo Dong and Dr. Xiaoxia Guo, who provided informative support on anode and electrolyte.

In addition, I would like to thank all my collaborator during my doctoral study, including Prof. Dan Brett, Prof. Paul Shearing, Prof. K. Holt, Dr. Sanjayan Sathasivam, Dr. Kristopher Page, Dr. Steve Firth, Mr. Martin Vickers, Dr. Abil Aliev, Dr. Xiyi Li and Dr. Liqun Kang at UCL. Thanks to the support from Arunabhiram Chutia, who inspired me a lot and contributed to the computational collaboration work in Chapter 5. Thanks to Dr. Zhuanfang Jing and Mr. Jianrui Feng, who kindly helped me with me the computational collaboration work in Chapter 3 and Chapter 4. Indeed, I would like to sincerely thank all the group members from Prof. Parkin's research group. Especially Dr. Siyu Zhao, Dr. Zhengyu Zhang, Dr. Yiding Jiao, Dr. Juntao Li, Dr. Jintao Li, Dr. Guanxu Chen, Dr. Longxiang Liu, Dr. Yeshu Tan, Mr. Tianlei Wang and Mr. Liquan Zhang. It is my honour to work with you during such a great time. Long last our friendship. Thanks to Miss Jiayi Wang, who has shown me the purity of the human spirit and enriched my life with small little things

Finally, I would like to express my deepest gratitude to my family for their unspoken love and unwavering support for my life choices.

Table of Contents

Declaration	i
Abstract	ii
Impact statement	iv
Acknowledgements	xii
Table of Contents	1
Table of Figures	5
List of Tables	13
List of Abbreviations	14
Chapter 1: Overview of Rechargeable Battery Technologies, Pro	blems and Strategies.17
1.1 Background of rechargeable battery technologies	19
1.1.1 Lithium-ion batteries	20
1.1.2 Lithium-sulphur batteries	22
1.1.3 Sodium-ion batteries	24
1.1.4 Proton batteries	26
1.1.5 Calcium-ion batteries	28
1.1.6 Magnesium-ion batteries	30
1.1.7 Aluminium-ion batteries	31
1.2 Aqueous zinc-ion battery research problems	33
1.2.1 Cathode material dissolution	33
1.2.2 Parasitic byproducts formation	35
1.2.3 Cathode material phase change	37
1.2.4 Sluggish charge transfer kinetics	40
1.2.5 Zinc dendrite	42
1.2.6 Corrosion and passivation	43
1.3 Research strategies for aqueous zinc-ion batteries	45
1.3.1 Pre-intercalation strategies	45
1.3.2 Defect engineering	47
1.3.3 Cathode-electrolyte-interface modification	49
1.3.4 Structural optimisation	50
1.3.5 Interface functionalisation	52
1.3.6 Polymer coating	54

	1.3.7 Solid electrolyte interface fabrication	55
	1.3.8 Electrolyte additives	57
	1.3.9 Concentrated electrolyte (water-in-salt)	59
	1.3.10 Zn ²⁺ solvation cluster regulation	61
1.4 R	References	64
Chaj	pter 2: Battery Materials Characterisation Technologies	80
	2.1 X-ray photoelectron spectroscopy	81
	2.2 Infrared spectroscopy	82
	2.3 X-ray diffraction	82
	2.4 Raman spectroscopy	83
	2.5 Scanning electron microscopy	84
	2.6 Transmission electron microscopy	84
	2.7 Scanning transmission electron microscopy	85
	2.8 Digital microscopy	85
	2.9 Contact angle measurement	85
	2.10 X-ray Fluorescence	86
	2.11 Solid-state NMR	86
Cha	pter 3: Surface Protection Layer via Rapid Sputtering Strategy for S	table Aqueous
-	e-ion Batteries	-
3.1 Iı	ntroduction	89
3.2 E	Experimental section	91
	3.2.1 Chemicals	91
	3.2.2 Cathode material Na _{0.65} Mn ₂ O ₄ ·H ₂ O synthesis	91
	3.2.3 Modification of anode electrode <i>via</i> sputtering process	92
	3.2.4 Fabrication of cathode materials	
	3.2.5 Fabrication of the electrochemical cell	93
	3.2.6 Electrochemical characterisation	93
	3.2.7 Material characterisation	93
3.3 R	Result and discussion	94
	3.3.1 Optimisation of the sputtering parameters	
	3.3.2 Zinc anode characterisation	
	3.3.3 Cathode characterisation	103

3.3.4 Theoretical simulations	107
3.3.5 Ex-situ & in-situ characterisation	110
3.3.6 Electrochemical characterisation of CN10@Zn	119
3.3.7 Technical-economic assessment	126
3.4 Conclusion	127
3.5 References	127
Chapter 4: Minute Amount of Fluorinated Surfactant Additives Enabl	e High
Performance Zinc-ion Batteries	131
4.1 Introduction	132
4.2 Experimental section	134
4.2.1 Chemicals	134
4.2.2 Cathode preparation	134
4.2.3 Materials characterisation	134
4.2.4 Electrochemical evaluation	135
4.2.5 Details of molecular dynamics simulation	135
4.2.6 Estimation of the capacitive and diffusion-controlled contributions	136
4.2.7 Estimation of Zn ²⁺ transference number	137
4.3 Results and discussion	137
4.3.1 Electrolyte characterisation	137
4.3.2 Anode characterisation	142
4.3.3 Ex-situ characterisation	145
4.4.4 Electrochemical characterisation	148
4.3.5 Molecular dynamics simulation	163
4.4 Conclusion	164
4.5 References	166
Chapter 5: Highly Stable Manganese Oxide Cathode Material Enabled by G	rotthuss
Topochemistry for Aqueous Zinc-ion Batteries	168
5.1 Introduction	169
5.2 Experimental section	
5.2.1 Chemicals	172
5.2.2 Material synthesis	172
5.2.3 Material characterisation	172

5.2.4 Electrochemical measurements	173
5.2.5 Estimation of capacitive and diffusion-controlled contributions	174
5.2.6 Detailed information on galvanostatic intermittent titration technique	174
5.2.7 DFT computational details	175
5.3 Results and discussion	177
5.3.1 Cathode materials characterisation	177
5.3.2 DFT simulation on proton transfer	187
5.3.3 Ex-situ characterisation	189
5.3.4 Electrochemical characterisation	194
5.4 Conclusion	199
5.5 References	201
Chapter 6: Summary and Perspectives	204
6.1 Summary	205
6.2 Challenges	208
6.3 Perspectives.	210
6.3.1. Enlarging working window for aqueous electrolyte	210
6.3.2. Increasing specific capacity	210
6.3.3. Increasing loading amount of active materials	212
Publication list	213
Academic activities	214

Table of Figures

Figure 1.1	Approximate ranges of specific capacities, average discharge potentials, and crystal structures of common high-voltage LIBs cathodes: (a) Comparison with commercial cathodes; (b) Crystal structures of LiMO ₂ and x Li ₂ MnO ₃ · (1-x) LiMO ₂ ; (c) Gravimetric capacities; (d) Volumetric capacities of selected cathodes. Reprinted with permission from ref. ^[15] Copyright 2020 Royal Society of Chemistry20
Figure 1.2	Schematic illustrations of the strategies and operation mechanisms of the modified sulphur host, electrolyte systems, functional separators, and anode surface engineering for the inhibition of LiPSs shuttle. Reprinted with permission from ref. ^[25] Copyright 2022 John Wiley and Sons
Figure 1.3	Recent research progress in sodium-ion batteries: (a) Cathode, (b) Anode, (c) Electrolyte and (d) Binder. Reproduced with permission from Ref. [30] Copyright 2017 Royal Society of Chemistry
Figure 1.4	The impact of proton storage on electrochemical performance. Reprinted with permission from ref. [36] Copyright 2022 UESTC and John Wiley & Sons26
Figure 1.5	Cyclic voltammograms of EC: PC electrolytes at a scan rate of 0.5 Mv s ⁻¹ , showing (a) 0.3 M concentration of different salts at 100°C; (b) 0.65 M concentration of Ca(BF ₄) ₂ at 75°C and 100°C; and (c) Various Ca(BF ₄) ₂ concentrations ranging from 0.3 M to 0.8 M at 100°C. Insets in (a) show an expanded scale, and insets in (b) and (c) display onset potentials for the redox process. Reprinted with permission from ref. ^[44] Copyright 2017 Springer Nature.
Figure 1.6	(a) Competition between solvent molecules and anions for coordination with Mg ²⁺ . Reproduced with permission from ref. ^[50] Copyright 2020, Elsevier. b) Modification of the solvation structure in Mg(ClO ₄) ₂ /ACN electrolyte with the addition of DME. Reproduced with permission from ref. ^[51] Copyright 2018 John Wiley and Sons
Figure 1.7	(a) Comparison of gravimetric and volumetric capacities as well as cost, abundance, standard potentials, cation radius and charge density of cations for Li, Na, K, Zn and Al. [56, 57] (b) Schematic illustration of the discharge process in an Al–air battery with aqueous KOH electrolyte showing the movement of hydroxide ions to the anode causing undesired corrosion and passivation phenomena. (c) Schematic of the discharge process in an Al-ion battery with non-aqueous ionic liquid electrolyte including a representation of intercalated chloroaluminate anions in the graphite cathode. Reprinted with permission from ref. [52] Copyright 2020 Springer Nature
Figure 1.8	Pourbaix diagram for (a) Manganese oxides and (b) Vanadium oxides. Schematic illustration of dissolution processes for (c) Inorganic cathodes, (d) Organic cathodes, and (e) Iodine cathodes. Reprinted with permission from ref. Copyright 2024 Wiley VCH GmbH.

zinc met Reprodu for 10 ⁻⁶	natic of the Zn ²⁺ solvation process and interfacial interaction between the all anode and the electrolyte. (b) Electric field simulation of zinc anodes. ced with permission from ref. ^[75] Springer Nature. (c) Pourbaix diagram mol L ⁻¹ Zn ²⁺ . Reproduced with permission from Ref. ^[76] Copyright 2022 ociety of Chemistry.
the MnO Discharg and (c) A the initia first cycl Zn//MnO	on of the combined intercalation and conversion reaction mechanism of 22 cathode. XRD patterns of the α-MnO ₂ cathode at various stages: (a) ed to 1.4 V in the initial cycle, (b) Fully charged state in the initial cycle, after 100 cycles. Schematic illustration of the phase evolution: (d) During I discharge process, (e) During the initial charge process, and (f) After the e. (g) Schematic depiction of the dissolution—deposition mechanism in the D ₂ battery. Reprinted with permission from ref. Copyright 2020 in Chemical Society
Reducin Tailoring (e) Des function	ommon strategies for performance improvement and their rationale: (a) g dimensions of active materials; (b) Formation of composites; (c) g particle morphology; (d) Design of coatings or shells on active particles; gn of functional binders; (f) Flexible electrodes; (g) Doping and alisation; (h) Modification of electrolytes from liquid to solid. Reprinted mission from ref. Copyright 2020 Royal Society of Chemistry41
Formation	lo demonstration and Multi-level Tomography investigation of Dendrite on and Dissolution in Zinc Batteries. Reprinted with permission from Copyright 2019 Elsevier
profile.	on of the ammonium preintercalated manganese oxide material and GCD Reprinted with permission from ref. ^[138] Copyright 2023 Wiley-VCH
energy s	Gibbs free energy of different models; (b) The schematic illustration of the torage mechanism in the $Zn\ V_d-V_2O_3$ cells. Reprinted with permission [155] Copyright 2021 Springer Nature
	on of surface modification methods for cathode materials. Reprinted with on from ref. [156] Copyright 2023 Elsevier
_	ary of the surface modification and structural design for zinc anode. d with permission from ref. ^[172] Copyright 2023 Springer Nature50
(3D-LFC	sition on (a) Bare Zn, (b) 3D graphene matrices of longitudinal direction GC), and (c) Radial direction (3D-RFGC). Reprinted with permission from Copyright 2023 Springer Nature
preparati	ation and characterisation of porous PMMA coating. Scheme of the on process (a) and mechanism (b) of porous PMMA coating. Reprinted mission from ref. [203] Copyright 2024 John Wiley and Sons
	on of the structure and functions of SEI on zinc anodes. Reprinted with on from ref. [212] Copyright 2023 Wiley-VCH GmbH

Figure 1.20 Summary of the electrolytes additives strategies for AZIBs. Reprinted with permission from ref. [217] Copyright 2024 Elsevier
Figure 1.21 Development timeline of concentrated electrolytes in AZIBs. Reprinted with permission from ref. [254] Copyright 2022 Elsevier
Figure 1.22 Schematics of solvation structure and HER mechanism at electrode/electrolyte interface. Left: Diluted interface formed during Zn-plating (Zn ²⁺ desolvation) with competition HER; Right: Concentrated interface formed during Zn-stripping (Zn ²⁺ solvation) with corrosion HER. Reprinted with permission from ref. [266] Copyright 2024 American Chemical Society
Figure 1.23 (a) Schematic diagram of the interplay among Zn ²⁺ , TFSI ⁻ , and Ace to form eutectic solutions. (b) Molecular electrostatic potential energy surface. (c) Illustration of representative environment of active Zn species within the ZES. Reprinted with permission from ref. ^[249] Copyright 2019 Springer Nature63
Figure 3.1 Illustration of the issues in bare Zn anode and sputtered CN10@Zn anode. 89
Figure 3.2 Schematic illustration of (a) the corrosion of Zn anodes in aqueous electrolytes; (b) Homogenous zinc deposition with a sputtered carbon layer in aqueous electrolytes. 90
Figure 3.3 Illustration of the sputtering process
Figure 3.4 3D laser scanning confocal microscopy of zinc anodes with different sputtering voltage: (a) 1.5 V; (b) 3.5 V; (c) 5 V
Figure 3.5 3D laser scanning confocal microscopy of zinc anodes with different sputtering time (a) 1 second; (b) 3 seconds; (c) 5 seconds; (d) 10 seconds95
Figure 3.6 Galvanostatic cycling of symmetrical Zn cells with CN3@Zn (3 seconds sputtering) at 1 mA cm ⁻² and 1 mAh cm ⁻² 96
Figure 3.7 Optical image of the sputtering sample sputtered in low vacuum: 0.5 mbar96
Figure 3.8 Microscopy characterisation of CN10@Zn: (a,b) Digital images; (c) Side-view SEM image; (d) TEM image
Figure 3.9 XRD characterisation of the sputtered CN10@Zn and the bare Zn98
Figure 3.10 (a) Side-view SEM profile of CN10@Zn; EDS mapping images of CN10@Zn: (b) Carbon; (c) Nitrogen; (d) Oxygen
Figure 3.11 Raman characterisation of CN10@Zn anode99
Figure 3.12 XPS analysis: (a) Survey profiles of CN10@Zn and bare Zn; (b) C 1s profiles of CN10@Zn and bare Zn; (c) N 1s profile of CN10@Zn; (d) Depth profile of CN10@Zn

Figure 3.13	3 XPS O 1s depth profiles of the sputtered CN10@Zn anode101
Figure 3.14	Contact angle of 2 M ZnSO ₄ electrolyte on the bare Zn anode and CN10@Zn anode
Figure 3.15	5 Sputtered anode mechanical testing: (a) Hammering; (b) Bending; (c) Folding; (d) Twisting
Figure 3.16	SEM images of Na _{0.65} Mn ₂ O ₄ cathode material103
Figure 3.1°	7 (a) SEM image of Na _{0.65} Mn ₂ O ₄ ; EDS mapping profiles of Na _{0.65} Mn ₂ O ₄ ; EDS mapping images for (b) Na; (c) Mn and (d) O; Elements ratio: (e) by atom weight; (f) by atom ratio
Figure 3.18	3 XRF characterisation of Na _{0.65} Mn ₂ O ₄
Figure 3.1	9 (a) XRD profile of Na _{0.65} Mn ₂ O ₄ cathode material; (b) Crystal structure of Na _{0.65} Mn ₂ O ₄ 106
Figure 3.20	O DFT simulation on oxygen species: Charge density of (a) Bridge oxygen; (b) Hydroxyl oxygen; (c) Edge oxygen; (d) Adsorption energy comparison of different oxygen sites
Figure 3.21	DFT simulation on nitrogen species: Charge density of (a) Carbon; (b) Pyridinic N; (c) Pyridinic neighbour N; (d) Graphic N; (e) Pyrrolic N; (f) Pyrrolic neighbour N; (g) Adsorption energy comparison of different N species
Figure 3.22	2 Electrostatic field distribution diagram the anodes: (a) Zn and (b) CN10@Zn. 109
Figure 3.2	3 COMSOL simulations of the electric field distribution: (a) Bare Zn and (b) CN10@Zn109
Figure 3.24	Digital images of the immersion experiments in 2 M ZnSO ₄ electrolyte: (a,b) Bare Zn anode; (c,d) CN10@Zn anode. Scale bar: 10 mm
Figure 3.25	5 Cross-sectional optical micrographs of (a) CN10@Zn and (b) Bare Zn soaked in 2 M ZnSO ₄ electrolyte for 36 hours. Scale bar: 1.0 mm111
Figure 3.26	5 Ex-situ digital images after cycling: (a) CN10@Zn anode; (b) Bare Zn anode. 112
Figure 3.27	Ex-situ SEM images of the CN10@Zn anode
Figure 3.28	3 Ex-situ SEM images of the bare Zn anode
Figure 3.29	9 3D laser scanning confocal microscopy of the anodes cycled in 2 M ZnSO ₄ electrolyte: (a) CN10@Zn; (b) Bare Zn113
Figure 3.30	SEM images of the Zn anode after sputtering treatment

Figure 3.31	In-situ optical microscopy images: (a) CN10@Zn; (b) Bare Zn114
Figure 3.32	Ex- situ EDS mapping of CN10@Zn
Figure 3.33	Ex-situ EDS mapping of the bare Zn anode
1	Ex-situ characterisation of CN10@Zn: (a) Ex-situ N 1s profiles; (b) Ex-situ C 1s profiles; (c) Ex-situ Zn 2p profiles; (d) Ex-situ XRD images comparison of the sputtered anode and the bare Zn anode
Figure 3.35	Ex-situ XPS S 2p profile of the bare Zn anode and the CN10@Zn zinc anode. 117
Figure 3.36	Ex-situ SEM and EDS mapping images of Na _{0.65} Mn ₂ O ₄ cathode materials118
6	Electrochemical characterisation: (a) Linear sweep scanning profiles of CN10@Zn anode and the bare Zn anode; (b) CA testing profiles of the sputtered CN10@Zn anode and the bare Zn anode
	EIS profiles from 30°C to 70°C; (a) Bare Zn anode; (b) CN10@Zn anode; (c) Activation energy analysis of the CN10@Zn anode and the bare Zn anode120
	(a) CE results of the CN10@Zn anode and the bare Zn anode; Relevant voltageareal capacity profiles: (b) CN10@Zn and (c) Zn
(Electrochemical measurements: (a) Rate testing profiles of Zn symmetrical cells; Galvanostatic cycling of symmetrical Zn cells with CN10@Zn and Zn: (b) at 1 mA cm ⁻² and 1 mAh cm ⁻² ; (c) at 4 mA cm ⁻² and 2 mAh cm ⁻² ; (d) at 5 mA cm ⁻² and 5 mAh cm ⁻²
_	(a) CV curves of $Zn Na_{0.65}Mn_2O_4$ under 0.2 mV s ⁻¹ ; (b) EIS profiles of $Zn Na_{0.65}Mn_2O_4$
	(a) Voltage-specific capacity curves at a current density of 1 A g ⁻¹ ; (b) Long-term cycling performance
_	(a) Rate performance of Zn Na _{0.65} Mn ₂ O ₄ batteries; Voltage-specific capacity profiles: (b) CN10@Zn; (c) Bare Zn
1	Performance comparison: (a) Key metrics comparison between CN10@Zn and bare Zn anodes; (b) Thickness-lifespan comparison of CN10@Zn with other studies
-	(a) Battery pack cost contribution for aqueous electrode processing; [40] (b) Comparison of the processing time of different zinc anode modification methods
Figure 4.1 S	Schematic diagram of Zn ²⁺ ions deposition process: (a) Pristine electrolyte; (b) trolyte. 133

Figure 4.2 Surface tension curve of the PFOA electrolytes	137
Figure 4.3 pH values of 3 M ZnSO ₄ electrolytes with varying PFOA addition amounts	138
Figure 4.4 Contact angles measurements on Zn anodes with different electrolytes	139
Figure 4.5 Contact angles measurements on Na _{0.65} Mn ₂ O ₄ with different electrolytes	139
Figure 4.6 ¹ H NMR spectrum of the PFOA electrolyte	140
Figure 4.7 ¹⁹ F NMR spectrum of the PFOA electrolyte.	140
Figure 4.8 ATR-FTIR spectra of different electrolytes.	141
Figure 4.9 Raman spectra of different electrolytes.	141
Figure 4.10 Microscopy characterisation of zinc anodes after immersion experiment i PFOA electrolyte: (a) SEM; EDS mapping images: (b) F; (c) C; (d) Zn	
Figure 4.11 FTIR spectra of zinc anodes soaked in the PFOA electrolyte	142
Figure 4.12 Digital images of zinc anodes after immersion experiment: (a,b) in the prelectrolyte and (c, d) in the PFOA electrolyte	
Figure 4.13 Optical microscopy observations of zinc anodes immersed in the prelectrolyte (a-c) and the PFOA electrolyte (d-f)	
Figure 4.14 XPS analysis of the anodes cycled in PFOA electrolytes: (a) F 1s; (b) C 1s	145
Figure 4.15 <i>Ex-situ</i> XRD profiles of the anodes after cycling for 50 cycles at 1 mA cm ⁻² .	145
Figure 4.16 <i>Ex-situ</i> SEM profiles of the anodes after cycling: (a,b) in PFOA electrolyte; in pristine electrolyte	
Figure 4.17 <i>In-situ</i> optical microscopy of the zinc symmetric cells cycled in difference electrolytes: (a) Pristine electrolyte; (b) PFOA electrolyte. Scale bar: 50 μm	
Figure 4.18 LSV scans of different electrolytes.	148
Figure 4.19 Linear polarisation curves of Zn foils in different electrolytes.	149
Figure 4.20 CV curves of Zn symmetric cells in different electrolytes under 1 mV s ⁻¹ scan	
Figure 4.21 Zn plating and stripping CV curves in Zn Ti cells	150
Figure 4.22 Ion-transport properties of pristine electrolyte (3 M ZnSO ₄)	151
Figure 4.23 Ion transport properties of PFOA electrolyte (3 M ZnSO ₄ 0.25 mM PFOA).	151

-	Ion-transport properties of electrolyte with PFOA additive (3 M ZnSO ₄ 10 mM PFOA)
Figure 4.25	Zn ²⁺ transference number in different electrolytes
Figure 4.26	CE in different electrolytes using Cu Zn cells
-	Voltage-capacity curves using Cu Zn cells in different electrolytes: (a) PFO electrolyte; (b) Pristine electrolyte
-	Voltage-time curves of zinc plating and stripping on copper substrates in different electrolytes: (a) PFOA electrolyte; (b) Pristine electrolyte
	Rate performance of Zn symmetric cells measured at stepwise current densities of 0.2, 0.5, 1, 2, 5, 10, 5, 2, 1, 0.5, 0.2 mA cm ⁻²
	Long-term cycling using the Zn symmetric cell in different electrolytes under mA cm ⁻² 15
Figure 4.31	XRD profile of Na _{0.65} Mn ₂ O ₄
Figure 4.32	Raman curve of Na _{0.65} Mn ₂ O ₄ self-standing electrode mixed with PTFE15
Figure 4.33	In-situ Raman spectra of Na _{0.65} Mn ₂ O ₄ cathode cycled in the PFOA electrolyte
	CV curves of $Na_{0.65}Mn_2O_4 Zn$ cells under different scan rate: (a) 0.1 mV s ⁻¹ ; (b) 0.5 mV s ⁻¹ ; (a) 1 mV s ⁻¹ ; (d) 5 mV s ⁻¹
Figure 4.35	EIS profiles of $Na_{0.65}Mn_2O_4\ Zn$ cells with different electrolytes
	CV plots of Na _{0.65} Mn ₂ O ₄ Zn at scan rates of 0.1 to 0.5 mV s ⁻¹ : (a) in 3 M ZnSO 0.2 M MnSO ₄ 0.25 mM PFOA, (b) in 3 M ZnSO ₄ 0.2 M MnSO ₄
-	Fitting results of b value in different electrolytes: (a) Pristine electrolyte; (b) PFO electrolyte
	Capacitive contribution (grey region) to the electrochemical response current at mV s ⁻¹ : (a) PFOA electrolyte; (b) Pristine electrolyte16
Figure 4.39	Capacitive contribution in the PFOA electrolytes (a) and pristine electrolytes (b
Figure 4.40	$Na_{0.65}Mn_2O_4 \ Zn \; GCD \; testing \; with \; different \; electrolytes. \\ \\ \\ \\ \\ \\ \\ \\ \\ \\ \\ \\ \\ \\ \\ \\ \\ \\ \\$
-	(a) Rate performance; Corresponding voltage-specific capacity curves: (b) PFO electrolyte: (c) Pristine electrolyte

Figure 4.42	2 Molecular dynamic simulations: (a) Simulation model of the pristine electrolyte. (b) H ₂ O molecule distribution in the Zn ²⁺ first hydration layer of the pristine electrolyte. (c) Simulation model of electrolyte with PFOA additive. (d) H ₂ O molecule distribution in the Zn ²⁺ first hydration layer of the electrolyte with PFOA additive
Figure 4.43	Radial distribution functions of (a) Zn ²⁺ ions and (b) water molecule, where Ow represents the oxygen atoms in water molecules163
Figure 5.1	(a) Illustration of hopping Grotthuss mechanism for proton conductivity; (b) Newton's cradle illustration of proton hopping <i>via</i> Grotthuss mechanism in NiMn ₃ O ₇ lattice; (c) Illustration of hydrated proton hopping <i>via</i> Grotthuss mechanism.
Figure 5.2	Illustration of the basic $Mn_{6/7}O_2$ unit of AMn_3O_7 MLL structure (A = Zn, Ni, Na etc.)
Figure 5.3	XRD characterisations of cathode materials with different pre-intercalated cations: (a) Zn ²⁺ ; (b) Ca ²⁺ ; (c) Co ²⁺ ; (d) Ni ²⁺ ; (e) Magnified Ni ²⁺ 178
Figure 5.4	XRD characterisations of cathode materials synthesised under varying conditions: (a) NH ₄ Cl concentrations; (b) Temperatures
Figure 5.5	Microscopy characterisations for V _m -NMO: (a) SEM image for V _m -NMO; (b) EDS mapping images of V _m -NMO: (b) Ni; (c) Mn; (d) O
Figure 5.6	Microscopy characterisations for NMO: (a) SEM image; (b) TEM image. EDS mapping images: (c) Ni; (d) Mn; and (e) O
Figure 5.7	Microscopy images for V _m -NMO: (a,b) HRTEM; (c,d) STEM181
Figure 5.8	XPS spectra of cathode materials: (a) V _m -NMO XPS survey; (b) NMO XPS survey; (c) V _m -NMO Mn 2p; (d) NMO Mn 2p; (e) Elemental ratio; (f) Mn 3s183
Figure 5.9	Raman spectra of cathode materials: (a) V _m -NMO; (b) NMO184
Figure 5.10	XAFS fitting on the Mn-Mn coordination numbers
Figure 5.11	(a) TGA analysis of cathode materials; (b) FTIR spectra of cathode materials. 185
Figure 5.12	Contact angle measurements of 3 M Zn(OTf) ₂ electrolyte on cathodes: (a-c) NMO; (d-f) V _m -NMO
Figure 5.13	Adsorption of proton (a) on inter-layer water molecules; (b) on the Mn ⁴⁺ ion; (c) on the O ²⁻ ions of the NiMn ₃ O ₇ layer

vaca	nncies
	T simulation of the migration energy barrier of NiMn ₃ O ₇ lattice with and lout vacancies
_	$situ$ Ni 2p characterisation of cathode materials: (a) V_m -NMO; (b) NMO; (c) XAFS profiles of Ni L-edge of cathode materials in different states189
2p;	situ characterisation of V _m -NMO. Ex-situ XPS profiles of V _m -NMO: (a) Mn (b) Zn 2p; (c) Ex-situ Mn L _{3,2} -edge NEXAFS profiles; (d) Ex-situ O K-edge XAFS profiles
Figure 5.18 <i>Ex-s</i>	situ XRD characterisation of the V _m -NMO cathode material192
	cital images: (a-d) Unfolded separators after cycling; (e) V _m -NMO and NMO erials immersed in electrolyte for seven days
NM b va	ctrochemical analysis of the cathode materials: (a) Initial three cycles of V _m -O CV curves after activation; (b) CV comparison of V _m -NMO and NMO; (c,d) lue fitting for V _m -NMO; (e) Capacitive contribution under 0.5 mV s ⁻¹ scan rate V _m -NMO; (f) Capacitive contribution ratio for V _m -NMO
cont	ctrochemical analysis of NMO: (a,b) b value fitting for NMO; (c) Capacitive cribution under 0.5 mV s ⁻¹ scan rate for NMO; (d) Capacitive contribution ratio NMO
	T testing profiles: (a) V _m -NMO; (b) NMO; Corresponding diffusion coefficient ysis: (c) Charge; (d) Discharge
(a) I capa perfe	etrochemical performances of as-prepared Zn V _m -NMO and Zn NMO batteries. EIS profiles of V _m -NMO and NMO; (b) Rate performance; Voltage-specific acity profiles of cathode materials: (c) V _m -NMO; (d) NMO; (e) Cycling formance of V _m -NMO and NMO at 0.2 A g ⁻¹ ; (f) Cycling performance of V _m -NMO and Zn NMO batteries at 5 A g ⁻¹
List of Tab	les
	ages of AZIBs over nonaqueous Li/Na/K ion batteries. ^[10-13] Reprinted with ion from ref. ^[14] Copyright 2019 Royal Society of Chemistry19
	electric charge sets and Lennard-Jones parameters for the AMBER force field.

Figure 5.14 DFT simulation of proton adsorption sites in $NiMn_3O_7$ with and without Mn^{4+}

List of Abbreviations

Abbreviation	Full description				
ALD	Atomic Layer Deposition				
AMIBs	Aqueous Metal Ion Batteries				
APBs	Aqueous Proton Batteries				
ATR	Attenuated Total Reflectance				
ATR-FTIR	Attenuated Total Reflectance Fourier-Transform				
AIRT IIIC	Infrared Spectroscopy				
AZIBs	Aqueous Zinc-Ion Batteries				
CA	Chronoamperometry				
CEM	Cation-Exchange Membrane				
CE	Coulombic Efficiency				
CEI	Cathode-Electrolyte Interface				
CIBs	Calcium-Ion Batteries				
CVD	Chemical Vapour Deposition				
CV	Cyclic Voltammetry				
DFT	Density Functional Theory				
DMSO	Dimethyl Sulfoxide				
EDS	Energy Dispersive Spectroscopy				
EG	Ethylene Glycol				
EIS	Electrochemical Impedance Spectroscopy				
EXAFS	Extended X-ray Absorption Fine Structure				
FTIR	Fourier-Transform Infrared Spectroscopy				
FWHM	Full Width at Half Maximum				
GCD	Galvanostatic Charge/Discharge Tests				
GITT	Galvanostatic Intermittent Titration Technique				
GIXRD	Grazing Incidence X-ray Diffraction				
GGA	Generalised Gradient Approximation				

Abbreviation	Full description				
HER	Hydrogen Evolution Reaction				
HRTEM	High Resolution Transmission Electron Microscopy				
IR	Infrared Spectroscopy				
LDHs	Layered Double Hydroxides				
LIB	Lithium-Ion Battery				
LSV	Linear Sweep Voltammetry				
MD	Molecular Dynamics				
MLL	Maple-Leaf-Lattice				
MSD	Mean Square Displacement				
NCA	Lithium Nickel Cobalt Aluminium Oxide				
NEXAFS	Near Edge X-ray Absorption Fine Structure				
NMC	Lithium Nickel Manganese Cobalt Oxide				
NMP	N-methyl-2-pyrrolidone				
OER	Oxygen Evolution Reaction				
ORR	Oxygen Reduction Reaction				
PA	Polyamide				
PFOA	Perfluorooctanoic Acid				
PPM	Parts Per Million				
PVDF	Poly(vinylidene fluoride)				
PTFE	Polytetrafluoroethylene				
SDBS	Sodium Dodecylbenzene Sulfonate				
SEI	Solid Electrolyte Interphase				
SEM	Scanning Electron Microscopy				
SHE	Standard Hydrogen Electrode				
STEM	Scanning Transmission Electron Microscopy				
SDS	Sodium Dodecyl Sulfate				
TEY	Total Electron Yield				
TGA	Thermogravimetric Analysis				

Abbreviation	n Full description			
TEM	Transmission Electron Microscopy			
VASP	Vienna Ab-initio Simulation Package			
XAS	X-ray Adsorption Spectroscopy			
XPS	X-ray Photoelectron Spectroscopy			
XRD	X-ray Diffraction			
XRF	X-ray Fluorescence			

Chapter 1: Overview of Rechargeable Battery Technologies,
Problems and Strategies

Rechargeable batteries offer indispensable advantages such as short construction periods and compact size, making them well-suited for use at various distributed locations. This chapter aims to summarise a wide range of representative battery technologies, assessing their practicality and potential for innovation. Pay comparing them with aqueous zinc-ion batteries (AZIBs), AZIBs show the advantages including less-flammable, cost-effective, and environmentally friendly. These advantages set the target area for AZIBs as grid energy storage, while abundant, cost-effective zinc metal can reduce the cost per kilowatt-hour (kWh) of energy storage. The less-flammable aqueous electrolyte also contributes to the safety of the system. The high-rate performance and long-life span of AZIBs also meet the criteria for grid energy storage.

To achieve the successful application of AZIBs, the intrinsic problems, including water-related side reactions and dendrite formation. Solving these problems further leads to technical challenges, for example, the facile preparation of Zn anode protection layer and the inhibition of dendrite formation using proper electrolyte additives. Besides, as water provides a unique coordination environment for charge carriers, new mechanisms are needed to further enhance the ion transport properties of aqueous zinc ion batteries. These problems are also faced by other kinds of battery systems, and the proposed solutions for other batteries can be transferred into the toolbox for solving the problems in AZIBs.^[8, 9]

1.1 Background of rechargeable battery technologies

Monovalent ion batteries are widely investigated and some of them are already or nearly customised, including lithium-ion batteries and sodium-ion batteries. However, safety concerns remain due to the flammable organic electrolytes in these batteries. This instinct drawback leads to numerous accidents, including electrical vehicle self-initiation and mobile phone battery explosions. Compared with these monovalent batteries, zinc-ion batteries have relatively high volumetric capacity due to the transfer of two electrons per ion. The advantage of AZIBs is highlighted, which include non-flammable electrolyte, completive volumetric specific capacity, and low cost, mitigating the safety concerns and suiting for the application including grid energy storage. Besides, most of the mechanisms and materials listed below can potentially be transferable to the research of AZIBs.

Characteristics	Li	Na	K	Zn
Ionic radius [Å]	0.76	1.02	1.38	0.75
Cost of metal anode (USD) kg ⁻¹	19.2	3.1	13.1	2.2
Volumetric capacity (mAh m ⁻³)	2042	1050	609	5857
Capacity density (mAh cm ⁻³)	2061	1129	610	5855
Ionic conductivity (S cm ⁻¹)	$10^{-3} - 10^{-2}$ (organic electrolytes)			10 ⁻¹ – 6 (aqueous liquid electrolytes)
Safety	Low			High

Table 1 Advantages of AZIBs over nonaqueous Li/Na/K ion batteries.^[10-13] Reprinted with permission from ref.^[14] Copyright 2019 Royal Society of Chemistry.

1.1.1 Lithium-ion batteries

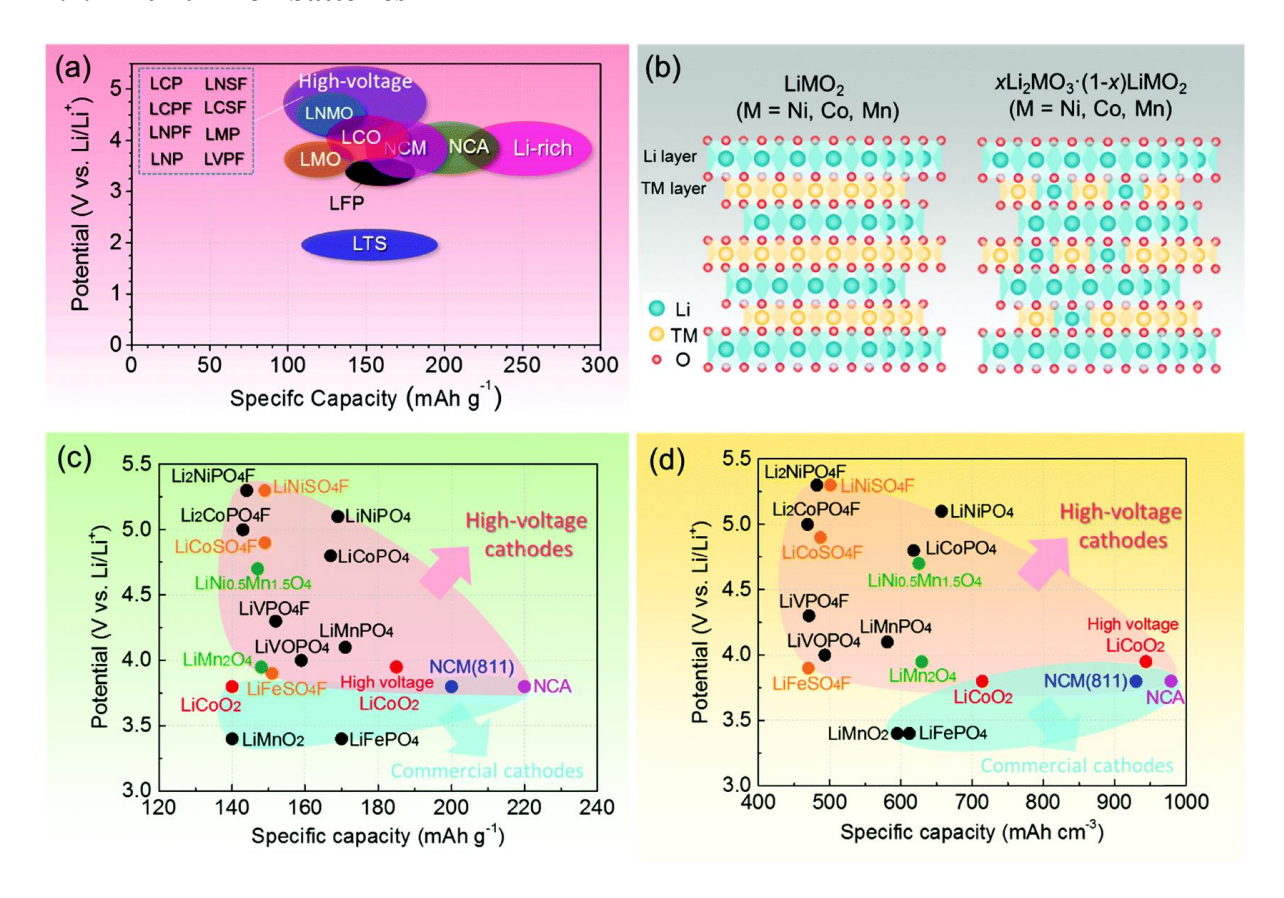


Figure 1.1 Approximate ranges of specific capacities, average discharge potentials, and crystal structures of common high-voltage LIBs cathodes: (a) Comparison with commercial cathodes; (b) Crystal structures of LiMO₂ and x Li₂MnO₃· (1-x) LiMO₂; (c) Gravimetric capacities; (d) Volumetric capacities of selected cathodes. Reprinted with permission from ref.^[15] Copyright 2020 Royal Society of Chemistry.

Lithium-ion batteries are among the most advanced rechargeable energy storage solutions available.^[16] Global electric vehicle (EV) lithium-ion cell manufacturing reached 747 GWh in 2020 and is projected to grow to 2,492 GWh by 2024.^[17] In the U.S., annual deployment of lithium-battery-based stationary energy storage is expected to increase from 1.5 GW in 2020 to 7.8 GW in 2025, potentially reaching 8.5 GW by 2030.^[18] Since the development of LiCoO₂ in 1991, lithium-ion batteries have benefited from relatively high energy density and a well-established supply chain.^[19] The six major lithium-ion battery (LIB) materials include lithium nickel manganese cobalt oxide (NMC), lithium nickel cobalt aluminium oxide (NCA), lithium iron phosphate (LFP), lithium cobalt oxide (LCO), lithium manganese oxide (LMO), and lithium titanate (LTO).^[20] NMC, for instance, leverages a high proportion of nickel to enhance

the battery's energy density. Successful commercial variants of NMC include NMC811 (comprising 80% nickel, 10% manganese, and 10% cobalt), NMC532, and NMC622.

Significant advances in battery energy storage technologies over the past decade have increased LIB energy density to 200-300 Wh/kg and decreased battery pack costs by approximately 85%, reaching \$143/kWh in 2020.^[21] Despite these achievements, challenges remain for lithium-based batteries, most lithium-ion batteries use graphite anodes, while the cathode composition varies and typically includes lithium, nickel, manganese, cobalt, or iron. This composition is critical to the battery's capacity, power, performance, cost, safety, and lifespan. Major manufacturing countries rely heavily on imported raw minerals like lithium, nickel, and cobalt, posing a risk to supply chain stability.^[22] The ongoing challenge of scaling up clean technology supply chains to meet the demands of economic development and high-quality living standards continues to drive research into energy storage solutions that offer higher energy density, lower costs, faster charging times, and more robust systems. Addressing these challenges is crucial for the continued development and deployment of efficient and sustainable energy storage solutions.

It is essential to optimise the singly charged cations used in lithium-ion batteries, involving adopting multiple-electron redox couples or multivalent working ions such as Mg^{2+} or Zn^{2+} instead of Li^+ . [23, 24] This shift necessitates a comprehensive redesign of the electrolyte, anode, and multiple-electron redox centre systems, which is a focal point in current research aimed at developing battery systems beyond conventional lithium-ion technology.

1.1.2 Lithium-sulphur batteries

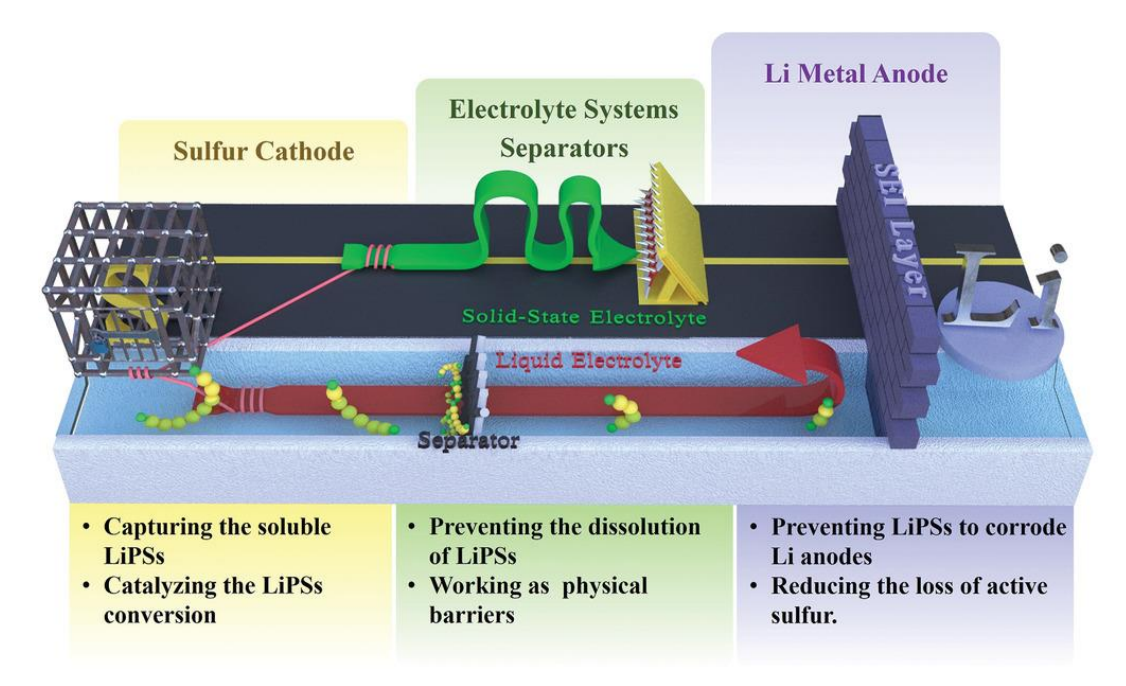


Figure 1.2 Schematic illustrations of the strategies and operation mechanisms of the modified sulphur host, electrolyte systems, functional separators, and anode surface engineering for the inhibition of LiPSs shuttle. Reprinted with permission from ref.^[25] Copyright 2022 John Wiley and Sons.

Lithium-sulphur (Li-S) batteries leverage earth-abundant and high-capacity sulphur as the positive electrode. The multivalence of sulphur allows it to adopt a wide variety of oxidation states, and its relatively low density makes Li-S batteries one of the most promising high-capacity and low-cost battery systems. [26] The redox process in lithium-sulphur (Li-S) batteries operates via lithium polysulphide (LiPS) intermediates, comprising Li₂S_x chains that extend to the final component, Li₂S, where x = 1. Despite these significant advantages, Li-S batteries face several intrinsic challenges that need resolution for practical application.

The solid sulphur and Li₂S are inherently insulating, leading to low utilisation of active materials and substantial electrochemical polarisation. Additionally, the high-volume expansion (~80%) of solid sulphur into Li₂S exerts considerable stress on the host structure, causing the detachment of sulphur species from the conductive substrate. Another challenge is the notorious shuttle effect caused by soluble lithium polysulphides, resulting in the loss of active materials and a rapid decrease in capacity.^[25] Furthermore, the growth of lithium dendrites, induced by non-uniform lithium deposition and the formation of a passivation layer

from chemical reactions between active LiPSs and fresh lithium, leads to rapid battery decay and potential safety hazards.

High sulphur loading in electrodes is crucial for the successful market implementation of Li-S technology. However, these challenges are exacerbated in high-loading cathodes due to the difficulty in maintaining a continuous electron/Li⁺ channel over thick cathodes and protecting the anodes from LiPS corrosion and dendrite formation at high currents. Despite advancements in suppressing the polysulphide shuttle effect, the current cycle performance of Li-S batteries still falls short of practical demands.

Innovative strategies have been developed to address these challenges. Cheng et al. introduced the d-p hybridisation state between single-atom catalysts (SACs) and Li-S species, guiding the design of SACs for Li-S batteries.^[27] Transition metals with low atomic numbers, such as titanium (Ti), form strong bonds with lithium polysulphides (LiPSs) and lithium sulphide (Li₂S), reducing energy barriers for LiPSs reduction and Li₂S oxidation. Ti SACs enable high specific energy levels with low catalyst loading and high area-sulphur loading through an effective 3D conductive transport network. Geng et al. introduced a method for creating threedimensional porous graphitic carbon composites incorporating sulphur nanoparticles (3D S@PGC).^[28] These composites achieve high sulphur content (up to 90 wt%) and exhibit remarkable performance, including high sulphur utilisation, impressive specific capacity, long cycling life, and excellent rate capability even at high charge/discharge currents. Conventional electrolytes and additives have also been explored to address capacity decay. Huang et al. proposed an electrochemical approach to revive stored Li₂S and reactivate non-functioning Li-S batteries in non-aqueous electrolytes (NSEs). [29] Utilising solvents such as diglyme, acetonitrile, and 1,2-dimethoxyethane, Li-S batteries demonstrated enhanced cycling stability and faster dynamics.

These advancements in optimising both cathode architecture and electrolyte composition highlight the importance of improving the overall performance and longevity of Li-S battery systems. Continued research and development in these areas are critical to the development of robust, high-capacity energy storage solutions.

1.1.3 Sodium-ion batteries

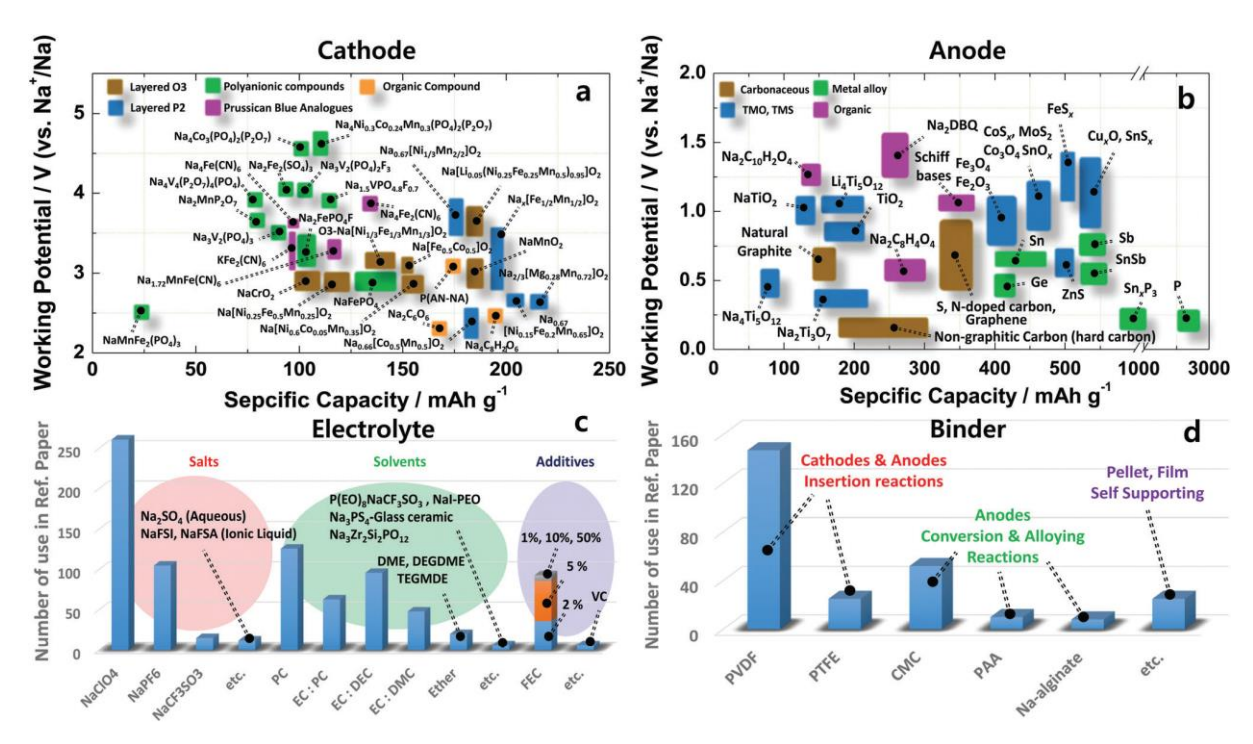


Figure 1.3 Recent research progress in sodium-ion batteries: (a) Cathode, (b) Anode, (c) Electrolyte and (d) Binder. Reproduced with permission from Ref. [30] Copyright 2017 Royal Society of Chemistry.

Compared to lithium, sodium operates using the same mechanism, utilises the same electrolyte, and employs similar manufacturing technology, making it a promising candidate for rapid commercialisation. Sodium is abundant in the Earth's crust and available at a lower cost than lithium, presenting potential advantages for sodium-ion batteries (SIBs) over LIBs.^[31] Due to the similar ionic radius of sodium (Na⁺) and lithium (Li⁺), many cathode materials used in LIBs can also be utilised in SIBs. However, there are distinct differences between these systems. Na⁺ ions are larger, with a radius of 1.02 Å compared to 0.76 Å for Li⁺ ions. This size difference impacts phase stability, transport properties, and interphase formation. Sodium is also heavier, weighing 23 g mol⁻¹ compared to lithium's 6.9 g mol⁻¹, and has a higher standard electrode potential at 2.71 V vs. SHE, compared to 3.02 V vs. SHE for lithium. Consequently, SIBs typically have lower energy density. [32] Nonetheless, the mass of cyclable Li or Na that constitutes only a small fraction of the overall component weight, with capacity primarily influenced by the host structures' properties. Therefore, transitioning from LIBs to SIBs should theoretically not affect energy density. Additionally, aluminium, which exhibits an alloy reaction with lithium at voltages below 0.1 V vs. Li/Li⁺, is suitable as a current collector for anodes in sodium cells. This makes aluminium a more economical choice compared to copper when used as an anode current collector for SIBs. These factors highlight the potential and advantages of SIBs in future energy storage applications.

Research on SIBs is significantly hindered by the lack of suitable anode materials. Graphite anodes, commonly used in LIBs, are typically unsuitable for SIBs due to the interlayer distance of graphite being 0.34 nm, which is slightly smaller than the theoretical minimum required for Na⁺ ion insertion of 0.37 nm. Currently, most research concentrates on hard carbon materials that rely on graphite nano-crystallites and nanovoids. However, these materials are not ideal, and they can only operate within a limited potential range. Anode materials for SIBs are categorised based on the reaction mechanisms during sodiation/desodiation processes. Carbonaceous and titanium-based oxides have been extensively studied due to their ability to undergo insertion reactions. Adelhelm et al. demonstrated that the limitations of graphite can be overcome by utilising co-intercalation phenomena in a diglyme-based electrolyte. [33] The resulting compound is a stage-I ternary intercalation compound with an approximate stoichiometry of Na(diglyme)₂C₂₀. This electrode reaction is characterised by impressive energy efficiency, minimal irreversible loss in the initial cycle, and exceptional cycle life, maintaining capacities of nearly 100 mAh g⁻¹ for 1,000 cycles with coulomb efficiencies exceeding 99.87%. Conversion reactions have also shown promise. Balaya et al. suggested that Fe₃O₄ materials could potentially be involved in conversion reactions with Na⁺ ions at a discharge voltage of 0.04 V, following the reaction: Fe₃O₄ + 8 e⁻ + 8 Na⁺ \rightarrow 3 Fe + 4 Na₂O.^[34] Alloying reactions are another area of interest. Metals including Sn and Bi, metalloids such as Si, Ge, As, and Sb, and polyatomic nonmetal compounds like P from groups 14 or 15 of the periodic table have garnered significant attention as potential anode materials for SIBs. Mulder et al. found that it is possible to achieve reversible electrochemical sodium ion uptake in silicon at room temperature. Both initial amorphous and crystalline Si play significant roles in the electrochemical sodiation process, where Si and NaSi coexist during Na insertion into amorphous Si and on the surface of Si crystallites.^[35] A solid solution desodiation reaction is observed during Na extraction. These studies underscore the diverse strategies and significant potential for developing effective anode materials for sodium-ion batteries, critical for advancing this technology in energy storage applications.

1.1.4 Proton batteries

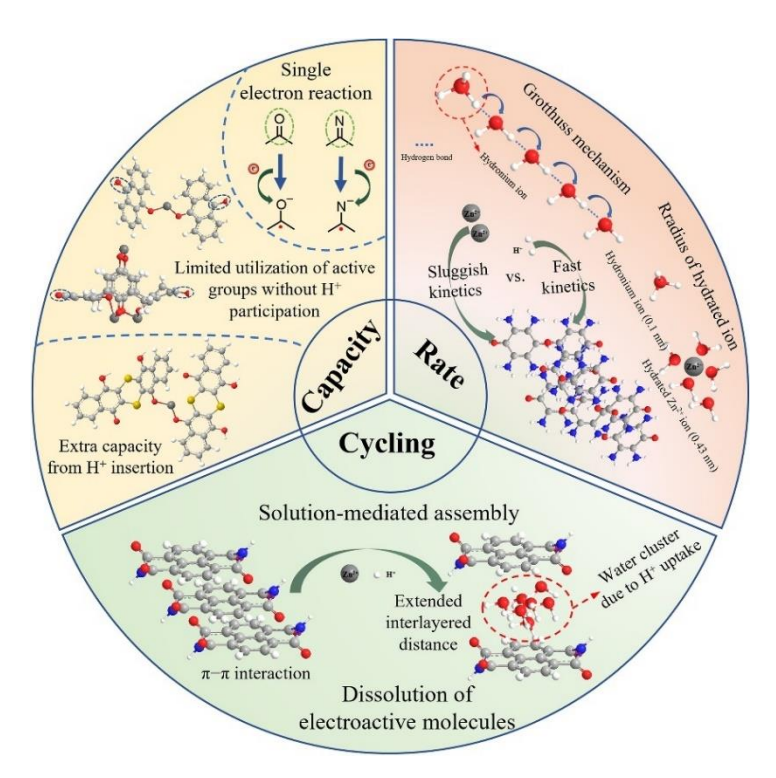


Figure 1.4 The impact of proton storage on electrochemical performance. Reprinted with permission from ref.^[36] Copyright 2022 UESTC and John Wiley & Sons.

Compared to AZIBs, aqueous proton batteries (APBs) offer significant advantages, including superior ion conductivity within host structures and exceptional rate performance. These benefits arise from the unique Grotthuss conduction mechanism of protons in the aqueous electrolyte and host materials. This mechanism allows protons to move rapidly along the hydrogen-bonding network through oxygen "bridges," eliminating the need for energyintensive desolvation of metal ions and accelerating ion uptake. While aqueous metal-ion batteries (AMIBs) have the potential for high theoretical specific capacities, their ion diffusion kinetics are limited, necessitating battery systems capable of rapid charging. Aqueous metalproton batteries (AMPBs) Based on proton insertion and extraction, have been developed to address the challenges of traditional batteries. These batteries operate similarly to traditional AMIBs but use a distinct redox mechanism. During charging and discharging, the cathode releases or absorbs protons supplied by water molecules instead of metal ions. This protonbased approach reduces the volume expansion of cathode materials, preventing periodic stress that could negatively impact device performance. Additionally, the elevated electrolyte pH during discharge hinders hydrogen formation in the initial charging phase, enhancing stability during cycling.

Protons, as non-metallic charge carriers, offer numerous advantages. The abundance of hydrogen on Earth ensures the sustainability and affordability of proton batteries. The low molar mass of protons allows for higher electrode capacity, and the smaller hydrated ion radius of H⁺ promotes improved diffusion kinetics while minimising volume expansion during deintercalation and intercalation processes.^[37] Driven by the intriguing field of proton chemistry, researchers are exploring a wide range of inorganic and organic materials with exceptional capabilities to keep pace with the rapid advancements in APBs technology. Currently, cathode materials for APBs are primarily divided into two categories: inorganic and organic. For organic materials, Niu et al. developed an aqueous Pb-quinone battery using pchloranil/reduced graphene oxide (PCHL-rGO) in an H₂SO₄ electrolyte, which exhibits H⁺ insertion chemistry, resulting in rapid reaction kinetics and excellent rate capability. [38] Ji et al. reported findings on the hydronium intercalation into a crystalline organic electrode of PTCDA. [39] This electrode demonstrates a specific capacity of 85 mAh g⁻¹, reversible structural changes throughout cycling, and a relatively stable cycling life. Ex-situ XRD revealed a noticeable yet reversible lattice expansion, confirming that the intercalating ions are hydronium ions rather than bare protons. This research indicates that all-organic proton batteries typically consist of two distinct molecules with significant disparity in the redox peak position between the anode and cathode, leading to a more intricate operation process and increased costs. For inorganic materials, Dai et al. prepared H_xMn₂O₄ microspheres with a spinel structure using a straightforward cation exchange method.^[40] XRD and Raman patterns indicated that the spinel framework of MnO₆ octahedron in ZnMn₂O₄ remained unchanged following the removal of Zn²⁺ ions. The presence of H⁺ ions was confirmed through EDS, EA, TG, and XPS analyses. The impressive performance of the H_{1.57}Mn₂O₄ electrode is attributed to its stable spinel structure, porous morphology, and favourable tunnel sites for the insertion and extraction of H⁺ and Zn²⁺ ions. Wang et al. observed different reaction kinetics in electrodeposited MnO₂ during discharging when H⁺ and Zn²⁺ were successively inserted.^[24] The MnO₂, deposited through electrodeposition, consists of nanocrystals with particle sizes usually smaller than 10 nm. This structure provides numerous contact interfaces between the electrode and electrolyte and shorter paths for ion diffusion, allowing even slow electrochemical reactions to occur. The Zn/MnO₂ battery demonstrates stability lasting up to 10,000 cycles at 6.5 C, with an impressively low-capacity decay rate of only 0.007% per cycle. These advancements in both organic and inorganic materials highlight the ongoing progress and potential of APBs in achieving high-performance and durable energy storage solutions.

Zinc-ion batteries have a high volumetric capacity due to the transfer of two electrons per ion. While it is not the only multivalent charge carrier (e.g., Mg²⁺, Al³⁺), it has some practical advantages in aqueous environment than other multivalents. First, zinc anode is relatively stable in air or aqueous electrolytes, while aluminium and magnesium anodes tend to form passivation layers that hinder the transport of ions. Second, zinc ions have improved ion mobility than other multivalent ions, which leads to enhanced rate performance. The further development of AZIBs can benefit from leveraging some common principles and strategies faced by multivalent batteries (e.g., dendrite formation inhibition, ion diffusion enhancement). The following introduction on multivalent ion batteries aims to summarise these transformable strategies.

1.1.5 Calcium-ion batteries

Calcium, widely distributed throughout the Earth's crust, stands as the fifth most abundant element. It boasts global resource availability, non-toxicity, and excellent thermal stability. The redox potential of Ca/Ca²⁺ is -2.87 V versus the standard hydrogen electrode (SHE), closely mirroring that of Li/Li⁺. Calcium metal's volumetric and gravimetric capacities are remarkably high, reaching values of 2,073 mAh cm⁻³ and 1,337 mAh g⁻¹, respectively.^[41] Additionally, Ca²⁺ ions exhibit smaller charge density and polarisation strength compared to other multivalent metal ions such as Mg²⁺, Al³⁺, and Zn²⁺, resulting in superior diffusion kinetics and higher power density. Consequently, calcium-ion batteries (CIBs) are highly promising for large-scale energy storage solutions, offering significant potential for the future of energy technology.

Despite the promise of CIBs, several challenges must be addressed for their successful development. The viscosity of the electrolyte in CIBs is higher compared to LIBs and NIBs, primarily due to strong ion pairing between calcium ions and electrolyte molecules, which results in lower ion mobility. Furthermore, CIBs typically require operation at elevated temperatures, ranging from 50 to 100° C. [42] Increasing the operating temperature can lead to the formation of side products such as CaCl₂, Ca(OH)₂, and CaCO₃ during the electrochemical process, which do not conduct calcium. Additionally, the formation of CaF₂ from electrolyte decomposition hinders the Coulombic efficiency (CE) of calcium deposition. [43] Recent studies have shown promising results in addressing these challenges. For instance, Palacin et al. demonstrated the practicality of calcium anodes operating at 100° C using a 0.45 M Ca(BF₄)₂ in ethylene carbonate (EC) electrolyte. [44] Symmetric Ca//Ca cells in this electrolyte exhibited

excellent cyclability, with stable SEI formation allowing Ca²⁺ ions to pass through. Bruce et al. provided evidence of successful calcium plating and stripping at room temperature, achieving capacities of 1 mAh cm⁻² at a rate of 1 mA cm⁻² with low polarisation and repeatability for over 50 cycles.^[45] These findings highlight the potential for further development and optimisation of calcium-ion battery technology, proving that substantial amounts of calcium can be effectively plated and stripped with minimal polarisation.

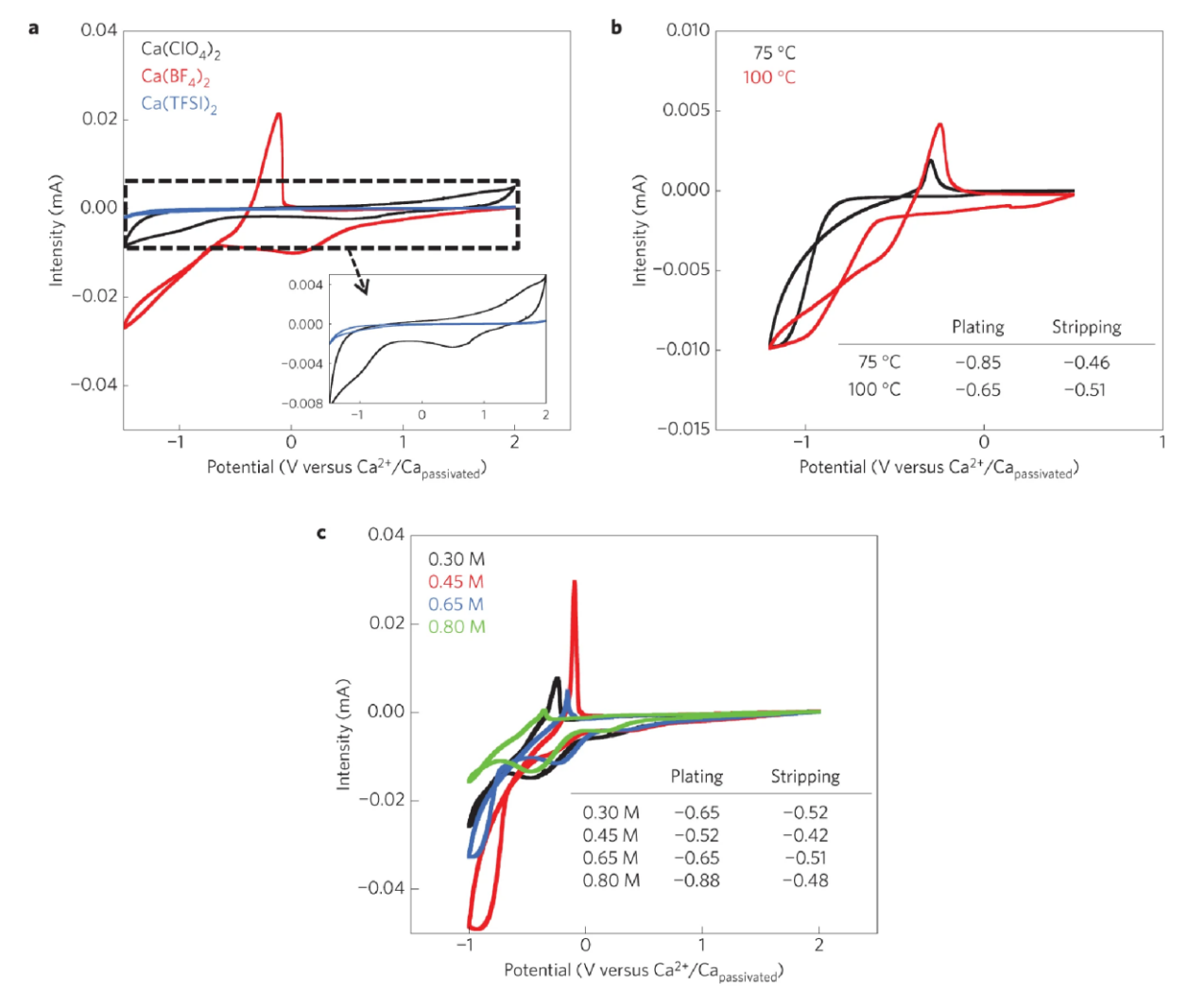


Figure 1.5 Cyclic voltammograms of EC: PC electrolytes at a scan rate of 0.5 Mv s⁻¹, showing: (a) 0.3 M concentration of different salts at 100°C; (b) 0.65 M concentration of Ca(BF₄)₂ at 75°C and 100°C; and (c) Various Ca(BF₄)₂ concentrations ranging from 0.3 M to 0.8 M at 100°C. Insets in (a) show an expanded scale, and insets in (b) and (c) display onset potentials for the redox process. Reprinted with permission from ref.^[44] Copyright 2017 Springer Nature.

1.1.6 Magnesium-ion batteries

Compared to other ion storage systems, Mg^{2+} can be reduced to its metallic form with a more uniform structure, allowing for deposition without dendrites even at high current densities. Magnesium (Mg^{2+}) is smaller than lithium (Li^+), with a size of 0.72 Å compared to the 0.76 Å size of Li. Moreover, Mg metal is much less reactive than either Li or Na, which eases constraints on safety and manufacturing. However, Mg cannot be plated onto conventional Mg metal due to the formation of a passivation layer. Magnesium-ion batteries MIBs operate at lower voltages compared to LIBs, with the reduction potential of Mg being 0.67 V more positive than that of Li (-2.37 V vs. -3.04 V vs. SHE, respectively). Magnesium cathode materials are observed or expected to operate approximately 1 V lower than the same material in LIBs. The cell voltage can be expressed in terms of the Gibbs free energy using the equation $V = -\Delta G/nF$, where ΔG represents the difference in Gibbs free energy between the relevant cathode and anode reactions, n represents the number of electrons exchanged, and F denotes the Faraday constant. This theoretical framework underpins the potential advantages of magnesium as an anode material, offering significant promise for the development of high-energy-density storage systems.

High-performance MIBs rely on the efficient and reversible shuttling of Mg²⁺ between the cathode and anode. However, the bivalent nature of Mg²⁺ charge carriers introduces a significant polarising effect, generating strong interactions with polar species or moieties. [47] Aurbach et. al have developed rechargeable Mg battery systems that demonstrate substantial potential for various applications. [48] These systems utilise electrolyte solutions containing Mg organohaloaluminate salts paired with Mg_xMo₃S₄ cathodes, which facilitate the reversible intercalation of Mg ions and exhibit relatively fast kinetics. Nazar et al. introduced a new material, a thiospinel, which displays fully reversible Mg²⁺ electrochemical cycling when paired with a Mg anode. [49] This finding is supported by diffraction and first-principles calculations. The capacity of this thiospinel material reaches nearly 80 % of its theoretical value at a practical rate (C/5) at 60°C, resulting in a specific energy of 230 Wh kg⁻¹, twice the capacity of the Chevrel benchmark. These results underscore the advantages of using "soft" anions to enable the effective movement of divalent cations in practical applications, highlighting the significant progress in the development of high-performance Mg batteries.

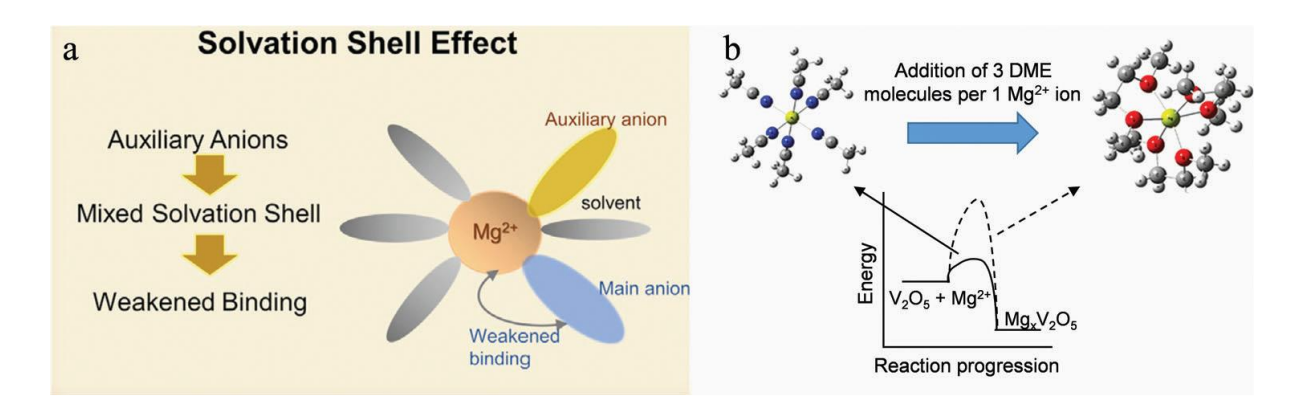


Figure 1.6 (a) Competition between solvent molecules and anions for coordination with Mg²⁺. Reproduced with permission from ref.^[50] Copyright 2020, Elsevier. b) Modification of the solvation structure in Mg(ClO₄)₂/ACN electrolyte with the addition of DME. Reproduced with permission from ref.^[51] Copyright 2018 John Wiley and Sons.

1.1.7 Aluminium-ion batteries

With its three-electron redox properties (Al3+/Al), resulting in high capacity, low cost, low flammability, easy handling, and low reactivity, aluminium-based (Al-based) batteries have the potential to serve as a viable alternative to LIB systems. Aluminium boasts an impressive specific capacity per mass unit of 2,980 Ah kg⁻¹ and the highest capacity per unit volume at 8,046 Ah L⁻¹. Given its relatively low atomic weight, aluminium demonstrates great potential as an anode material. However, the development of aluminium-based batteries has been impeded by several significant challenges.^[52] One major obstacle is the lack of suitable electrolyte compositions that can facilitate the reversible plating and stripping of Al³⁺ ions. The formation of a mixed cationic and anionic solid electrolyte interphase (SEI) layer obstructs the migration of divalent ions and further complicates the issue. Additionally, problems such as hydrogen side reactions and anode corrosion present challenges for the widespread implementation of aluminium-ion batteries. Overcoming these hurdles is essential for advancing the development and application of Al-based batteries in energy storage systems. Nonaqueous electrolytes, especially room-temperature ionic electrolytes, are highly favoured due to their low vapour pressure and wide electrochemical windows.^[53] Chloro-aluminatebased ionic liquids have been extensively studied as system electrolytes. For instance, Dai et al. reported the potential for C-Cl bonding formation at the graphite edge, which could occur through a reaction between a chlorine atom in the AlCl₄ anion and a carbon atom on the graphite layer edge. [54] Using natural graphite flake film as the cathode, along with an aluminium anode in an ionic liquid electrolyte, significantly increased the capacity of the

Al/NG battery to 110 mAh g⁻¹, compared to 66 mAh g⁻¹ for a similar cell made with pyrolytic graphite. Choi et al. introduced a tetradiketone macrocycle as a high-capacity cathode material for divalent aluminium-ion batteries (AIBs).^[55] The design utilises the radical destabilisation effect in the active molecule to selectively promote divalent ion storage. Through a combination of density functional theory (DFT) calculations and experimental analyses, it was discovered that the carbonyl groups at each corner of the TDK can bind with a divalent AlCl²⁺ ion upon reduction. This unique binding mechanism allows for an impressive specific capacity of 350 mAh g⁻¹ as an AIB cathode. Additionally, TDK demonstrated outstanding cyclability, retaining 78% of its capacity after 8,000 cycles.

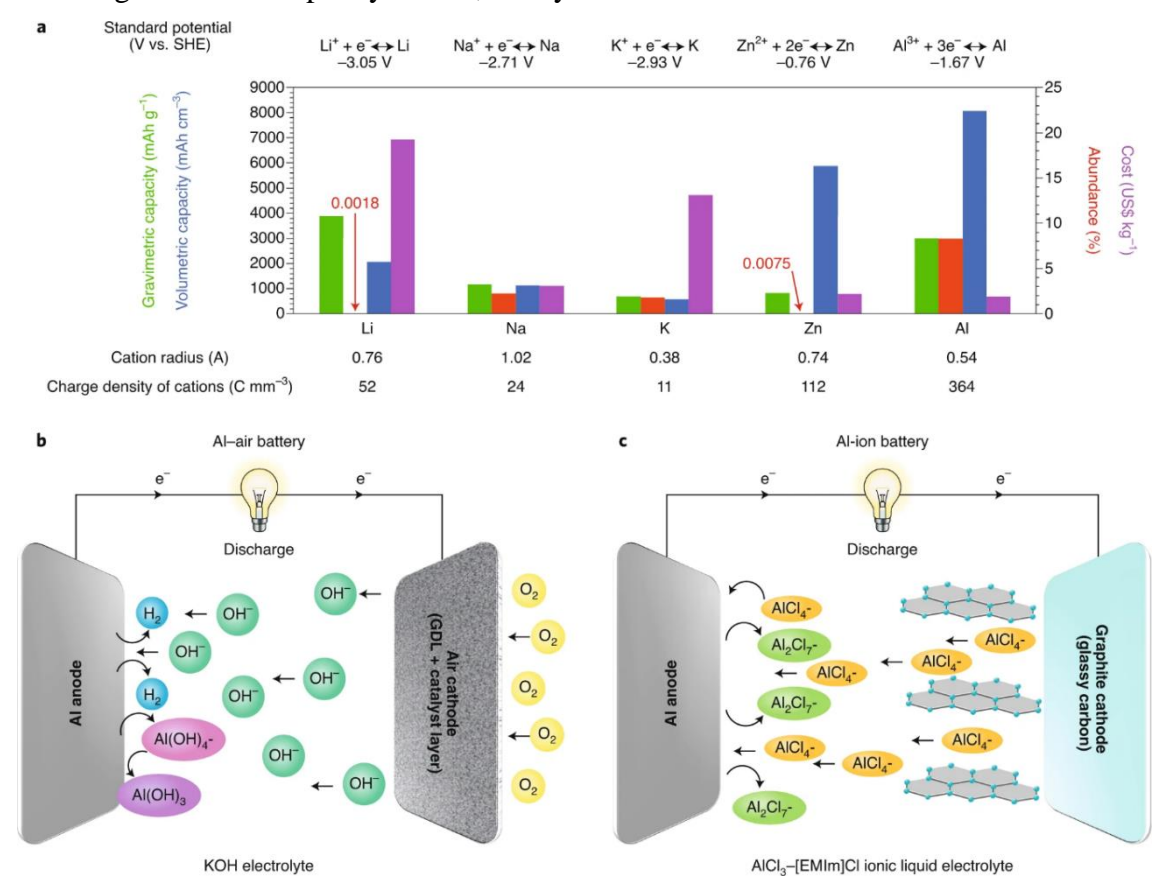


Figure 1.7 (a) Comparison of gravimetric and volumetric capacities as well as cost, abundance, standard potentials, cation radius and charge density of cations for Li, Na, K, Zn and Al. [56, 57] (b) Schematic illustration of the discharge process in an Al–air battery with aqueous KOH electrolyte showing the movement of hydroxide ions to the anode causing undesired corrosion and passivation phenomena. (c) Schematic of the discharge process in an Al-ion battery with non-aqueous ionic liquid electrolyte including a representation of intercalated chloroaluminate anions in the graphite cathode. Reprinted with permission from ref. [52] Copyright 2020 Springer Nature.

1.2 Aqueous zinc-ion battery research problems

The research problem for zinc ion batteries is mostly related to the aqueous electrolyte. For the anode part, it leads to the side reactions including HER and the formation of zinc hydrated sulfate at the interface. For the cathode part, it leads to the dissolution of cathode materials due to the water solubility of transition metal ions like Mn²⁺ and Prussian blue analogues. Besides, dendrite formation is inherent to AZIBs, and this problem becomes more obvious in high current densities. In summary, AZIBs have the advantage of high ion conductivity and higher safety, but at the cost of water-related side reactions and additional desolvation energy during cycling. These issues combined with the unclear energy storage mechanism in aqueous system, hinder the further development of AZIBs. These problems also lead to rethinking the role of water in AZIBs, including how to mitigate the side reactions and explore the potential benefits of aqueous systems. The following cases details the pain points and relevant solutions in zincion battery research.

1.2.1 Cathode material dissolution

Cathode materials containing transition metal ions exhibit multiple valence states, leading to various crystal structures. Taking manganese-based materials as an example, manganese typically displays a mixture of Mn³⁺ and Mn⁴⁺ in its oxide form. During the charging process, the ratio of Mn^{3+} increases due to the intercalation of H^+/Zn^{2+} ions.^[58] High-spin Mn^{3+} , with an electron configuration of t_{2g}^3 e_g^1 in the 3d orbital, usually results in a Jahn-Teller distortion, making it susceptible to changes during cycling. [59] This is the underlying cause of the instability of cathode materials. The redox reactions in cathode materials in AZIBs vary depending on the type of electrolyte salt and the pH value of the aqueous electrolyte. The dissolution is related to the solubility of intermediate products formed between the electrode and electrolyte. For instance, AZIBs experience hydrogen evolution reaction (HER) and oxygen evolution reaction (OER) at the edges of the working potential. Oxygen evolution increases the acidity of the electrolyte, leading to the corrosion of manganese oxide and the formation of MnOOH. [60] The dissolution of the cathode material can be observed through the colour change of the separator after cycling and the colour change of the rinse solution during the synthesis of cathode materials. This dissolution problem becomes more pronounced when attempting to increase the energy density of AZIBs by expanding the working voltage window, underscoring the importance of optimising electrolyte composition and operating conditions to reduce cathode instability and enhance overall performance and longevity.^[61]

Vanadium-based cathodes experience significant dissolution when cycled in aqueous ZnSO₄ and Zn(CF₃SO₃)₂ in AZIBs, primarily due to the high polarity of water molecules and anions.^[61] Structural disintegration is exacerbated during cycling by the simultaneous insertion of coordinated water molecules and Zn²⁺ ions into the interlayer spacing or tunnels of vanadium cathodes. This process forms hydrogen bonds with the lattice oxygen, reducing V-O bond strength. [62] Capacity fading is notable in V-based cathodes at low current densities, although they exhibit excellent cyclability at high rates due to the inhibited vanadium dissolution. The dissolution process is complex because of the multivalence of vanadium. Boyd et al. found that vanadium dissolution is significantly influenced by the activity of H⁺ in the aqueous electrolyte. [63] At a pH below 3.0, vanadium exists as VO²⁺ when the potential is under 0.45 V vs. SHE and 1.21 V vs. Zn/Zn²⁺. For pH levels between 3.0 and 6.0, vanadium compounds transform into VOH²⁺, requiring a reduced potential for full conversion (-0.05 V vs. SHE for pH = 3, -0.60 V vs. SHE for pH = 6). When the operating potential exceeds 0.40 V (vs. SHE, 1.06 V vs. Zn/Zn²⁺), H₃V₂O₇⁻ becomes the primary dissolved species in mildly acidic electrolytes, indicating that vanadium dissolution is prevalent in slightly acidic environments. The disintegration mechanism of halogen cathodes is more complex than that of vanadium and manganese-based materials. [64, 65] In non-aqueous electrolytes, the reaction pathway of $I^- \leftrightarrow I_3^ \leftrightarrow$ I₂ is less efficient compared to the one-step conversion process of I⁻ \leftrightarrow I₂ in aqueous rechargeable Zn//I₂ batteries. Formation of the I₃⁻ intermediate decreases the efficiency of iodine species, leading to lower energy density and stability due to its high solubility in aqueous electrolytes. The liquid-liquid conversion reaction mechanism in Zn//I₂ batteries demonstrates rapid kinetics and excellent rate capabilities, making it a promising option for liquid-flow batteries. During charging, the accumulation of I₂ leads to the formation of polyiodide species like I₅, I₇, and I₉. These soluble species, along with I₃, migrate towards the Zn anode due to the concentration gradient, causing irreversible reactions between polyiodides and Zn metals. This results in the loss of active material at both the cathode and anode, compromising battery performance.

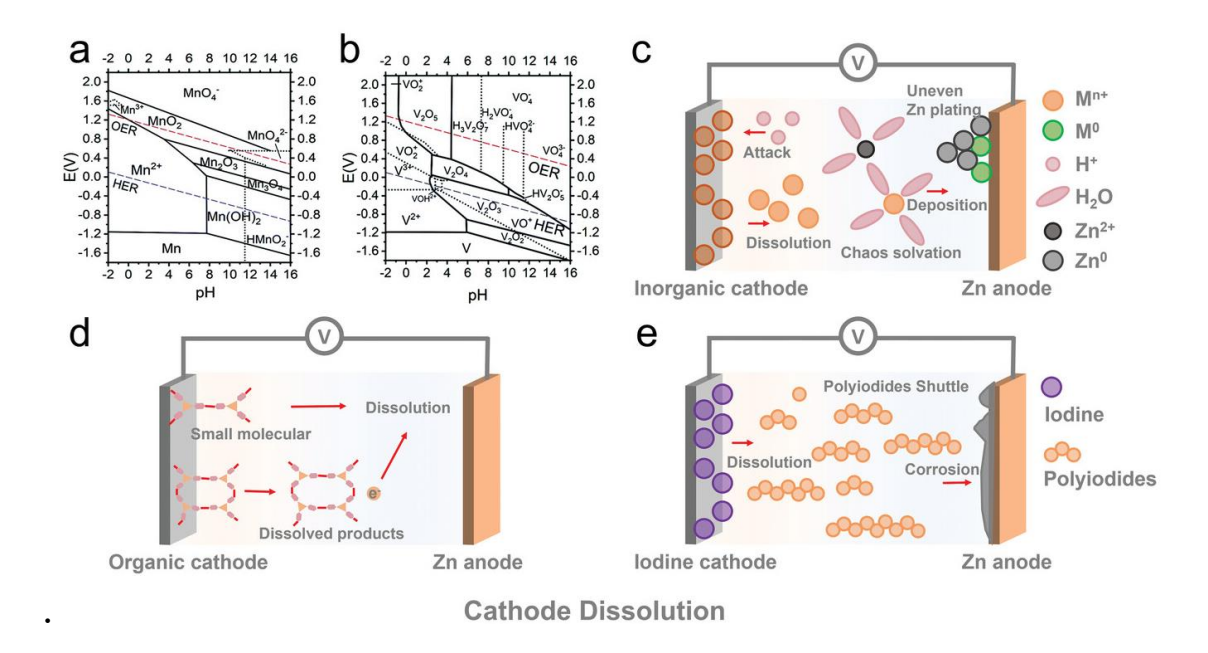


Figure 1.8 Pourbaix diagram for (a) Manganese oxides and (b) Vanadium oxides. Schematic illustration of dissolution processes for (c) Inorganic cathodes, (d) Organic cathodes, and (e) Iodine cathodes. Reprinted with permission from ref.^[66] Copyright 2024 Wiley VCH GmbH.

1.2.2 Parasitic byproducts formation

Water, as a high polarity electrolyte, can undergo potential OER and HER within the cycling voltage range of AZIBs. [67] The HER consumes H⁺ in the electrolyte, generating OH⁻ ions that react with Zn²⁺ and SO₄²⁻.[68] Conversely, OER reactions generate H⁺, leading to the dissolution of cathode materials.^[69] Repeated discharge and charge cycles exacerbate the formation of unforeseen byproducts. The choice of electrolytes plays a crucial role in the energy storage performance of AZIBs. Side reactions such as HER and OER are highly dependent on the pH value, which is influenced by the composition and concentration of the aqueous electrolyte. [70] A significant number of byproducts, primarily zinc salts, are generated at the cathode during repeated charging and discharging cycles. These byproducts contribute to increased interfacial impedance and decreased cathode capacity over time. The primary unwanted products for cathode materials facilitating H⁺ intercalation are layered double hydroxides (LDHs), which form due to the increase in OH⁻ concentration caused by H⁺ consumption on the cathode side.^[71] The generated OH ions react with Zn2+ and various anions, leading to the formation of byproducts that depend on the type of anion present. In ZnSO₄ aqueous electrolyte, the main byproduct is Zn₄SO₄(OH)₆·5H₂O, whereas in ZnCl₂ aqueous electrolyte, Zn₅(OH)₈Cl₂·H₂O is the commonly identified byproduct.

Additional byproducts such as $Zn_x(CF_3SO_3)_y(OH)_{2x-y}\cdot nH_2O$, $Zn_{12}(CF_3SO_3)_9(OH)_{15}\cdot xH_2O$, and Zn₄ClO₄(OH)₇ can be generated in Zn(CF₃SO₃)₂ and ZnClO₄ aqueous electrolytes, respectively. The crystalline structure of anion-based byproducts varies based on interlayer distances, which are approximately 10, 11, and 13 angstroms for Zn₆(NO₃)₂(OH)₈·2H₂O, Zn₄SO₄(OH)₆·5H₂O, and Zn_x(CF₃SO₃)_v(OH)_{2x-v}·nH₂O, respectively. The Zn_x(CF₃SO₃)_v(OH)_{2x-v}·nH₂O compound, with the widest interlayer, demonstrates significant enhancement in capacity due to the expanded 3D Zn²⁺ diffusion pathway. In addition to electrolyte pH, other variables like dissolved O₂, Mn³⁺ ions, and free water have been found to influence the creation of LDH products.^[72] The function of these chemicals remains incompletely understood. Various beneficial outcomes have been suggested, such as stabilising the chemical environment of cathode materials (specifically, the pH of electrolytes) and preventing cathode dissolution. Conversely, detrimental effects like heightened interfacial impedance and the depletion of electrolyte and Zn supplies have also been identified. The pros and cons of LDHs are clearly outlined. When using cathode materials that involve H⁺ intercalation, an increase in localised OH concentration is unavoidable. This requires the production of LDHs with high ionic resistance to stabilise pH changes. Instead of merely crediting enhanced cycling stability to the creation of LDHs, it may be more suitable to consider this as a consequence of self-regulation within the electrolyte. It is important to acknowledge that this passive adaptation may not be the most efficient strategy, as its effectiveness is limited. An effective solution to this issue is adding pH buffering additives like ZnO, La(OH)₃, and Mg(OH)₂ to the electrolytes.^[73,74] This helps maintain a steady solution environment without leading to bulk electrolyte consumption or increased impedance.

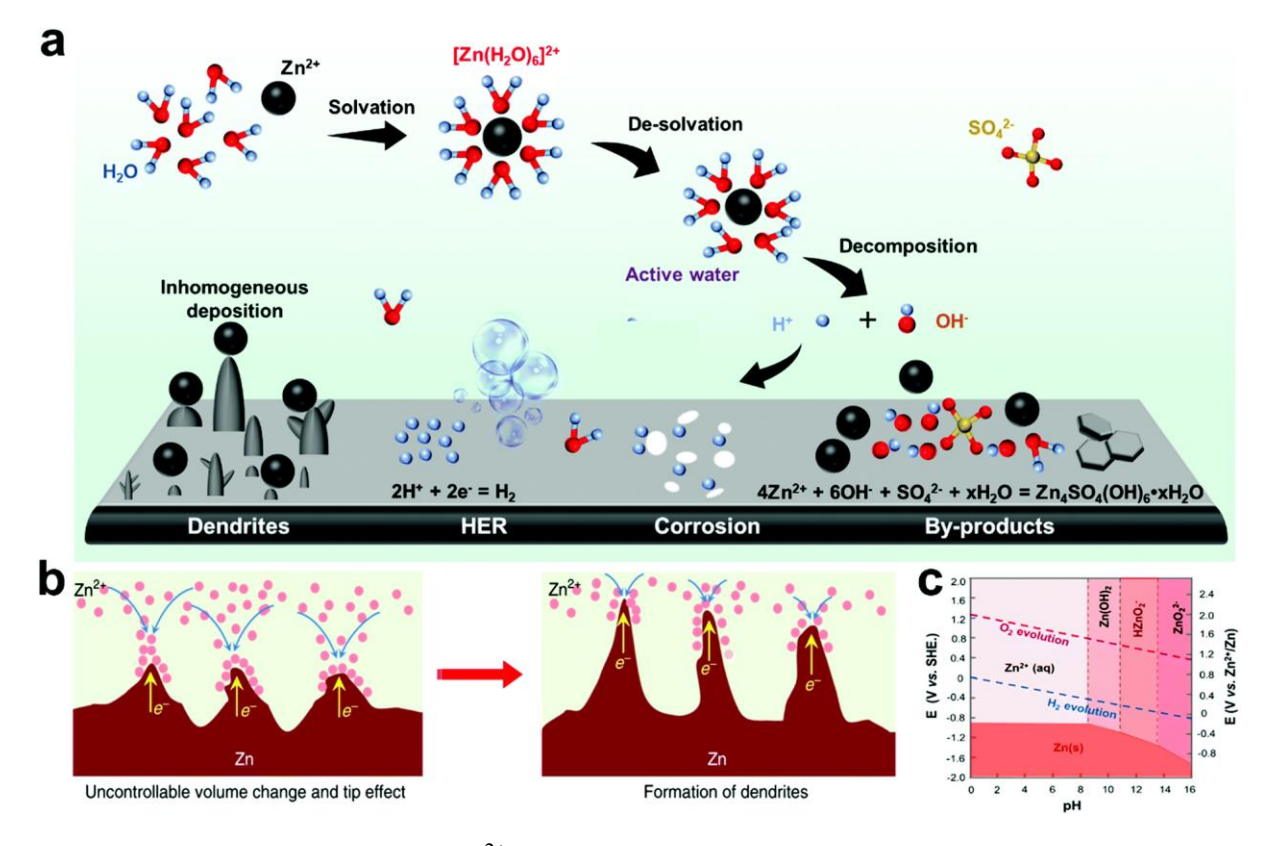


Figure 1.9 (a) Schematic of the Zn^{2+} solvation process and interfacial interaction between the zinc metal anode and the electrolyte. (b) Electric field simulation of zinc anodes. Reproduced with permission from ref.^[75] Springer Nature. (c) Pourbaix diagram for 10^{-6} mol L^{-1} Zn^{2+} . Reproduced with permission from Ref.^[76] Copyright 2022 Royal Society of Chemistry.

1.2.3 Cathode material phase change

Phase changes in cathode materials are inevitable due to the intercalation of charge carriers, significantly impacting the performance and stability of AZIBs. Understanding these changes is crucial for insights into the storage and degradation mechanisms of intercalation cathodes. In inorganic cathodes, these phase changes often manifest as structural deformations, primarily dependent on the intercalation/de-intercalation mechanisms within specific crystal structures.^[77] Zinc ions (Zn²⁺) form strong bonds with electronegative atoms such as oxygen due to their large size (0.76 Å) and strong electrostatic attraction.^[78] This bonding can induce significant stress within host materials during insertion/extraction, potentially leading to structural collapse or phase transitions.^[79]

This issue is prevalent in cathodes based on chalcogenides and manganese (Mn), which exhibit various polymorph species. Irreversible phase changes have been observed in several MnO₂ polymorphs (β -, γ -, and δ -) after extended cycling, resulting in the formation of spinel ZnMn₂O₄. [80] This compound is highly stable, with a formation energy of -1293.3 kJ mol⁻¹,

making zinc extraction during charging highly unfavourable. $^{[66]}$ The spinel ZnMn₂O₄ also exhibits strong Zn migration barriers, hindering the movement of Zn²⁺ ions into its lattice. Although substantial volume fluctuations occur when Zn²⁺ or other charge carriers are inserted/extracted, there is a lack of systematic research on the microstructural or macrostructural changes in cathode materials.

Another phase change occurs in pre-intercalation-type inorganic cathode materials, where pre-intercalated ions in the lattice may be deintercalated into the electrolyte or be replaced by Zn²⁺ ions.^[81] Additionally, phase changes can be influenced by electrolyte additives containing extra metal ions, such as potassium or sodium ions, which may intercalate into the cathode lattice during cycling.^[82, 83] Understanding these processes is essential for optimising electrolyte composition and operating conditions to enhance the overall performance and longevity of zinc-based batteries.

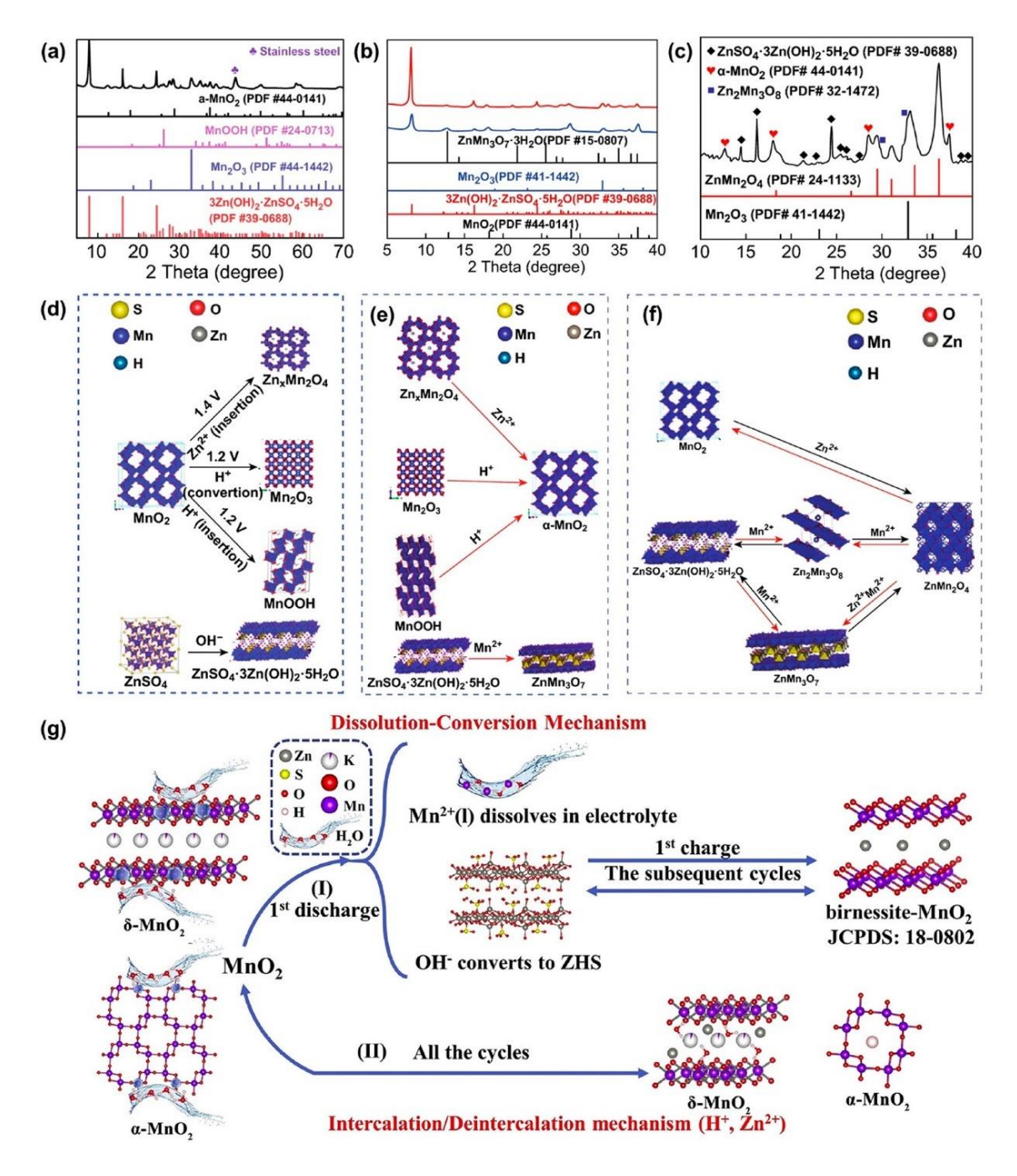


Figure 1.10 Illustration of the combined intercalation and conversion reaction mechanism of the MnO₂ cathode. XRD patterns of the α-MnO₂ cathode at various stages: (a) Discharged to 1.4 V in the initial cycle, (b) Fully charged state in the initial cycle, and (c) After 100 cycles. Schematic illustration of the phase evolution: (d) During the initial discharge process, (e) During the initial charge process, and (f) After the first cycle. (g) Schematic depiction of the dissolution–deposition mechanism in the Zn//MnO₂ battery.^[84] Reprinted with permission from ref.^[85] Copyright 2020 American Chemical Society.

1.2.4 Sluggish charge transfer kinetics

Charge transfer kinetics in electrodes can be categorised into ionic transport and electron transport kinetics. Regarding ionic transfer kinetics, divalent Zn^{2+} ions exhibit strong electrostatic interactions with H_2O molecules in aqueous electrolytes, forming a solvent structure of $[Zn-(H_2O)_6]^{2+}$.[86-88] This increases the effective ion size to 5.5 Å, compared to the 0.76 Å for Zn^{2+} , a more pronounced effect than observed with monovalent charge carriers like Li^+ or Na^+ . Consequently, the lattice distance in cathode materials may be too narrow for the intercalation of these divalent ions. Before Zn^{2+} can be incorporated into cathode materials, a substantial amount of energy is required to facilitate the desolvation process, freeing Zn^{2+} from the dense H_2O solvation sheath.[89, 90]

Cathode materials involving Zn²⁺ intercalation processes, such as Mn-based, V-based, and polyanionic cathodes, are significantly limited by the desolvation penalty of hydrated Zn²⁺.^[91,92] The +2 charge of Zn²⁺ causes significant electrostatic repulsion, resulting in slower solid-state diffusion kinetics compared to single-charged ions.^[93] Solid-state diffusion is intrinsically linked to the structure of the cathode materials. The theoretical capacity of Mn-based cathodes is complex due to their crystallographic polymorphs, which include distinct ion diffusion pathways.^[94] The electrochemical storage performance of these cathode materials is significantly influenced by the rate of charge transfer. Slow kinetics can lead to considerable electrochemical polarisation, reducing storage capacity and rate capability.^[95] Currently, the solvation/desolvation mechanisms near the electrode/electrolyte interface are not well understood. Gaining insight into the key parameters that control the diffusion of Zn²⁺ ions in various cathodes will be crucial for customising cathode materials to enhance rate performance and capacity.

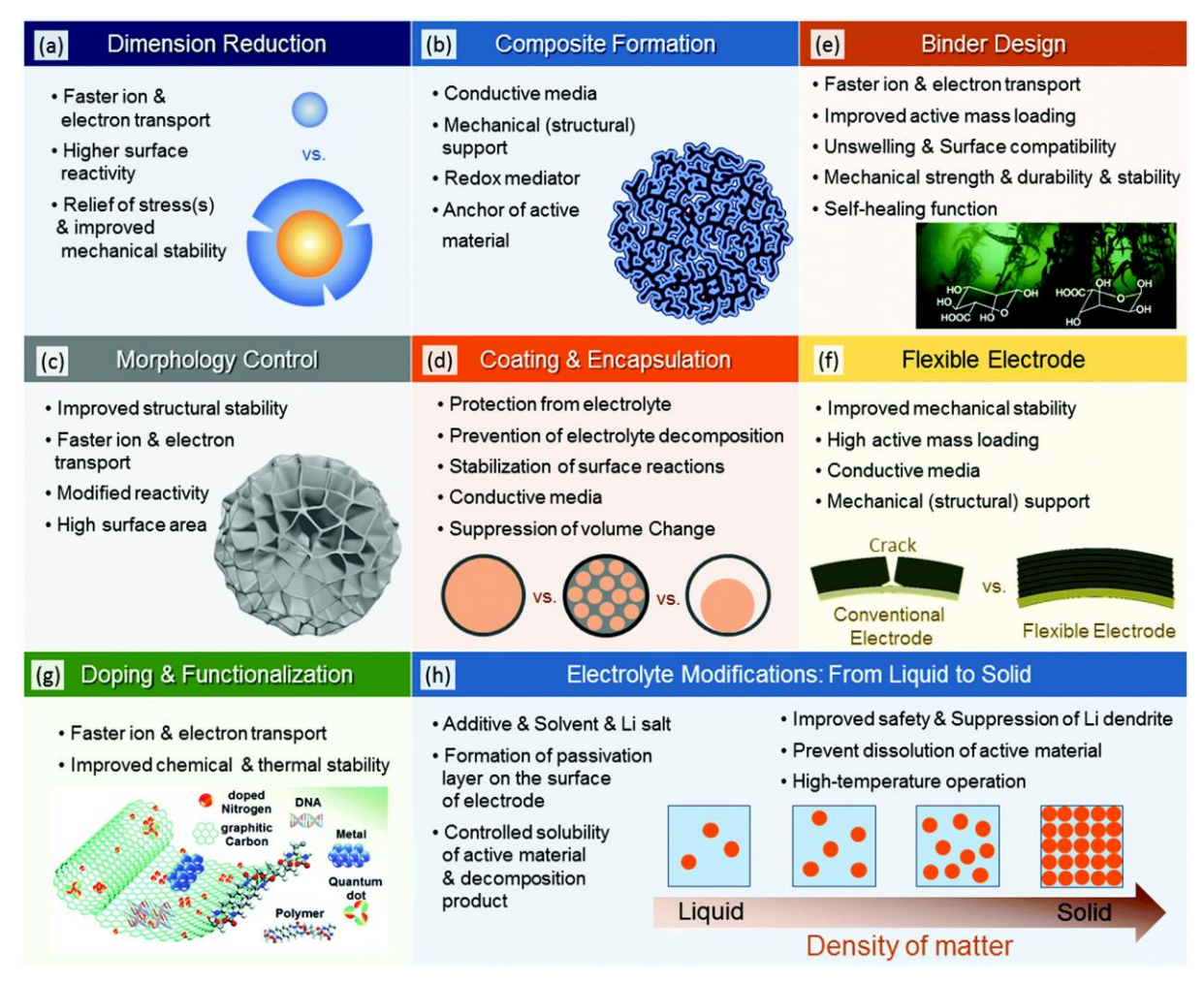


Figure 1.11 Most common strategies for performance improvement and their rationale: (a) Reducing dimensions of active materials; (b) Formation of composites; (c) Tailoring particle morphology; (d) Design of coatings or shells on active particles; (e) Design of functional binders; (f) Flexible electrodes; (g) Doping and functionalisation; (h) Modification of electrolytes from liquid to solid. Reprinted with permission from ref.^[15] Copyright 2020 Royal Society of Chemistry.

1.2.5 Zinc dendrite

The issue of metal dendrites is a well-recognised challenge in the battery industry, particularly for the emerging Zinc-ion Battery (ZIB) technology, following the commercialisation of Lithium-ion Batteries (LIBs). The academic community has a solid grasp of the zinc dendrite formation mechanism, providing pathways for addressing this problem. Zinc dendrites typically form due to uneven nucleation driven by imperfect surface qualities such as non-uniform electric fields, uneven ion distribution, and unrestricted lateral movement of zinc ions on the surface. [96, 97]

During the initial phase of battery cycling, zinc ions are typically reduced at favourable charge transfer sites, forming small protrusions on the anode surface. These protrusions attract more zinc ions due to their lower surface energy, leading to dendrite formation. The "tip effect" of dendrites enhances the local electric field, promoting further dendrite growth. [98, 99] As dendrites expand, they can eventually penetrate the separator, growing uncontrollably until they break off from the electrode, forming "dead zinc."[100-102] High current densities exacerbate the creation of non-uniform electric fields and ion distributions, accelerating zinc dendrite growth and potentially causing short circuits in the battery. Conversely, low current densities can slightly suppress dendrite growth. [103, 104] Consistent nucleation is crucial, favouring smooth electrodes, defect-free surfaces, and well-dispersed nucleation sites for ZIB applications. The uneven distribution of zinc ions on the electrode surface, the interface where zinc is deposited, and the distribution of electric field density, ion concentration, and nucleation sites all influence zinc dendrite formation. [105-107]

Dendrites create a loose structure and rough surface, increasing the specific surface area of the anode and leading to side reactions such as corrosion and hydrogen evolution (HER). [108, 109] As dendrites accumulate and grow, they thicken the battery, potentially puncturing the separator and causing short circuits. When dendrites fracture and separate from the current collector, they form "dead zinc," significantly reducing the CE and capacity of the zinc anode. Additionally, these broken dendrites interact with the electrolyte, producing by-products that increase impedance and reduce the battery's CE.

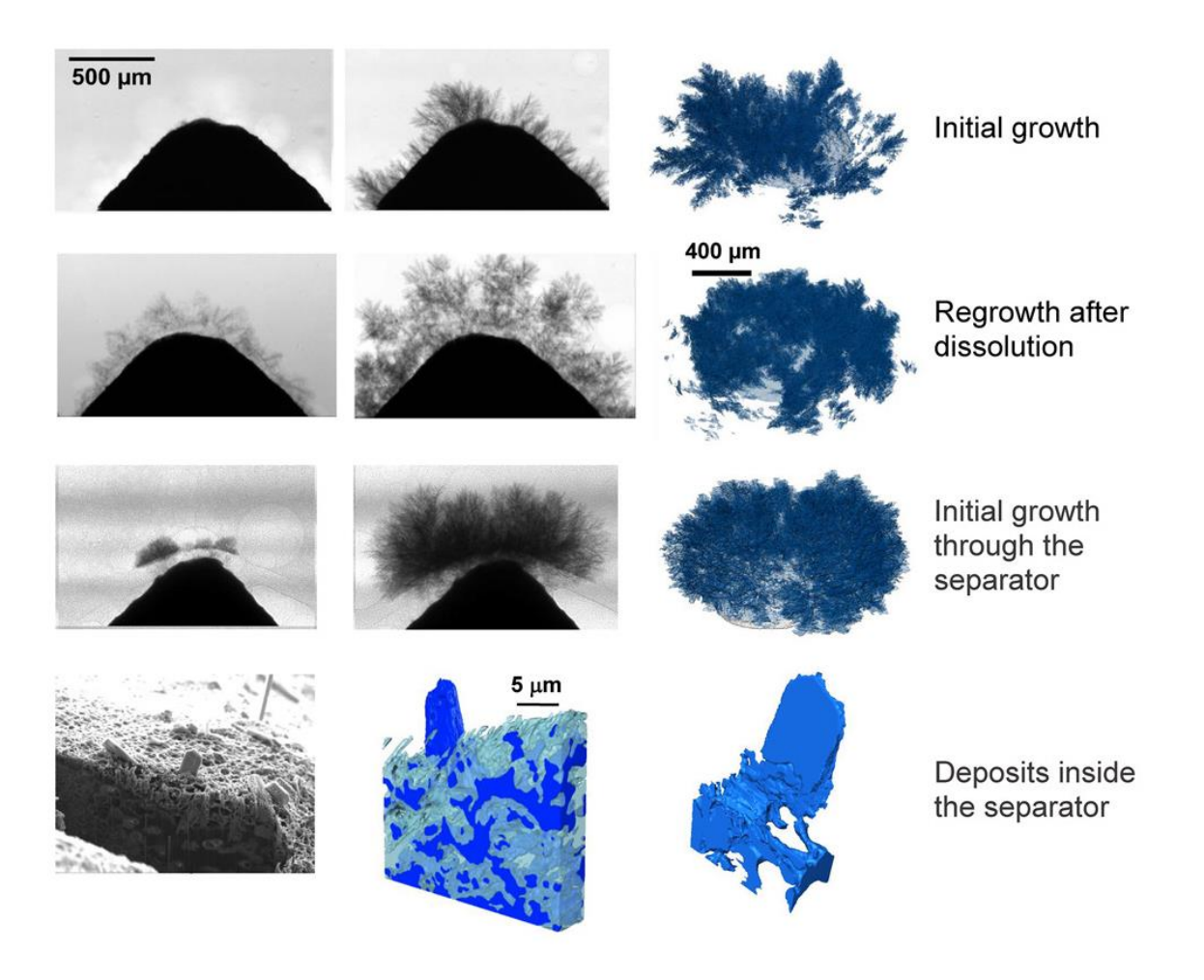


Figure 1.12 Operando demonstration and Multi-level Tomography investigation of Dendrite Formation and Dissolution in Zinc Batteries. Reprinted with permission from ref.^[110] Copyright 2019 Elsevier.

1.2.6 Corrosion and passivation

During discharge in AZIBs, metallic zinc undergoes oxidation to Zn^{2+} , which subsequently attracts anions such as OH^- and SO_4^{2-} . This process triggers the formation of electrochemical corrosion products through side reactions, mirroring the effects of chemical corrosion. The electrochemical corrosion of active zinc significantly diminishes the charge/discharge efficiency and overall capacity of ZIBs. The generation of by-products, such as $ZnSO_4(OH)_2 \cdot 3$ H_2O , depletes active zinc ions and the electrolyte, contributing to capacity degradation. [111, 112] These insoluble by-products adhere to the electrode surface, blocking active nucleation sites and creating rough protrusions on the zinc anode surface. This results in an uneven surface that promotes the growth of zinc dendrites. [113-115] Additionally, these secondary products have low conductivity, increasing the overall impedance of the battery and impeding the movement of electrons and ions at the positive electrode. This deactivation of the positive electrode further

reduces the battery's efficiency in storing charge, underscoring the need for effective strategies to mitigate these corrosion effects and enhance ZIB performance.

Hydrogen by-products can be generated through both chemical and electrochemical corrosion processes, serving a distinct role compared to the solid by-products previously discussed. Despite the thermodynamics favouring the reduction of Zn²⁺ under neutral and slightly acidic conditions, this process is generally hindered by slow surface reactions, low proton activity, and the substantial overpotential required for the HER at the zinc surface. [116, 117] However, under specific circumstances such as significant polarisation during charging, high current density, and low potential, HER can occur within minutes. The impacts of HER on battery performance are multifaceted: (1) The irreversible HER competes with the reversible zinc deposition, continuously consuming the zinc metal anode and reducing the battery's reversibility, CE, and capacity; [118] (2) The flammable hydrogen gas produced during HER increases the internal pressure of the battery, potentially leading to cell inflation or explosion; [119] (3) HER depletes protons near the electrolyte-zinc interface, leading to the production of corrosive substances and the formation of a passivation layer, ultimately degrading or causing the failure of battery performance.^[120] Addressing these issues is critical for improving the safety, efficiency, and longevity of ZIBs. Future research must focus on developing strategies to mitigate HER and its associated impacts to enhance the overall performance of ZIBs. The design principles for anode materials in ZIBs are guided by several key criteria to ensure optimal performance and longevity: providing a stable structure capable of withstanding prolonged zinc ion plating and stripping cycles, offering ample space with interconnected pathways for rapid ion transport and storage, ensuring a large surface area with numerous active sites for uniform zinc deposition, maintaining high conductivity and hydrophilicity for efficient electrolyte infiltration, and retaining both physical and chemical stability in acidic or alkaline electrolytes to endure the electrochemical environment over extended use. [121] These principles are crucial for the development of high-performance, durable anodes for zinc ion batteries.

1.3 Research strategies for aqueous zinc-ion batteries

Sluggish ion diffusion within host materials is often attributed to strong cation-cation repulsion and cation-anion attraction. [122] Calculated ion migration pathways reveal that ions are initially inserted into the lattice at sub-optimal coordination sites and subsequently migrate to more favourable positions, thereby enhancing ion conductivity within the lattice. Reducing the ionicity of the host material can also prove advantageous. For instance, metal-sulphide bonds are less ionic than metal-oxide bonds, which decreases the metal charge and reduces cation repulsion, thus improving ion diffusion. [123] Additionally, a solvent co-insertion strategy can shield ions during diffusion. Introducing water molecules into a non-aqueous electrolyte can shield the coulombic interactions between multivalent ions and the host material, facilitating improved ion migration. Furthermore, the use of nanomaterials reduces the diffusion length from the electrode surface to the bulk material, thereby increasing ion diffusion performance. These strategies collectively enhance ion diffusion capabilities within host materials, addressing the challenges posed by strong ionic interactions and significantly improving overall battery performance.

1.3.1 Pre-intercalation strategies

The pre-intercalation strategy has garnered substantial attention as a potent method to enhance the electrochemical performance of cathode materials, such as vanadate, [124] manganese oxide, [125] and layered LiCoO₂[126] in recent years. This approach has demonstrated significant potential, particularly for MnO₂ materials, in improving battery performance. Numerous assessments and evaluations have been conducted, highlighting the advantages of pre-intercalation in this context. However, a comprehensive analysis of the pre-intercalation approach in cathode materials for next-generation batteries remains absent. Over the past five years, many studies have emerged, focusing on enhancing the electrochemical performance of electrode materials through pre-intercalation. These methods involve incorporating ions or molecules into the tunnel or interlayer hosts either before battery cycling or during production. The intercalated guest species, which can include ions, inorganic/organic molecules, [127] and polymers [128] interact electrostatically and physically with the host framework and carrier ions through chemical bonding or coordination. These interactions significantly benefit the structural integrity of the hosts and enhance the transport kinetics of the carrier ions.

Various methods can be employed to produce preintercalated materials, including hydrothermal synthesis, calcification treatment, ion-exchange reactions, [128] aqueous/organic interfacial synthesis, and electrochemical processes. These techniques aim to address the suboptimal performance of MnO₂ materials, primarily due to their inherently low electronic conductivity. For example, Yuan et al. suggested that preintercalated K⁺ ions in the 2 x 2 tunnels of α-MnO₂ can enhance electronic conductivity and Li⁺ diffusivity, thereby overcoming this limitation. [129] MnO₂ materials experience slow diffusion kinetics for different carrier ions, particularly multivalent ions such as Zn²⁺ and Mg²⁺. Kang et al. proposed that the activation barrier for Li⁺ movement in layered lithium transition metal oxides is significantly influenced by the interlayer spacing and electrostatic interactions between inserted Li⁺ ions and host anions. [130]

Expanding the space between layers and reducing the electrostatic interactions between carrier ions and host anions by utilising the "charge shielding" effect of crystal water has been documented in numerous studies as a method to enhance the diffusion rate of carrier ions in MnO₂ cathodes for various battery applications. [131, 132] However, the tunnel/layer structure of MnO₂ materials can become greatly deformed or destroyed over time, leading to the dissolution of Mn²⁺, the creation of inactive spinel-type materials, and ultimately a decrease in capacity. Pre-intercalation significantly decreases capacity fading caused by structural instability during cycling by minimising volumetric changes during the insertion/extraction of carrier ions. Various compounds, such as polyaniline preintercalated δ -MnO₂, [133] 3D M_xMnO₂ (M = Li, Na, K, Co, and Mg), [134] alkali ion intercalated compounds A–M–O (A = Li, Na, K, Rb; M = V, Mo, Co, Mn), [135] TMA⁺ stabilised δ -MnO₂, [136] and K⁺ intercalated MnO₂[137] have been used as cathodes in Li-ion, Na-ion, K-ion, Mg-ion, and Zn-ion batteries to achieve long-lasting reversibility.

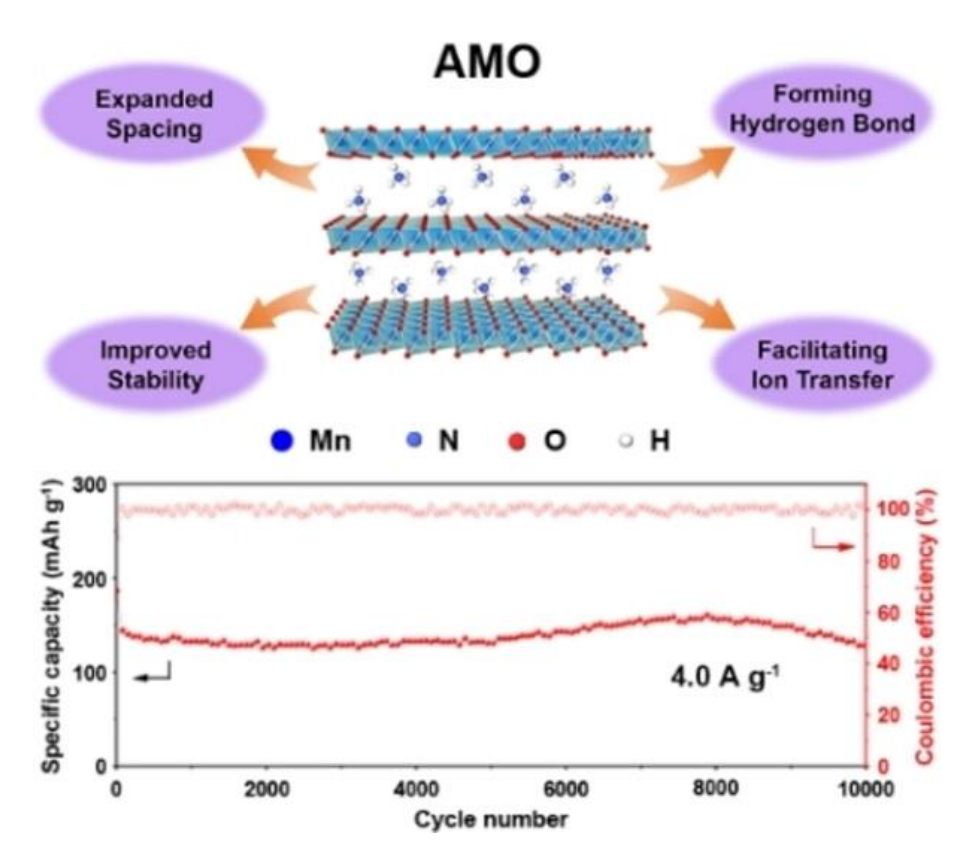


Figure 1.13 Illustration of the ammonium preintercalated manganese oxide material and GCD profile. Reprinted with permission from ref.^[138] Copyright 2023 Wiley-VCH GmbH.

1.3.2 Defect engineering

Defect engineering is now widely recognised as an effective method for altering the electrical properties of materials. This approach has been extensively employed to modify manganese-based oxides for use in AZIBs, leading to significant enhancements in their electrochemical performance. Various forms of defect engineering have been utilised in designing manganese-based oxides for AZIBs. These can be categorised into four main groups: oxygen vacancy, [139, 140] cation vacancy, [141-143] cationic doping, [144-146] and anionic doping. [147, 148] Among these, oxygen vacancy is the most well-documented strategy, followed by cation vacancy and cationic doping. The primary improvement mechanisms include increased energy storage sites, enhanced ion diffusion and electron transfer kinetics, and improved structural stability.

Material defects can be classified based on their production methods, such as atomic vacancies, interstitial defects, substitutional defects, and higher-dimensional defects like dislocations, grain boundaries, and precipitates. Vacancy and doping are crucial strategies for introducing new functions, such as electrical, magnetic, and optical properties, to manganese-based oxides among the various forms of defects. Defect engineering has been increasingly utilised in

research on electrochemical energy storage devices due to their potential unique electrical features.

Introducing defects into cathode materials has been shown to enhance ion storage capacity and significantly improve the electrochemical performance of AZIBs. Previous studies have demonstrated that defects can increase the number of active sites for ion anchoring, thereby enhancing electrochemical performance. For example, oxygen-deficient MnO_2 exhibits a thermoneutral Gibbs free energy value for Zn^{2+} adsorption near the oxygen vacancy, which results in a substantially accessible electrochemically active surface area. [149, 150] This enlarged surface area boosts the surface capacitive contribution, ultimately increasing capacity. A higher quantity of electrons becomes accessible to the delocalised electron cloud of the electrode, potentially enhancing its capacity. Defect engineering also plays a crucial role in controlling the electrical conductivity, energy barrier for Zn^{2+} diffusion, and overall ion diffusion kinetics. Oxygen vacancies, in particular, can increase the donor density in the cathode, thereby reducing the energy required for electron transport and charge transfer. [151, 152] Furthermore, the presence of oxygen vacancies may create openings in the [MnO_6] polyhedron structure, facilitating ion travel along the ab-plane. [153, 154] This process significantly enhances the electrochemical reactivity and electrode kinetics, leading to improved battery performance.

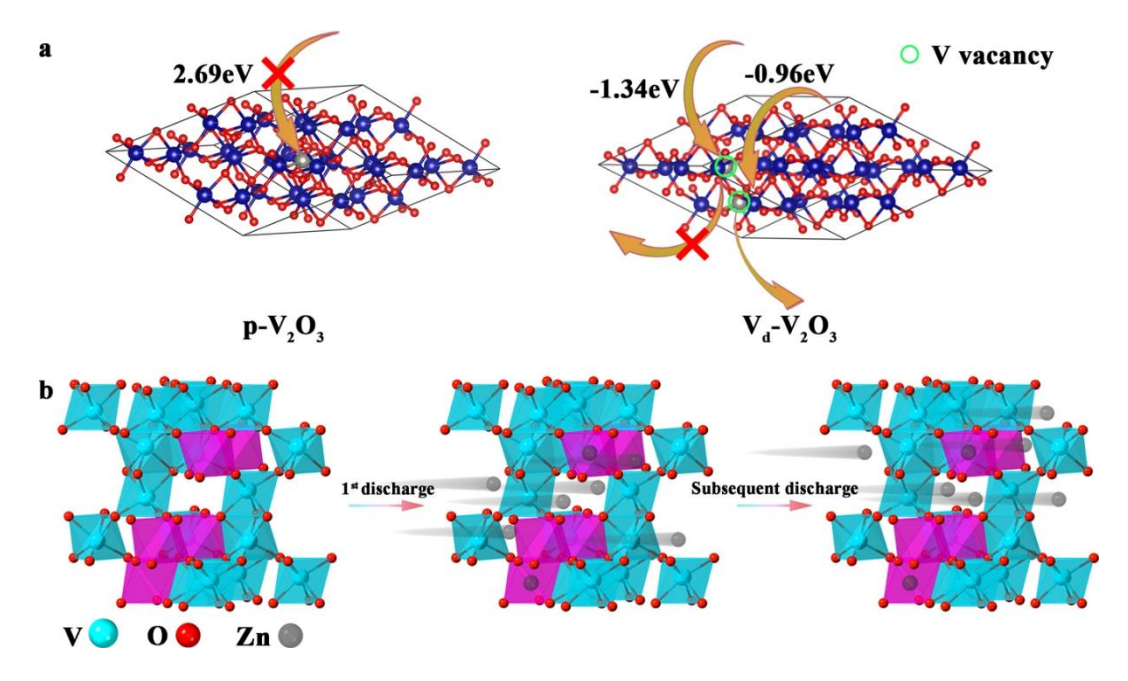


Figure 1.14 (a) The Gibbs free energy of different models; (b) The schematic illustration of the energy storage mechanism in the $Zn||V_d-V_2O_3$ cells. Reprinted with permission from ref.^[155] Copyright 2021 Springer Nature.

1.3.3 Cathode-electrolyte-interface modification

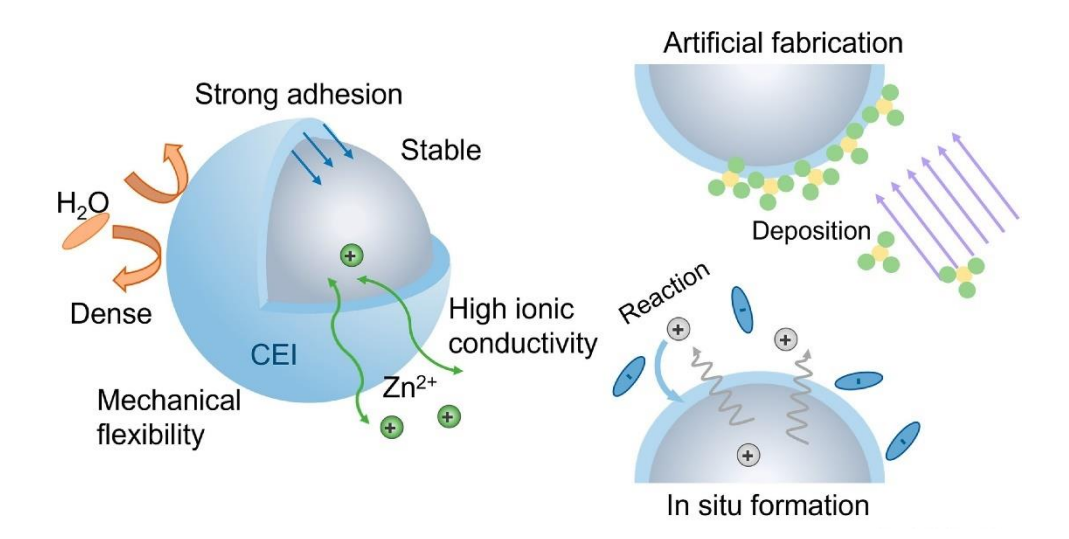


Figure 1.15 Illustration of surface modification methods for cathode materials. Reprinted with permission from ref.^[156] Copyright 2023 Elsevier.

The primary challenges in the cathode-electrolyte interface (CEI) of AZIBs include inadequate interfacial compatibility, [156] cathode material dissolution, [157] and byproduct formation. [158] Addressing these issues involves strategies such as electrolyte optimisation [159] and the coating of cathode materials. [160] Optimising the electrolyte is crucial for improving interface problems. For instance, adding Mn²⁺ to the electrolyte can mitigate the dissolution issue in Mn-based cathode materials and enhance cycling stability without altering the redox reaction of the MnO₂ electrode. [161] This occurs because Mn²⁺ addition can inhibit the Jahn–Teller effect on the cathode's surface. Similarly, the concept of solution equilibrium has been applied to V-based cathode materials with the addition of cationic additives like Na⁺, thereby stabilising the cathode and improving overall performance. [162]

Enhancing interfacial compatibility in ZIBs can be achieved through electrolyte optimisation and inhibiting cathode dissolution. [163] In the Zn/LiFePO₄ battery, a hybrid electrolyte containing 1 M Zn(SO₃CF₃)₂ and 1 M Li(SO₃CF₃) shows significant improvements with the inclusion of Sodium dodecylbenzene sulfonate (SDBS) additives. [164, 165] These additives decrease the contact angle between the electrolyte and cathode, enhancing the hydrophilicity of LiFePO₄ towards water. Molecular dynamics (MD) simulations reveal that the tail of the SDBS surfactant attaches to the LiFePO₄ surface, promoting water molecule binding and speeding up Li⁺ ion movement at the boundary. The overpotential of LiFePO₄ with SDBS additives is notably lower than that of LiFePO₄ without additives, indicating a decrease in electrochemical reaction resistance.

Another effective method to address CEI issues is applying coatings to cathode materials. Coatings enhance cathode hydrophobicity, facilitating the removal of water molecules from hydrated Zn²⁺ at the CEI and promoting efficient zinc ion insertion into host materials. [166-168] Achieving an optimum water contact angle (WCA) is crucial for enhancing electrochemical performance through CEI modifications. [169, 170] In addition to artificial coatings, innovative *insitu* coatings can address CEI issues. An *in-situ* electrochemical charging approach can create a single-component cathode-based SEI, such as CaSO₄·2H₂O, in a Ca₂MnO₄ cathode for aqueous ZIBs. [171] The CaSO₄·2H₂O layer exhibits electronic insulation and ionic conduction characteristics, making it a suitable SEI film that successfully prevents material dissolution on the cathode side.

Despite various methods like electrolyte optimisation and surface coating being employed to alter the CEI, there is still a lack of thorough understanding regarding its formation mechanism and structure. Enhancing the electrochemical performance of ZIBs necessitates a focus on improving ion and electron transport at the CEI. Addressing these challenges is crucial for the development and optimisation of high-performance ZIBs, providing a pathway towards more efficient and durable energy storage solutions.

1.3.4 Structural optimisation

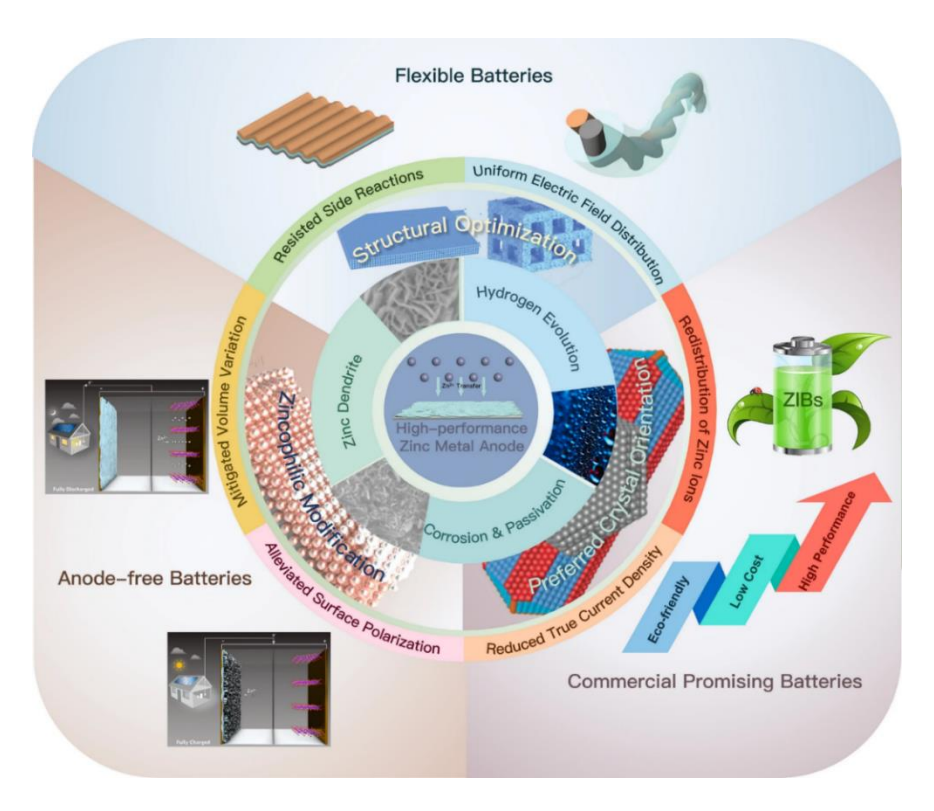


Figure 1.16 Summary of the surface modification and structural design for zinc anode. Reprinted with permission from ref.^[172] Copyright 2023 Springer Nature.

Commercial zinc foil, characterised by its two-dimensional plane and low specific surface area, poses a challenge for achieving a homogeneous electric field, thereby promoting the formation of zinc dendrites during cycling.^[173, 174] A promising solution is to develop three-dimensional (3D) zinc anodes.^[175-177] The 3D configuration significantly increases the surface area of the zinc anode and reduces the overpotential for zinc ion deposition in AZIBs. This enhancement facilitates more uniform Zn²⁺ distribution, thereby mitigating the formation of dendrites and byproducts. To elucidate, 3D zinc anodes can be categorised into several types: fibrous,^[178] porous,^[179] ridge-like,^[180] and plated zinc anodes.^[181, 182] Each of these structures offers distinct advantages in improving ion transport kinetics and enhancing overall electrochemical performance. By transitioning from traditional 2D zinc foil to innovative 3D zinc anode designs, key challenges in zinc-ion battery technology can be addressed and pave the way for more efficient and durable energy storage solutions.

Carbon material is one of the most classical examples of structural optimisation. [183-186] It offers inherent advantages including excellent conductivity, abundant availability, cost-effectiveness, environmental friendliness, and robust stability. To effectively modify the anode of AZIBs, it is crucial to minimise the formation of zinc dendrites and prevent side reactions such as hydrogen evolution and self-corrosion. Extensive research has focused on developing anodes from carbon-based materials with high specific capacitance. Materials such as graphene, [187] carbon nanotubes, [187] activated carbon, [188] and other carbon derivatives [189] are particularly suitable for enhancing Zn anodes. These carbon-based materials provide numerous nucleation sites, promote uniform zinc deposition, and inhibit dendrite formation, thereby significantly improving electrochemical performance. By leveraging these properties, a structural optimisation strategy can substantially enhance the efficiency and longevity of AZIBs.

1.3.5 Interface functionalisation

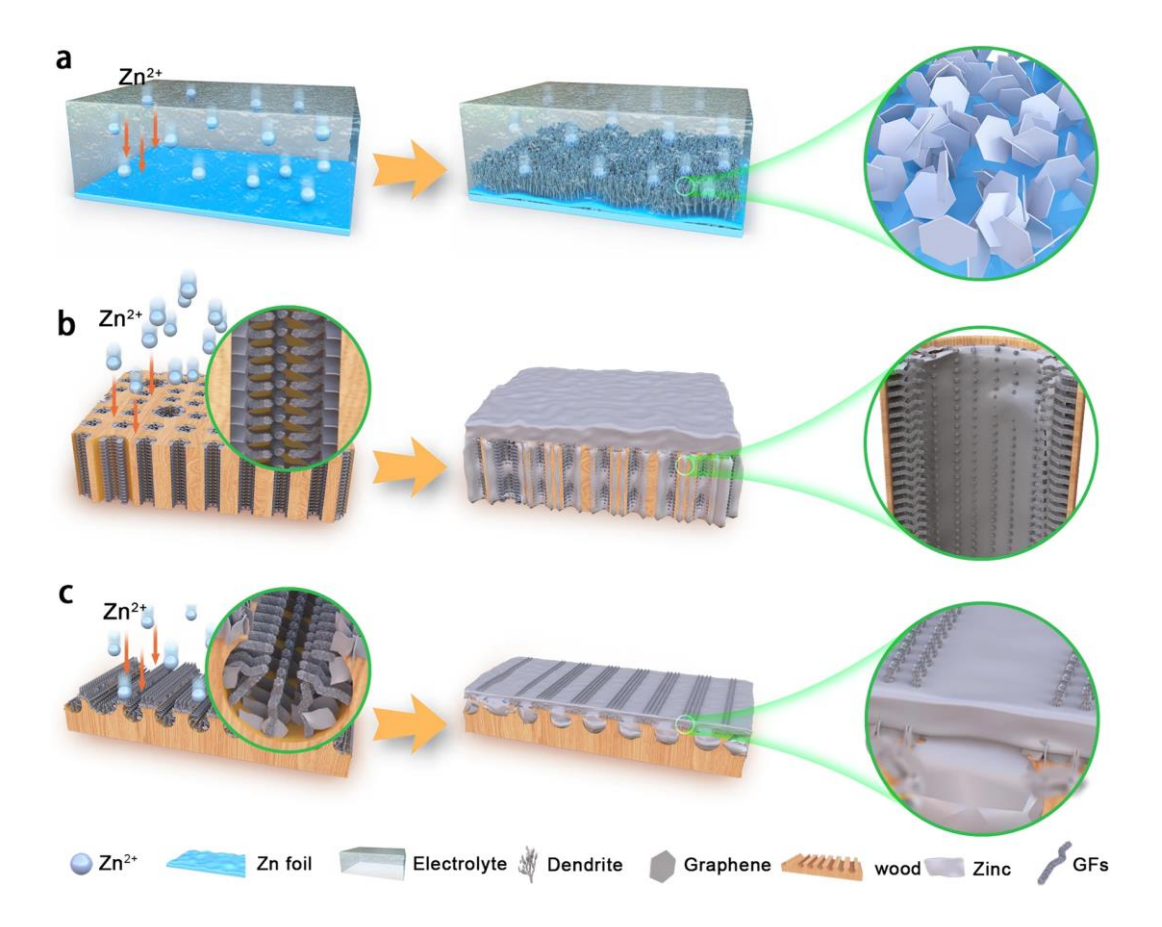


Figure 1.17 Zn deposition on (a) Bare Zn, (b) 3D graphene matrices of longitudinal direction (3D-LFGC), and (c) Radial direction (3D-RFGC). Reprinted with permission from ref.^[190] Copyright 2023 Springer Nature.

Building the right interface is considered a highly effective method for enhancing battery performance. [191-193] The interface between the electrode and the electrolyte in a battery system serves as a hub of complex chemical reactions and various physical and chemical interactions, playing a crucial role in maintaining battery life. [106] A stable interfacial coating can prevent direct contact between the electrolyte and the electrode, thereby avoiding side reactions that produce electrochemically inactive "dead" zinc. Additionally, such an interface can induce uniform Zn²⁺ deposition, preventing dendrite growth. [194] Currently, various materials have been proposed as protective coatings to safeguard the zinc electrode.

Metal-based materials are increasingly recognised as promising coating materials for Zn-ion batteries due to their strong affinity for zinc (zincophilicity) and high electrical conductivity. These properties enhance nucleation sites for Zn²⁺, facilitating uniform Zn²⁺ deposition.^[195, 196] Certain metals, owing to their consistent interfacial electric field, effectively attract Zn²⁺ ions and expedite ion movement, thereby inhibiting the growth of large and irregular dendrites or

protrusions. Qiao et al. conducted an in-depth examination of metallic coatings using both *insitu* and *ex-situ* characterisation techniques.^[197] Their findings revealed that the metal layer on the Zn surface functions as both a corrosion inhibitor and a nucleation agent, effectively preventing corrosion of the Zn electrode. The modified inner layer significantly inhibited dendrite formation, resulting in an electrode that maintained a consistent and compact Zn coating even after extended cycling. These insights underscore the potential of metallic coatings to enhance the performance and durability of Zn-ion batteries through improved electrode stability and uniform zinc deposition.

In addition to metal-based coatings, inorganic non-metallic materials such as metal oxides,^[198, 199] kaolin,^[179] and conductive salts^[200, 201] have been widely utilised in interface engineering processes. For example, Mai et al. developed a binder-free and ultrathin ZrO₂ coating on a Zn anode using an atomic layer deposition (ALD) process.^[202] This coating effectively controlled the nucleation sites of Zn²⁺ and facilitated the rapid transport of Zn²⁺, thereby improving the overall performance of the Zn anode. This approach prevents dendritic development and side reactions, thereby enhancing the electrochemical efficiency of the Zn anode.

By leveraging the properties of both metallic and inorganic non-metallic coatings, significant improvements in the performance and longevity of Zn-ion batteries can be achieved. These coating strategies address key challenges such as dendrite formation, corrosion, and uneven Zn deposition, paving the way for more reliable and durable energy storage solutions.

1.3.6 Polymer coating

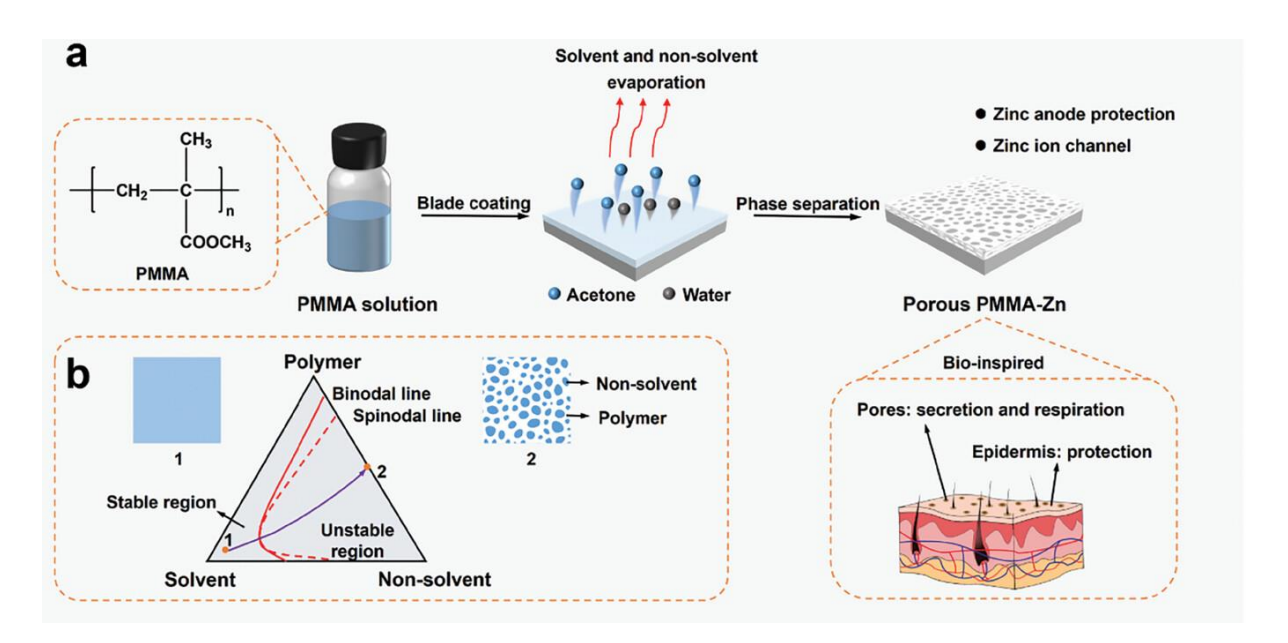


Figure 1.18 Fabrication and characterisation of porous PMMA coating. Scheme of the preparation process (a) and mechanism (b) of porous PMMA coating. Reprinted with permission from ref.^[203] Copyright 2024 John Wiley and Sons.

Organic polymers, renowned for their numerous functional groups capable of interacting with metal ions and exceptional film-forming properties, have emerged as effective coatings for zinc anodes in AZIBs.^[204] These coatings facilitate uniform zinc deposition and mitigate side reactions, significantly enhancing anode performance.^[205-207] Cui et al. leveraged advanced electroplating concepts to utilise polyamide (PA) as a coating layer, aiming to improve the longevity and deep rechargeability of zinc anodes.^[208] The PA coating was applied by casting a solution of PA and Zn(TfO)₂ in anhydrous formic acid onto zinc foil. This process resulted in a robust interface characterised by strong binding action, chemical stability, and exceptional mechanical toughness and flexibility. Furthermore, the polar amide groups in PA molecules provided hydrogen bonding capabilities and coordination sites, which limited water and oxygen infiltration and reduced free water content on the zinc surface.

Despite these advantages, the hydrophobic nature of some polymers can increase the nucleation barrier and restrict ion diffusion, leading to enhanced polarisation during Zn plating and stripping.^[209, 210] To address these limitations, a hybrid organic-inorganic approach has been developed, combining the beneficial characteristics of both polymers and inorganic materials. Pan's team created an organic-inorganic hybrid coating layer integrating Zn-X zeolite and Nafion-85.^[211] This hybrid layer forms a well-bridged organic-inorganic interface, with Zn-X

zeolite featuring pore sizes smaller than 0.74 nm, significantly less than the 4 nm channel size in Nafion. This configuration effectively blocks anions while allowing free movement of zinc ions on the surface and interior of the Zn-X zeolite. Ion permeability tests demonstrated that adding 5 wt% Zn-X to the Nafion layer reduced the permeability of SO_4^{2-} anions from 2.04 x 10^{-9} cm² s⁻¹ to 0.61 x 10^{-9} cm² s⁻¹. Furthermore, the interaction of zinc ions with R-SO₃ in Nafion decreases Zn^{2+} desolvation energy, enhancing kinetics and promoting uniform Zn plating.

These advancements underscore the potential of utilising polymer and hybrid organic-inorganic coatings to improve zinc anode performance. By leveraging the unique properties of these materials, significant progress can be made toward developing more efficient and durable AZIBs, addressing key challenges such as dendrite formation, side reactions, and polarisation. This pathway offers a promising direction for the advancement of zinc-ion battery technology, with implications for enhanced energy storage solutions in various applications.

1.3.7 Solid electrolyte interface fabrication



Figure 1.19 Illustration of the structure and functions of SEI on zinc anodes. Reprinted with permission from ref.^[212] Copyright 2023 Wiley-VCH GmbH.

The fundamental properties of electrolytes are intricately tied to the electrochemical behaviour of zinc metal anodes, affecting critical parameters such as capacity, stability range, and cycle

efficiency. The choice of electrolyte is pivotal, as it plays a major role in the formation of the solid electrolyte interface (SEI), which in turn influences the cycle stability of battery systems. The characteristics of electrolytes significantly impact charge transfer kinetics at the electrode-electrolyte interface, thereby altering the overall performance of the battery.^[213] To achieve optimal zinc deposition processes and enhance the efficiency of zinc-ion battery systems, it is essential to design electrolytes with tailored properties.

Zhao et al. presented the development of a lean-water ionic liquid electrolyte for aqueous zinc metal batteries. [214] This electrolyte forms a hydrophobic tri-layer interface, consisting of two layers of hydrophobic OTF⁻ and EMIM⁺, followed by a loosely attached water layer. The anion crowding interface promotes OTF decomposition, creating a mechanically graded solid electrolyte interface layer that effectively suppresses dendrite formation and enhances mechanical stability. This configuration extends beyond the traditional Gouy-Chapman-Stern electrochemical double layer model. [215] Leveraging this hydrophobic tri-layer interface, the electrolyte achieves a broad electrochemical working window of 2.93 V and maintains high zinc ion conductivity at 17.3 mS cm⁻¹. Introducing inorganic crystallites into a solid-electrolyte interphase (SEI) significantly enhances the reversibility of the Zn anode. However, the structure-performance relationship of the SEI remains unclear due to unresolved states of its inorganic and organic components. Zhi et al. have successfully constructed a highly effective SEI for AZIBs using a bi-solvent electrolyte, with its composition and structure resolved by cryogenic transmission electron microscopy (TEM). [216] The as-prepared full cells demonstrate a high Zn utilisation ratio of 54% under areal capacity of 3.2 mAh cm⁻² and stable cycling over 1,800 h under 5,600 mAh cm⁻². This SEI, characterised by a highly fluorinated, amorphous inorganic ZnF_x uniformly distributed within an organic matrix, differs from typical mosaic and multilayer SEIs that contain crystalline inorganics. It offers improved structural integrity, mechanical toughness, and Zn²⁺ ion conductivity. However, numerous questions remain in the research of SEI, such as the decomposition mechanism of additives in dilute aqueous electrolytes and a deeper understanding of the role of water in the SEI formation process. With the rapid development of nanotechnology, achieving a high-performance practical zinc anode is promising.

1.3.8 Electrolyte additives

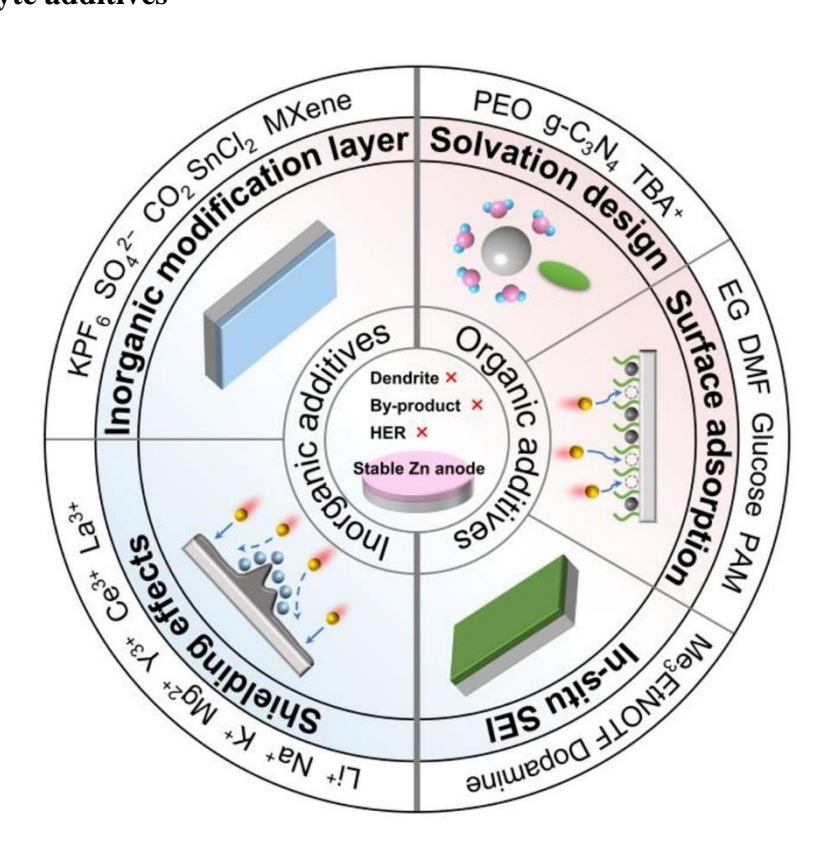


Figure 1.20 Summary of the electrolytes additives strategies for AZIBs. Reprinted with permission from ref.^[217] Copyright 2024 Elsevier.

The fundamental characteristics of electrolytes are intrinsically tied to the electrochemical behaviour of zinc metal anodes, affecting parameters such as capacity, stability range, and cycle efficiency. Electrolyte additives play a vital role in enhancing various critical aspects of electrolytes, such as ionic conductivity, [218, 219] viscosity, [220, 221] solubility, [222, 223] electrochemical window, [224-226] and chemical/thermal stability. [227, 228] The primary function of these additives is to improve specific properties of the electrolyte without fundamentally altering its nature or hindering its ability to support electrochemical reactions within the battery. It is crucial to carefully select and develop electrolyte additives compatible with the specific electrochemical system to enhance performance without compromising the electrolyte's inherent properties. To prevent adverse effects, the dosage of electrolyte additives must be meticulously controlled, typically kept below 20% by weight or volume. Excessive amounts or incorrect concentrations can lead to undesirable outcomes, making it essential to determine the optimal amount to minimise negative effects and achieve improved battery performance. Inorganic and organic additives are broadly categorised to enhance the performance of AZMBs. Inorganic ionic additives like MnSO₄, [229] Na₂SO₄, [230] and CoSO₄ [231] have been employed to

regulate the dissolution equilibrium of cathodes such as MnO₂, NaV₃O₈·1.5H₂O, and Co₃O₄. Water-soluble organic additives with various functional groups have garnered increased attention for their ability to alter the dissolution and deposition behaviour of Zn electrodes. These additives contribute to forming a favourable interface between the electrode and electrolyte by regulating the electrochemical properties of the electrolytes, such as Zn²⁺ coordination. Organic additives can be classified based on their components and functions into categories such as small heteroatom compounds, [228, 232] supramolecular macrocycles, [233, 234] polyols, [235, 236] organic weak acids, [237] organic salts, [238] ionic liquids, [239] zwitterions (including amino acids), [240] surfactants, [241] and polymers. [242]

Electrolyte additives protect zinc metal anodes through multiple mechanisms, including electrostatic shielding, [243] regulation of electrodeposition orientation, [244], *in-situ* formation of SEI/protective layers, [245] preferential adsorption on the Zn surface, [246] and other specific effects such as regulation of the hydrogen-bond network and formation of a pH buffer layer. [247, 248] Studies have demonstrated that carefully selected additives can effectively address the complex challenges associated with zinc metal anodes. These functions often operate synergistically rather than independently, indicating that a specific type of electrolyte additive may impart various protective effects on the Zn anode. For instance, manipulating the solvation sheath can sometimes lead to the formation of a more desirable SEI on the Zn anode's surface. [249] Additionally, the regeneration of the hydrogen-bond network typically accompanies changes in the solvation structure, while the selective adsorption of the electrolyte additive on the zinc surface is often necessary to regulate electrodeposition orientation.

In addition to the role of additives to the Zn anode protection, several factors contribute to the instability of cathode materials in AZIBs. Material dissolution, particularly involving vanadium (V) and manganese (Mn), is a significant concern. The dissolution of Mn is often driven by the classic Jahn-Teller effect, where distortion of the manganese oxygen octahedron causes trivalent manganese to undergo a disproportionation reaction, forming divalent manganese ions. The relevant reaction equations are listed below:

$$\frac{1}{2}MnO_2 + \frac{1}{6}ZnSO_4 + H^+ + \frac{1}{2}Zn + \frac{2}{3}H_2O \leftrightarrow \frac{1}{2}Mn^{2+} + \frac{1}{6}ZnSO_4[Zn(OH)_2]_3 \cdot 4H_2O$$

$$[Mn^{2+}] = [ZnSO_4]^{\frac{1}{3}} \cdot [H^+]^2 \cdot e^{\frac{-2\Delta G_0}{RT}}$$

This process leads to interface dissolution and ultimately the collapse of the material's internal structure. Instability arises when the cathode crystal structure collapses, with divalent zinc ions strongly binding to the host structure, exacerbating structural damage and material shedding. Additionally, mechanical stress induced by repeated ion insertion and removal causes

expansion and contraction of the cathode material, leading to electrode stress and capacity loss. Cathode protection strategies predominantly focus on Mn-based and V-based materials, emphasising the importance of electrolyte-cathode interaction in enhancing stability and longevity. For instance, Mn²⁺ additives have been shown to inhibit manganese dissolution and facilitate the formation of protective layers, significantly improving the performance of Mn-based cathodes.^[250, 251] The reaction equation follows:

$$Mn^{2+} + xH_2O \leftrightarrow MnO_x + 2xH^+ + 2e^-$$

Similarly, Na⁺ and Mg²⁺ additives have been employed to stabilise V-based cathodes, demonstrating the critical role of additive selection in maintaining structural integrity and electrochemical efficiency.^[252, 253] These insights underscore the importance of strategic electrolyte additive selection and development, along with cathode protection strategies, to enhance the performance and durability of AZIBs.

1.3.9 Concentrated electrolyte (water-in-salt)

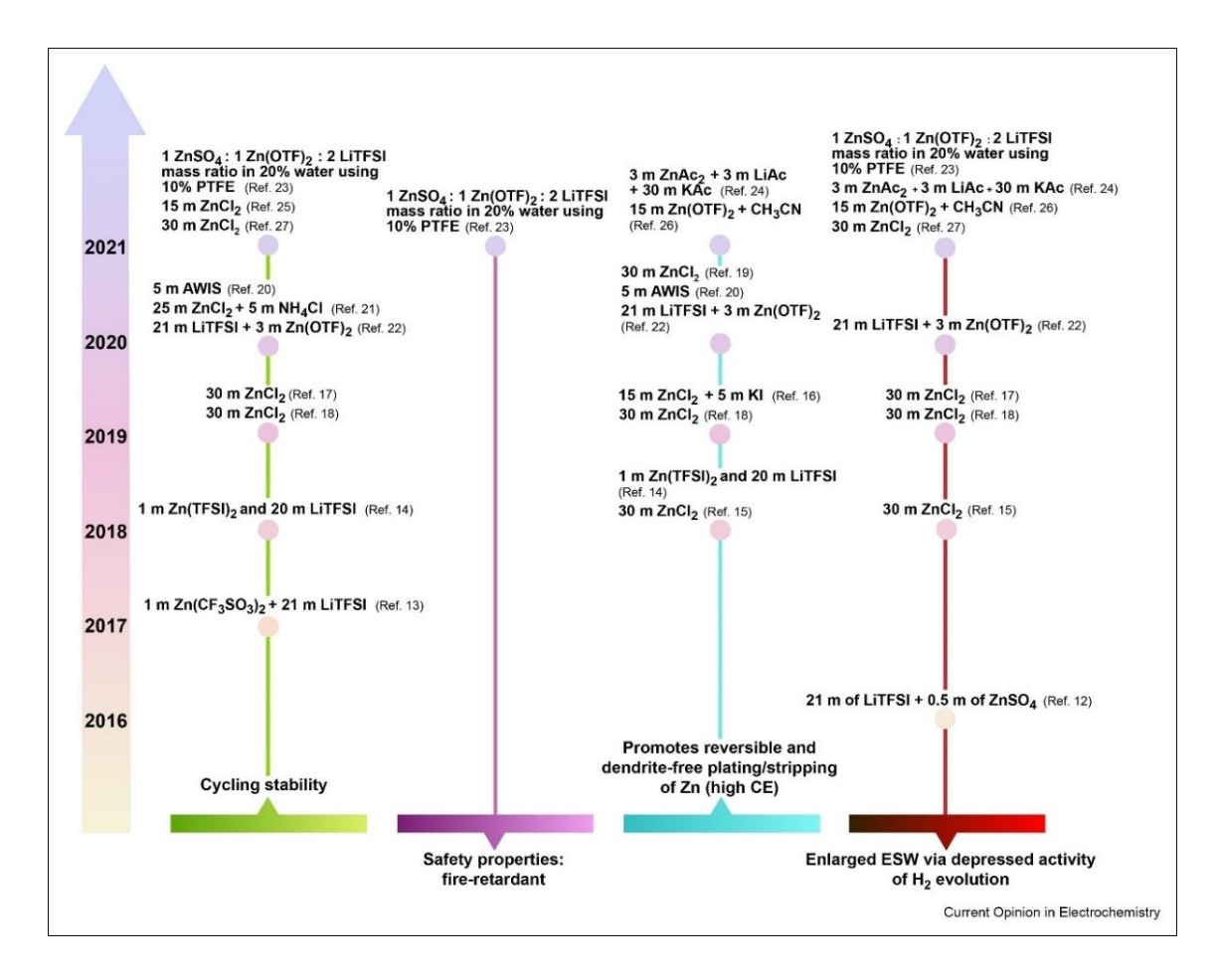


Figure 1.21 Development timeline of concentrated electrolytes in AZIBs. Reprinted with permission from ref.^[254] Copyright 2022 Elsevier.

In aqueous electrolytes, water molecules exist in two forms: solvated water molecules and free water molecules. In a commonly used 2 M ZnSO₄ electrolyte, the ratio of Zn²⁺ to water is approximately 1:56.^[255] Given that one Zn²⁺ ion typically forms a stable solvation structure with six water molecules, around 90% of the water molecules in a 2 M ZnSO₄ electrolyte function as free water.^[256-258] At the electrode/electrolyte interface, these free water molecules readily react with metallic zinc, leading to hydrogen evolution and electrode degradation. This results in poor cycling stability by continuously consuming the Zn metal electrode and compromising the CE of Zn plating/stripping. Therefore, it is crucial to reduce the amount of free water molecules in the electrolyte to minimise side reactions and enhance the reversibility of Zn plating/stripping.

One effective strategy to address this issue is the development of highly concentrated electrolytes. Examples include the hybrid "solvent-in-salt" electrolyte containing 1 m Zn(TFSI)₂ and 20 m LiTFSI,^[259, 260] 30 M ZnCl₂ solution,^[261] eutectic electrolytes,^[91, 262] and other types of highly concentrated electrolytes.^[263-265] In aqueous ZnCl₂ solutions, typically 1 m, the ionic species [Zn(OH₂)₆]²⁺ and [Zn(OH₂)₂Cl₄]₂ are present. However, in a 30 M ZnCl₂ solution, the octahedral coordination for all Zn²⁺ ions cannot be supported by the stoichiometry of ZnCl₂~1.8 H₂O, essentially rendering the electrolyte an ionic liquid with minimal free water molecules. This "water-in-salt" electrolyte features a high salt-to-water ratio, significantly reducing the amount of free water and associated water-induced processes. These advanced electrolytes effectively suppress adverse effects and dendritic growth, enhancing the performance and longevity of AZIBs. However, their increased cost may limit widespread adoption. Balancing performance improvements with cost considerations remains a critical challenge in the development of practical, scalable solutions for AZIBs.

1.3.10 Zn²⁺ solvation cluster regulation

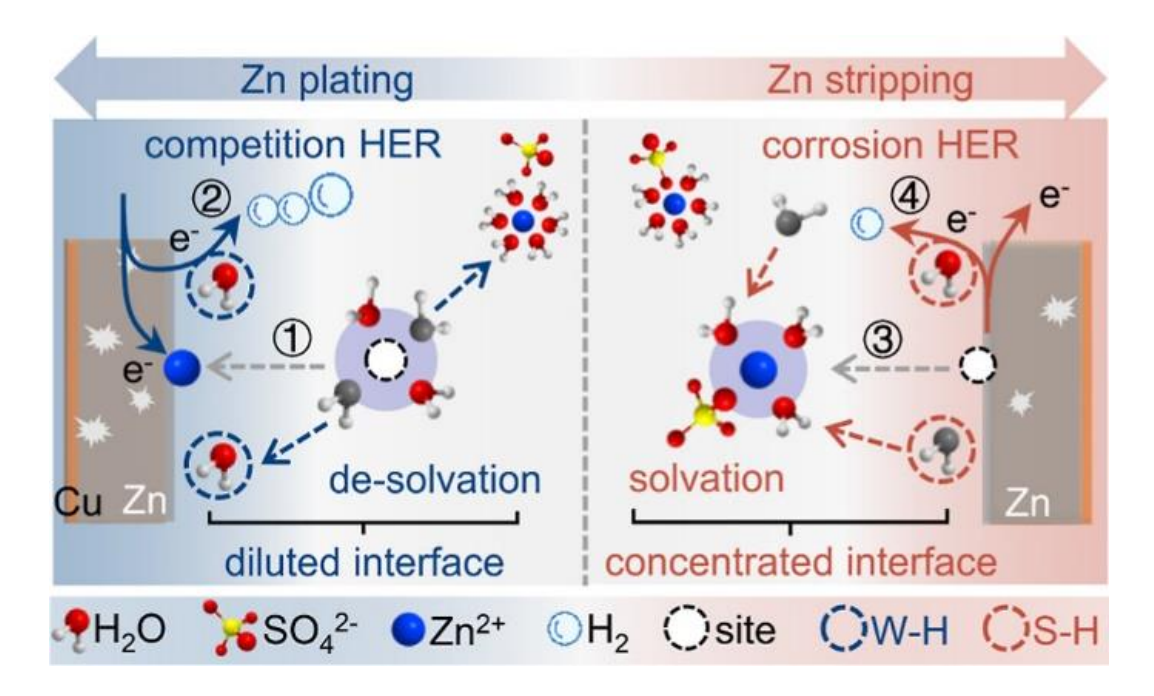


Figure 1.22 Schematics of solvation structure and HER mechanism at electrode/electrolyte interface. Left: Diluted interface formed during Zn-plating (Zn²⁺ desolvation) with competition HER; Right: Concentrated interface formed during Zn-stripping (Zn²⁺ solvation) with corrosion HER. Reprinted with permission from ref.^[266] Copyright 2024 American Chemical Society.

As previously mentioned, a stable solvation structure is formed by six water molecules coordinating with one Zn²⁺ ion. This strong solvation creates a significant energy barrier during the de-solvation and deposition processes of Zn²⁺ ions, resulting in a high overpotential for Zn plating and stripping. Recently, numerous studies have focused on improving Zn anode performance by reducing the solvation effects between Zn²⁺ and water, leading to more uniform deposition.^[76, 267, 268] Various strategies have been proposed to alter Zn²⁺ solvation, one of which is the antisolvent approach.^[269-271] An antisolvent is a type of solvent that can mix with the primary solvent but cannot dissolve the solute, effectively modifying the solvation environment and enhancing the performance of Zn anodes by minimising solvation-induced challenges. Take methanol as an example, by adding methanol as an antisolvent to a 2 M ZnSO₄ electrolyte, the water molecules surrounding Zn²⁺ ions are gradually replaced by methanol.^[271] This substitution decreases the solvation strength of Zn²⁺ and alters the overall solvation arrangement. When a substantial amount of antisolvent is introduced, ZnSO₄ re-crystallises in the electrolyte, significantly disrupting the Zn²⁺ solvation structure with water. The hydrogen

bond interactions between the antisolvent and water are crucial in reducing water activity and inhibiting Zn^{2+} activity, thereby preventing water-induced side reactions. Other solvents with similar characteristics, such as ethylene glycol (EG) and dimethyl sulfoxide (DMSO), have also been documented. Research indicates that EG can substitute a water molecule in the first Zn^{2+} solvation layer, reducing the proportion of Zn^{2+} solvated with water due to the hydrogen bond interactions between EG and water. Additionally, EG enhances the electrochemical performance of ZIBs at low temperatures due to its low freezing point. In the case of DMSO, its higher Gutmann donor number of 29.8, compared to 18 for H_2O , enables it to replace H_2O in the Zn^{2+} solvation sheath without significantly affecting Zn^{2+} ion transfer kinetics. Moreover, DMSO deposition forms a robust protective layer on the Zn anode, preventing water reduction and inhibiting Zn dendrite growth. These findings highlight the potential of using antisolvents to modify the solvation environment of Zn^{2+} , thereby enhancing the performance and stability of zinc anodes in AZIBs.

Altering the Zn²⁺ solvation structure can effectively decrease the solvation energy with water, thereby enhancing Zn reversibility. However, the incorporation of additional solvents, particularly organic ones, can significantly impact electrolyte properties such as ionic conductivity and flammability. For instance, the use of an organic solvent like ethyl alcohol could potentially reduce the ionic conductivity of the electrolyte. This reduction in conductivity may lead to lower power density in the batteries and pose a higher safety risk due to increased flammability. Consequently, it is crucial to carefully consider the trade-offs associated with introducing organic solvents into the electrolyte to balance improved Zn reversibility with the maintenance of desirable electrolyte properties and overall battery safety. These considerations underscore the need for continued research and development in optimising electrolyte formulations to enhance the efficiency, safety, and practicality of AZIBs for large-scale energy storage solutions.

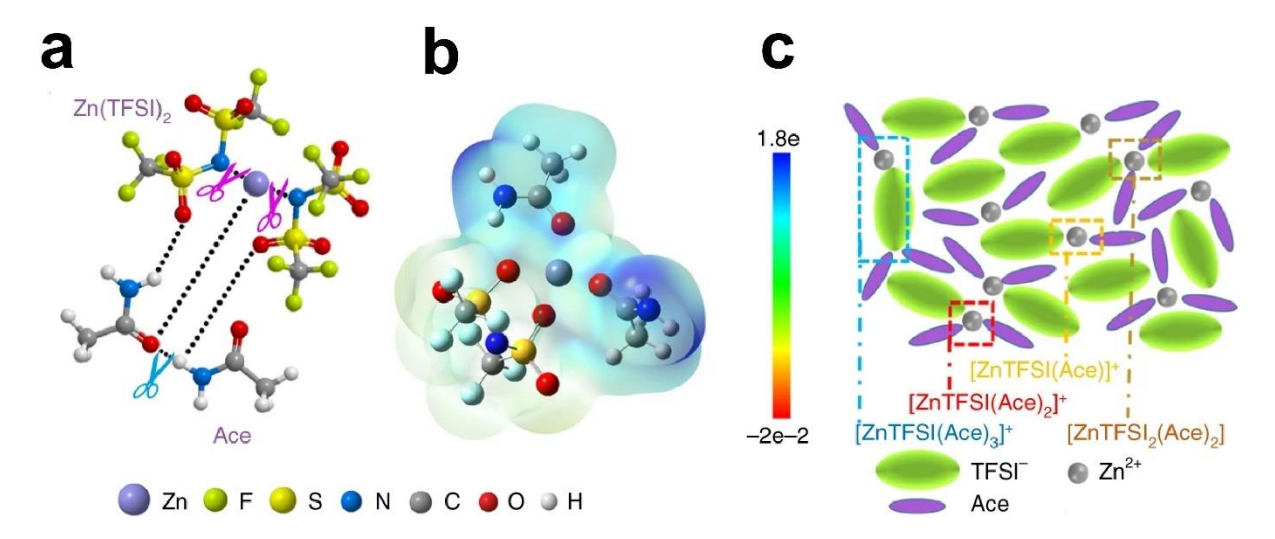


Figure 1.23 (a) Schematic diagram of the interplay among Zn²⁺, TFSI⁻, and Ace to form eutectic solutions. (b) Molecular electrostatic potential energy surface. (c) Illustration of representative environment of active Zn species within the ZES. Reprinted with permission from ref.^[249] Copyright 2019 Springer Nature.

1.4 References

- [1] Z. Zhu, T. Jiang, M. Ali, Y. Meng, Y. Jin, Y. Cui, W. Chen, *Chemical Reviews* **2022**, *122*, 16610.
- [2] D. Deng, Energy Science & Engineering 2015, 3, 385.
- [3] T. Jiang, P. He, G. Wang, Y. Shen, C.-W. Nan, L.-Z. Fan, *Advanced Energy Materials* **2020**, *10*, 1903376.
- [4] P. P. Lopes, V. R. Stamenkovic, *Science* **2020**, *369*, 923.
- [5] Y. Zhang, C.-g. Zhou, J. Yang, S.-c. Xue, H.-l. Gao, X.-h. Yan, Q.-y. Huo, S.-w. Wang, Y. Cao, J. Yan, K.-z. Gao, L.-x. Wang, *Journal of Power Sources* **2022**, *520*, 230800.
- [6] J. Noack, N. Roznyatovskaya, T. Herr, P. Fischer, *Angewandte Chemie International Edition* **2015**, *54*, 9776.
- [7] J. Winsberg, T. Hagemann, T. Janoschka, M. D. Hager, U. S. Schubert, *Angewandte Chemie International Edition* **2017**, *56*, 686.
- [8]K. Mongird, V. V. Viswanathan, P. J. Balducci, M. J. E. Alam, V. Fotedar, V. S. Koritarov, B. Hadjerioua, Pacific Northwest National Lab.(PNNL), Richland, WA (United States), **2019**.
- [9] P. Ralon, M. Taylor, A. Ilas, H. Diaz-Bone, K. Kairies, *International Renewable Energy Agency: Abu Dhabi, United Arab Emirates* **2017**, *164*.
- [10] E. J. Berg, C. Villevieille, D. Streich, S. Trabesinger, P. Novák, *Journal of The Electrochemical Society* **2015**, *162*, A2468.
- [11] L. Fan, R. Ma, J. Wang, H. Yang, B. Lu, Advanced Materials 2018, 30, 1805486.
- [12] C. Li, X. Zhang, W. He, *Journal of Materials Science: Materials in Electronics* **2018**, *29*, 14353.
- [13] M. Song, H. Tan, D. Chao, H. J. Fan, Advanced Functional Materials 2018, 28, 1802564.
- [14] B. Tang, L. Shan, S. Liang, J. Zhou, Energy & Environmental Science 2019, 12, 3288.
- [15] F. Wu, J. Maier, Y. Yu, Chemical Society Reviews 2020, 49, 1569.
- [16] M. M. Thackeray, C. Wolverton, E. D. Isaacs, *Energy & Environmental Science* **2012**, *5*, 7854.
- [17]N. Schadlow, A. Herman, B. Helwig, *Powering innovations: A strategic approach to America's advanced battery technology*, Hudson Institute, 2021.
- [18] W. E. Alnaser, N. W. Alnaser, Renewable and Sustainable Energy Reviews 2011, 15, 3074.
- [19] T. Takeuchi, T. Kyuna, H. Morimoto, S.-i. Tobishima, *Journal of Power Sources* **2011**, *196*, 2790.

- [20] G. E. Blomgren, Journal of The Electrochemical Society 2016, 164, A5019.
- [21] J. Xu, X. Cai, S. Cai, Y. Shao, C. Hu, S. Lu, S. Ding, *ENERGY & ENVIRONMENTAL MATERIALS* **2023**, *6*, e12450.
- [22] S. Van den Brink, R. Kleijn, B. Sprecher, A. Tukker, *Resources, Conservation and Recycling* **2020**, *156*, 104743.
- [23] X. Fan, R. R. Gaddam, N. A. Kumar, X. S. Zhao, *Advanced Energy Materials* **2017**, 7, 1700317.
- [24] W. Sun, F. Wang, S. Hou, C. Yang, X. Fan, Z. Ma, T. Gao, F. Han, R. Hu, M. Zhu, C. Wang, *J. Am. Chem. Soc.* **2017**, *139*, 9775.
- [25] Y. Huang, L. Lin, C. Zhang, L. Liu, Y. Li, Z. Qiao, J. Lin, Q. Wei, L. Wang, Q. Xie, *Advanced Science* **2022**, *9*, 2106004.
- [26] Y. Li, S. Guo, Matter 2021, 4, 1142.
- [27] Z. Han, S. Zhao, J. Xiao, X. Zhong, J. Sheng, W. Lv, Q. Zhang, G. Zhou, H.-M. Cheng, *Advanced Materials* **2021**, *33*, 2105947.
- [28] G. Li, J. Sun, W. Hou, S. Jiang, Y. Huang, J. Geng, *Nature communications* **2016**, 7, 10601.
- [29] X. Qi, F. Yang, P. Sang, Z. Zhu, X. Jin, Y. Pan, J. Ji, R. Jiang, H. Du, Y. Ji, Y. Fu, L. Qie, Y. Huang, *Angewandte Chemie International Edition* **2023**, *62*, e202218803.
- [30] J.-Y. Hwang, S.-T. Myung, Y.-K. Sun, Chemical Society Reviews 2017, 46, 3529.
- [31] P. Adelhelm, P. Hartmann, C. L. Bender, M. Busche, C. Eufinger, J. Janek, *Beilstein journal of nanotechnology* **2015**, *6*, 1016.
- [32] M. D. Slater, D. Kim, E. Lee, C. S. Johnson, *Advanced Functional Materials* **2013**, *23*, 947.
- [33] B. Jache, P. Adelhelm, Angewandte Chemie International Edition 2014, 53, 10169.
- [34] S. Hariharan, K. Saravanan, V. Ramar, P. Balaya, *Physical Chemistry Chemical Physics* **2013**, *15*, 2945.
- [35] Y. Xu, E. Swaans, S. Basak, H. W. Zandbergen, D. M. Borsa, F. M. Mulder, *Adv. Energy Mater.* **2016**, *6*, 1501436.
- [36] X. Deng, J. K. Sarpong, G. Zhang, J. Hao, X. Zhao, L. Li, H. Li, C. Han, B. Li, *InfoMat* **2023**, *5*, e12382.
- [37] M. Shi, P. Das, Z.-S. Wu, T.-g. Liu, X. Zhang, Advanced Materials 2023, 35, 2302199.

- [38] F. Yue, Z. Tie, S. Deng, S. Wang, M. Yang, Z. Niu, *Angewandte Chemie International Edition* **2021**, *60*, 13882.
- [39] X. Wang, C. Bommier, Z. Jian, Z. Li, R. S. Chandrabose, I. A. Rodríguez-Pérez, P. A. Greaney, X. Ji, *Angewandte Chemie International Edition* **2017**, *56*, 2909.
- [40] Y. Wu, K. Zhang, S. Chen, Y. Liu, Y. Tao, X. Zhang, Y. Ding, S. Dai, ACS Applied Energy Materials 2020, 3, 319.
- [41] X. Xue, T. Huang, Y. Zhang, J. Qi, F. Wei, Y. Sui, Z. Jin, *Advanced Functional Materials* **2023**, *33*, 2306377.
- [42] M. Wang, C. Jiang, S. Zhang, X. Song, Y. Tang, H.-M. Cheng, *Nature Chemistry* **2018**, *10*, 667.
- [43] A. Shyamsunder, L. E. Blanc, A. Assoud, L. F. Nazar, ACS Energy Letters 2019, 4, 2271.
- [44] A. Ponrouch, C. Frontera, F. Bardé, M. R. Palacín, Nature Materials 2016, 15, 169.
- [45] D. Wang, X. Gao, Y. Chen, L. Jin, C. Kuss, P. G. Bruce, *Nature Materials* **2018**, *17*, 16.
- [46] G. Yoon, D.-H. Kim, I. Park, D. Chang, B. Kim, B. Lee, K. Oh, K. Kang, *Advanced Functional Materials* **2017**, *27*, 1702887.
- [47] F. Liu, T. Wang, X. Liu, L.-Z. Fan, Advanced Energy Materials 2021, 11, 2000787.
- [48] D. Aurbach, Z. Lu, A. Schechter, Y. Gofer, H. Gizbar, R. Turgeman, Y. Cohen, M. Moshkovich, E. Levi, *Nature* **2000**, *407*, 724.
- [49] X. Sun, P. Bonnick, V. Duffort, M. Liu, Z. Rong, K. A. Persson, G. Ceder, L. F. Nazar, *Energy & Environmental Science* **2016**, *9*, 2273.
- [50] Y. Gofer, O. Chusid, H. Gizbar, Y. Viestfrid, H. E. Gottlieb, V. Marks, D. Aurbach, *Electrochemical and Solid-State Letters* **2006**, *9*, A257.
- [51] Z. Li, J. Häcker, M. Fichtner, Z. Zhao-Karger, *Advanced Energy Materials* **2023**, *13*, 2300682.
- [52] E. Faegh, B. Ng, D. Hayman, W. E. Mustain, *Nature Energy* **2021**, *6*, 21.
- [53] F. Ambroz, T. J. Macdonald, T. Nann, Advanced Energy Materials 2017, 7, 1602093.
- [54] D.-Y. Wang, C.-Y. Wei, M.-C. Lin, C.-J. Pan, H.-L. Chou, H.-A. Chen, M. Gong, Y. Wu, C. Yuan, M. Angell, Y.-J. Hsieh, Y.-H. Chen, C.-Y. Wen, C.-W. Chen, B.-J. Hwang, C.-C. Chen, H. Dai, *Nature Communications* **2017**, *8*, 14283.
- [55] D.-J. Yoo, M. Heeney, F. Glöcklhofer, J. W. Choi, *Nature Communications* **2021**, *12*, 2386.
- [56] Y. Zhang, S. Liu, Y. Ji, J. Ma, H. Yu, Advanced Materials 2018, 30, 1706310.

- [57] J. Xu, Y. Dou, Z. Wei, J. Ma, Y. Deng, Y. Li, H. Liu, S. Dou, *Advanced Science* **2017**, *4*, 1700146.
- [58] C. Li, H. Yuan, T. Liu, R. Zhang, J. Zhu, H. Cui, Y. Wang, D. Cao, D. Wang, C. Zhi, *Angewandte Chemie* **2024**, *136*, e202403504.
- [59] Z. Xiao, F. Xia, L. Xu, X. Wang, J. Meng, H. Wang, X. Zhang, L. Geng, J. Wu, L. Mai, *Advanced Functional Materials* **2022**, *32*, 2108244.
- [60] L. An, C. Wei, M. Lu, H. Liu, Y. Chen, G. G. Scherer, A. C. Fisher, P. Xi, Z. J. Xu, C. H. Yan, *Advanced materials* **2021**, *33*, 2006328.
- [61] B. Wu, Y. Mu, Z. Li, M. Li, L. Zeng, T. Zhao, Chinese Chemical Letters 2023, 34, 107629.
- [62] J. Goclon, R. Grybos, M. Witko, J. Hafner, *Phys. Rev. B: Condens. Matter* **2009**, *79*, 075439.
- [63] S. Boyd, V. Augustyn, *Inorganic Chemistry Frontiers* **2018**, *5*, 999.
- [64] S. Wang, Y. Wang, Z. Wei, J. Zhu, Z. Chen, H. Hong, Q. Xiong, D. Zhang, S. Li, S. Wang, Y. Huang, C. Zhi, *Advanced Materials* **2024**, *36*, 2401924.
- [65] Q. Zhang, Y. Ma, Y. Lu, Y. Ni, L. Lin, Z. Hao, Z. Yan, Q. Zhao, J. Chen, *Journal of the American Chemical Society* **2022**, *144*, 18435.
- [66] G. Li, L. Sun, S. Zhang, C. Zhang, H. Jin, K. Davey, G. Liang, S. Liu, J. Mao, Z. Guo, *Advanced Functional Materials* **2024**, *34*, 2301291.
- [67] Y. Xu, C. Wang, Y. Huang, J. Fu, Nano Energy **2021**, 80, 105545.
- [68] Z. Xiang, Y. Qiu, X. Guo, K. Qi, Z.-L. Xu, B. Y. Xia, *Energy & Environmental Science* **2024**, *17*, 3409.
- [69] D. Wang, T. Sheng, J. Chen, H.-F. Wang, P. Hu, *Nature Catalysis* **2018**, *1*, 291.
- [70] Z. Zhou, Z. Pei, L. Wei, S. Zhao, X. Jian, Y. Chen, *Energy & Environmental Science* **2020**, *13*, 3185.
- [71] J. Meng, Y. Song, Z. Qin, Z. Wang, X. Mu, J. Wang, X.-X. Liu, *Advanced Functional Materials* **2022**, *32*, 2204026.
- [72] Q. Wang, D. O'Hare, Chemical Reviews **2012**, 112, 4124.
- [73] W. Zhang, Y. Dai, R. Chen, Z. Xu, J. Li, W. Zong, H. Li, Z. Li, Z. Zhang, J. Zhu, *Angewandte Chemie International Edition* **2023**, *62*, e202212695.
- [74] Y. Zou, Z. Guo, J. Zhou, Q. Zheng, X. Shan, L. Zhao, *Journal of Alloys and Compounds* **2022**, *918*, 165547.

- [75] J.-M. Oh, C. C. Venters, C. Di, A. M. Pinto, L. Wan, I. Younis, Z. Cai, C. Arai, B. R. So, J. Duan, G. Dreyfuss, *Nature Communications* **2020**, *11*, 1.
- [76] J. Cao, D. Zhang, X. Zhang, Z. Zeng, J. Qin, Y. Huang, *Energy & Environmental Science* **2022**, *15*, 499.
- [77] S. Sun, J. Li, C. Xu, T. Zhai, H. Xia, Journal of Materials Chemistry A 2022, 10, 19231.
- [78] G. Fang, S. Liang, Z. Chen, P. Cui, X. Zheng, A. Pan, B. Lu, X. Lu, J. Zhou, *Advanced Functional Materials* **2019**, *29*, 1905267.
- [79] M. J. Park, H. Yaghoobnejad Asl, S. Therese, A. Manthiram, *Journal of Materials Chemistry A* **2019**, 7, 7159.
- [80] C. Zuo, F. Xiong, J. Wang, Y. An, L. Zhang, Q. An, *Advanced Functional Materials* **2022**, 32, 2202975.
- [81] F. Zhang, X. Sun, M. Du, X. Zhang, W. Dong, Y. Sang, J. Wang, Y. Li, H. Liu, S. Wang, *ENERGY & ENVIRONMENTAL MATERIALS* **2021**, *4*, 620.
- [82] X. Liu, Y. Sun, Y. Tong, X. Wang, J. Zheng, Y. Wu, H. Li, L. Niu, Y. Hou, *Nano Energy* **2021**, *86*, 106070.
- [83] X. Chen, X. Shen, T.-Z. Hou, R. Zhang, H.-J. Peng, Q. Zhang, *Chem* **2020**, *6*, 2242.
- [84] X. Guo, J. Zhou, C. Bai, X. Li, G. Fang, S. Liang, *Materials Today Energy* **2020**, *16*, 100396.
- [85] X. Jia, C. Liu, Z. G. Neale, J. Yang, G. Cao, Chemical Reviews 2020, 120, 7795.
- [86] Z. Lv, Y. Tan, Y. Kang, J. Yang, X. Cheng, W. Meng, Y. Zhang, C. C. Li, J. Zhao, Y. Yang, *Science China Chemistry* **2023**, *66*, 1537.
- [87] D. Kundu, S. H. Vajargah, L. Wan, B. Adams, D. Prendergast, L. F. Nazar, *Energy & Environmental Science* **2018**, *11*, 881.
- [88] M. Huang, X. Wang, X. Liu, L. Mai, Advanced Materials 2022, 34, 2105611.
- [89] W. Deng, Z. Deng, Y. Chen, R. Feng, X. Wang, *Angewandte Chemie International Edition* **2024**, *63*, e202316499.
- [90] B. Zhang, L. Qin, Y. Fang, Y. Chai, X. Xie, B. Lu, S. Liang, J. Zhou, *Science Bulletin* **2022**, *67*, 955.
- [91] C. Li, R. Kingsbury, A. S. Thind, A. Shyamsunder, T. T. Fister, R. F. Klie, K. A. Persson, L. F. Nazar, *Nat. Commun.* **2023**, *14*, 3067.
- [92] Y. Wang, Z. Wang, W. K. Pang, W. Lie, J. A. Yuwono, G. Liang, S. Liu, A. M. D. Angelo, J. Deng, Y. Fan, K. Davey, B. Li, Z. Guo, *Nature Communications* **2023**, *14*, 2720.

- [93] M. Peschke, A. T. Blades, P. Kebarle, *Journal of the American Chemical Society* **2000**, *122*, 10440.
- [94] H. Li, W. Zhang, K. Sun, J. Guo, K. Yuan, J. Fu, T. Zhang, X. Zhang, H. Long, Z. Zhang, Y. Lai, H. Sun, *Advanced Energy Materials* **2021**, *11*, 2100867.
- [95] S. Huang, R. Tang, X. Liu, Y. Zhang, Y. Tang, Z. Wen, M. Ye, Y. Yang, C. C. Li, *Energy & Environmental Science* **2024**, *17*, 591.
- [96] P. He, J. Huang, *Advanced Materials* **2022**, *34*, 2109872.
- [97] P. He, J. Huang, ACS Energy Letters 2021, 6, 1990.
- [98] A. Wang, Q. Deng, L. Deng, X. Guan, J. Luo, Advanced Functional Materials 2019, 29, 1902630.
- [99] A. Jana, S. I. Woo, K. Vikrant, R. E. García, Energy & Environmental Science 2019, 12, 3595.
- [100] S. Wang, Z. Huang, J. Zhu, Y. Wang, D. Li, Z. Wei, H. Hong, D. Zhang, Q. Xiong, S. Li, *Advanced Materials* **2024**, 2406451.
- [101] G. Chang, S. Liu, Y. Fu, X. Hao, W. Jin, X. Ji, J. Hu, *Advanced Materials Interfaces* **2019**, *6*, 1901358.
- [102] C. Xie, S. Liu, Z. Yang, H. Ji, S. Zhou, H. Wu, C. Hu, Y. Tang, X. Ji, Q. Zhang, *Angewandte Chemie International Edition* **2023**, *62*, e202218612.
- [103] Y. Zuo, K. Wang, P. Pei, M. Wei, X. Liu, Y. Xiao, P. Zhang, *Materials Today Energy* **2021**, *20*, 100692.
- [104] M. K. Aslam, Y. Niu, T. Hussain, H. Tabassum, W. Tang, M. Xu, R. Ahuja, *Nano Energy* **2021**, *86*, 106142.
- [105] Z. Cao, P. Zhuang, X. Zhang, M. Ye, J. Shen, P. M. Ajayan, *Advanced Energy Materials* **2020**, *10*, 2001599.
- [106] Q. Zhang, J. Luan, Y. Tang, X. Ji, H. Wang, Angew. Chem. Int. Ed. 2020, 59, 13180.
- [107] K. Wang, Y. Xiao, P. Pei, X. Liu, Y. Wang, Journal of the Electrochemical Society 2019, 166, D389.
- [108] Q. Yang, Q. Li, Z. Liu, D. Wang, Y. Guo, X. Li, Y. Tang, H. Li, B. Dong, C. Zhi, *Advanced Materials* **2020**, *32*, 2001854.
- [109] W. Liu, P. Liu, D. Mitlin, Chemical Society Reviews 2020, 49, 7284.
- [110] V. Yufit, F. Tariq, D. S. Eastwood, M. Biton, B. Wu, P. D. Lee, N. P. Brandon, *Joule* **2019**, *3*, 485.

- [111] H. Zhang, Y. Wu, J. Yu, T. Jiang, M. Wu, Adv. Funct. Mater. 2024, 34, 2301912.
- [112] H. J. Kim, S. Kim, K. Heo, J. H. Lim, H. Yashiro, S. T. Myung, *Advanced Energy Materials* **2023**, *13*, 2203189.
- [113] W. Wang, G. Huang, Y. Wang, Z. Cao, L. Cavallo, M. N. Hedhili, H. N. Alshareef, *Advanced Energy Materials* **2022**, *12*, 2102797.
- [114] H. Cheng, S. Zhang, W. Guo, Q. Wu, Z. Shen, L. Wang, W. Zhong, D. Li, B. Zhang, C. Liu, *Advanced Science* **2024**, *11*, 2307052.
- [115] J. Zhu, Z. Tie, S. Bi, Z. Niu, Angewandte Chemie **2024**, e202403712.
- [116] N. Zhang, S. Huang, Z. Yuan, J. Zhu, Z. Zhao, Z. Niu, *Angewandte Chemie International Edition* **2021**, *60*, 2861.
- [117] J. Hao, B. Li, X. Li, X. Zeng, S. Zhang, F. Yang, S. Liu, D. Li, C. Wu, Z. Guo, *Advanced Materials* **2020**, *32*, 2003021.
- [118] Y. Yang, H. Yang, R. Zhu, H. Zhou, Energy & Environmental Science 2023, 16, 2723.
- [119] Y. Jin, Z. Zheng, D. Wei, X. Jiang, H. Lu, L. Sun, F. Tao, D. Guo, Y. Liu, J. Gao, *Joule* **2020**, *4*, 1714.
- [120] Y. Zhang, X. Zheng, N. Wang, W.-H. Lai, Y. Liu, S.-L. Chou, H.-K. Liu, S.-X. Dou, Y.-X. Wang, *Chemical Science* **2022**, *13*, 14246.
- [121] J. Cao, D. Zhang, C. Gu, X. Wang, S. Wang, X. Zhang, J. Qin, Z. S. Wu, *Advanced Energy Materials* **2021**, *11*, 2101299.
- [122] Z. Liu, Y. Huang, Y. Huang, Q. Yang, X. Li, Z. Huang, C. Zhi, *Chemical Society Reviews* **2020**, *49*, 180.
- [123] M. R. Harrison, M. G. Francesconi, Coordination Chemistry Reviews 2011, 255, 451.
- [124] Y. Xu, G. Fan, P. X. Sun, Y. Guo, Y. Wang, X. Gu, L. Wu, L. Yu, *Angewandte Chemie International Edition* **2023**, *62*, e202303529.
- [125] L. Liu, Y. C. Wu, L. Huang, K. Liu, B. Duployer, P. Rozier, P. L. Taberna, P. Simon, *Advanced Energy Materials* **2021**, *11*, 2101287.
- [126] S. Laubach, S. Laubach, P. C. Schmidt, D. Ensling, S. Schmid, W. Jaegermann, A. Thißen, K. Nikolowski, H. Ehrenberg, *Physical Chemistry Chemical Physics* **2009**, *11*, 3278.
- [127] Q. Zhao, A. Song, S. Ding, R. Qin, Y. Cui, S. Li, F. Pan, *Advanced Materials* **2020**, *32*, 2002450.
- [128] B. Yang, A. G. Tamirat, D. Bin, Y. Yao, H. Lu, Y. Xia, *Advanced Functional Materials* **2021**, *31*, 2104543.

- [129] Y. Yuan, C. Zhan, K. He, H. Chen, W. Yao, S. Sharifi-Asl, B. Song, Z. Yang, A. Nie, X. Luo, H. Wang, S. M. Wood, K. Amine, M. S. Islam, J. Lu, R. Shahbazian-Yassar, *Nature Communications* **2016**, *7*, 13374.
- [130] K. Kang, G. Ceder, *Physical Review B* **2006**, *74*, 094105.
- [131] K. W. Nam, H. Kim, J. H. Choi, J. W. Choi, *Energy & Environmental Science* **2019**, *12*, 1999.
- [132] H. Li, W. Zhang, K. Sun, J. Guo, K. Yuan, J. Fu, T. Zhang, X. Zhang, H. Long, Z. Zhang, *Advanced Energy Materials* **2021**, *11*, 2100867.
- [133] J. Huang, Z. Wang, M. Hou, X. Dong, Y. Liu, Y. Wang, Y. Xia, *Nature communications* **2018**, *9*, 2906.
- [134] L. Yan, B. Liu, J. Hao, Y. Han, C. Zhu, F. Liu, X. Zou, Y. Zhou, B. Xiang, *Journal of Energy Chemistry* **2023**, *82*, 88.
- [135] Y. Yang, Y. Tang, S. Liang, Z. Wu, G. Fang, X. Cao, C. Wang, T. Lin, A. Pan, J. Zhou, *Nano Energy* **2019**, *61*, 617.
- [136] Z. Zhou, J. Tong, X. Zou, Y. Wang, Y. Bai, Y. Yang, Y. Li, C. Wang, S. Liu, *Journal of Materials Chemistry A* **2024**, *12*, 10923.
- [137] G. Liu, H. Huang, R. Bi, X. Xiao, T. Ma, L. Zhang, *Journal of Materials Chemistry A* **2019**, 7, 20806.
- [138] H. Yao, H. Yu, Y. Zheng, N. W. Li, S. Li, D. Luan, X. W. Lou, L. Yu, *Angewandte Chemie International Edition* **2023**, *62*, e202315257.
- [139] S. Lee, W. Jin, S. H. Kim, S. H. Joo, G. Nam, P. Oh, Y. K. Kim, S. K. Kwak, J. Cho, *Angewandte Chemie International Edition* **2019**, *58*, 10478.
- [140] Y. Xu, M. Zhou, X. Wang, C. Wang, L. Liang, F. Grote, M. Wu, Y. Mi, Y. Lei, *Angewandte Chemie* **2015**, *127*, 8892.
- [141] X. Liu, L. Zhao, H. Xu, Q. Huang, Y. Wang, C. Hou, Y. Hou, J. Wang, F. Dang, J. Zhang, *Advanced Energy Materials* **2020**, *10*, 2001415.
- [142] R. Zheng, D. Du, Y. Yan, S. Liu, X. Wang, C. Shu, *Advanced Functional Materials* **2024**, 2316440.
- [143] Z. Li, Q. Zhang, L. Hencz, J. Liu, P. Kaghazchi, J. Han, L. Wang, S. Zhang, *Nano Energy* **2021**, *89*, 106331.
- [144] X. Hou, T. Katsumata, Y. Kimura, Y. Tamenori, K. Nitta, H. Yamagishi, K. Amezawa, T. Nakamura, *ACS Applied Energy Materials* **2023**, *6*, 2072.
- [145] Z. Lin, K. Fan, T. Liu, Z. Xu, G. Chen, H. Zhang, H. Li, X. Guo, X. Zhang, Y. Zhu, *Nano-micro letters* **2024**, *16*, 48.

- [146] L. Xiong, Y. Xu, T. Tao, J. B. Goodenough, Journal of Power Sources 2012, 199, 214.
- [147] M. Chen, L. Zhou, T. Wang, H. Xia, H. K. Liu, S. X. Dou, S. Chou, *Advanced Functional Materials* **2023**, *33*, 2214786.
- [148] J. Xie, F. Yu, J. Zhao, W. Guo, H.-L. Zhang, G. Cui, Q. Zhang, *Energy Storage Materials* **2020**, *33*, 283.
- [149] H. Zhang, Y. Zhang, Y. Liu, X. Shi, Y. Zhang, L. Bai, Q. Wang, L. Sun, ACS Applied Materials & Interfaces 2022, 14, 36668.
- [150] T. Xiong, Z. G. Yu, H. Wu, Y. Du, Q. Xie, J. Chen, Y. W. Zhang, S. J. Pennycook, W. S. V. Lee, J. Xue, *Advanced Energy Materials* **2019**, *9*, 1803815.
- [151] Y. Zeng, Z. Lai, Y. Han, H. Zhang, S. Xie, X. Lu, Advanced Materials 2018, 30, 1802396.
- [152] J. Jin, Y. Liu, X. Zhao, H. Liu, S. Deng, Q. Shen, Y. Hou, H. Qi, X. Xing, L. Jiao, *Angewandte Chemie* **2023**, *135*, e202219230.
- [153] H. Yu, G. Qin, J. Wang, X. Zhao, L. Li, X. Yu, X. Zhang, Z. Lu, X. Yang, *ACS Catalysis* **2022**, *12*, 12890.
- [154] Y. Yuan, C. Liu, B. W. Byles, W. Yao, B. Song, M. Cheng, Z. Huang, K. Amine, E. Pomerantseva, R. Shahbazian-Yassar, *Joule* **2019**, *3*, 471.
- [155] K. Zhu, S. Wei, H. Shou, F. Shen, S. Chen, P. Zhang, C. Wang, Y. Cao, X. Guo, M. Luo, *Nature Communications* **2021**, *12*, 6878.
- [156] Z. Xing, G. Xu, J. Han, G. Chen, B. Lu, S. Liang, J. Zhou, *Trends in Chemistry* **2023**, 5, 380.
- [157] W. Liu, J. Li, W. Li, H. Xu, C. Zhang, X. Qiu, *Nature Communications* **2020**, *11*, 3629.
- [158] S. P. Kühn, K. Edström, M. Winter, I. Cekic-Laskovic, *Advanced Materials Interfaces* **2022**, *9*, 2102078.
- [159] J. Huang, J. Liu, J. He, M. Wu, S. Qi, H. Wang, F. Li, J. Ma, *Angewandte Chemie* **2021**, *133*, 20885.
- [160] J.-N. Zhang, Q. Li, Y. Wang, J. Zheng, X. Yu, H. Li, *Energy Storage Materials* **2018**, *14*, 1.
- [161] Y. Shirazi Moghadam, A. El Kharbachi, T. Diemant, G. Melinte, Y. Hu, M. Fichtner, *Chemistry of Materials* **2021**, *33*, 8235.
- [162] R. Andris, D. Omo-Lamai, M. J. Zachman, E. Pomerantseva, ACS Applied Energy Materials 2023, 6, 9926.
- [163] M. Zhou, Y. Chen, G. Fang, S. Liang, Energy Storage Materials 2022, 45, 618.

- [164] B. W. Olbasa, C. J. Huang, F. W. Fenta, S. K. Jiang, S. A. Chala, H. C. Tao, Y. Nikodimos, C. C. Wang, H. S. Sheu, Y. W. Yang, *Advanced Functional Materials* **2022**, *32*, 2103959.
- [165] R. K. Ghavami, Z. Rafiei, S. M. Tabatabaei, Journal of Power Sources 2007, 164, 934.
- [166] X. Zhang, J. Li, H. Ao, D. Liu, L. Shi, C. Wang, Y. Zhu, Y. Qian, *Energy Storage Materials* **2020**, *30*, 337.
- [167] Y. Dai, J. Li, C. Zhang, R. Lu, X. Tao, K. A. Owusu, G. He, Y. Zhou, J. Lu, *ACS Energy Letters* **2023**, *8*, 4762.
- [168] H. Dong, R. Liu, X. Hu, F. Zhao, L. Kang, L. Liu, J. Li, Y. Tan, Y. Zhou, D. J. Brett, *Advanced Science* **2023**, *10*, 2205084.
- [169] K. Guan, L. Tao, R. Yang, H. Zhang, N. Wang, H. Wan, J. Cui, J. Zhang, H. Wang, H. Wang, *Advanced Energy Materials* **2022**, *12*, 2103557.
- [170] H. Liu, Z. Xin, B. Cao, Z. Xu, B. Xu, Q. Zhu, J. L. Yang, B. Zhang, H. J. Fan, *Advanced Functional Materials* **2024**, *34*, 2309840.
- [171] M. Du, F. Zhang, X. Zhang, W. Dong, Y. Sang, J. Wang, H. Liu, S. Wang, *Science China Chemistry* **2020**, *63*, 1767.
- [172] Y. Gong, B. Wang, H. Ren, D. Li, D. Wang, H. Liu, S. Dou, *Nano-Micro Letters* **2023**, *15*, 208.
- [173] Y. Yan, C. Shu, T. Zeng, X. Wen, S. Liu, D. Deng, Y. Zeng, ACS nano 2022, 16, 9150.
- [174] M. Fayette, H. J. Chang, I. A. Rodríguez-Pérez, X. Li, D. Reed, ACS applied materials & interfaces 2020, 12, 42763.
- [175] Y. Mu, Z. Li, B.-k. Wu, H. Huang, F. Wu, Y. Chu, L. Zou, M. Yang, J. He, L. Ye, *Nature Communications* **2023**, *14*, 4205.
- [176] L. Zeng, H. He, H. Chen, D. Luo, J. He, C. Zhang, *Advanced Energy Materials* **2022**, *12*, 2103708.
- [177] Z. Bie, Q. Yang, X. Cai, Z. Chen, Z. Jiao, J. Zhu, Z. Li, J. Liu, W. Song, C. Zhi, *Advanced Energy Materials* **2022**, *12*, 2202683.
- [178] Z. Shen, L. Luo, C. Li, J. Pu, J. Xie, L. Wang, Z. Huai, Z. Dai, Y. Yao, G. Hong, *Advanced Energy Materials* **2021**, *11*, 2100214.
- [179] C. Deng, X. Xie, J. Han, Y. Tang, J. Gao, C. Liu, X. Shi, J. Zhou, S. Liang, *Adv. Funct. Mater.* **2020**, *30*, 2000599.
- [180] J. Wang, Z. Cai, R. Xiao, Y. Ou, R. Zhan, Z. Yuan, Y. Sun, ACS applied materials & interfaces 2020, 12, 23028.

- [181] Q. Zhu, G. Sun, S. Qiao, D. Wang, Z. Cui, W. Zhang, J. Liu, *Advanced Materials* **2024**, *36*, 2308577.
- [182] J. Cao, J. Wu, H. Wu, Y. Jin, D. Luo, X. Yang, L. Zhang, D. Zhang, J. Qin, J. Lu, *Advanced Functional Materials* **2024**, 2401537.
- [183] T. Zhang, F. Ran, Advanced Functional Materials 2021, 31, 2010041.
- [184] D. Chen, W. Zhang, K. Luo, Y. Song, Y. Zhong, Y. Liu, G. Wang, B. Zhong, Z. Wu, X. Guo, *Energy & Environmental Science* **2021**, *14*, 2244.
- [185] A. Bianco, Y. Chen, E. Frackowiak, M. Holzinger, N. Koratkar, V. Meunier, S. Mikhailovsky, M. Strano, J. M. Tascon, M. Terrones, *Carbon* **2020**, *161*, 373.
- [186] H. Geng, Y. Peng, L. Qu, H. Zhang, M. Wu, *Advanced Energy Materials* **2020**, *10*, 1903030.
- [187] J. Zhou, M. Xie, F. Wu, Y. Mei, Y. Hao, R. Huang, G. Wei, A. Liu, L. Li, R. Chen, *Advanced Materials* **2021**, *33*, 2101649.
- [188] Y. Qian, C. Meng, J. He, X. Dong, Journal of Power Sources 2020, 480, 228871.
- [189] Y. Li, Y.-F. Guo, Z.-X. Li, P.-F. Wang, Y. Xie, T.-F. Yi, *Energy Storage Materials* **2024**, 103300.
- [190] Y. Mu, Z. Li, B.-k. Wu, H. Huang, F. Wu, Y. Chu, L. Zou, M. Yang, J. He, L. Ye, M. Han, T. Zhao, L. Zeng, *Nature Communications* **2023**, *14*, 4205.
- [191] D. Atkins, E. Ayerbe, A. Benayad, F. G. Capone, E. Capria, I. E. Castelli, I. Cekic-Laskovic, R. Ciria, L. Dudy, K. Edström, *Advanced Energy Materials* **2022**, *12*, 2102687.
- [192] K. X. Wang, X. H. Li, J. S. Chen, Advanced Materials 2015, 27, 527.
- [193] A. M. Tripathi, W.-N. Su, B. J. Hwang, Chemical Society Reviews 2018, 47, 736.
- [194] Z. Guo, L. Fan, C. Zhao, A. Chen, N. Liu, Y. Zhang, N. Zhang, Adv. Mater. 2022, 34, 2105133.
- [195] B. Li, X. Zhang, T. Wang, Z. He, B. Lu, S. Liang, J. Zhou, *Nano-Micro Letters* **2022**, *14*, 1.
- [196] W. Lu, C. Zhang, H. Zhang, X. Li, ACS Energy Letters **2021**, 6, 2765.
- [197] F. Xie, H. Li, X. Wang, X. Zhi, D. Chao, K. Davey, S. Z. Qiao, *Advanced Energy Materials* **2021**, *11*, 2003419.
- [198] Z. Shi, S. Chen, Z. Xu, Z. Liu, J. Guo, J. Yin, P. Xu, N. Zhang, W. Zhang, H. N. Alshareef, *Advanced Energy Materials* **2023**, *13*, 2300331.

- [199] H. Liu, J. G. Wang, W. Hua, H. Sun, Y. Huyan, S. Tian, Z. Hou, J. Yang, C. Wei, F. Kang, *Advanced Science* **2021**, *8*, 2102612.
- [200] S. Liu, J. Vongsvivut, Y. Wang, R. Zhang, F. Yang, S. Zhang, K. Davey, J. Mao, Z. Guo, *Angewandte Chemie International Edition* **2023**, *62*, e202215600.
- [201] P. Cao, X. Zhou, A. Wei, Q. Meng, H. Ye, W. Liu, J. Tang, J. Yang, *Advanced Functional Materials* **2021**, *31*, 2100398.
- [202] Y. Liu, T. Guo, Q. Liu, F. Xiong, M. Huang, Y. An, J. Wang, Q. An, C. Liu, L. Mai, *Materials Today Energy* **2022**, *28*, 101056.
- [203] H. Bian, C. Wang, Y. Wang, Y. Ren, Y. Ge, H. Wu, B. Wang, D. Chen, B. Yang, D. Bin, Y. Li, J. Gu, Y. Ma, S. Tang, X. Meng, H. Lu, *Adv. Funct. Mater.* **2024**, 2401760.
- [204] A. Khayum, M. Ghosh, V. Vijayakumar, A. Halder, M. Nurhuda, S. Kumar, M. Addicoat, S. Kurungot, R. Banerjee, *Chemical science* **2019**, *10*, 8889.
- [205] D. Luo, M. Li, Q. Ma, G. Wen, H. Dou, B. Ren, Y. Liu, X. Wang, L. Shui, Z. Chen, *Chemical Society Reviews* **2022**, *51*, 2917.
- [206] F. Ye, Q. Liu, H. Dong, K. Guan, Z. Chen, N. Ju, L. Hu, *Angewandte Chemie* **2022**, *134*, e202214244.
- [207] S. Muench, A. Wild, C. Friebe, B. Häupler, T. Janoschka, U. S. Schubert, *Chemical Reviews* **2016**, *116*, 9438.
- [208] Z. Zhao, J. Zhao, Z. Hu, J. Li, J. Li, Y. Zhang, C. Wang, G. Cui, *Energy & Environmental Science* **2019**, *12*, 1938.
- [209] B. Niu, Z. Li, D. Luo, X. Ma, Q. Yang, Y.-E. Liu, X. Yu, X. He, Y. Qiao, X. Wang, *Energy & Environmental Science* **2023**, *16*, 1662.
- [210] I. T. S. Li, G. C. Walker, *Proceedings of the National Academy of Sciences* **2011**, *108*, 16527.
- [211] Y. Cui, Q. Zhao, X. Wu, X. Chen, J. Yang, Y. Wang, R. Qin, S. Ding, Y. Song, J. Wu, *Angewandte Chemie International Edition* **2020**, *59*, 16594.
- [212] Y. Li, Z. Yu, J. Huang, Y. Wang, Y. Xia, *Angewandte Chemie International Edition* **2023**, 62, e202309957.
- [213] D. Wang, D. Lv, H. Liu, S. Zhang, C. Wang, C. Wang, J. Yang, Y. Qian, *Angewandte Chemie International Edition* **2022**, *61*, e202212839.
- [214] C. Liu, W. Xu, L. Zhang, D. Zhang, W. Xu, X. Liao, W. Chen, Y. Cao, M. C. Li, C. Mei, *Angewandte Chemie International Edition* **2024**, *63*, e202318063.
- [215] J. M. Black, D. Walters, A. Labuda, G. Feng, P. C. Hillesheim, S. Dai, P. T. Cummings, S. V. Kalinin, R. Proksch, N. Balke, *Nano Letters* **2013**, *13*, 5954.

- [216] G. Liang, Z. Tang, B. Han, J. Zhu, A. Chen, Q. Li, Z. Chen, Z. Huang, X. Li, Q. Yang, C. Zhi, *Advanced Materials* **2023**, *35*, 2210051.
- [217] H. Ren, S. Li, B. Wang, Y. Gong, H. Zhang, J. Wang, Q. Lv, D. Wang, H. Liu, S. Dou, *Energy Storage Materials* **2024**, *68*, 103364.
- [218] Z. Liu, R. Wang, Q. Ma, J. Wan, S. Zhang, L. Zhang, H. Li, Q. Luo, J. Wu, T. Zhou, *Advanced Functional Materials* **2024**, *34*, 2214538.
- [219] K. Guo, C. Zhu, H. Wang, S. Qi, J. Huang, D. Wu, J. Ma, *Advanced Energy Materials* **2023**, *13*, 2204272.
- [220] Y. Cui, Y. He, W. Yu, W. Shang, J. Yu, P. Tan, *ACS Applied Materials & Interfaces* **2023**, *15*, 3028.
- [221] S. Kim, Y. M. Kwon, K. Y. Cho, S. Yoon, *Electrochimica Acta* **2021**, *391*, 138927.
- [222] Y. Geng, L. Pan, Z. Peng, Z. Sun, H. Lin, C. Mao, L. Wang, L. Dai, H. Liu, K. Pan, Energy Storage Materials 2022, 51, 733.
- [223] Y. Dong, L. Miao, G. Ma, S. Di, Y. Wang, L. Wang, J. Xu, N. Zhang, *Chemical science* **2021**, *12*, 5843.
- [224] F. Zhao, Z. Jing, X. Guo, J. Li, H. Dong, Y. Tan, L. Liu, Y. Zhou, R. Owen, P. R. Shearing, *Energy Storage Materials* **2022**, *53*, 638.
- [225] X. Guo, Z. Zhang, J. Li, N. Luo, G.-L. Chai, T. S. Miller, F. Lai, P. Shearing, D. J. Brett, D. Han, *ACS Energy Letters* **2021**, *6*, 395.
- [226] Y. Shang, P. Kumar, T. Musso, U. Mittal, Q. Du, X. Liang, D. Kundu, *Advanced Functional Materials* **2022**, *32*, 2200606.
- [227] K. Xu, Chemical reviews 2014, 114, 11503.
- [228] G. Wang, Q. K. Zhang, X. Q. Zhang, J. Lu, C. Pei, D. Min, J. Q. Huang, H. S. Park, *Advanced Energy Materials* **2024**, 2304557.
- [229] H. Chen, S. Cai, Y. Wu, W. Wang, M. Xu, S.-J. Bao, *Materials Today Energy* **2021**, *20*, 100646.
- [230] R. Sun, D. Han, C. Cui, Z. Han, X. Guo, B. Zhang, Y. Guo, Y. Liu, Z. Weng, Q. H. Yang, *Angewandte Chemie International Edition* **2023**, *62*, e202303557.
- [231] Y. Zhu, M. Ge, F. Ma, Q. Wang, P. Huang, C. Lai, *Advanced Functional Materials* **2024**, *34*, 2301964.
- [232] Y. Bu, Q. Kang, Z. Zhu, H. Zhang, Y. Li, S. Wang, S. Tang, L. Pan, L. Yang, H. Liang, *Advanced Science* **2024**, 2404323.

- [233] A. Jana, S. Bähring, M. Ishida, S. Goeb, D. Canevet, M. Sallé, J. O. Jeppesen, J. L. Sessler, *Chemical Society Reviews* **2018**, *47*, 5614.
- [234] K. Zhao, G. Fan, J. Liu, F. Liu, J. Li, X. Zhou, Y. Ni, M. Yu, Y.-M. Zhang, H. Su, *Journal of the American Chemical Society* **2022**, *144*, 11129.
- [235] S. Zhao, Y. Zuo, T. Liu, S. Zhai, Y. Dai, Z. Guo, Y. Wang, Q. He, L. Xia, C. Zhi, *Advanced Energy Materials* **2021**, *11*, 2101749.
- [236] H. Wang, M. Zhu, H. Wang, C. Li, Z. Ren, Y. Zhang, S. Chen, H. Li, D. Chen, Z. Bai, Energy Storage Materials 2024, 67, 103238.
- [237] M. Li, K. Xie, R. Peng, B. Yuan, Q. Wang, C. Wang, Small 2022, 18, 2107398.
- [238] A. Bayaguud, X. Luo, Y. Fu, C. Zhu, ACS Energy Letters 2020, 5, 3012.
- [239] Z. Liu, T. Cui, G. Pulletikurthi, A. Lahiri, T. Carstens, M. Olschewski, F. Endres, *Angewandte Chemie International Edition* **2016**, *55*, 2889.
- [240] H. Yu, D. Chen, X. Ni, P. Qing, C. Yan, W. Wei, J. Ma, X. Ji, Y. Chen, L. Chen, *Energy & Environmental Science* **2023**, *16*, 2684.
- [241] Y. Lin, Y. Li, Z. Mai, G. Yang, C. Wang, *Advanced Energy Materials* **2023**, *13*, 2301999.
- [242] M. Yan, N. Dong, X. Zhao, Y. Sun, H. Pan, ACS Energy Letters 2021, 6, 3236.
- [243] Z. Hu, F. Zhang, Y. Zhao, H. Wang, Y. Huang, F. Wu, R. Chen, L. Li, *Advanced Materials* **2022**, *34*, 2203104.
- [244] R. Zhao, H. Wang, H. Du, Y. Yang, Z. Gao, L. Qie, Y. Huang, *Nature Communications* **2022**, *13*, 3252.
- [245] X. Zeng, J. Mao, J. Hao, J. Liu, S. Liu, Z. Wang, Y. Wang, S. Zhang, T. Zheng, J. Liu, *Advanced Materials* **2021**, *33*, 2007416.
- [246] H. Tang, N. Hu, L. Ma, H. Weng, D. Huang, J. Zhu, H. Yang, Z. Chen, X. Yin, J. Xu, *Advanced Functional Materials* **2024**, 2402484.
- [247] D. Sheng, X. Liu, Z. Yang, M. Zhang, Y. Li, P. Ren, X. Yan, Z. X. Shen, D. Chao, *Advanced Functional Materials* **2024**, 2402014.
- [248] K. Ouyang, S. Chen, W. Ling, M. Cui, Q. Ma, K. Zhang, P. Zhang, Y. Huang, *Angewandte Chemie* **2023**, *135*, e202311988.
- [249] H. Qiu, X. Du, J. Zhao, Y. Wang, J. Ju, Z. Chen, Z. Hu, D. Yan, X. Zhou, G. Cui, *Nature Communications* **2019**, *10*, 5374.
- [250] V. Soundharrajan, B. Sambandam, S. Kim, S. Islam, J. Jo, S. Kim, V. Mathew, Y.-k. Sun, J. Kim, *Energy Storage Materials* **2020**, *28*, 407.

- [251] Y. Liu, Z. Qin, X. Yang, X. Sun, Advanced Functional Materials 2022, 32, 2106994.
- [252] C. Zhang, Y. Huang, X. Xu, Z. Chen, G. Xiao, Y. Zhong, X. Wang, C. Gu, J. Tu, *Energy & Environmental Science* **2024**.
- [253] P. Gao, Q. Ru, H. Yan, S. Cheng, Y. Liu, X. Hou, L. Wei, F. Chi-Chung Ling, *ChemElectroChem* **2020**, 7, 283.
- [254] T. F. Burton, R. Jommongkol, Y. Zhu, S. Deebansok, K. Chitbankluai, J. Deng, O. Fontaine, *Current Opinion in Electrochemistry* **2022**, *35*, 101070.
- [255] J. Chen, Z. Yan, K. Li, A. Hu, B. Yang, T. Li, M. He, Y. Li, Z. Wei Seh, J. Long, *Battery Energy* **2024**, *3*, 20230063.
- [256] D. Asthagiri, L. R. Pratt, M. E. Paulaitis, S. B. Rempe, *Journal of the American Chemical Society* **2004**, *126*, 1285.
- [257] Q. Zhang, Y. Ma, Y. Lu, X. Zhou, L. Lin, L. Li, Z. Yan, Q. Zhao, K. Zhang, J. Chen, *Angewandte Chemie* **2021**, *133*, 23545.
- [258] Z. Zhang, Z. He, N. Wang, F. Wang, C. Du, J. Ruan, Q. Li, D. Sun, F. Fang, F. Wang, *Advanced Functional Materials* **2023**, *33*, 2214648.
- [259] Y. Zhang, G. Wan, N. H. Lewis, J. Mars, S. E. Bone, H.-G. Steinrück, M. R. Lukatskaya, N. J. Weadock, M. Bajdich, O. Borodin, *ACS Energy Letters* **2021**, *6*, 3458.
- [260] F. Wang, O. Borodin, T. Gao, X. Fan, W. Sun, F. Han, A. Faraone, J. A. Dura, K. Xu, C. Wang, *Nature materials* **2018**, *17*, 543.
- [261] D. Hoang, Y. Li, M. S. Jung, S. K. Sandstrom, A. M. Scida, H. Jiang, T. C. Gallagher, B. A. Pollard, R. Jensen, N. C. Chiu, *Advanced Energy Materials* **2023**, *13*, 2301712.
- [262] L. Geng, J. Meng, X. Wang, C. Han, K. Han, Z. Xiao, M. Huang, P. Xu, L. Zhang, L. Zhou, *Angewandte Chemie International Edition* **2022**, *61*, e202206717.
- [263] Y. Zhu, J. Yin, X. Zheng, A.-H. Emwas, Y. Lei, O. F. Mohammed, Y. Cui, H. N. Alshareef, *Energy & Environmental Science* **2021**, *14*, 4463.
- [264] D. Chao, S.-Z. Qiao, Joule 2020, 4, 1846.
- [265] L. Qian, H. Zhu, T. Qin, R. Yao, J. Zhao, F. Kang, C. Yang, *Advanced Functional Materials* **2023**, *33*, 2301118.
- [266] X. Yu, M. Chen, Z. Li, X. Tan, H. Zhang, J. Wang, Y. Tang, J. Xu, W. Yin, Y. Yang, *Journal of the American Chemical Society* **2024**.
- [267] K. Zhu, L. Wu, C. Guo, J. Pu, Y. Liu, X. Chen, Y. Chen, P. Xue, J. Han, Y. Yao, *Advanced Functional Materials* **2023**, *33*, 2305098.

- [268] D. Li, T. Sun, T. Ma, W. Zhang, Q. Sun, M. Cheng, Z. Zha, W. Xie, Z. Tao, *Advanced Functional Materials* **2024**, 2405145.
- [269] P. Sun, L. Ma, W. Zhou, M. Qiu, Z. Wang, D. Chao, W. Mai, *Angewandte Chemie* **2021**, 133, 18395.
- [270] X. Shi, J. Xie, J. Wang, S. Xie, Z. Yang, X. Lu, *Nature Communications* **2024**, *15*, 302.
- [271] J. Hao, L. Yuan, C. Ye, D. Chao, K. Davey, Z. Guo, S. Z. Qiao, *Angewandte Chemie International Edition* **2021**, *60*, 7366.
- [272] W. Kao-ian, M. T. Nguyen, T. Yonezawa, R. Pornprasertsuk, J. Qin, S. Siwamogsatham, S. Kheawhom, *Materials Today Energy* **2021**, *21*, 100738.

Chapter 2: B	attery Material	ls Characterisa	ation Technologies

This chapter summarises the main aspects of the fundamental characterisation methods for aqueous zinc ion batteries and is followed by the limitations of these characterisation methods from a practical perspective.

2.1 X-ray photoelectron spectroscopy

X-ray Photoelectron Spectroscopy (XPS) provides comprehensive information for aqueous zinc-ion battery research by offering detailed insights into the composition and elemental ratio of samples, analysing the chemical environment of various elements, and identifying phases on the surface. For instance, XPS surveys combined with depth profiles can determine composition changes in the SEI layer, which is crucial for understanding the stability and efficiency of batteries. High-resolution spectra allow researchers to monitor valence changes in transition metal oxides within cathode materials, providing vital data on how these materials perform under different conditions. Additionally, the F 1s spectrum can distinguish between organic and inorganic fluorine species in the SEI, further enhancing the understanding of the battery's internal chemistry.

However, XPS has several limitations that must be considered. The judgment of the researcher and the settings of the fitting software can significantly influence the results of XPS analysis. Parameters such as baseline type, line shape, and full width at half maximum (FWHM) largely depend on the researcher's experience, leading to variability in results. This subjectivity can affect the reproducibility and reliability of data across different studies and research groups. Moreover, XPS depth etching cannot provide precise depth values because the etching source, such as argon, interacts differently with various surfaces, resulting in rough estimations rather than exact measurements. This imprecision complicates the interpretation of depth profiles. Another limitation is that XPS data is restricted to relatively small areas covered by the X-ray beam, which may not accurately represent the entire surface's chemical composition, especially in cases of corrosion or *in-situ* formation of SEI. This spatial limitation means that important variations across the surface may be missed. Additionally, XPS requires samples to be dry, which poses a challenge for AZIBs where water plays a critical role in reactions. Since XPS is performed under vacuum conditions, water molecules are removed before testing, potentially leading to inaccuracies in representing the real environment of the electrode or other components. For example, ex-situ XPS cathode material samples often need to be dried in a vacuum oven overnight, during which time self-discharge can occur, affecting the accuracy of valence analysis and overall findings.

2.2 Infrared spectroscopy

Infrared (IR) spectroscopy offers valuable insights into the chemical environment within various components of AZIBs. First, IR profiles can provide detailed information about the chemical environment of the aqueous electrolyte. For instance, when investigating electrolyte additives, shifts in the anion peaks can indicate changes in the solvation structure of the electrolyte. Second, IR spectroscopy can detect the formation of the SEI or other by-products. In particular, the *in-situ* formation of carbon-fluorine species in the SEI can be observed in the 1,400 – 1,100 cm⁻¹ range. Third, IR profiles can reveal the content of lattice water in the cathode material. Fourth, IR spectroscopy can be utilised to monitor the intercalation of organic species into the cathode material. For example, in hybrid zinc-ion batteries where ammonium ions serve as charge carriers, changes in the NH⁴⁺ IR signal can illustrate the intercalation and deintercalation processes during cycling.

However, there are limitations to the application of IR spectroscopy in AZIBs. The penetration depth of the IR beam is limited, making it challenging to obtain information about changes in bulk materials. Additionally, the sample signal can be easily overshadowed by signals from by-products such as Zn(OH)₂SO₄. Furthermore, the sensitivity of IR spectroscopy in aqueous systems is low due to the strong absorption of the IR signal by water molecules. This results in a dominant O-H stretching peak, which can obscure other relatively weak signals and make it difficult to detect subtle changes during battery operation. These challenges highlight the need for advanced techniques and improved methodologies to fully leverage IR spectroscopy for the study of AZIBs.

2.3 X-ray diffraction

X-ray diffraction (XRD) serves as a crucial tool for illustrating the lattice structure and phase changes in zinc-ion battery research. Firstly, XRD data can be employed for phase identification, aiding in the synthesis of novel materials and enhancing the understanding of by-products' structures. Additionally, XRD provides practical information on lattice parameters, such as lattice distances in layered materials, by monitoring peak shifts during different charge and discharge states. Moreover, XRD is instrumental in defect engineering research, probing for defect-induced peak shifts, preferred orientations, or changes in intensities, thereby offering insights into material behaviour and stability.

Despite its advantages, XRD characterisation of AZIBs presents certain limitations. For thin film materials, grazing incidence XRD (GIXRD) is typically used; however, the XRD beam

only covers a small area of the thin film, thus limiting the GIXRD results to the specific area under the beam spot. Furthermore, XRD characterisation is constrained to materials with a certain level of crystallinity. Amorphous or low-crystallinity samples produce weak or overly broad XRD signals that are challenging to analyse. For instance, carbon materials, which are widely utilised in battery research, exhibit signals that are difficult to detect and provide limited information. These limitations underscore the need for complementary techniques and advanced methodologies to maximise the utility of XRD in the study of AZIBs.

2.4 Raman spectroscopy

Raman spectroscopy is an invaluable tool for illustrating the chemical environment and monitoring phase changes during the cycling of AZIBs. Firstly, *in-situ* Raman spectroscopy can provide real-time information on metal-oxygen vibration modes and structural changes. For instance, the shifts and recovery of in-plane and out-of-plane Mn-O vibration Raman peaks during zinc-ion intercalation and deintercalation can be observed. Additionally, the formation of the SEI from electrolyte decomposition generates specific Raman signals. For example, Raman peaks around 522 cm⁻¹ are widely used to monitor the ZnF₂ component in research on zinc anode protection. Furthermore, Raman spectroscopy can provide insights into the structure of water or aqueous solutions, such as monitoring changes in the hydrogen bond environment through the Raman O-H stretching shift.

However, there are certain limitations to the application of Raman spectroscopy in AZIBs. Being a surface-sensitive technique, Raman spectroscopy faces challenges in capturing structural changes in the sample when by-products are generated on the surface, as these by-product signals can become stronger during cycling and obscure the sample's structural signals. Additionally, Raman spectroscopy only provides information limited to the laser penetration depth, typically within 10 μm, meaning bulk sample changes may differ from those illustrated by Raman results. Moreover, due to fluorescence noise, Raman spectroscopy is not sensitive to the generation of minute amounts of products. For example, in Chapter 3, the potential by-products of fluorinated surfactants cycled in AZIBs were not distinguishable from the fluorescence noise. These limitations highlight the need for complementary analytical techniques to obtain a comprehensive understanding of the materials and processes in AZIBs.

2.5 Scanning electron microscopy

Scanning electron microscopy (SEM) provides direct information on the morphology of asprepared samples, making it an essential tool for zinc-ion battery research. SEM can be utilised in three detailed directions: firstly, it can directly probe as-prepared cathode materials, offering evidence of the diameter and evenness of nanomaterials. Secondly, SEM can highlight morphology changes after cycling, such as monitoring zinc dendrite formation on the anode. By comparing morphological differences, SEM can provide a brief evaluation of zinc anode modification methods. Thirdly, SEM can offer side-view images of electrodes, providing information on the thickness and evenness of surface modification layers or the solid electrolyte interface.

However, SEM has certain limitations. It is primarily suitable for non-magnetic or weakly magnetic samples, as strong magnetic samples can cause deflection of electron beams. Additionally, some SEM chambers are limited to dry samples, requiring *ex-situ* samples to be dried and placed in a vacuum environment, which can potentially alter the sample state. Furthermore, the quality of SEM images depends on the sample's conductivity. Transition metal oxides, such as zinc oxide or manganese oxide, are typically semiconductors and thus require additional carbon or gold coating to enhance conductivity before SEM testing. These limitations necessitate careful preparation and consideration when using SEM for zinc-ion battery analysis.

2.6 Transmission electron microscopy

TEM can image the nano-morphology of samples, providing direct images of the diameter of nanoplates and nanorods. At high magnification, specific lattice faces can be probed, allowing for the study of lattice distances in layered samples and comparison with XRD results. Furthermore, *ex-situ* TEM technology can provide evidence of lattice breathing, where changes in lattice distance during charging and discharging cycles can be observed.

However, there are limitations to the use of TEM technology for AZIBs. The sample preparation process for TEM is more suited to samples that can be dispersed in solution. For metals like zinc, the preparation process is complex and time-consuming. Additionally, the preparation of TEM samples often involves meticulous techniques to ensure thinness and uniformity, which can be challenging for certain materials. These constraints highlight the need for complementary techniques and careful planning in the use of TEM for analysing zinc-ion battery materials.

2.7 Scanning transmission electron microscopy

Scanning transmission electron microscopy (STEM) provides atomic-level information about samples, enabling direct monitoring of defect distributions such as vacancies or grain boundaries. Additionally, STEM can illustrate the distribution of specific elements within the cathode or the SEI and cathode electrolyte interphase (CEI) layers, offering detailed insights into the material composition and structural integrity of AZIBs.

However, STEM has limitations in the study of AZIBs. One significant issue is beam damage, which can occur under high magnification due to high-energy electrons. This damage can lead to the displacement of elements in inorganic samples or the degradation of organic samples, potentially altering the sample's original structure and composition. These challenges necessitate careful optimisation of imaging conditions and complementary analytical techniques to minimise artefacts and ensure accurate characterisation of zinc-ion battery materials.

2.8 Digital microscopy

Digital microscopy offers high-resolution imaging that rivals SEM. Firstly, it can provide micrometre-level images in ambient environments, enabling the study of electrochemical processes during cycling and recording these processes in video format. For example, with proper cell design, *in-situ* monitoring of dendrite growth can be achieved. Secondly, digital microscopy can offer 3D morphology scanning, providing information on surface roughness or by-product formation along the surface.

However, digital microscopy has limitations for AZIBs. The working distance of the lens restricts the height between the lens and the sample to a few centimetres, limiting the space available for *in-situ* cells. This constraint requires careful design and optimisation of experimental setups to fully utilise digital microscopy in the study of AZIBs.

2.9 Contact angle measurement

Contact angle measurement is a valuable technique for assessing the wettability of electrolytes on electrode surfaces. This method provides crucial insights into how well an electrolyte spreads across an electrode, which can impact the performance and efficiency of AZIBs. By measuring the contact angle, researchers can infer the interactions between the electrolyte and electrode surface.

However, interpreting contact angle measurements is complex due to the multitude of influencing factors. Surface functional groups, surface roughness, surface tension, and the three-dimensional structure of the electrode can all affect the contact angle. These variables must be carefully considered to accurately understand and optimise wettability in zinc-ion battery systems. This complexity underscores the need for comprehensive analysis and controlled experimental conditions in contact angle studies.

2.10 X-ray Fluorescence

X-ray fluorescence (XRF) offers a straightforward method for detecting elements in a sample and determining their elemental ratios. This technique is particularly valuable in the analysis of AZIBs, providing comprehensive elemental composition data. XRF's ability to cover a larger measurement area makes it suitable for bulk analysis, capturing a more representative elemental distribution within the sample.

However, the elemental ratios obtained from XRF often differ from those acquired through other methods such as XPS or energy dispersive spectroscopy (EDS). This discrepancy arises because XRF measures a larger area, yielding bulk measurement results, while XPS and EDS are limited to smaller, more localised regions. Consequently, XRF can provide a broader overview of elemental distribution, whereas XPS and EDS offer detailed spot-specific analysis. Understanding these differences is crucial for accurately interpreting and comparing elemental data from various analytical techniques.

2.11 Solid-state NMR

Nuclear magnetic resonance (NMR), particularly solid-state NMR, provides valuable insights into phase identification and charge carrier dynamics in AZIBs. This technique enables the detailed study of the local chemical environment and ionic mobility within the battery materials, offering crucial information for enhancing battery performance and longevity.

However, solid-state NMR has several limitations. Firstly, its sensitivity is lower compared to liquid NMR, posing challenges for sample preparation which requires several hundred milligrams of active materials. This is especially complicated for *ex-situ* research on cathode materials due to the low charge depth in high current density testing and the lengthy preparation times for samples cycled at low current densities. Secondly, solid-state NMR relies on isotopes, which are relatively expensive and may introduce different mechanisms compared to common chemicals. Thirdly, the acquisition duration for solid-state NMR is longer than for some other

characterisation methods, and prolonged exposure of the sample to the atmosphere during preparation can lead to potential changes from its original state. These limitations necessitate careful planning and optimisation in the use of solid-state NMR for zinc-ion battery research.

Chapter 3: Surface Protection Layer *via* Rapid Sputtering Strategy for Stable Aqueous Zinc Ion Batteries

3.1 Introduction

AZIBs are a promising solution for next-generation electrochemical energy storage due to their abundance, cost-effectiveness, and eco-friendliness. As a result, they are now being extensively investigated. The zinc anode exhibits a high volumetric capacity (5,853 mAh cm⁻³), which surpasses that of Li (2,061 mAh cm⁻³), Mg (3,833 mAh cm⁻³), and Ca (2,072 mAh cm⁻³). This remarkable advantage makes AZIBs a suitable solution for grid energy storage [3-5]. Despite the inherent advantages of Zn anodes, critical challenges associated with water-related side reactions remain, leading to dendrite formation, corrosion, and unregulated hydrogen evolution. This chapter focuses on the Zn anode modification strategies to increase the interfacial stability and improve the zinc anode cycling performance.

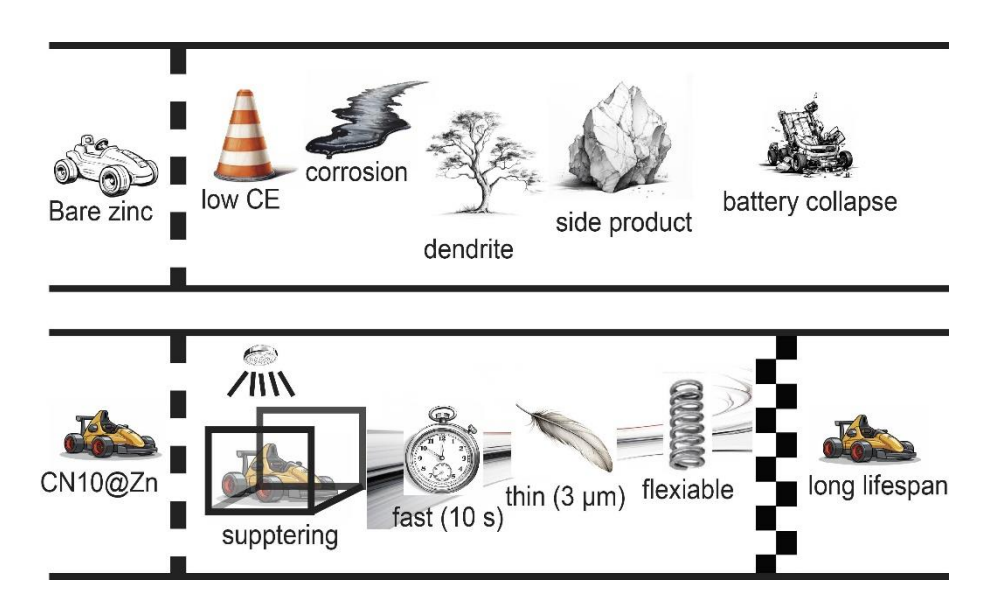


Figure 3.1 Illustration of the issues in bare Zn anode and sputtered CN10@Zn anode.

There are various methods for the Zn anode modification, such as 0D surface dopants methods, 2D surface protective layer^[9-13] and 3D structure fabrication.^[14-18] The current zinc anode modification methods are relatively time-consuming, and the thickness of modification layer needs to be further controlled.^[19-22] According to the inherent properties of AZIBs, Zn anode modification is supposed to meet a few practical points: First, the protective layer needs to be electrochemically stable against corrosion and side reactions in the long-term^[23-25]. Second, the materials used for fabrication should be highly conductive to allow for efficient charge transfer through the protective layer to reduce concentration polarisation and enable faster reaction kinetics under high current density.^[26-30] Third, the modification process should be facile and time-effective,^[31-34] avoiding complicated manual labour, reducing processing time, and

enabling continuous manufacturing to fulfil the demands of industrial production. [35-37] Electroplating, sputtering and chemical vapour deposition (CVD) fulfil these points. However, theoretically, the sputtering method, along with the sputtered ions formed from the target, has the highest kinetic energy compared to other two methods. These ions can bombard the zinc anode surface, creating a physical bond with the substrate while penetrating the surface to a certain depth, leading to stronger adhesion between the sputtering layer and the zinc anode. Besides, from the practical point of view, electroplating requires an electrolyte, which is inefficient because the electrolyte needs additional resin removal and drying after treatment. The CVD method relies on surface reactions to grow 'layer by layer', weaking the bonding between the protection layer and the substrate, which can lead to delamination and peeling. Thus, the sputtering method is theoretically and practically ideal for building the surface protection layer of Zn anode.

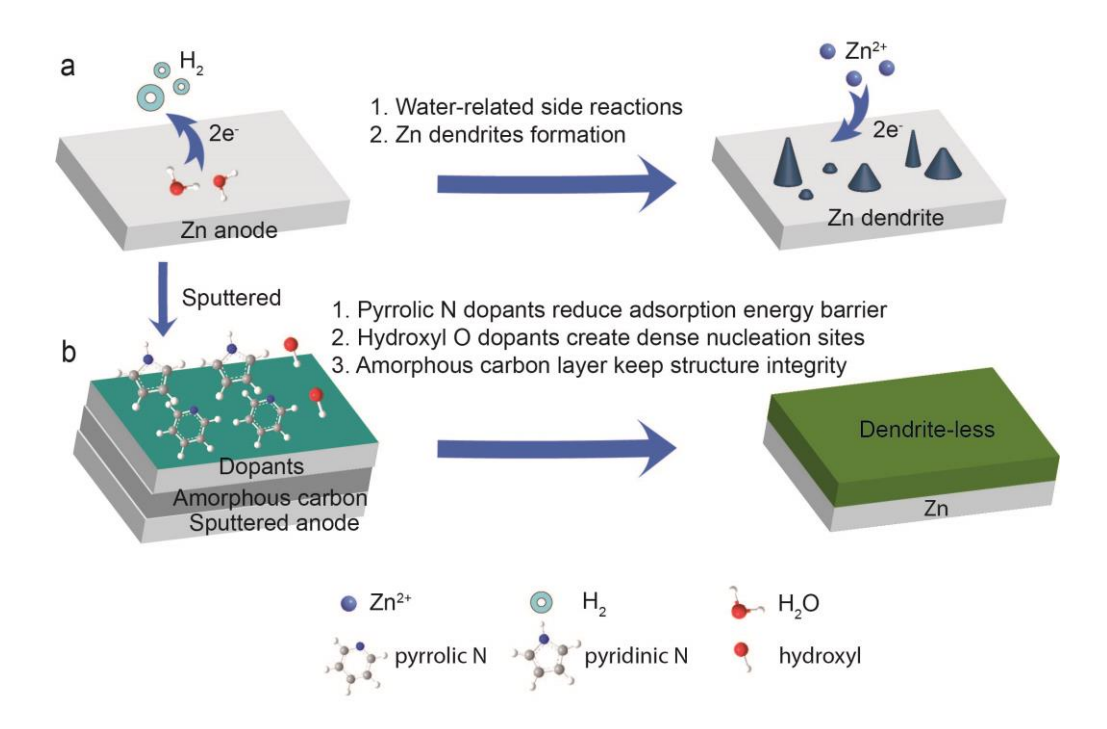


Figure 3.2 Schematic illustration of (a) the corrosion of Zn anodes in aqueous electrolytes; (b) Homogenous zinc deposition with a sputtered carbon layer in aqueous electrolytes.

In this thesis a rapid sputtering method was adopted to enable an ultrathin protective layer to form homogeneously on the Zn anode. A plasma of ionised argon bombarded a carbon target with nitrogen and oxygen species to sputter the carbon atoms (along with the dopants) onto the Zn anode, creating a uniform sputtered layer. The optimised CN10@Zn anodes are created after only 10 seconds rapid sputtering with a 3 µm thickness. (**Figure 3.2**) The synergistic collaboration between dopants, hydrophilicity, and nucleation dynamics in the sputtering layer

contributes to the regulation of zinc deposition and the inhibition of side reactions. As a result, CN10@Zn presents a lifespan of 2,100 hours in symmetric cells, a CE of 99.8% for 2,700 cycles in Cu||Zn half-cells, and a capacity retention of 89% when paired with $Na_{0.65}Mn_2O_4$ cathode materials. This work provides a rapid anode modification strategy for high-energy-density devices.

3.2 Experimental section

3.2.1 Chemicals

Zinc sulfate heptahydrate (ZnSO₄·7H₂O, ACS reagent, 99%), Hydrogen Peroxide Solution (H₂O₂, 30 % (w/w) in H₂O), Manganese sulfate monohydrate (Mn₂SO₄·H₂O, ACS reagent, 98%) and poly(vinylidene fluoride) (PVDF, average M_w ~534,000 by GPC, powder) were purchased from Sigma-Aldrich (UK) Co., Ltd. YP-50F active carbon was purchased from Kuraray Chemical Company, Japan. All materials were used as received without further purification.

3.2.2 Cathode material Na_{0.65}Mn₂O₄·H₂O synthesis

A co-precipitation method was introduced to synthesise the manganese oxide cathode material Na_{0.65}Mn₂O₄·H₂O. Solution A was prepared by mixing 15 mmol of manganese nitrate tetrahydrate with 55 mmol of sodium hydroxide. Solution B was prepared by diluting 12 ml of 30 wt% hydrogen peroxide with 90 ml of deionised water. Both solutions were stirred at ambient temperature for 10 minutes. Subsequently, solution B was rapidly poured into solution A, and the mixture was immediately sealed. The combined solution was then subjected to vigorous stirring for 15 minutes. The resultant mixture was left stationary in an ice-water bath overnight. The black precipitate formed was collected and rinsed with water three times and a fine dark brown powder was subsequently obtained through freeze drying.

3.2.3 Modification of anode electrode via sputtering process

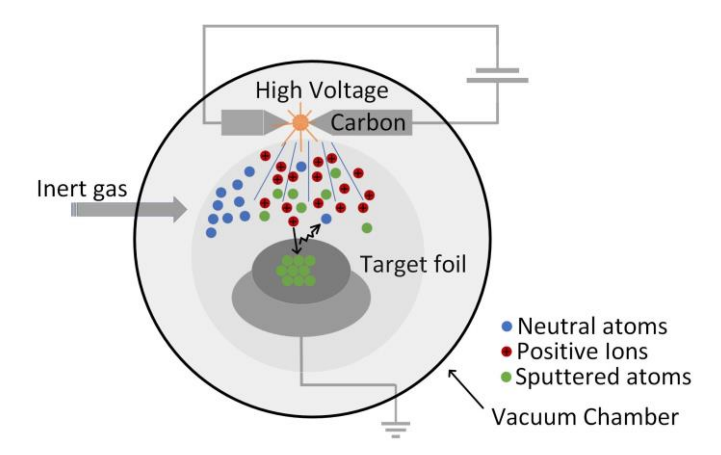


Figure 3.3 Illustration of the sputtering process.

The sputtered zinc anode was prepared in two steps. First, zinc foil was polished using sandpaper sequentially from 1,000, 1,500 to 3,000 grit to remove the surface oxidised layer ZnO, then cut into 5 cm x 5 cm pieces. In the second step the zinc anode was transferred into the sputtering chamber. A doped carbon rod was installed in the sputtering chamber. The sputtering time was set to 10 seconds, and a sputtering distance of 5 - 10 cm was controlled. After the chamber was vacuumed, the anode was then sputtered with a thin modification layer.

3.2.4 Fabrication of cathode materials

Carbon paper was cut into 7 cm x 7 cm square sizes. Sodium manganese oxide, carbon black (super P) and PVDF (50 mg mL⁻¹ in N-methyl-2-pyrrolidone, NMP) were weighed, mixed and ground in a mortar in a weight ratio of 7: 2:1. The as-prepared slurry was coated on the carbon paper and dried in a vacuum oven for 12 hours at 70°C. The loading amount was controlled in the range of 2 - 2.5 mg cm⁻². Zinc metal foil with a thickness of 20 μm was fully polished with sandpapers and rinsed with water to remove the surface oxide layer and other impurities. The electrolyte for symmetric cells and Cu-Zn cells tested in this chapter is 2 M ZnSO₄. 0.1 M MnSO₄ is specifically added to the electrolyte for the testing using Na_{0.65}Mn₂O₄ as cathode material. Whatman[®] GF/A grade glass microfiber was used as the battery separator. A stainless-steel plate with a thickness of 1 μm was applied to the coin cell's inner space. A washer was placed in the coin cell to support the inner space. The diameter of the cathode and anode are both 16 mm, and the diameter of the separator is 18 mm. 100 μl electrolyte was added onto the separator before integrating the coin cell.

3.2.5 Fabrication of the electrochemical cell

Zn symmetric cells were prepared by utilising two zinc anodes as working and counter electrodes. The thickness of zinc anodes in symmetric cells is 80 µm and the diameter is 16 mm. Cu-Zn cells were used to analyse the CE of zinc deposition on zinc anode. The diameter of the copper foil is 16mm.

3.2.6 Electrochemical characterisation

Linear sweep scan, electrochemical impedance spectroscopy (EIS), cyclic voltammetry (CV) testing, and activation energy testing were performed on Biologic VSP device. Battery gravimetric cell tests were conducted on Neware battery testing system. Galvanostatic intermittent titration technique (GITT) was introduced to analyse the zinc ion diffusion coefficients with a resting time of 20 minutes. The current density for CE testing is 1 mA cm⁻², 0.5 mAh cm⁻². EIS measurements were conducted within the 0.1 Hz to 10⁵ Hz frequency range.

3.2.7 Material characterisation

Raman data was collected using Renishaw Raman microscope with a laser wavelength of 514.5 nm. XPS data was obtained using a Thermo scientific K-alpha photoelectron spectrometer and analysed using Casa XPS software. Adventitious carbon binding energy was calibrated to 284.8 eV. The XPS depth spectrum was obtained by stepwise argon (Ar) atom etching. SEM was performed using a JEOL-JSM-6700F field emission scanning electron microscope. The SEM samples were coated with Au with a sputter time of 10 seconds. XRD patterns were collected on a Bruker D8 advance X-ray diffractometer using Cu K α radiation (λ =1.5406 Å). The optical microscopy and 3D laser scanning confocal microscopy were performed using a Keyence VHX-7000 digital microscope.

3.3 Result and discussion

3.3.1 Optimisation of the sputtering parameters

The sputtering parameters have an obvious effect on the evenness and thickness of the sputtering layer, including the sputtering voltage, the sputtering time and vacuum degree. 3D laser scanning confocal microscopy was used as a straightforward method to analyse the sputtering layer morphology.

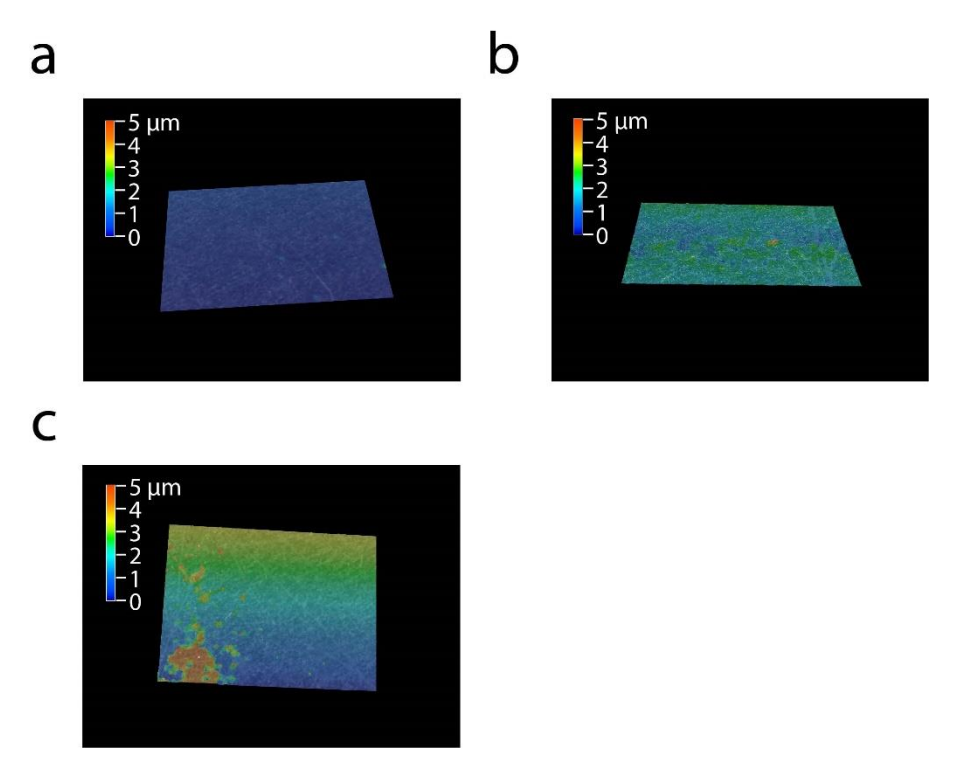


Figure 3.4 3D laser scanning confocal microscopy of zinc anodes with different sputtering voltage: (a) 1.5 V; (b) 3.5 V; (c) 5 V.

The sputtering voltage has a direct effect on the sputtering ions' bombarding energy, which further influences the sputtering layer. The working voltage range of the sputtering instrument is from 0 V to 5 V. To identify the optimised condition, the Zn anodes were sputtered under four voltage parameters, 1.5 V, 3.5 V, and 5 V.

The activation of the sputtering process requires a specific threshold voltage to initiate ion bombardment. As observed in **Figure 3.4a**, distinct sputtered spots become visible starting at 1.5 V, indicating that this value represents the lower voltage limit necessary for the sputtering process to commence. Higher voltages lead to the increase the sputtering rate, with efficient sputtering achieved at 3.5 V and the as-prepared sputtering layer is uniform. Further increasing the sputtering voltage to 5 V results in an increase of layer thickness, high voltage close to the instrument's limit leads to an unstable sputtering process. As shown in **Figure 3.4c**, an obvious

sputtering hump was observed, owing to the less regulated sputtering process at high voltages. Considering the evenness of the sputtering layer, 3.5 V was set as the working voltage in the following experiment.

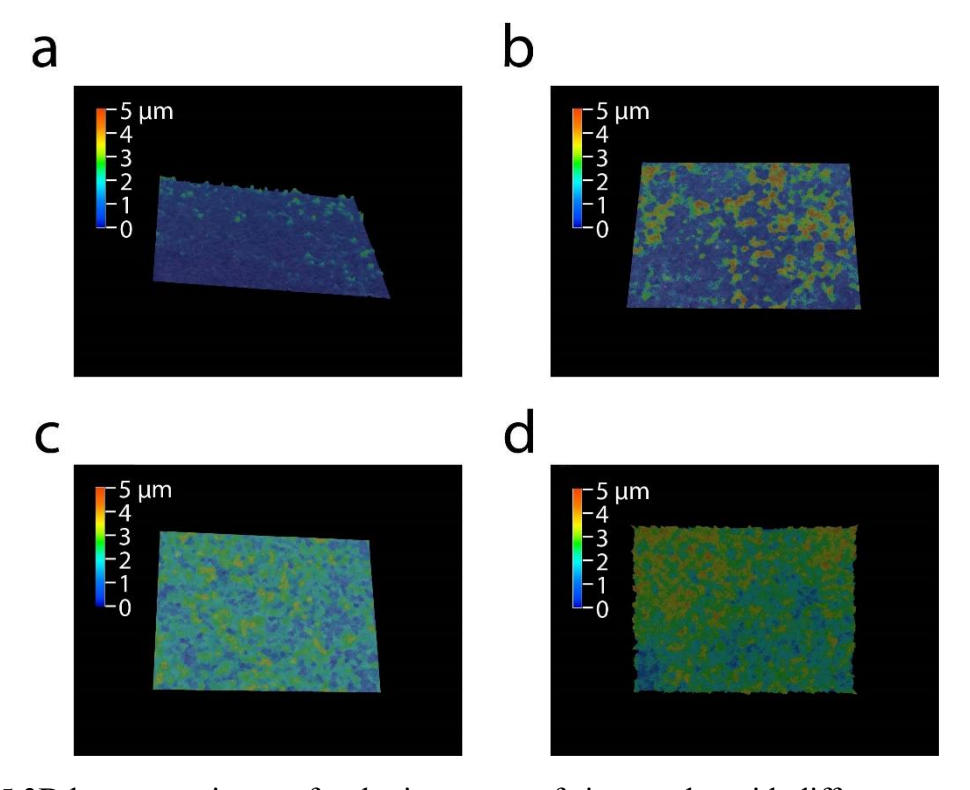


Figure 3.5 3D laser scanning confocal microscopy of zinc anodes with different sputtering time: (a) 1 second; (b) 3 seconds; (c) 5 seconds; (d) 10 seconds.

The sputtering time also has a significant effect on the building of sputtering layer. As shown in **Figure 3.5**, sputtering time less than three seconds could not fully cover the surface of the Zinc anode. By further increasing the sputtering time to five seconds, obvious sputtering layer initially formed. After ten seconds, the sputtering layer evenly covers the zinc anode without forming any peak or valley area, proving that ten seconds is the optimised time setting. Although further increasing the treatment time can increase the thickness of the sputtering layer, considering the evenness and the effectiveness of the sputtering layer, the sputtering parameters were set to ten seconds.

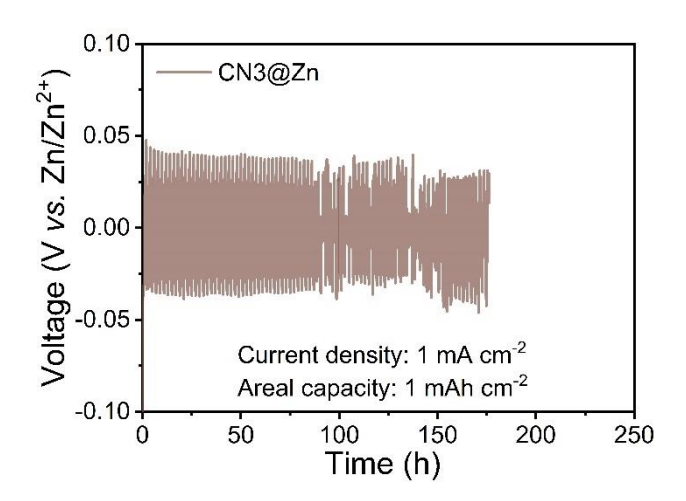


Figure 3.6 Galvanostatic cycling of symmetrical Zn cells with CN3@Zn (3 seconds sputtering) at 1 mA cm⁻² and 1 mAh cm⁻².

The optimisation of the sputtering parameter has a significant influence on the performance of the as-prepared surface protection layer. To evaluate the thickness and the durability of the surface protection layer, galvanostatic cycling tests were conducted on symmetric Zn cells treated with different sputtering times. The symmetric cell's voltage-time curve in **Figure 3.7** shows that short sputtering time (3 seconds) undergoes fluctuation after 100 hours. The battery collapses after 175 hours, indicating that a short sputtering time is insufficient to fully cover the Zn anode surface. In contrast, galvanostatic cycling curves for sputtering times of ten seconds remain stable for more than 1000 hours without micro-shortcuts (**Figure 3.40**). These experiments confirm that ten seconds is the optimal sputtering time.

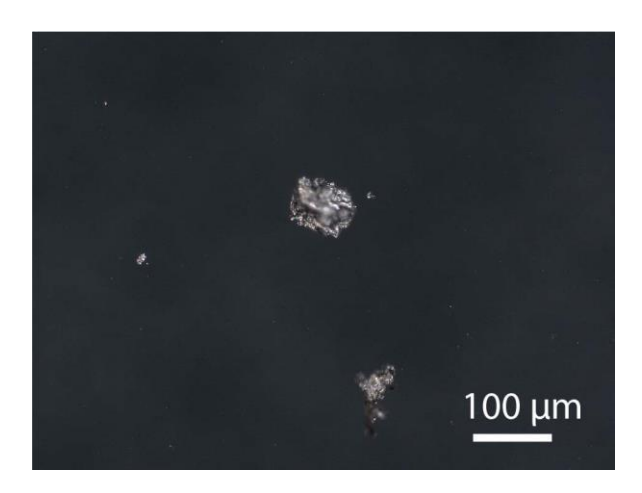


Figure 3.7 Optical image of the sputtering sample sputtered in low vacuum: 0.5 mbar.

For the sputtering pressure, sputtering process with chamber pressure below 0.5 mb was investigated. As shown in **Figure 3.6**, insufficient vacuum could lead to the formation of irregular carbon particles, indicating that insufficient vacuum causes turbulence in sputtering by introducing residual gas molecules that disrupt the flow of sputtered ions. The increased number of gas molecules in the chamber leads to frequent collisions with the sputtered carbon atoms and results in the formation of aggregates rather than a smooth, uniform layer. In contrast, no carbon aggregates were observed on the sample treated with sufficient vacuum.

3.3.2 Zinc anode characterisation

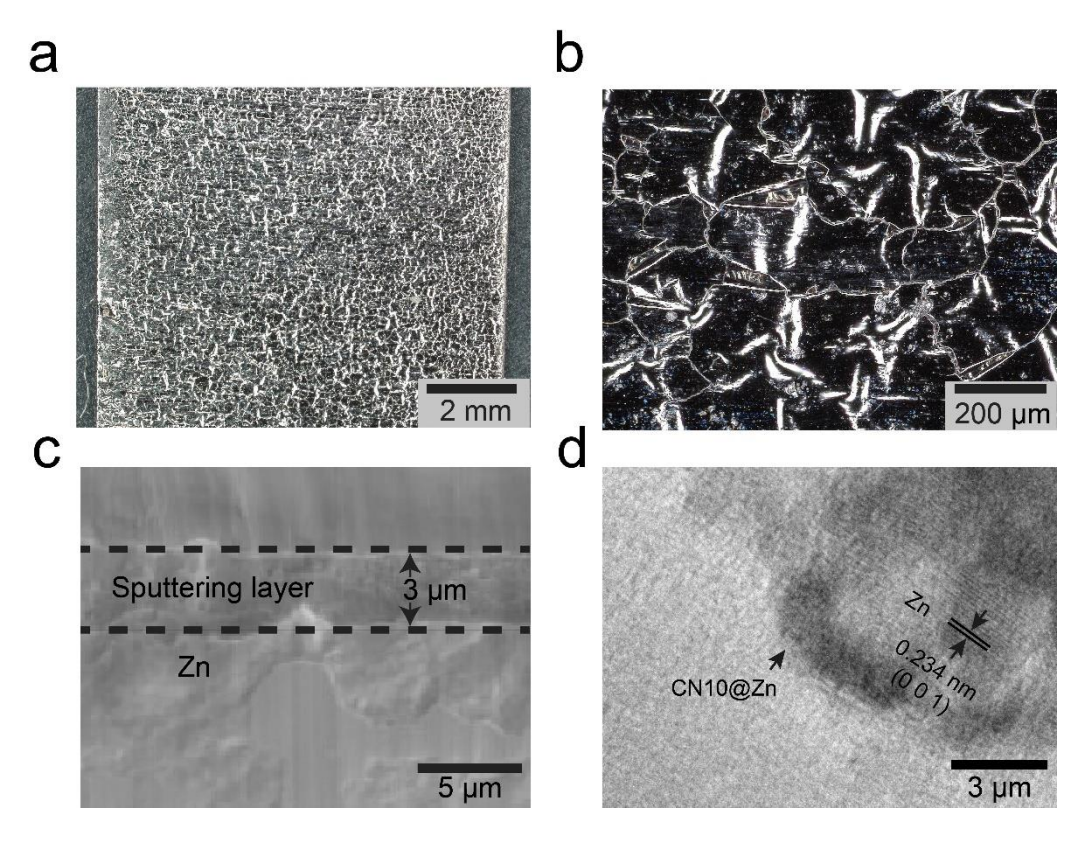


Figure 3.8 Microscopy characterisation of CN10@Zn: (a,b) Digital images; (c) Side-view SEM image; (d) TEM image.

The sputtering process has distinct impact for the surface morphology of the zinc anode surface. Zinc metal's melting point is only 419.5°C. The modification of the surface morphology originates from the high energy and high temperature plasma induced species etching the anode surface. As shown in **Figure 3.8**, CN10@Zn zinc anode is covered with crumbled foam-like sputtered layer, and the surface colour changes from metal silver to carbon grey after sputtering. This colour change is an indicator of the thickness change of the carbon material from the sputtering carbon source. The thickness of CN10@Zn is measured by a digital microscope

(Keyence VHX-7000), which shows a thickness of 3 μm. To further investigate the structure of the CN10@Zn, TEM was applied. TEM results in **Figure 3.8d** show amorphous carbon observed on the top of Zn structure.

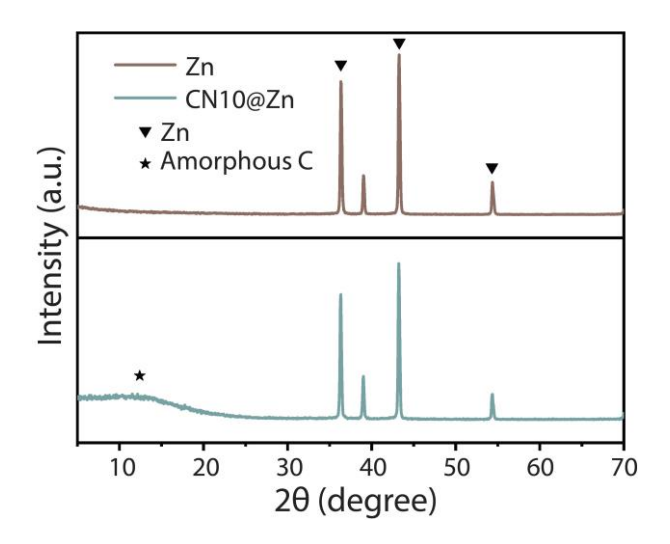


Figure 3.9 XRD characterisation of the sputtered CN10@Zn and the bare Zn.

The structure of the carbon species in CN10@Zn was investigated by XRD measurement. A broad peak around 10° indicates that the carbon layer is in amorphous type (**Figure 3.9**).

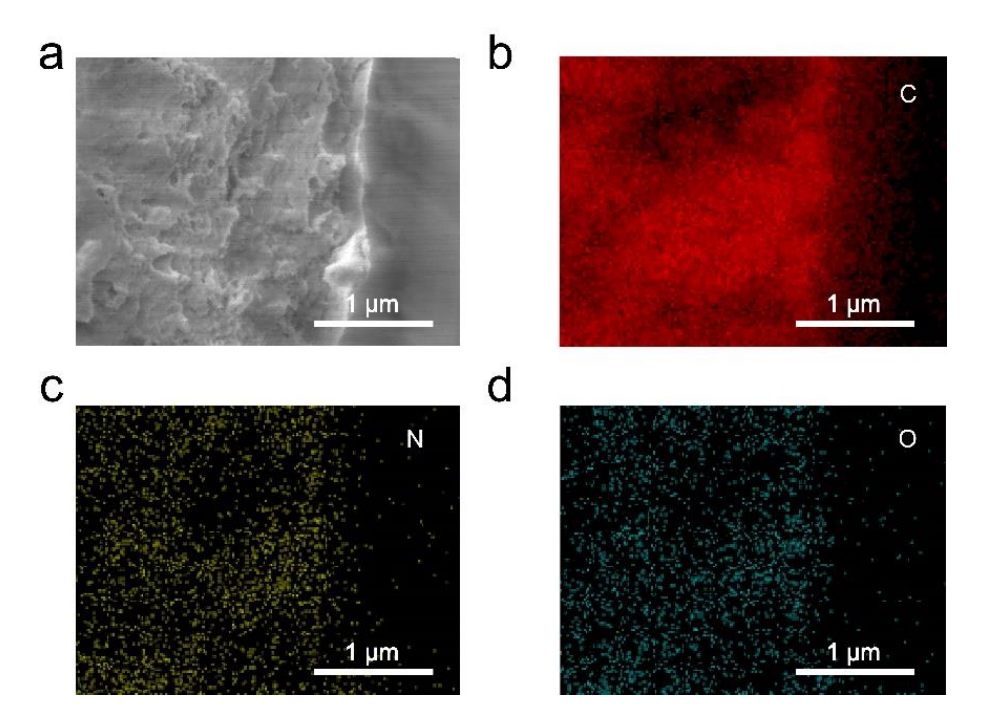


Figure 3.10 (a) Side-view SEM profile of CN10@Zn; EDS mapping images of CN10@Zn: (b) Carbon; (c) Nitrogen; (d) Oxygen.

The side-view SEM images reveal a porous structure of CN10@Zn, which is generated by the interaction with plasma species. Energy-dispersive X-ray spectroscopy (EDS) of CN10@Zn in **Figure 3.10** show a uniform distribution of C, N, and O elements throughout the structure, thereby verifying the even distribution of these elements across the CN10@Zn sputtering layer.

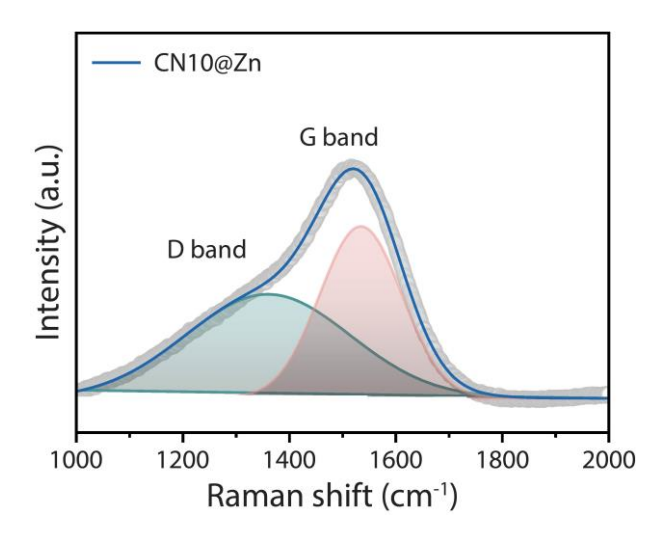


Figure 3.11 Raman characterisation of CN10@Zn anode.

Raman spectroscopy is widely used to characterise carbon-based materials. Two obvious peaks were observed in the Raman spectroscopy of CN10@Zn: the G peak (around 1580 cm⁻¹) and the D peak (around 1350 cm⁻¹). The G peak originates from the in-plane vibration of sp²-hybridised carbon atoms in the sputtered carbon layer (**Figure 3.11**), while the D peak is due to the structural defect and disorder in the amorphous carbon.

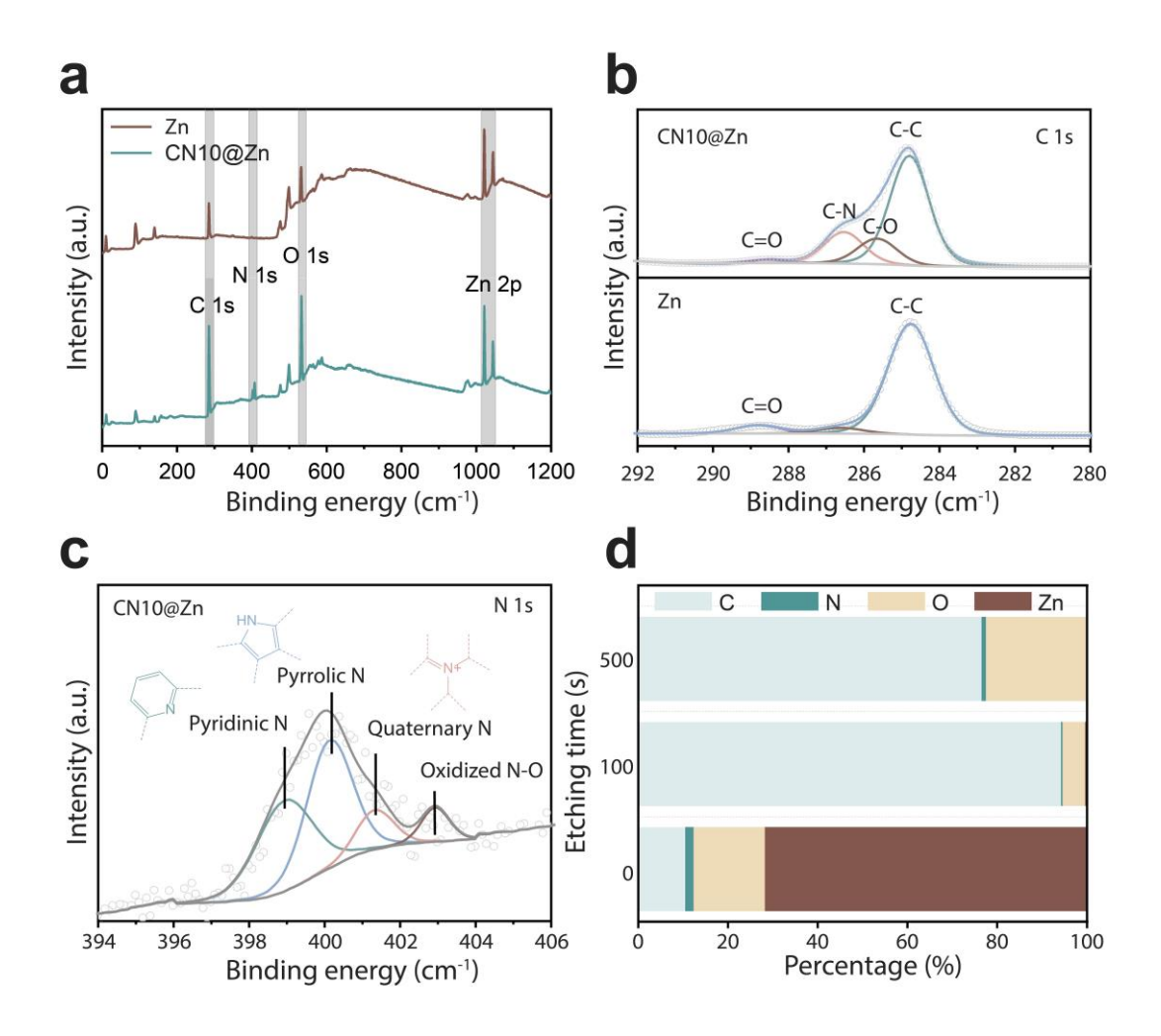


Figure 3.12 XPS analysis: (a) Survey profiles of CN10@Zn and bare Zn; (b) C 1s profiles of CN10@Zn and bare Zn; (c) N 1s profile of CN10@Zn; (d) Depth profile of CN10@Zn.

The surface functional group on the zinc anode is highly related to its reactivity, as the surface dopants can increase the surface polarisation and the surface electric field distribution. The doped nitrogen and oxygen elements in carbon source can be sputtered onto the CN10@Zn surface and enrich its chemistry environment during the sputtering process. This further leads to the generation of oxygen and nitrogen dopants along the sputtered anode surface. XPS spectra give information about the surface functional group type and the relevant bonding environment. As shown in **Figure 3.12b**, the C 1s spectrum of CN10@Zn shows the signal of C-N (286.1 eV), C=O (288.6 eV) and C-O (285.5 eV), indicating the existence of N and O species. The detailed identification of the nitrogen species in carried out by analysis N 1s profile, as shown in **Figure 3.12 c**, N species are mainly pyridinic N and pyrrolic N.

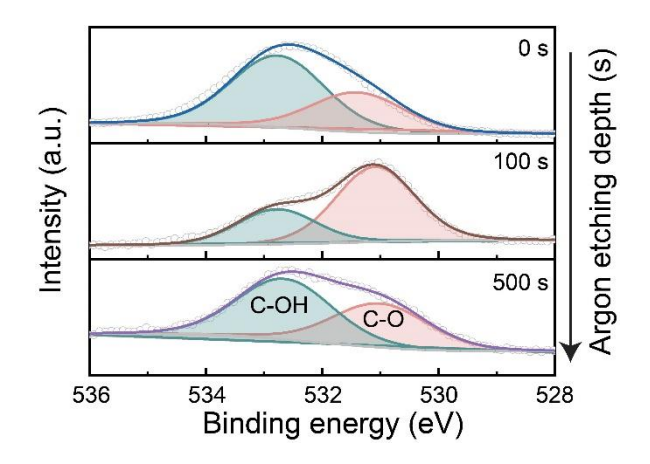


Figure 3.13 XPS O 1s depth profiles of the sputtered CN10@Zn anode.

XPS O 1s depth analysis was conducted to further analyse the interaction between carbon and oxygen in the sputtered layer. As shown in **Figure 3.13**, the O 1s XPS profiles reveal two peaks corresponding to O-H bonding and C-O bonding. The hydroxyl (O-H) bonding is the dominant peak in both the surface and the bottom layer, while C-O bonding is the major peak in the intermediate layer. The highly polar O-H bonding ensures strong adhesion to the zinc anode, keeping the sputtering layer firmly attached during Zn deposition.

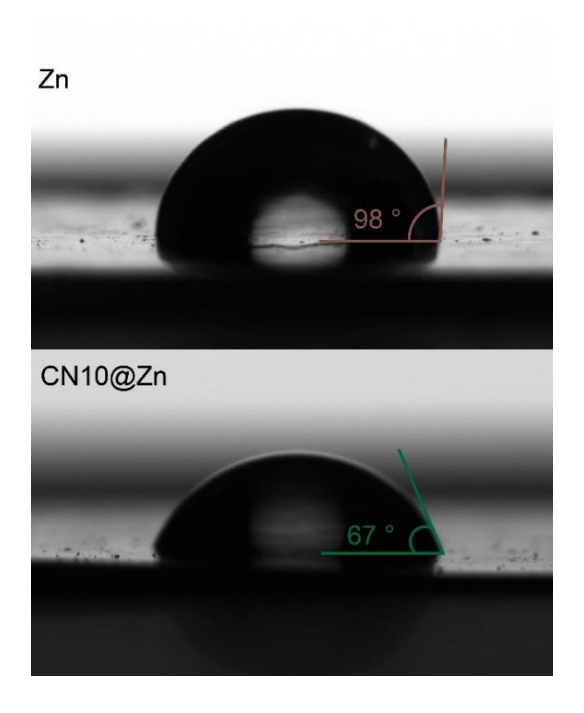


Figure 3.14 Contact angle of 2 M ZnSO₄ electrolyte on the bare Zn anode and CN10@Zn anode.

Compared to the bare Zn anode, CN10@Zn exhibits a reduced contact angle with the ZnSO₄ electrolyte (67° vs. 98°). The improved wettability of CN10@Zn facilitates the adherence of zinc ions from the electrolyte to the anode surface. The wettability difference arises from two primary factors: First, the sputtering process increases the surface roughness. A rougher surface

provides more surface area for the electrolyte to interact with. Second, as shown in the O 1s profile, the surface of CN10@Zn is rich in hydroxyl groups. These -OH species contribute to the hydrophilicity of CN10@Zn.

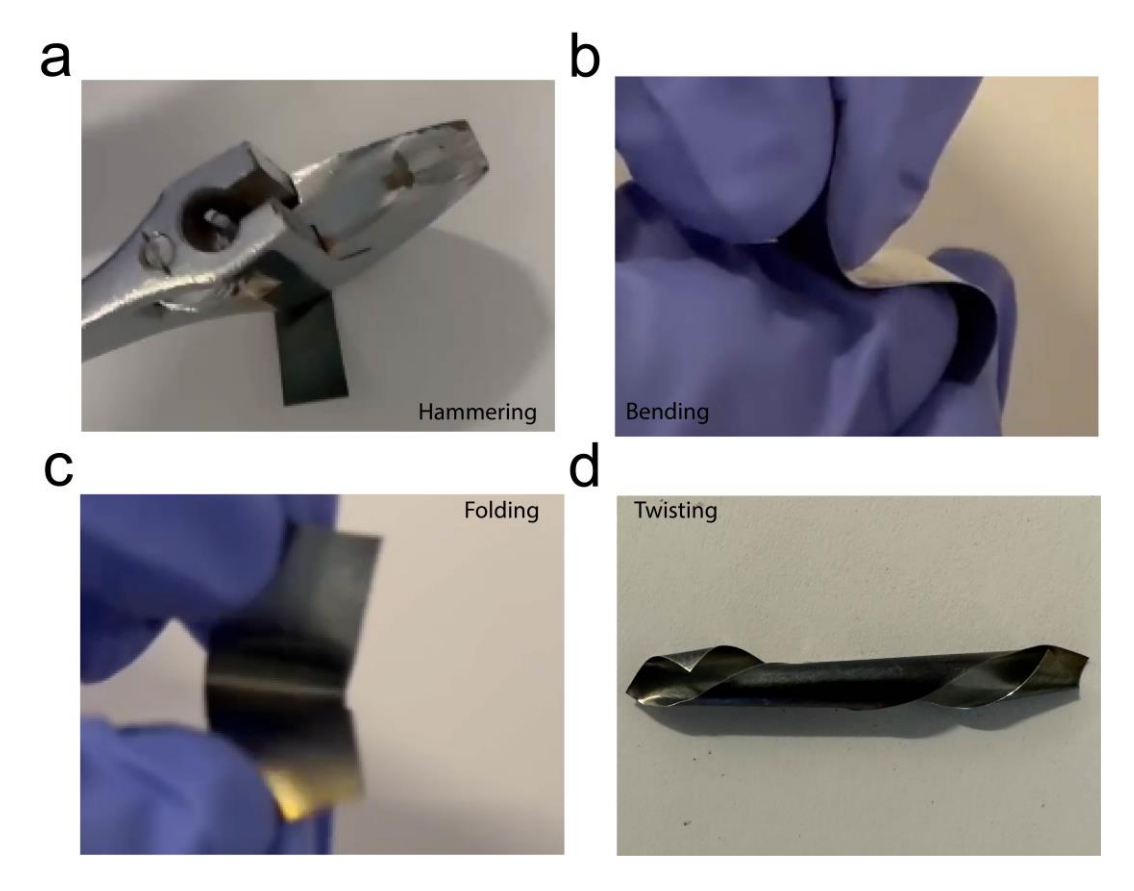


Figure 3.15 Sputtered anode mechanical testing: (a) Hammering; (b) Bending; (c) Folding; (d) Twisting.

CN10@Zn improves the adhesion between the zinc deposition and the substrate. This strong adhesion ensures a more stable and uniform layer of zinc during the deposition and dissolution processes, mitigating the risk of mechanical degradation at the electrode-electrolyte interface. This stability is particularly important when operating at higher current densities, as it helps maintain the integrity of the electrode structure. Mechanical tests, including hammering, bending, folding, and twisting (**Figure 3.15**), demonstrate that the sputtered layer remains intact on the zinc foils, indicating high tolerance to deformation and external forces. This durability is crucial for practical applications, including potential use in wearable devices.

3.3.3 Cathode characterisation

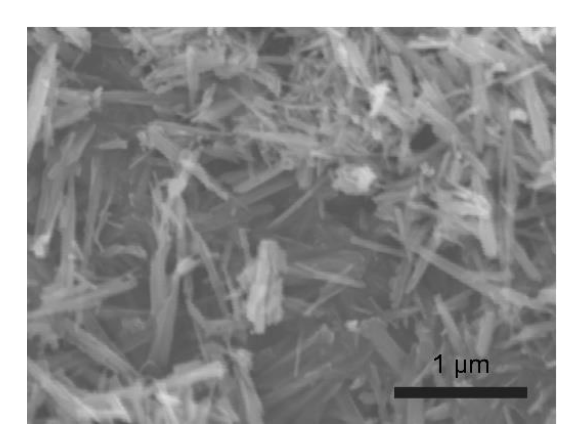


Figure 3.16 SEM images of Na_{0.65}Mn₂O₄ cathode material.

Na_{0.65}Mn₂O₄ is in δ phase and has a layered structure with sodium ions pre-intercalated in the interplane space, making it a benchmark for studying the compatibility between anode modification layers and the cathode materials. It was synthesised *via* co-precipitation method. The benefit of co-precipitation is that this method avoids the usage of high-pressure or high-temperature synthesis conditions. The as-prepared manganese oxide has a dark brown colour. The morphology was investigated by SEM. As shown in **Figure 3.16**, the morphology of Na_{0.65}Mn₂O₄ is rod-like, with an average length of 1 μ m.

Typically, manganese oxide materials exhibit morphologies such as nanorods, nanoplates, or nanoflowers, depending on the synthesis conditions. Hydrothermal synthesis typically leads to the formation of nanoflower or nanoplate morphology, which have relatively large surface area. The hydrothermal synthesis method will be detailed in Chapter 5 in the exploration of high-performance AZIBs cathode materials.

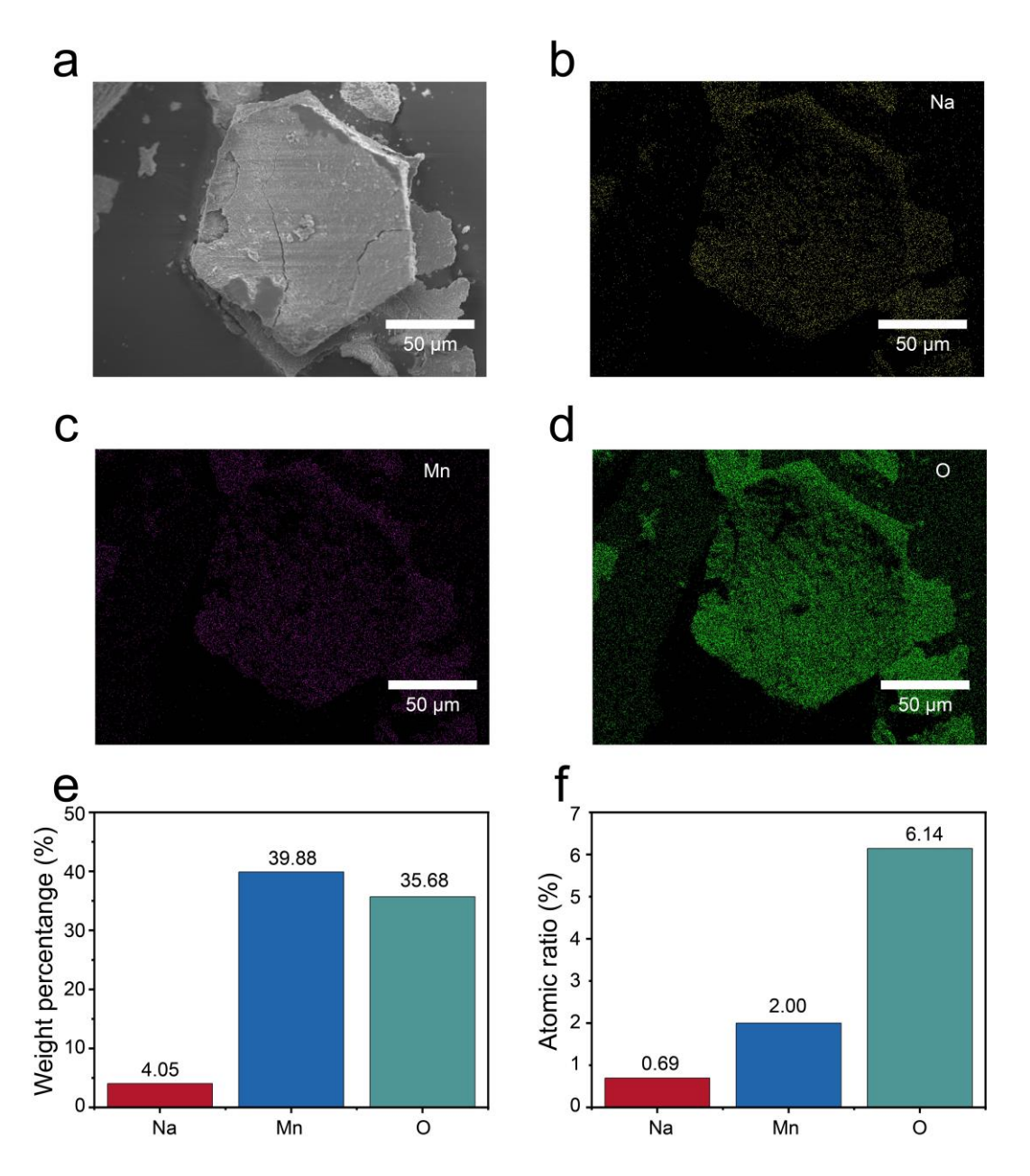


Figure 3.17 (a) SEM image of Na_{0.65}Mn₂O₄; EDS mapping profiles of Na_{0.65}Mn₂O₄; EDS mapping images for (b) Na; (c) Mn and (d) O; Elements ratio: (e) by atom weight; (f) by atom ratio.

After the successful synthesis of the cathode materials. EDS measurements were performed to study the element distribution in Na_{0.65}Mn₂O₄. As shown in **Figure 3.17 a-d**, the sodium, manganese and oxygen elements are distributed uniformly along the material surface, which indicates that the uniform pre-intercalation of sodium elements throughout the material surface. Besides EDS mapping for Na_{0.65}Mn₂O₄ could check if there are any residuals from the reactant. For example, potassium permanganate is widely used for the synthesis of manganese-based cathode material, thus potassium element signal is commonly monitored during the EDS

mapping result or XRF results, varying from ten to thousands of Parts Per Million (PPM) levels, depending on the usage amount during synthesis and the rinsing process after synthesis. The atom ratio of Na_{0.65}Mn₂O₄ is summarised in **Figure 3.17e**, the elemental weight ratio (wt%) of the Na, Mn, O elements is 4.05, 39.88 and 35.68. After considering their relative atomic mass that are 22.99, 54.94 and 15.99, the calculated atom ratio (at%) of Na, Mn and O are 0.69, 2.00, 6.14 (**Figure 3.17f**).

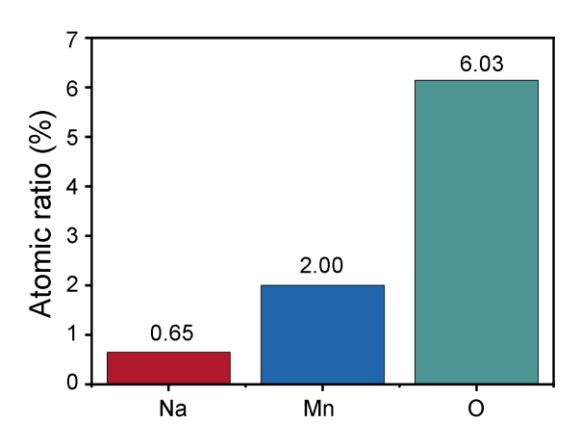


Figure 3.18 XRF characterisation of Na_{0.65}Mn₂O₄.

It is worth noting that the calculated atom ratio of Na is 0.69 according to EDS mapping results, which is slightly higher than the theoretical value 0.65. To further evaluate the elemental ratio of the as-prepared sodium manganese oxide, XRF measurement was performed. XRF uses the interaction of X-ray with the bulk material, making it suitable for analysing the element composition of the entire sample (**Figure 3.18**). The XRF result shows that the Na ratio is 0.65, consistent with the theoretical value. The difference between the EDS mapping and XRF results in this case highlights the importance of understanding the fundamental knowledge of characterisation technologies. Due to the limitation of electron beam energy in EDS mapping, the data obtained is restricted to a depth between 300 nm to 5,000 nm below the sample surface. The surface sodium concentration (0.69) is slightly higher than the inner part (0.65) is due to the intercalation energy barrier from surface to the bulk during the co-precipitation synthesis process. XRD characterisation was further performed to check if this difference can affect the crystal structure of Na_{0.65}Mn₂O₄.

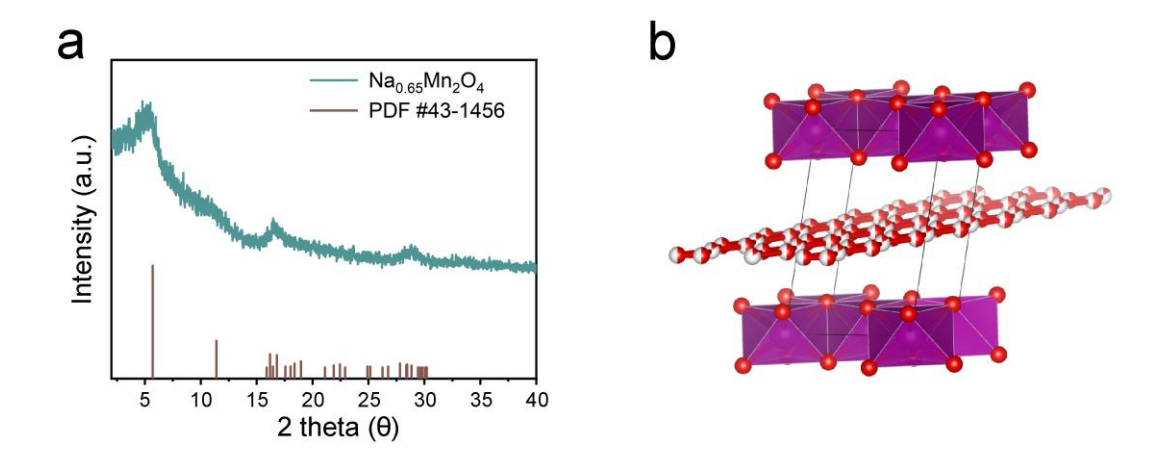


Figure 3.19 (a) XRD profile of $Na_{0.65}Mn_2O_4$ cathode material; (b) Crystal structure of $Na_{0.65}Mn_2O_4$.

The XRD characterisation can give insight into the lattice parameters of the as-prepared $Na_{0.65}Mn_2O_4$ cathode material. The interplane distance is an important parameter for layered materials like $Na_{0.65}Mn_2O_4$, as it is directly related intercalation/deintercalation of charge carriers. As shown in **Figure 3.19**, the XRD data of as-prepared material matches with PDF #43-1456 (Birnessite), with cell dimensions of 5.175 x 2.849 x 7.338 nm (90.0° x 103.1° x 90.0°), confirming the successful synthesis of $Na_{0.65}Mn_2O_4$. The significant peak located at 5.69° is associated with the (001) crystal face, with an interplane distance of 7.14 nm. Typically, a significant peak at a low angle indicates a large interlayer distance, which can facilitate the interaction of large, hydrated metal ions. This sufficient interplane distance indicate that $Na_{0.65}Mn_2O_4$ cathode material is suitable for AZIBs research, which is based on the transfer of large hydrated ions such as $Zn(H_2O)_6^{2+}$.

3.3.4 Theoretical simulations

The computational simulation reported in this chapter was done in collaboration with Jianrui Feng in Department of Chemistry, University College London. The relevant part was rewritten according to the results. DFT simulation was performed to study the Zn²⁺ adsorption mechanism on the CN10@Zn anode surface. Adsorption energy analysis was conducted on various oxygen and nitrogen species on the CN10@Zn surface. The simulation process also took into account the electronic structure, charge distribution, and local electrostatic potential of the CN10@Zn anode surface, revealing the interaction between CN10@Zn and Zn²⁺ ions.

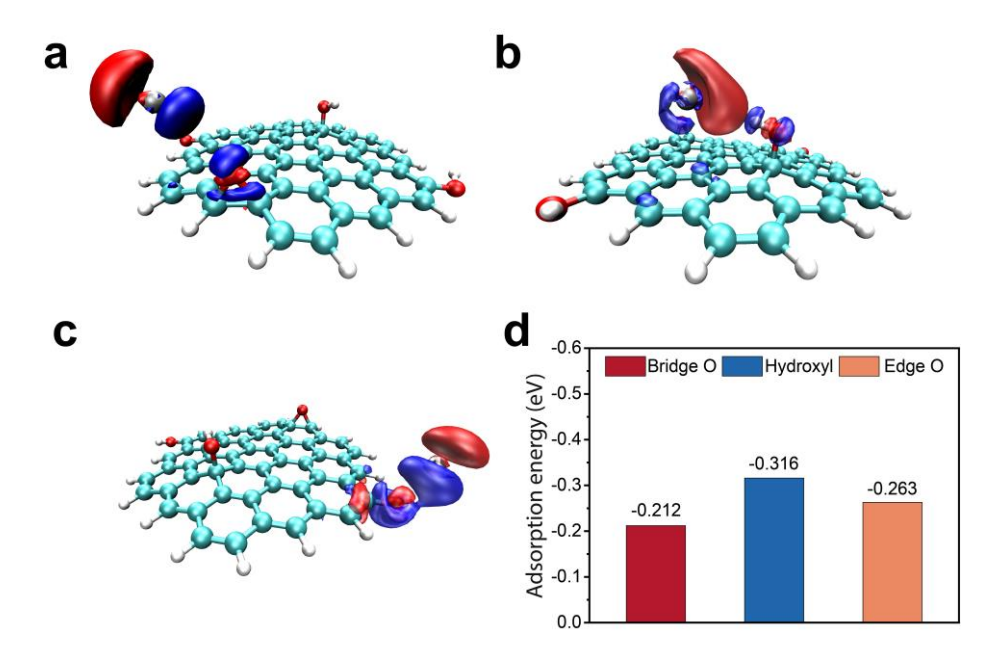


Figure 3.20 DFT simulation on oxygen species: Charge density of (a) Bridge oxygen; (b) Hydroxyl oxygen; (c) Edge oxygen; (d) Adsorption energy comparison of different oxygen sites.

The previous O 1s depth profile reveals that oxygen species vary along the depth in the CN10@Zn layer. Further DFT simulations on the charge density revealed the differences in adsorption energy among various oxygen species. Oxygen atoms, having higher electronegativity than carbon, create localised charge density around themselves and form polar regions (Figure 3.20a-c). Hydroxyl (OH) groups form stronger bonds with zinc ions due to the presence of lone pair electrons, requiring less energy for Zn²⁺ adsorption (-0.316 eV) (Figure 3.20d). In comparison, bridge oxygen (-0.212 eV) is shared by two other atoms, while edge oxygen (-0.263 eV) is located at the termination of a lattice, resulting in weaker interaction with Zn²⁺. This results are in line with the O 1s depth profile, confirms the role of oxygen species in CN10@Zn.

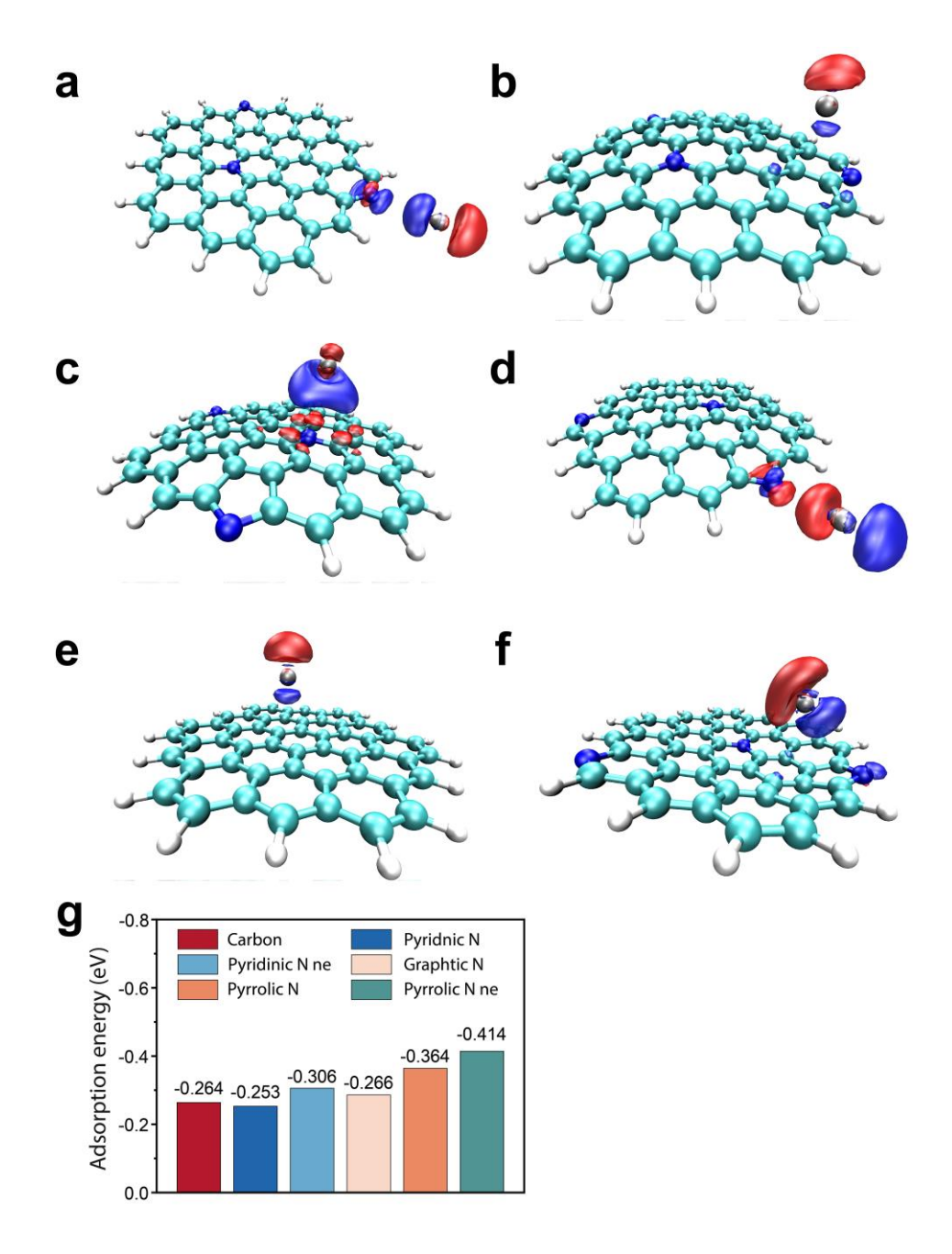


Figure 3.21 DFT simulation on nitrogen species: Charge density of (a) Carbon; (b) Pyridinic N; (c) Pyridinic neighbour N; (d) Graphic N; (e) Pyrrolic N; (f) Pyrrolic neighbour N; (g) Adsorption energy comparison of different N species.

DFT simulation on nitrogen species reveals that pyrrolic N plays an important role in tailoring the CN10@Zn adsorption behaviour. As shown in **Figure 3.21**. pyrrolic N (-0.364 eV) and its neighbouring N (-0.414 eV) exhibit lower adsorption energies than other nitrogen species in CN10@Zn, indicating that pyrrolic N interacts more favourably with zinc ions. This difference arises from the distinct chemical environments around the nitrogen atoms. Pyrrolic N is located within a five-membered ring environment, which is more flexible than the six-membered

aromatic ring environment of pyridinic N. Pyrrolic N can offer its lone pair of electrons for interaction, thereby enhancing the adsorption behaviour of Zn²⁺ on CN10@Zn.

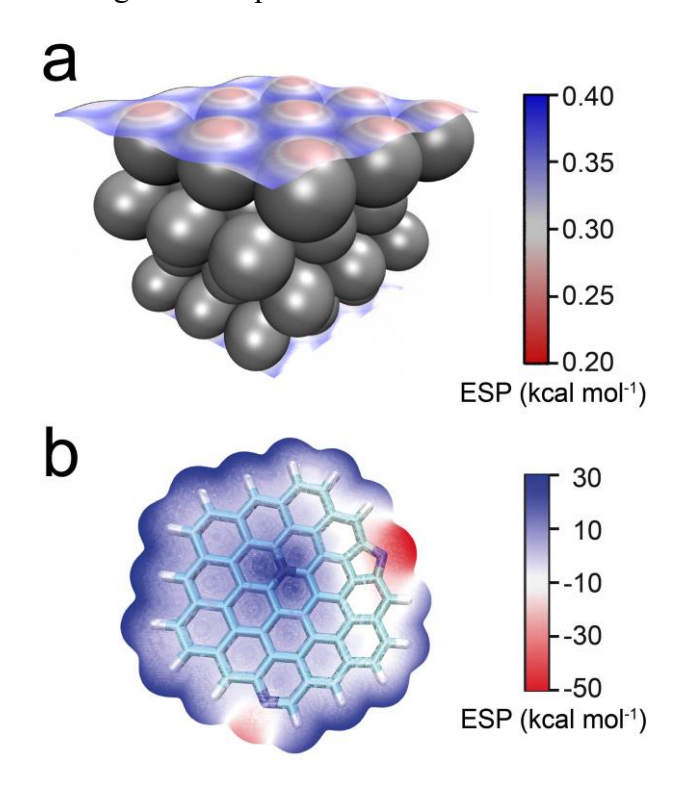


Figure 3.22 Electrostatic field distribution diagram the anodes: (a) Zn and (b) CN10@Zn.

The electrostatic field distributions of the bare Zn anode and CN10@Zn are presented in Figure 3.22. The simulation results indicate that pyrrolic N species introduce local variations in the charge distribution of CN10@Zn, demonstrating that nitrogen dopants not only provide strong adsorption sites, but also shape the distribution of the electric field by giving rise to surface dipoles.

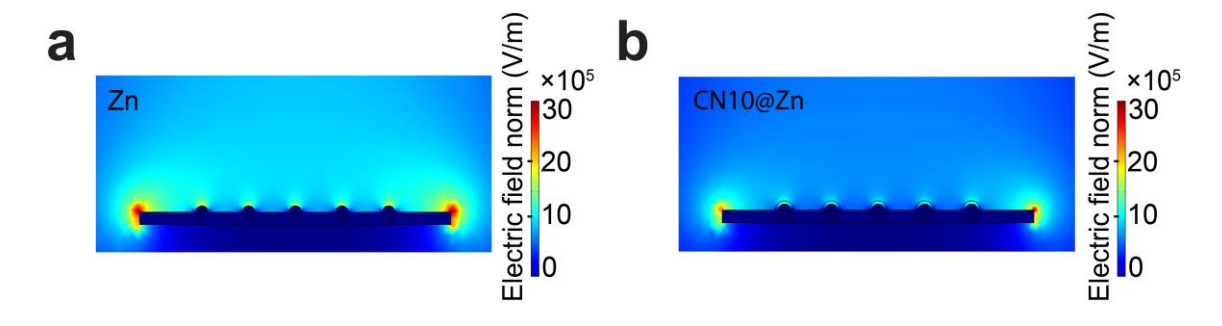


Figure 3.23 COMSOL simulations of the electric field distribution: (a) Bare Zn and (b) CN10@Zn.

Electric field intensity tends to concentrate around sharp tips with higher curvature, known as the 'tip effect'. The relationship between curvature (k) and charge density (σ) is illustrated by the following equation:

$$\sigma = \varepsilon E_o = \left(\frac{2k\Delta V}{e^{-2k\Delta n} - 1}\right)_{\wedge n o 0}$$

As a result, for the zinc anode, the curvature of anode edges and nucleation sites is higher compared to flat areas, leading to concentrated electric field intensity and ultimately causing uneven Zn ion nucleation and dendrite formation.

To investigate the differences between CN10@Zn and the bare Zn, COMSOL Multiphysics simulations were performed to analyse the electric field distribution on both anodes. As shown in **Figure 3.23a**, the bare Zn anode exhibits higher electric field intensity near the zinc nuclei surface. Consequently, the Zn²⁺ flux has a tendency to concentrate around nuclei sites on the bare Zn, leading to Zn dendrite formation and an uneven morphology after cycling. In contrast, CN10@Zn displays reduced electric field intensity (**Figure 3.23b**), promoting dense nucleation sites on the CN10@Zn surface due to the rich oxygen and nitrogen adsorption sites.^[38] The dense adsorption sites allow for a more uniform distribution of initial zinc deposition, reducing the chance of localised nuclei growth and resulting in uniform surface morphology during the Zn deposition.^[39]

3.3.5 Ex-situ & in-situ characterisation

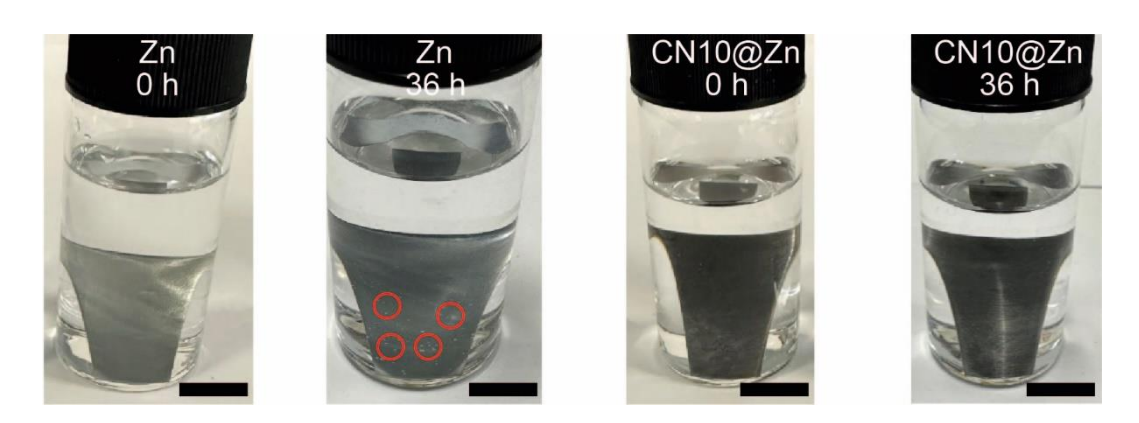


Figure 3.24 Digital images of the immersion experiments in 2 M ZnSO₄ electrolyte: (a,b) Bare Zn anode; (c,d) CN10@Zn anode. Scale bar: 10 mm.

Immersion experiments provide a facile and direct method to study the effectiveness and stability of the CN10@ZN. As shown in **Figure 3.24**, digital images of the bare Zn anode show significant hydrogen bubble formation after immersion experiments in 2 M ZnSO₄ electrolyte

for 36 hours. In contrast, the CN10@Zn anode shows no obvious bubble formation during the immersion experiment, indicating that CN10@Zn acts as a physical barrier that limits direct contact between the anode and corrosive species in the electrolyte. As a result, the hydrogen evolution that degrade the anode is regulated. Additionally, no significant colour change or peeling of the sputtered CN10@Zn is observed during the immersion experiment, illustrating the stability and effectiveness of the sputtered CN10@Zn layer.

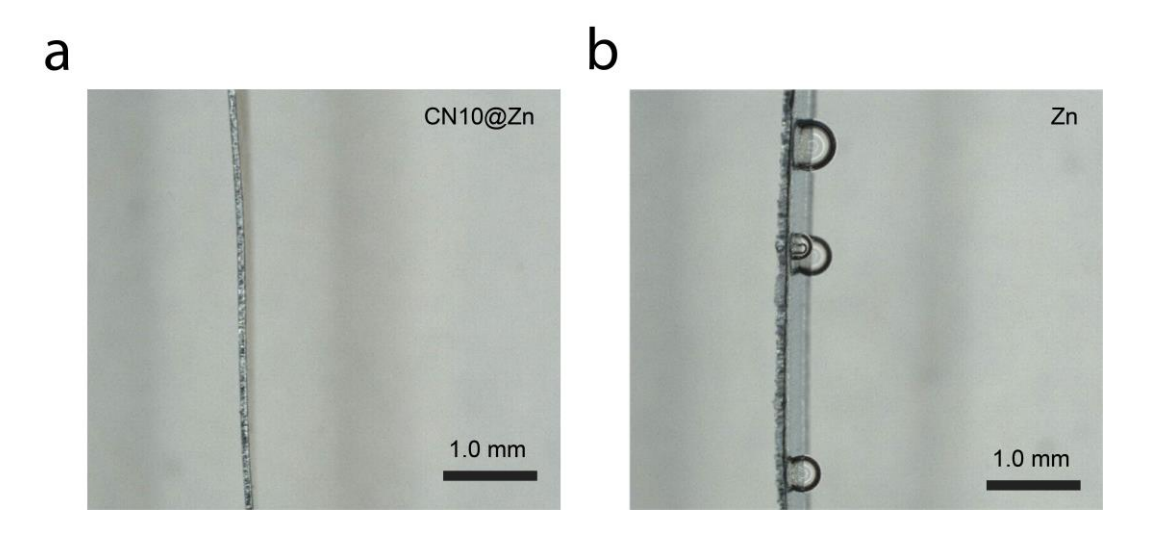


Figure 3.25 Cross-sectional optical micrographs of (a) CN10@Zn and (b) Bare Zn soaked in 2 M ZnSO₄ electrolyte for 36 hours. Scale bar: 1.0 mm.

To gain a better understanding of the bubble generation process, optical microscopy of immersion experiments was performed. As shown in **Figure 3.25**, significant hydrogen bubble formation is observed on the bare Zn anode of the immersion in 2 M ZnSO₄ electrolyte. During the immersion experiment, these hydrogen bubbles form and merge across the anode surface, displacing the electrolyte and isolating these surfaces from zinc stripping. This leads to low CE and uneven zinc plating and stripping across the bare Zn anode surface. In contrast, the CN10@Zn anode maintains the solid/liquid electrolyte/electrode interface without the disruption caused by gas phase. This indicates that CN10@Zn also acts as a physical barrier that limits the direct contact between the anode and corrosive species in the mildly acidic ZnSO₄ electrolyte. As a result, hydrogen evolution that would degrade the anode is effectively regulated by CN10@Zn. This shielding effect can further helps maintain the surface morphology of zinc anode during cycling and lead to the differences in surface composition between the two anodes.

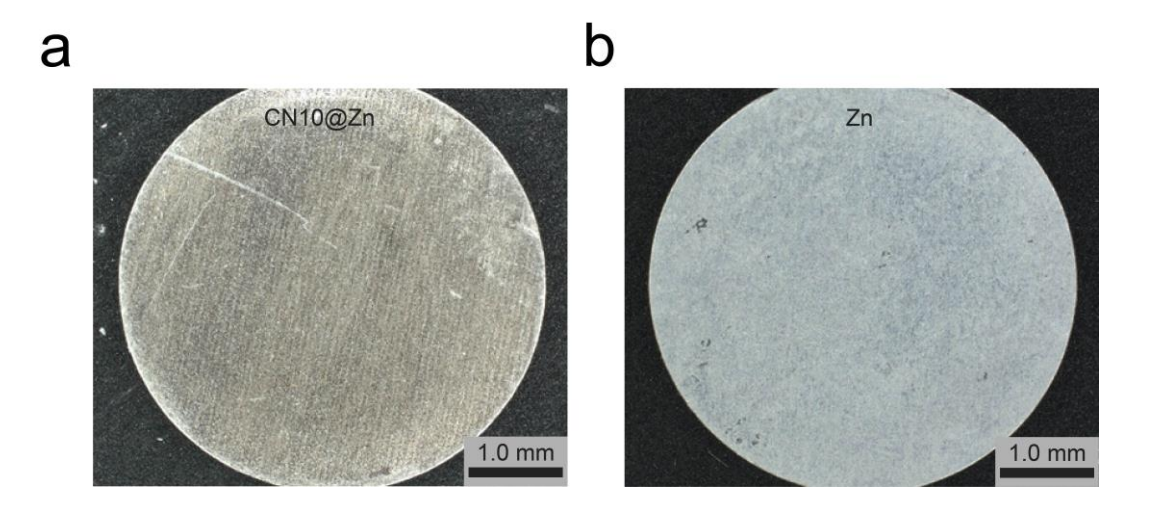


Figure 3.26 Ex-situ digital images after cycling: (a) CN10@Zn anode; (b) Bare Zn anode.

Digital images of CN10@Zn and the bare Zn anode were taken to illustrate the appearance differences of the anodes after cycling. As shown in **Figure 3.26**, the surface of CN10@Zn appears smooth, with fewer byproducts observed, and the CN10@Zn layer maintains uniformity on the surface. This indicates the stability and efficiency of CN10@Zn in regulating zinc deposition. In contrast, the bare Zn anode was covered by mossy side products, which are caused by unregulated water-related side reactions and further lead to dendrite formation.

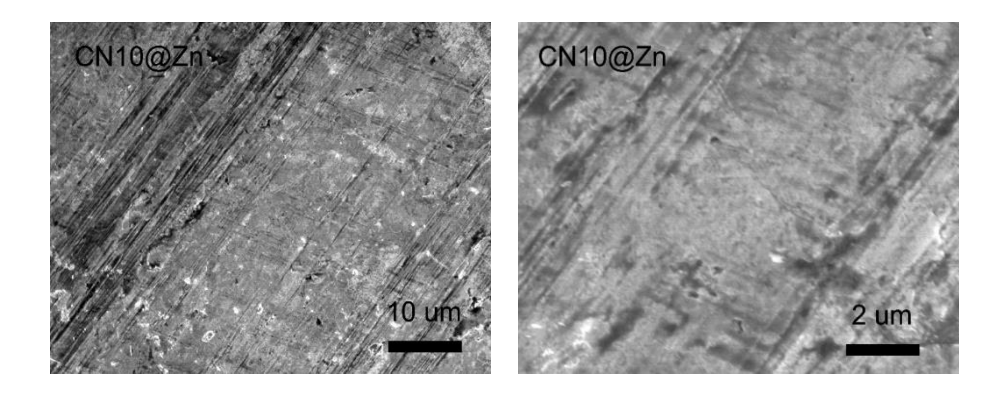


Figure 3.27 Ex-situ SEM images of the CN10@Zn anode.

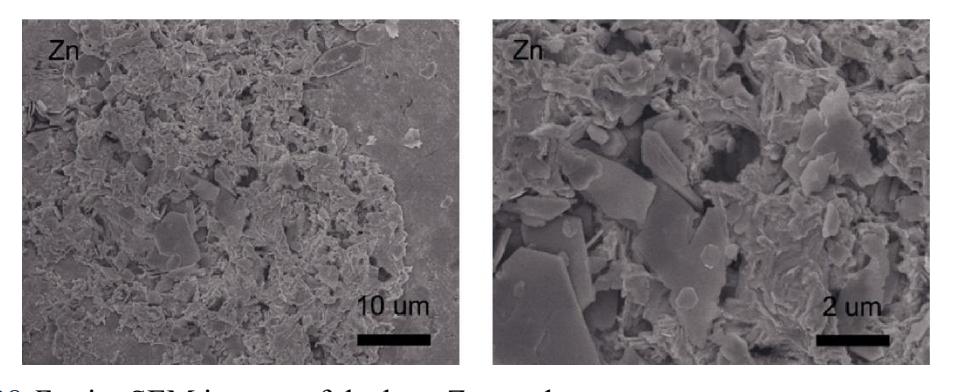


Figure 3.28 Ex-situ SEM images of the bare Zn anode.

Ex-situ SEM was performed to gain a close illustration of the morphological differences between the two anodes. Figure 3.27 shows the dendrite-less morphology of the CN10@Zn anode, indicating that CN10@Zn guides uniform Zn deposition. In comparison, the morphology of the bare Zn anode after cycling in Figure 3.28 is covered by a moss-like Zn agglomeration, a symptom of dendrite formation. These ex-situ SEM results combined with the digital images confirms the effectiveness of CN10@Zn on preventing the dendrite formation.

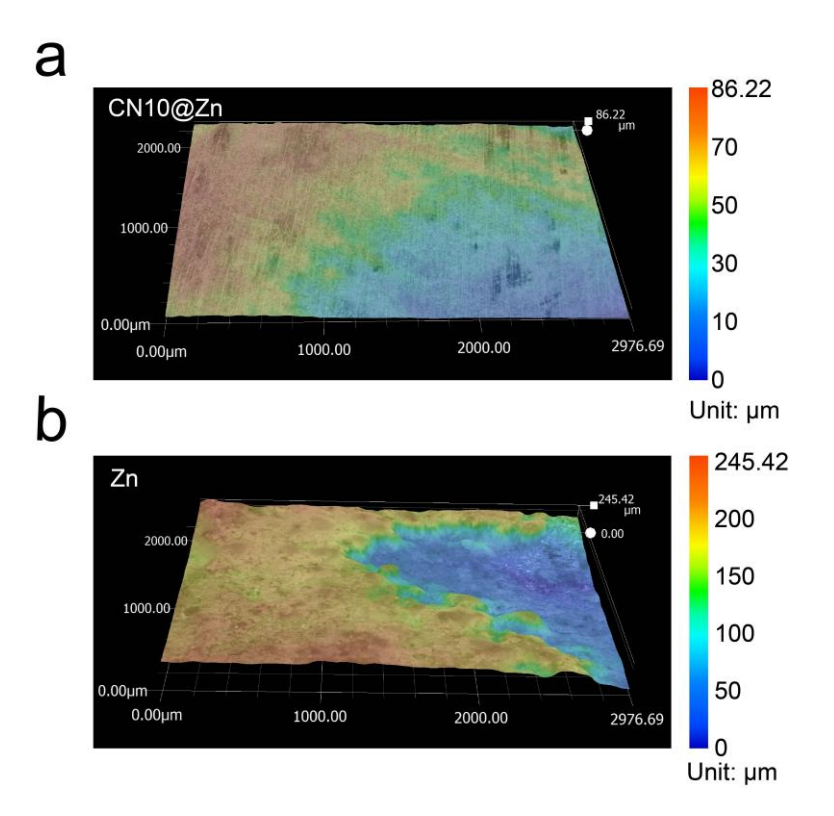


Figure 3.29 3D laser scanning confocal microscopy of the anodes cycled in 2 M ZnSO₄ electrolyte: (a) CN10@Zn; (b) Bare Zn.

The morphological evolution of both anodes was further demonstrated through 3D laser scanning confocal microscopy. After cycling, the surface of CN10@Zn remains smooth, showing an even Zn deposition process, as evidenced by an average roughness (R_a) of 86.22 µm (**Figure 3.29a**). In contrast, the bare Zn anode exhibits a significantly rougher morphology with an average roughness of 245.42 µm, characterised by peaks and valleys due to unregulated Zn deposition caused by 'tip effect' (**Figure 3.29b**). These dendrites increase the unevenness of the bare Zn anode, further accelerating side reactions. These results directly illustrate that the effectiveness of CN10@Zn can promote a uniform zinc deposition process.

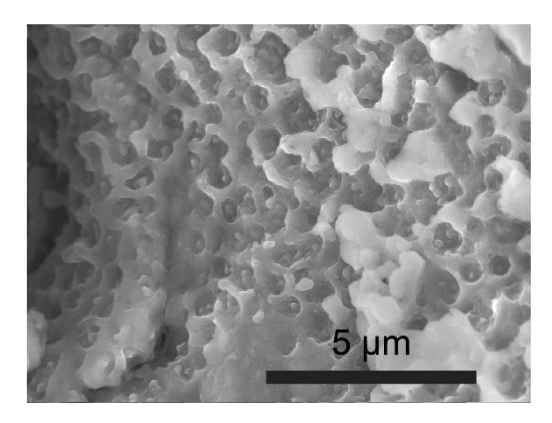


Figure 3.30 SEM images of the Zn anode after sputtering treatment.

As a high-energy treatment method, sputtering ions from the sputtering target can bombard the surface of the Zn anode. As shown in **Figure 3.30**, CN10@Zn has a Swiss-cheese-like porous morphology. This porous structure can act as ion diffusion pathways from the electrolytes to the Zn anode, mitigating the concentration difference at the interface and inhibiting the formation of Zn dendrite.

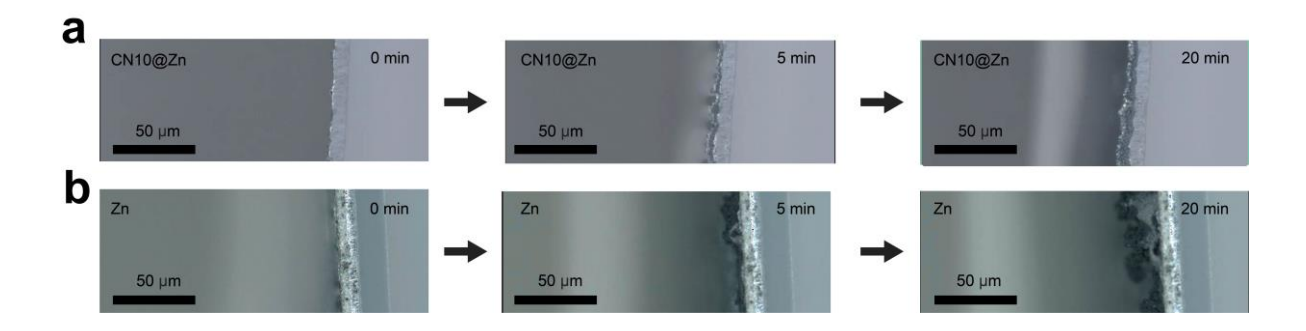


Figure 3.31 *In-situ* optical microscopy images: (a) CN10@Zn; (b) Bare Zn.

In-situ optical microscopy reveals the dendrite formation process and zinc deposition behaviour on the CN10@Zn anode and the bare Zn anode over different time intervals (Figure 3.31). No dendritic formation is observed on the sputtered CN10@Zn anode, and zinc deposition appears uniform across the anode surface. In comparison, the bare Zn anode exhibits obvious dendritic growth, characterised by a non-uniform morphology forming within 5 minutes in the Zn symmetric cell. Dendrite formation on the bare Zn anode highlight the limited controlled over zinc ion distribution process and less favourable deposition kinetics without a protection layer. These observations are consistent with the simulation results, indicating that CN10@Zn has an optimised Zn²⁺ adsorption and deposition process owing to the rich oxygen and nitrogen species. These sites form dense deposition sites that remain stable during zinc deposition, leading to uniform zinc deposition. The sputtered CN10@Zn anode's ability to suppress

dendritic growth and promote uniform deposition highlights the effectiveness of the oxygen and nitrogen species in the CN10@Zn.

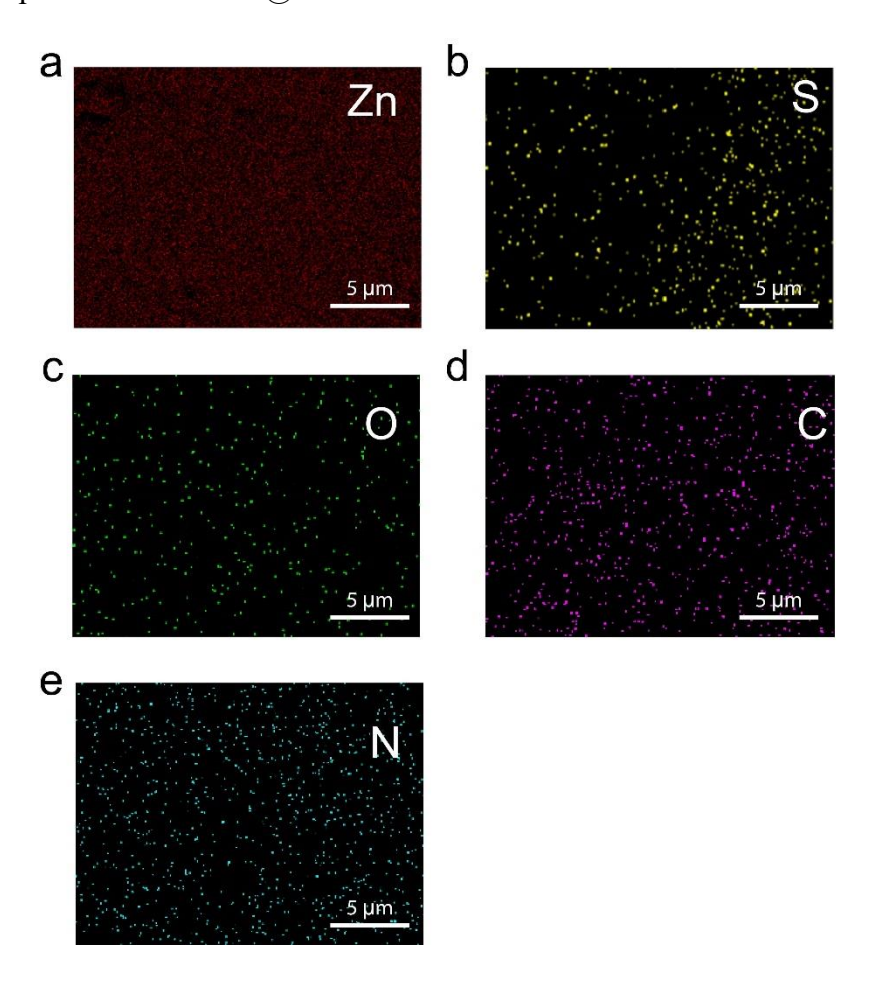


Figure 3.32 Ex- situ EDS mapping of CN10@Zn.

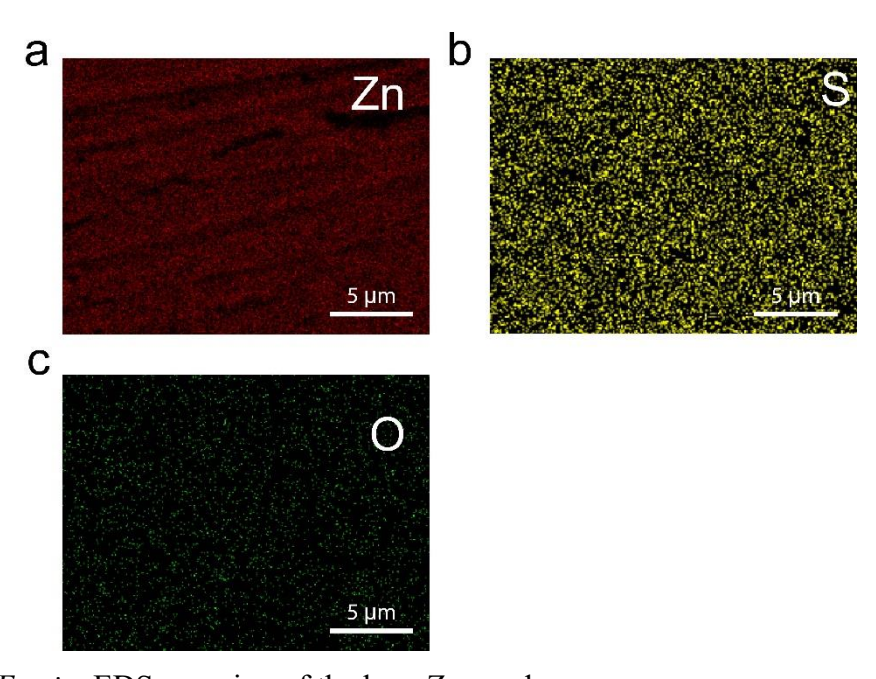


Figure 3.33 Ex-situ EDS mapping of the bare Zn anode.

The chemical environment of both anodes was further compared by *ex-situ* EDS mapping. As shown in **Figure 3.32**, the elements C, N, and O are uniformly distributed across the surface of the sputtered CN10@Zn anode after cycling, indicating that the sputtered layer, along with the oxygen and nitrogen species, remains stable. Additionally, there is no obvious S signal related to byproducts on the cycled CN10@Zn anode. In contrast, the EDS mapping of the bare Zn anode shows a distinct S element distribution across the surface (**Figure 3.33**). This difference in *ex-situ* EDS mapping, particularly the S 2p signal, indicates that the CN10@Zn protection layer effectively regulates the HER and maintains reversible zinc deposition reactions. These EDS mapping results are consistent with the other *ex-situ* measurements, further confirming the effectiveness of CN10@Zn.

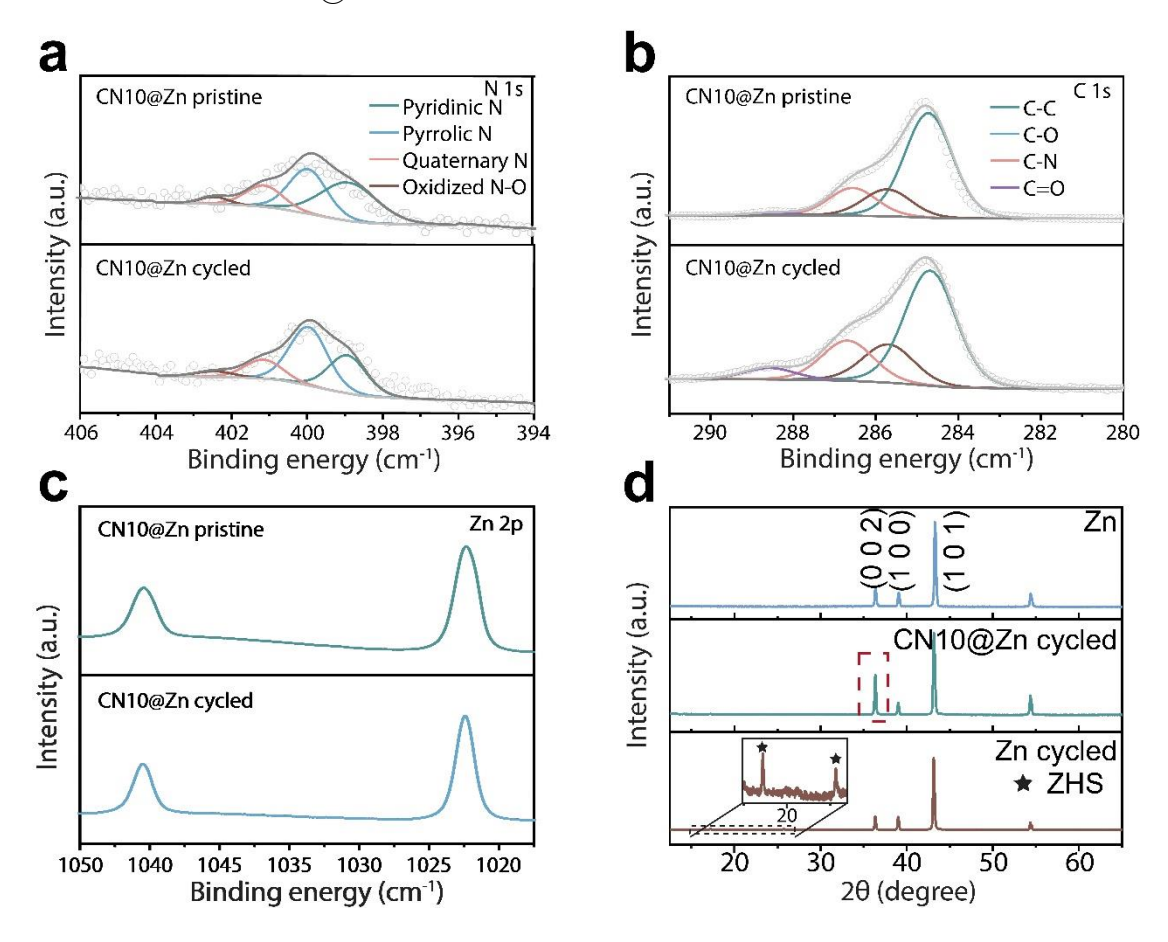


Figure 3.34 *Ex-situ* characterisation of CN10@Zn: (a) *Ex-situ* N 1s profiles; (b) *Ex-situ* C 1s profiles; (c) *Ex-situ* Zn 2p profiles; (d) *Ex-situ* XRD images comparison of the sputtered anode and the bare Zn anode.

The disassembled symmetric Zn cells were analysed to examine the chemical environment on anodes after cycling. *Ex-situ* high-resolution XPS results of N (**Figure 3.34a**), C (**Figure 3.34b**), and Zn (**Figure 3.34c**) in CN10@Zn show no significant differences before and after

cycling. This demonstrates that the chemical composition and bonding environment of CN10@Zn are preserved throughout the cycling process, underscoring its chemical stability during battery operation and suggesting minimal changes in its electronic structure. The high stability of the CN10@Zn protection layer contributes to a regulated zinc deposition process. Additionally, *ex-situ* XRD testing results (**Figure 3.34d**) reveal that CN10@Zn inhibits the formation of zinc sulfate hydroxide on the surface and increases the intensity of the Zn (002) crystal face. CN10@Zn promotes the preferential growth of the Zn (002) crystal face in Zn anodes by influencing surface energy and affecting nucleation and growth processes. The oxygen and nitrogen species in CN10@Zn alter the surface adsorption energy, causing the Zn (002) crystal face, which has lower surface energy, to grow preferentially. In contrast, zinc sulfate hydroxide peaks are present on the bare Zn anode after cycling, indicating unregulated side reactions on bare Zn anodes in the absence of the CN10@Zn protection layer.

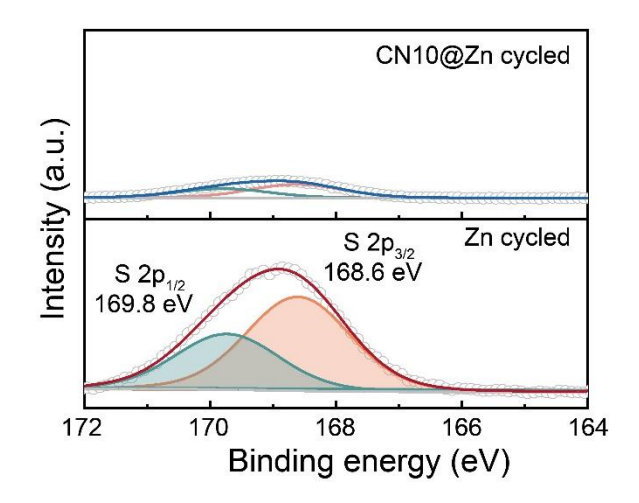


Figure 3.35 Ex-situ XPS S 2p profile of the bare Zn anode and the CN10@Zn zinc anode.

To further monitor the possible water-related side reactions on both anodes, *ex-situ* XPS S 2p analysis was performed. As shown in **Figure 3.35**, the two XPS signals located at 169.8 eV and 168.6 eV, correspond to S 2p 3/2 and S 2p 1/2, respectively. These peaks are attributed to the byproduct Zn₂(OH)₂SO₄ resulting from the unregulated HER on the bare Zn anode. In contrast, the S signal intensity of the cycled sputtered CN10@Zn anode is significantly lower than that of the cycled bare Zn anode, indicating that minimal zinc hydroxide sulfate byproduct is generated. The *ex-situ* XPS results, combined with the *ex-situ* XRD results, confirm that the HER is effectively restricted by the CN10@Zn protection layer.

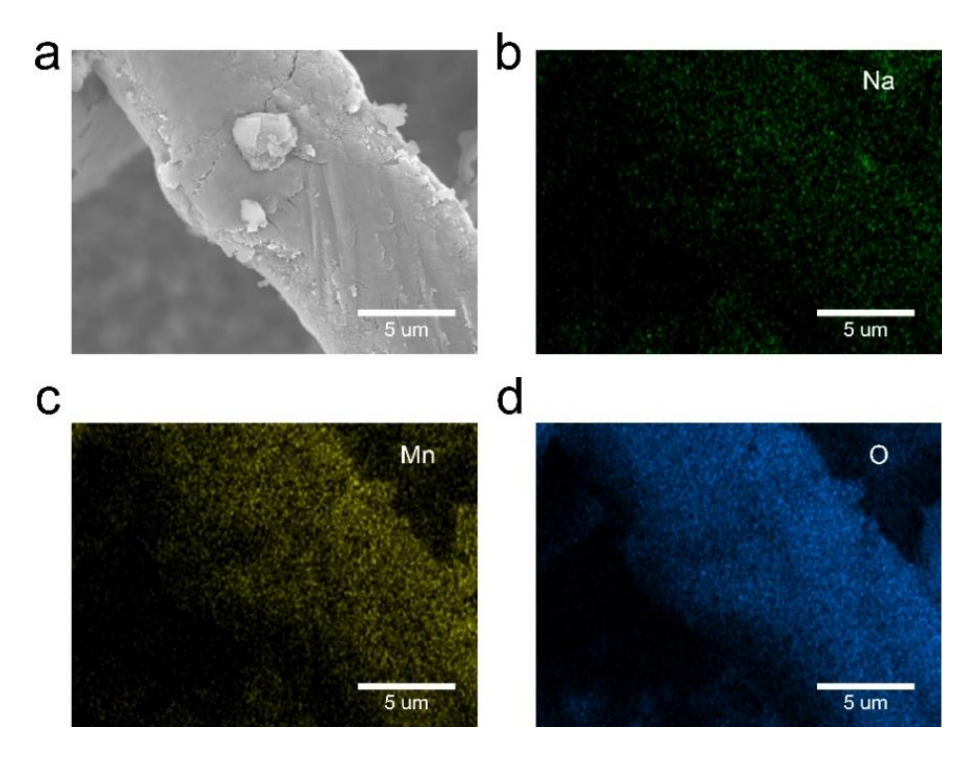


Figure 3.36 Ex-situ SEM and EDS mapping images of Na_{0.65}Mn₂O₄ cathode materials.

As shown in **Figure 3.36**, the morphology of the cathode material is stable after cycling and there is no obvious cracking on the cathode materials. The energy-dispersive spectroscopy mappings of the cathode material demonstrate that the Na, Mn and O elements are uniformly distributed on the Na_{0.65}Mn₂O₄ cathode surface, indicating that the sputtered CN10@Zn layer is compatible with the Na_{0.65}Mn₂O₄ cathode material.

3.3.6 Electrochemical characterisation of CN10@Zn

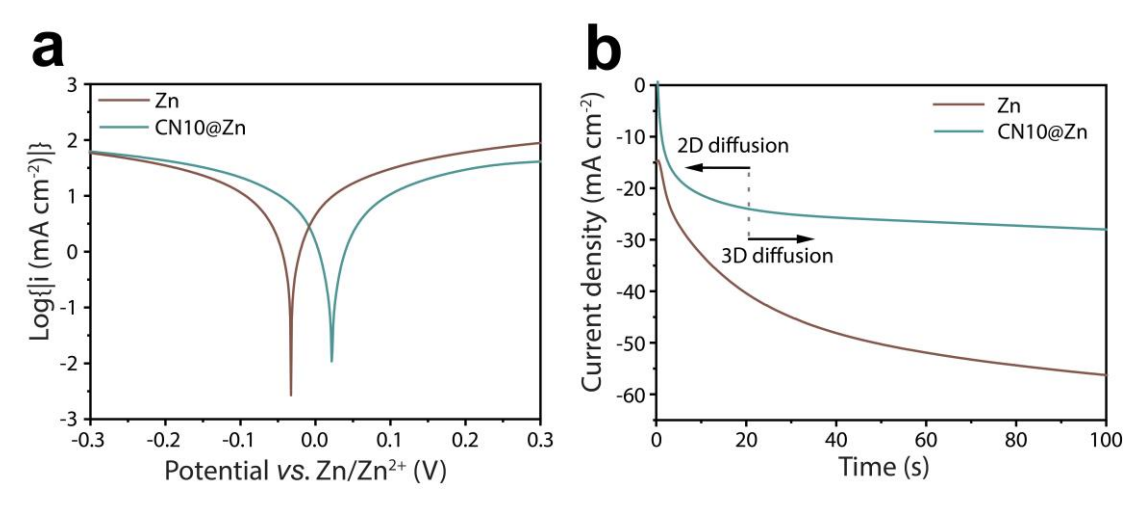


Figure 3.37 Electrochemical characterisation: (a) Linear sweep scanning profiles of CN10@Zn anode and the bare Zn anode; (b) CA testing profiles of the sputtered CN10@Zn anode and the bare Zn anode.

Electrochemical characterisation was performed to study the detailed corrosion and deposition behaviour of both anodes. The polarisation curves shown in **Figure 3.37a** illustrate that CN10@Zn has a more positive corrosion potential than the bare Zn anode, suggesting lower corrosion susceptibility. Chronoamperometry (CA) was conducted at a constant overpotential of -150 mV to provide information about the zinc nucleation and growth kinetics. During Zn nucleation, the current response changes as new nuclei form and grow. The current response with CN10@Zn became stable after 15 seconds, indicating that CN10@Zn facilitates a stable Zn 3D diffusion process after an initial 2D diffusion phase promoting homogeneous zinc deposition and preventing dendrite formation, resulting in a dendrite-less morphology during cycling (**Figure 3.37b**). In comparison, the bare Zn anode exhibits 2D diffusion during the zinc deposition process due to the uneven surface electrical distribution, and Zn²⁺ ions undergo localised reduction to Zn⁰ while the 3D diffusion is limited, this further leads to the dendrite formation on the bare Zn anode.

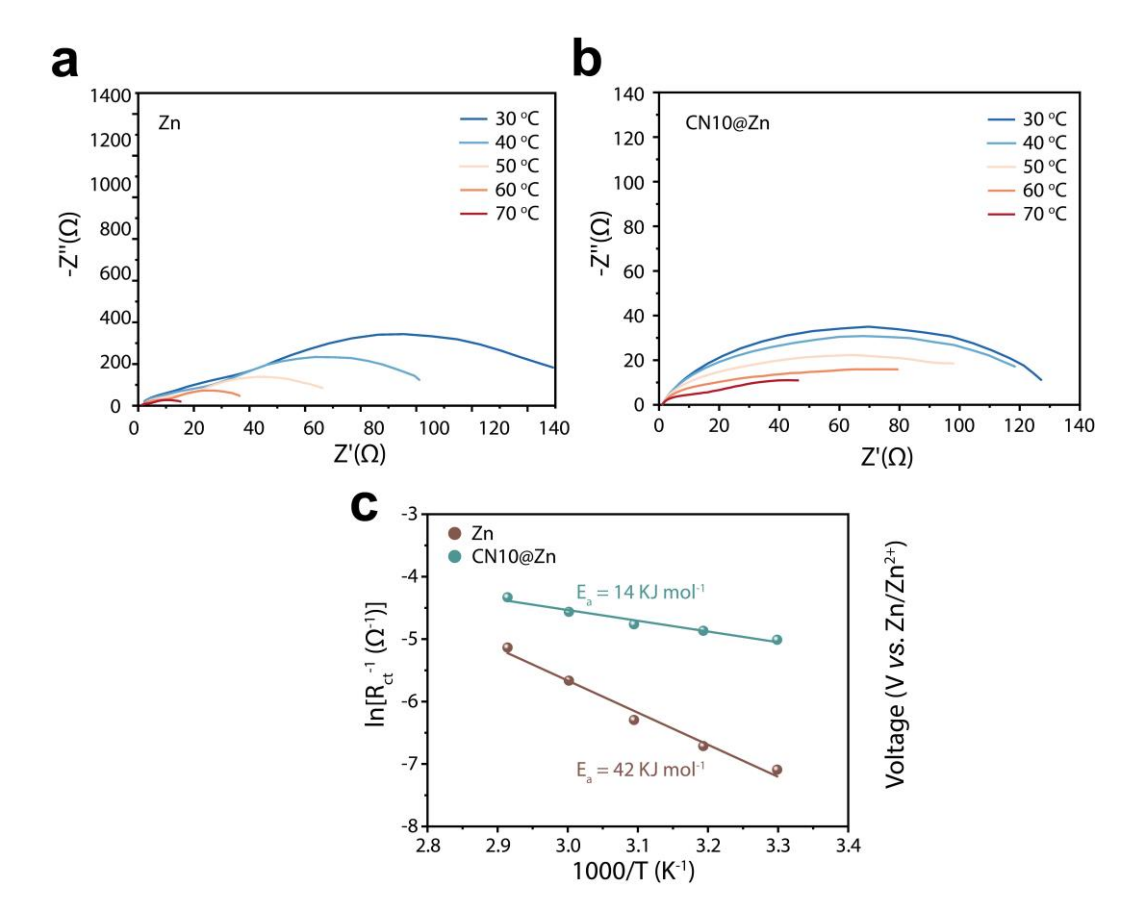


Figure 3.38 EIS profiles from 30°C to 70°C; (a) Bare Zn anode; (b) CN10@Zn anode; (c) Activation energy analysis of the CN10@Zn anode and the bare Zn anode.

Figure 3.38a and **Figure 3.38b** display the Nyquist plots of symmetric cells with sputtered CN10@Zn anode and the bare Zn in a temperature range from 30°C to 70°C. The charge-transfer resistance of the CN10@Zn anode symmetric cells remained low while varying the testing temperature and reaching a low impedance of 64 Ω at 70°C. In contrast, the bare Zn anode has a higher impedance in the same temperature range. This obvious difference is due to the side reactions and undesirable passivating byproduct generated on the bare anode, which influences the impedance response during testing. The obvious difference in impedance results illustrate that CN10@Zn remain stable and passivation resistance in a broad temperature range from 30°C to 70°C. These results are consistent with *ex-situ* XPS and XRD results.

Further analysis on activation energy follows to the Arrhenius equation:

$$\frac{1}{R_{ct}} = Aexp(-\frac{E_a}{RT})$$

 R_{ct} represents the charge-transfer resistance, A denotes the Arrhenius constant, E_a stands for the desolvation activation energy, R is the gas constant, and T corresponds to the absolute temperature. CN10@Zn exhibits a lower activation energy (14 kJ mol⁻¹) due to its modified

electronic structure and enhanced ion transport. **Figure 3.38c** shows the activation energy according to the Nyquist plots using CN10@Zn and Zn at different temperatures. CN10@Zn exhibits a lower activation energy (14 kJ mol⁻¹), which is significantly lower than the bare Zn anode (42 kJ mol⁻¹). This reduction in activation energy results from the enhanced Zn²⁺ adsorption behaviour and the regulated Zn deposition process, contributing to a higher CE with fewer side reactions during cycling.

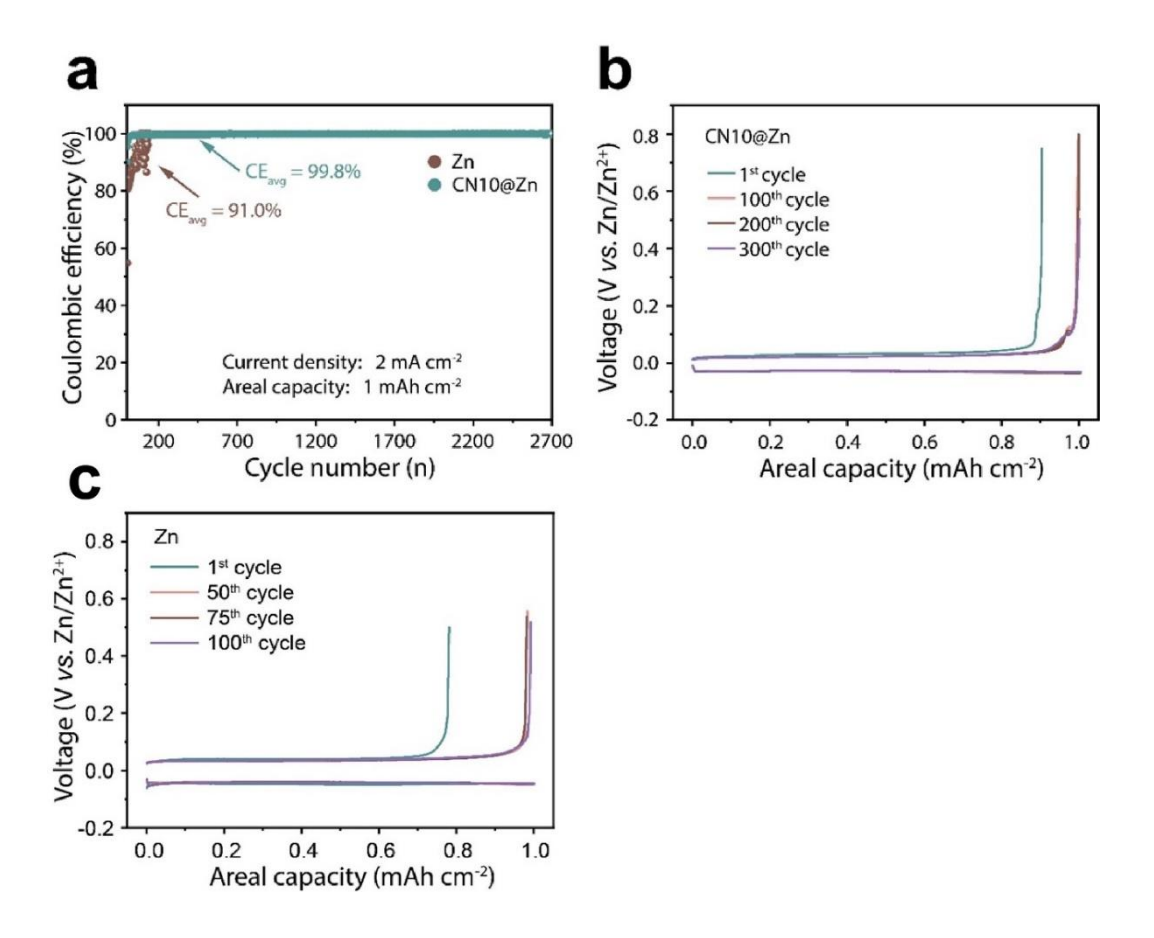


Figure 3.39 (a) CE results of the CN10@Zn anode and the bare Zn anode; Relevant voltage-areal capacity profiles: (b) CN10@Zn and (c) Zn.

Since copper is a commonly used substrate in electrochemical studies, it allows researchers to establish a benchmark for CE in zinc deposition. As shown in (**Figure 3.39a**), the Cu||CN10@Zn half-cell remained stable for 2,700 cycles with a high average CE of 99.8%. The high CE originates from the regulated water-related side reactions by the CN10@Zn anode. Additionally, introducing O and N polar functional groups in CN10@Zn improves the adhesion between the Cu substrate and the Zn deposited layer, ensuring a stable chemical environment and surface morphology for Zn deposition. In contrast, the Cu||Zn half-cell collapsed after 300 cycles, and the CE (91.0%) was obviously lower than that of CN10@Zn. This is due to the

accumulation of side products at the electrode-electrolyte interface, which increase the cell impedance and impedes charge transfer. The difference in Zn deposition reversibility of both anodes is further illustrate by the relevant voltage-areal capacity profile. As shown in **Figure 3.39b**. The zinc deposition plateaus overlap in cycles 100, 200, and 300 with CN10@Zn anode, illustrating the high reversibility of the zinc deposition process. The stable deposition potential also confirms that the surface morphology of CN10@Zn is maintained and the O, N species in CN10@Zn are highly stable due to the strong adhesion of CN10@Zn to the substrate; neither the detachment of particles nor the consumption of oxygen or nitrogen species was noted. In contrast, the Zn deposition plateaus change during cycling and the deposition polarisation is obviously higher than with CN10@Zn (**Figure 3.39c**). The improved CE of the CN10@Zn anode can further contribute to its long-term cycling performance.

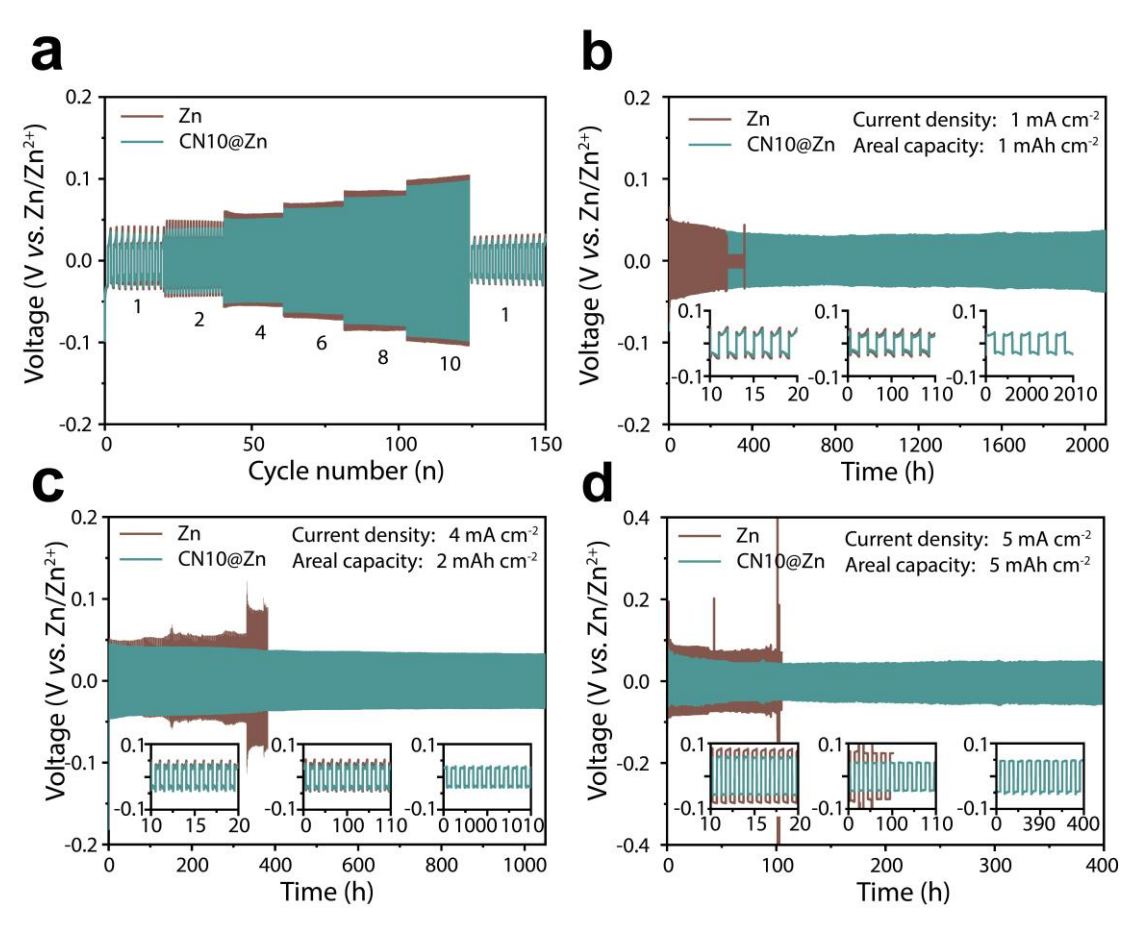


Figure 3.40 Electrochemical measurements: (a) Rate testing profiles of Zn symmetrical cells; Galvanostatic cycling of symmetrical Zn cells with CN10@Zn and Zn: (b) at 1 mA cm⁻² and 1 mAh cm⁻²; (c) at 4 mA cm⁻² and 2 mAh cm⁻²; (d) at 5 mA cm⁻² and 5 mAh cm⁻².

Zn symmetric cells were used to compare the reversibility of Zn deposition on both types of anodes. As shown in **Figure 3.40a**, the sputtering carbon layer exhibits a low voltage hysteresis

under various current densities, indicating that enriched N and O species on CN10@Zn regulate the Zn deposition process. The O and N species in CN10@Zn with low Zn²⁺ adsorption energy form dense nucleation sites. These densely distributed nucleation sites facilitate uniform Zn deposition during the deposition process. Furthermore, the water-related side reactions are regulated by CN10@Zn, contributing to the regulated charge transfer in the aqueous electrolyte without the disruption of hydrogen evolution side reactions. As a result, the overpotential required to drive the deposition process is decreased. The optimised zinc nucleation process further leads to a highly reversible zinc deposition process. As shown in Figure 3.40b, CN10@Zn significantly extends the lifespan of symmetric cells from 300 hours to 2,100 hours. Further investigation of the effectiveness of CN10@Zn was carried out by testing the symmetric cells in deep discharge under high current density. When increasing the current density to 4 mA cm⁻² and areal capacity to 2 mAh cm⁻², the plating/stripping process of CN10@Zn symmetric cell remains highly reversible, and the voltage signals are steady with a cycling life over 1,100 hours (Figure 3.40c). Even under a high current density of 5 mA cm⁻² and a high areal capacity of 5 mAh cm⁻², the symmetric cell also shows high stability and lasts for more than 400 hours (Figure 3.40d) with a stable voltage plateau. These results illustrate that the CN10@Zn layer significantly enhances the reversibility of zinc deposition, even under challenging conditions of high current density and deep discharge.

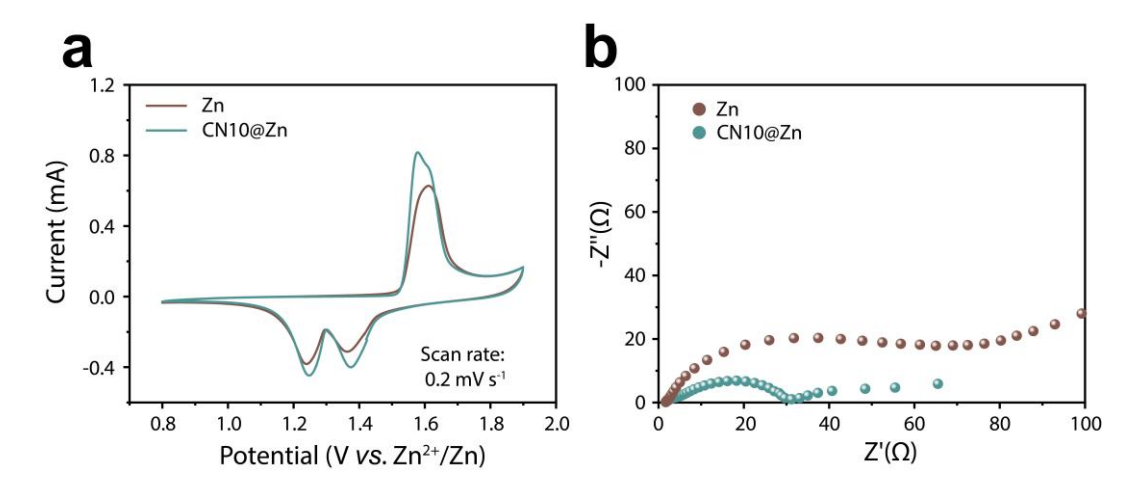


Figure 3.41 (a) CV curves of $Zn||Na_{0.65}Mn_2O_4$ under 0.2 mV s⁻¹; (b) EIS profiles of $Zn||Na_{0.65}Mn_2O_4$.

The highly reversible Zn deposition process and the regulation of water-related side reaction can contribute to the whole battery system, including the cathode material. A $Zn||Na_{0.65}Mn_2O_4$ system was introduced to assess the influence of the CN10@Zn sputtering layer on cathode key performance metrics such as capacity, rate capability, and cycling stability. In **Figure 3.41a**,

a negative shift in the charging process and a positive shift in the discharge process of CN10@Zn can be observed, indicating reduced polarisation. The pyrrole N species in CN10@Zn introduce new electronic states into the band structure of the anode material, altering the Fermi level position and density of states near it. Consequently, the energy required for electron transfer processes during redox reactions is reduced, leading to reduced polarisation and shifts in the redox peaks of the CV curves. Additionally, O species in CN10@Zn change the local electronic environment at the interface, providing additional active sites for zinc ion adsorption and desorption. This enhances ion accessibility, improves redox reaction kinetics, and results in lower polarisation.

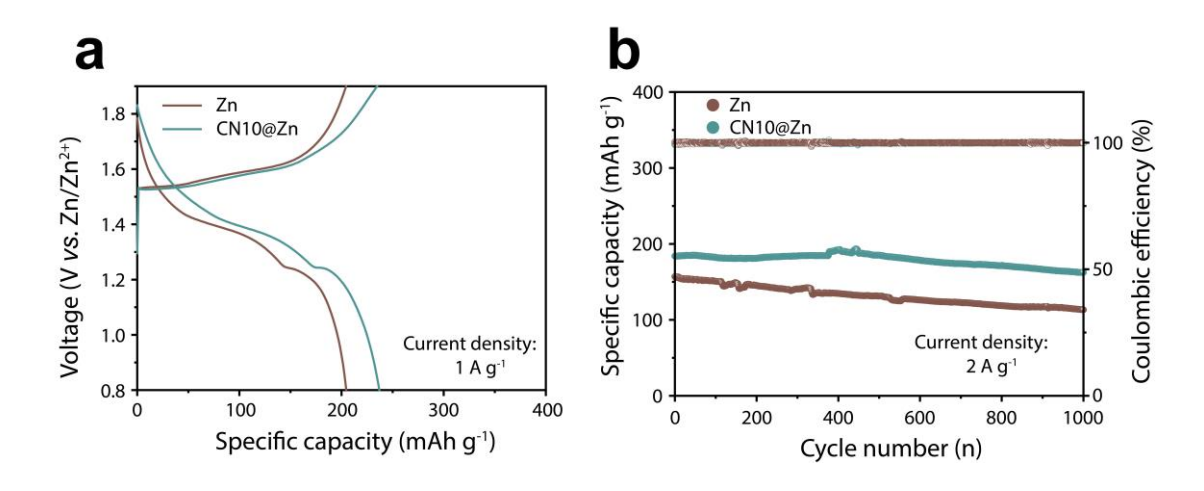


Figure 3.42 (a) Voltage-specific capacity curves at a current density of 1 A g⁻¹; (b) Long-term cycling performance.

The galvanostatic charge/discharge (GCD) profiles confirm the enhanced redox reaction kinetics of CN10@Zn in Zn||Na_{0.65}Mn₂O₄ cell. As shown in **Figure 3.42a**, CN10@Zn shows an enhanced storage capacity of 235 mAh g⁻¹ under 1 A g⁻¹ current density. The sputtered zinc anode exhibits a higher initial discharge capacity of 184 mAh g⁻¹ compared to 155 mAh g⁻¹ of that of bare Zn anode in the full cell configuration, indicating that CN10@Zn enhances the electrochemical activity of the anode by providing a favourable surface for charge transfer. Moreover, the bare Zn anode shows significant capacity fading, with a 28% capacity drop after cycling, associated with the lack of a protective layer leading to dendrite formation and accelerated corrosion. In contrast, the sputtered CN10@Zn anode demonstrates 89% capacity retention after 1,000 cycles, highlighting the effectiveness of CN10@Zn in enhancing electrochemical stability in AZIBs (**Figure 3.42b**).

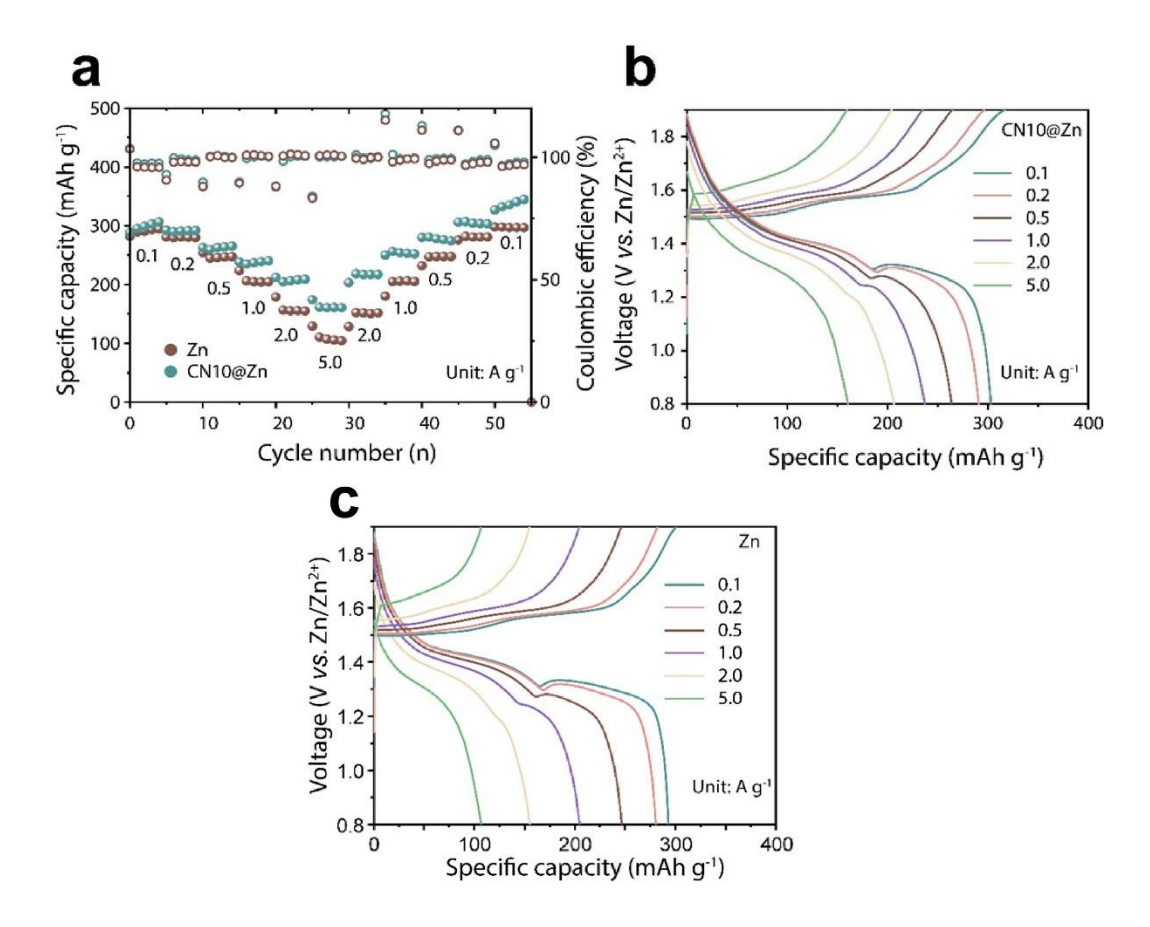


Figure 3.43 (a) Rate performance of $Zn||Na_{0.65}Mn_2O_4|$ batteries; Voltage-specific capacity profiles: (b) CN10@Zn; (c) Bare Zn.

The rate performance of CN10@Zn at various current densities (100 to 5,000 mAh g⁻¹) are illustrated in **Figure 3.43a**. As the current density increases stepwise, the corresponding specific capacity is retained at 303, 290, 262, 236, 206, and 160 mAh g⁻¹, outperforming the bare Zn anode's rate performance at 293, 280, 245, 204, 155, and 106 mAh g⁻¹, respectively. This rate performance is attributed to the synergistic effects of CN10@Zn on electron transport and interfacial properties, while the improved wettability ensures effective contact between the electrode and electrolyte, facilitating rapid ion transport and supporting high-rate performance. These results demonstrate the efficacy of the sputtering method in improving zinc-ion battery performance.

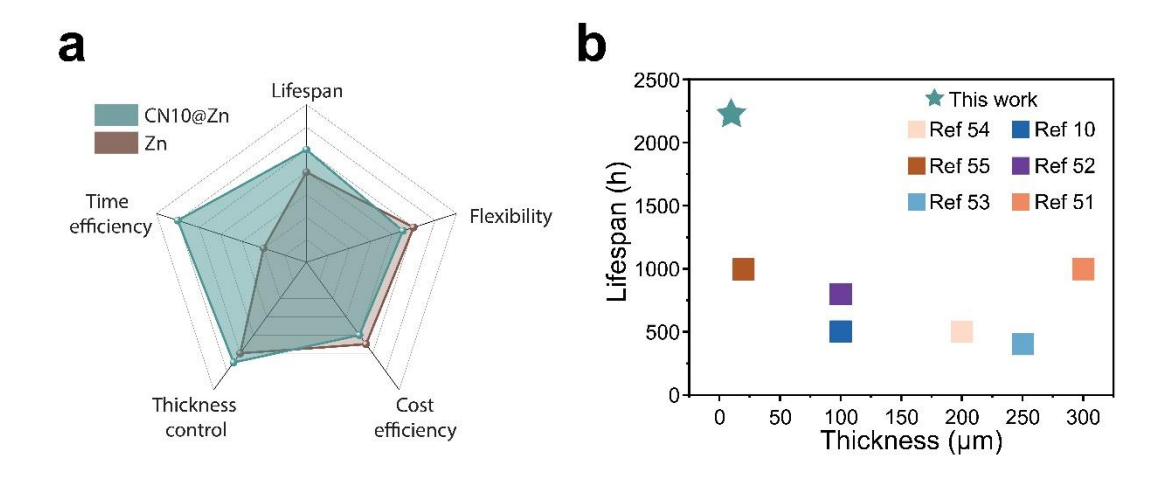


Figure 3.44 Performance comparison: (a) Key metrics comparison between CN10@Zn and bare Zn anodes; (b) Thickness-lifespan comparison of CN10@Zn with other studies.

3.3.7 Technical-economic assessment

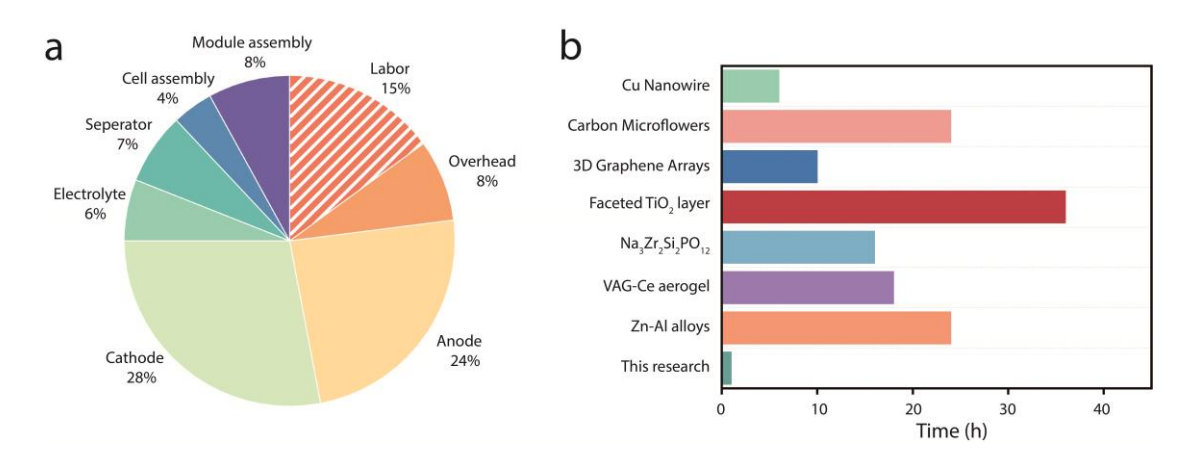


Figure 3.45 (a) Battery pack cost contribution for aqueous electrode processing;^[40] (b) Comparison of the processing time of different zinc anode modification methods.

As shown in **Figure 3.45a**, the labour cost accounts for 15% of the total battery cost during manufacturing. For a commercial battery pack with \$259.3 per kWh, labour cost during electrode processing and cell/pack construction costs around \$34 per kWh. [40,41] The thickness of most existing modification layers ranges from twenty to hundreds of micrometres, which is even higher than the consumed zinc foil. A Zn metal foil with a thickness less than 8.5 μm is enough to provide a capacity of 5 mAh cm⁻², sufficient to match most cathode capacities. [42,43] An advanced modification method for zinc anode is needed to fully leverage zinc metals' high volumetric capacity advantage. A labour cost saving of 25% is estimated for the anode coating processing time improvements from several hours to less than half an hour using the rapid sputtering method (**Figure 3.45b**). This will directly reduce the time and labour costs of

manufacturing zinc ion batteries. Additionally, the sputtering process could avoid using wet chemistry solvent and reactant, reducing total volatile organic compounds during electrode manufacturing and reducing the time and raw material cost on the electrode during the drying and formation process. These manufacturing advantages further highlight the benefits of the CN10@Zn sputtering layer, not only in terms of technology, but also concerning economic issues.

3.4 Conclusion

In conclusion, the rapid plasma sputtering method effectively creates an ultrathin, durable protective layer (CN10@Zn) on the Zn anode, significantly enhancing the performance of AZIBs. This approach reduces both the protection layer thickness to just 3 µm and the anode modification time to 10 seconds. The CN10@Zn layer inhibits dendrite growth and extends battery lifespan without compromising energy densities. Nitrogen dopants, particularly pyrrole N, serve as a driving force for zinc adsorption by creating surface dipoles and local variations in charge distribution. This facilitates zinc ion migration to the nitrogen dopant sites with reduced adsorption barriers. Additionally, the hydrophilicity of the sputtering layer is enhanced by hydroxyl oxygen dopants, forming strong adhesion to the zinc anode and improving ion accessibility, leading to dense nucleation sites for uniform zinc deposition. Benefiting from the controllable sputtering process and the optimised electric field distribution, the CN10@Zn anode exhibits highly reversible zinc plating/stripping behaviour, achieving a CE of 99.8% over 2,700 cycles in Cu||Zn half-cells. The dense deposition sites provided by the dopants ensure uniform zinc deposition in symmetric cells, extending the lifespan to 2,100 hours. The CN10@Zn anode remains stable under high current density (4 mA cm⁻²) for over 1,100 hours and maintains stability at a high areal capacity (5 mAh cm⁻²) for over 400 hours. In the CN10@Zn||Na_{0.65}Mn₂O₄ battery, the sputtering layer retained 89% capacity after 1,000 cycles with a CE of over 99%. In summary, these findings suggest that the rapid plasma sputtering method significantly enhances the performance of Zn anodes by simultaneously reducing the protection layer thickness and minimising anode modification time. This chapter provides a promising pathway for the development of future high-energy-density devices.

3.5 References

[1] Z. Shi, S. Chen, Z. Xu, Z. Liu, J. Guo, J. Yin, P. Xu, N. Zhang, W. Zhang, H. N. Alshareef, T. Liu, *Adv. Energy Mater.* **2023**, *13*, 2300331.

- [2] J. Yang, R. Zhao, Y. Wang, Z. Hu, Y. Wang, A. Zhang, C. Wu, Y. Bai, *Adv. Funct. Mater.* **2023**, *33*, 2213510.
- [3] M. Li, X. Wang, J. Hu, J. Zhu, C. Niu, H. Zhang, C. Li, B. Wu, C. Han, L. Mai, *Angew. Chem. Int. Ed.* **2023**, *135*, e202215552.
- [4] X. Chen, M. Li, Q. Li, Y. Chen, B. Wu, M. Lin, Q. An, L. Mai, *Energy Environ. Mater.* **2023**, e12480.
- [5] K. Zhao, C. Wang, Y. Yu, M. Yan, Q. Wei, P. He, Y. Dong, Z. Zhang, X. Wang, L. Mai, *Adv. Mater. Interfaces* **2018**, *5*, 1800848.
- [6] Z. Pan, X. Liu, J. Yang, X. Li, Z. Liu, X. J. Loh, J. Wang, *Adv. Energy Mater.* **2021**, *11*, 2100608.
- [7] Z. Shen, L. Luo, C. Li, J. Pu, J. Xie, L. Wang, Z. Huai, Z. Dai, Y. Yao, G. Hong, *Adv. Energy Mater.* **2021**, *11*, 2100214.
- [8] Q. Yang, Q. Li, Z. Liu, D. Wang, Y. Guo, X. Li, Y. Tang, H. Li, B. Dong, C. Zhi, *Adv. Mater.* **2020**, *32*, 2001854.
- [9] Z. Bie, Q. Yang, X. Cai, Z. Chen, Z. Jiao, J. Zhu, Z. Li, J. Liu, W. Song, C. Zhi, *Adv. Energy Mater.* **2022**, *12*, 2270186.
- [10] X. Xie, S. Liang, J. Gao, S. Guo, J. Guo, C. Wang, G. Xu, X. Wu, G. Chen, J. Zhou, *Energy Environ. Sci.* **2020**, *13*, 53.
- [11] B. Li, K. Yang, J. Ma, P. Shi, L. Chen, C. Chen, X. Hong, X. Cheng, M. C. Tang, Y. B. He, F. Kang, *Angew. Chem. Int. Ed.* **2022**, *61*, e202212587.
- [12] W. Du, E. H. Ang, Y. Yang, Y. Zhang, M. Ye, C. C. Li, *Energy Environ. Sci.* **2020**, *13*, 333.
- [13] Q. Zhang, J. Luan, X. Huang, Q. Wang, D. Sun, Y. Tang, X. Ji, H. Wang, *Nat. Commun.* **2020**, *11*, 3961.
- [14] C. Li, X. Xie, H. Liu, P. Wang, C. Deng, B. Lu, J. Zhou, S. Liang, *Natl. Sci. Rev.* **2022**, *9*, nwab177.
- [15] T. H. Wu, Y. Zhang, Z. D. Althouse, N. Liu, *Mater. Today Nano* **2019**, *6*, 100032.
- [16] J. Zhou, M. Xie, F. Wu, Y. Mei, Y. Hao, L. Li, R. Chen, Adv. Mater. 2022, 34, e2106897.
- [17] H. He, L. Zeng, D. Luo, J. He, X. Li, Z. Guo, C. Zhang, Adv. Mater. 2023, 35, e2211498.
- [18] P. Xue, C. Guo, L. Li, H. Li, D. Luo, L. Tan, Z. Chen, Adv. Mater. 2022, 34, e2110047.
- [19] R. Qin, Y. Wang, L. Yao, L. Yang, Q. Zhao, S. Ding, L. Liu, F. Pan, *Nano Energy* **2022**, *98*, 107333.

- [20] Q. Li, H. Wang, H. Yu, M. Fu, W. Liu, Q. Zhao, S. Huang, L. Zhou, W. Wei, X. Ji, Y. Chen, L. Chen, *Adv. Funct. Mater.* **2023**, 2303466.
- [21] S. Q. Li, L. Zhang, T. T. Liu, Y. W. Zhang, C. Guo, Y. Wang, F. H. Du, *Adv. Mater.* **2022**, *34*, e2201801.
- [22] H. Chen, Y. Yang, D. T. Boyle, Y. K. Jeong, R. Xu, L. S. de Vasconcelos, Z. Huang, H. Wang, H. Wang, W. Huang, H. Li, J. Wang, H. Gu, R. Matsumoto, K. Motohashi, Y. Nakayama, K. Zhao, Y. Cui, *Nat. Energy* **2021**, *6*, 790.
- [23] J. Zhou, Y. Mei, F. Wu, Y. Hao, W. Ma, L. Li, M. Xie, R. Chen, *Angew. Chem. Int. Ed.* **2023**, *62*, e202304454.
- [24] Q. Li, D. Wang, B. Yan, Y. Zhao, J. Fan, C. Zhi, *Angew. Chem. Int. Ed.* **2022**, *61*, e202202780.
- [25] X. Ge, W. Zhang, F. Song, B. Xie, J. Li, J. Wang, X. Wang, J. Zhao, G. Cui, *Adv. Funct. Mater.* **2022**, *32*, 2200429.
- [26] D. Chao, C. Zhu, M. Song, P. Liang, X. Zhang, N. H. Tiep, H. Zhao, J. Wang, R. Wang, H. Zhang, H. J. Fan, *Adv. Mater.* **2018**, *30*, e1803181.
- [27] X. Liu, Q. Lu, A. Yang, Y. Qian, Chin. Chem. Lett. 2023, 34, 107703.
- [28] C. Wang, Y. Gao, L. Sun, Y. Zhao, D. Yin, H. Wang, J. Cao, Y. Cheng, L. Wang, *Nano Res.* **2022**, *15*, 8076.
- [29] H. Dong, X. Hu, G. He, Nanoscale 2022, 14, 14544.
- [30] L. Dong, W. Yang, W. Yang, H. Tian, Y. Huang, X. Wang, C. Xu, C. Wang, F. Kang, G. Wang, *Chem. Eng. J.* **2020**, *384*, 123355.
- [31] H. Wang, R. Tan, Z. Yang, Y. Feng, X. Duan, J. Ma, Adv. Energy Mater. 2021, 11, 2000962.
- [32] X. Guo, Z. Zhang, J. Li, N. Luo, G.-L. Chai, T. S. Miller, F. Lai, P. Shearing, D. J. L. Brett, D. Han, Z. Weng, G. He, I. P. Parkin, *ACS Energy Lett.* **2021**, *6*, 395.
- [33] H. Qiu, X. Du, J. Zhao, Y. Wang, J. Ju, Z. Chen, Z. Hu, D. Yan, X. Zhou, G. Cui, *Nat. Commun* **2019**, *10*, 5374.
- [34] W. Zhang, Y. Dai, R. Chen, Z. Xu, J. Li, W. Zong, H. Li, Z. Li, Z. Zhang, J. Zhu, F. Guo, X. Gao, Z. Du, J. Chen, T. Wang, G. He, I. P. Parkin, *Angew. Chem. Int. Ed.* **2022**, *62*, e202212695.
- [35] J. B. Goodenough, ACS Catal. 2017, 7, 1132.
- [36] J. B. Goodenough, *Nat. Electron.* **2018**, *1*, 204.
- [37] J. B. Goodenough, Y. Kim, J. Power Sources 2011, 196, 6688.

- [38] K. Ellmer, J. Phys. D: Appl. Phys. 2000, 33, R17.
- [39] W. Li, P. Luo, M. Chen, X. Lin, L. Du, H. Song, Y. Lu, Z. Cui, *J. Mater. Chem. A* **2022**, *10*, 15161.
- [40] D. L. Wood, J. Li, C. Daniel, J. Power Sources 2015, 275, 234.
- [41] M. S. Ziegler, J. Song, J. E. Trancik, Energy Environ. Sci. 2021, 14, 6074.
- [42] S.-B. Wang, Q. Ran, R.-Q. Yao, H. Shi, Z. Wen, M. Zhao, X.-Y. Lang, Q. Jiang, *Nat. Commun.* **2020**, *11*, 1634.
- [43] R. Chen, C. Zhang, J. Li, Z. Du, F. Guo, W. Zhang, Y. Dai, W. Zong, X. Gao, J. Zhu, Y. Zhao, X. Wang, G. He, *Energy Environ. Sci.* **2023**, *16*, 254.

Chapter 4: Minute Amount of Fluorinated Surfactant Additives
Enable High Performance Zinc-Ion Batteries

4.1 Introduction

Driven by low carbon emission targets, research into sustainable energy harvesting devices is gaining increasing interest. The market size reached \$ 0.613 billion in 2020 and is projected to grow to \$1,129 billion by 2027. Low-cost and efficient energy storage technologies are essential for balancing electricity demand fluctuations.^[1] Rechargeable lithium-ion batteries, with their high energy density and long lifespan, dominate the secondary battery market. However, safety concerns with organic electrolytes and the rising cost of lithium components are driving research into alternatives like aqueous batteries for next-generation grid-scale storage.^[2-4]

AZIBs are particularly promising due to zinc's high theoretical capacities (5,855 mAh cm⁻³ and 820 mAh g⁻¹), suitable redox potential (-0.76 V vs. SHE), low cost, and abundance. These properties make AZIBs safe, cost-effective, and efficient for practical applications. Despite progress, AZIBs still face two major issues: a relatively low working potential window and solution-related side reactions.^[5] Enlarging the working window could enable more redox reactions from cathode materials and higher energy density. Additionally, since the reduction potential of Zn²⁺/Zn is more negative than that of the HER, water can be reduced to H₂ during zinc deposition, creating a corrosive environment. [6] This leads to inhomogeneous corrosion byproducts, reduced CE, zinc dendrite growth, separator penetration, and short-circuiting.^[7] Efforts to suppress side reactions and regulate dendrite growth have included several strategies. [8] Electrolyte additives like sodium dodecyl sulfate, [9] tetrabutylammonium sulfate, [10] arginine, [11] and lithium chloride [12] have been used to extend the lifespan of zinc anodes and increase battery stability. Surface/interface nanoscale modifications, such as building 3D interconnected ZnF₂ matrices, [13] controlling zinc lattice planes, [14] and coating zinc anodes with polymer glue, [15] have also been employed. Additionally, highly concentrated electrolytes, including Zn molten hydrates^[16] and trifluoromethanesulfonate, ^[17] have been explored. These approaches have shown promise in enhancing the performance of AZIBs, but they come with challenges. Volume changes during zinc plating and stripping can cause artificial layer failure due to cracking or inhomogeneous distribution. Moreover, the use of expensive salts and complex modification methods can undermine the low-cost advantage of AZIBs. [18]

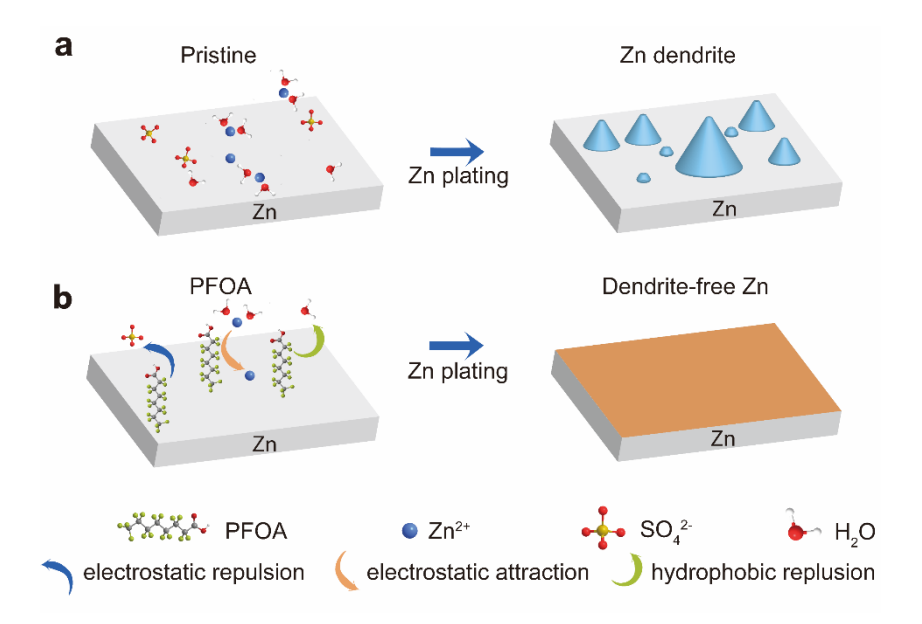


Figure 4.1 Schematic diagram of Zn²⁺ ions deposition process: (a) Pristine electrolyte; (b) PFOA elelctrolyte.

In this chapter, a cost-effective and efficient solution is presented: using a non-sacrificial fluorinated additive for the electrolyte, specifically perfluorooctanoic acid (PFOA). PFOA, with its strong electronegative perfluoroalkyl chains, forms an adsorption layer on the electrode surface. This layer facilitates Zn²⁺ migration near the interface and regulates anion sulfate transport to the zinc anode. The ultralow addition quantity of PFOA is sufficient to achieve significant improvements in AZIBs performance. The benefits of PFOA in the electrolyte are manifold. First, the working window of the electrolyte can be enlarged up to 2.1 V, thanks to the reduced free water molecules near the PFOA adsorption layer. This enlargement allows for more redox reactions from the cathode materials, leading to higher energy density. Second, the PFOA adsorption layer suppresses water-related side reactions, preventing the formation of H₂ and the associated corrosive environment. Third, the self-adjusting PFOA chains can tolerate volume changes during Zn plating and stripping, even at high current densities up to 10 A g⁻¹. This tolerance enhances the uniform deposition process and prevents the growth of zinc dendrites. The effectiveness of PFOA was illustrated using in-situ optical microscopy and confirmed by immersion experiments. The electrolyte with PFOA demonstrated enhanced anticorrosion properties and higher CE in Zn//Cu cells. The PFOA additive enabled long-term reversible deposition in zinc symmetric cells for over 2,200 hours and delivered a high-rate performance of 153 mAh g⁻¹ in Zn||Na_{0.65}Mn₂O₄ cells under a high current density of 5 A g⁻¹. In this chapter the use of PFOA as an electrolyte additive in AZIBs is shown to offer a simple, low-cost method to address the common issues of side reactions and low working potential

windows. By facilitating stable zinc plating/stripping and enlarging the electrolyte's working window, PFOA significantly enhances the performance and lifespan of AZIBs, making them more viable for grid-scale energy storage applications. This innovative approach represents a significant advancement in the development of sustainable energy storage technologies.

4.2 Experimental section

4.2.1 Chemicals

Zinc sulfate heptahydrate ($ZnSO_4\cdot 7H_2O$, ACS reagent, 99.0%), PFOA ($CF_3(CF_2)_6COOH$, 95%), hydrogen peroxide solution (H_2O_2 , 30% (w/w) in H_2O), Manganese sulfate monohydrate ($Mn_2SO_4\cdot H_2O$, ACS reagent, 98%), PVDF (average M_w ~534,000 by GPC, powder), NMP (ACS reagent, 99.0%) and polytetrafluoroethylene (PTFE, powder) were purchased from Sigma-Aldrich (UK) Co., Ltd. YP-50F active carbon was sourced from Kuraray Chemical Company, Japan. All materials were used as received without further purification.

4.2.2 Cathode preparation

The sodium pre-intercalated Na_{0.65}Mn₂O₄·1.31H₂O was synthesised using co-precipitation method. The cathode was fabricated by casting a mixed slurry consisting of the active material Na_{0.65}Mn₂O₄·1.31H₂O, PVDF, and Super P carbon in a weight ratio of 7:1:2 in NMP onto graphite paper. These electrodes were dried in a vacuum oven at 70°C for 12 hours. The average mass loading for the dried cathodes was 1.5–2.5 mg cm⁻².

4.2.3 Materials characterisation

XRD patterns were obtained using a Bruker X-ray D8 diffractometer (Cu-K α radiation). The morphology and chemical states of the as-prepared materials and zinc plates were evaluated using a scanning electron microscope (SEM; JEOL-JSM-6700F) and XPS (Thermo Scientific K-alpha photoelectron spectrometer), respectively. XPS data processing was performed using Casa XPS, calibrating adventitious carbon binding energy at 284.8 eV. Raman and FTIR data were obtained using a Raman spectrometer (Renishaw Raman microscope spectrometer with a laser wavelength of 514.5 nm) and attenuated total reflectance Fourier-transform infrared spectroscopy (ATR-FTIR, BRUKER, platinum-ATR). The mass of the active materials was accurately weighed using an Ohaus analytical balance (δ = 0.01 mg).

4.2.4 Electrochemical evaluation

CR2032 type coin cells with different aqueous electrolytes were assembled under ambient conditions. Battery performance tests were conducted using Neware battery testing systems to evaluate cycling stability. Additional electrochemical performance metrics, including CV and EIS, were measured using a Biologic VMP3 electrochemical workstation.

4.2.5 Details of molecular dynamics simulation

GROMACS 2019.31 was employed to investigate the hydration and movement characteristics of Zn²⁺ with or without PFOA in aqueous solution at 298.15 K. The electrostatic and Van der Waals interactions were treated using the Particle-Mesh-Ewald (PME) and cut-off methods, respectively. A cut-off distance of 1.6 nm was used for these interactions throughout energy minimisation, equilibration, and production. MD Simulations were carried out in a periodic cubic box (5.2 nm) containing 4,051 water molecules, 230 ZnSO₄, and 1 or 5 PFOA molecules.

Each simulation was equilibrated for 10 ns in the isobaric-isothermal (NPT) ensemble at 1 bar with the velocity-rescale thermostat and Berendsen coupling scheme. Then, a 50 ns simulation was performed in the NPT ensemble with a 1 fs time step. The velocity-rescale thermostat and Parrinello-Rahman barostat were used, with relaxation times of 0.1 ps for temperature and 1 ps for pressure. Trajectory data were collected every 5 ps for further analyses. ZnSO₄, solvents, and PFOA were represented with the AMBER force field, while the extended simple point charge (SPC/E) model was used for water. Molecular visualisation was performed using the Visual Molecular Dynamics (VMD) program.

-	Partial electric	Mass	Lennard-Jones parameters	
	charge sets		$\sigma(ext{\AA})$	$\varepsilon(\mathrm{KJ}{\cdot}\mathrm{mol}^{\text{-1}})$
Zn^{2+}	2.0000	65.4	1.95998	0.523
Ss	1.540804	32.06	3.56359	0.1046
Os	-0.885201	16.00	3.00001	0.71128
Ow	-0.8476	15.9994	3.15061	0.636386
Hw	0.4238	1.0080	0.0000	0.0000
Cf	0.414326	12.01	3.39967	0.359824
Ff	-0.18277	19.00	3.11815	0.255224
Of	-0.472	16.00	2.95992	0.87864
Oh	-0.565101	16.00	3.06647	0.880314
Hf	0.464	1.008	0.0000	0.0000

Table 2 Partial electric charge sets and Lennard-Jones parameters for the AMBER force field.

4.2.6 Estimation of the capacitive and diffusion-controlled contributions

To quantitatively evaluate the diffusion-controlled and capacitive contributions to current, CV curves at different sweep rates were measured. The measured peak current (i) and sweep rate (v) in CV scans generally follow a power-law relationship^[6, 19]:

$$i = av^b$$
$$log(i) = log(a) + b \times log(v)$$

where a and b are adjustable parameters. The b value can be determined by fitting the slope of the log(i) versus log(v) plot. A b value of 1.0 indicates capacitive-dominated charge storage behaviour, while a b value of 0.5 indicates ionic diffusion-controlled behaviour. For a quantitative analysis of diffusion-controlled and capacitive contributions in the current response, the integration of semi-infinite diffusion and capacitive-like processes is assumed, described by the following equation:

$$i = k_1 v + k_2 v^{1/2}$$

The diffusion-controlled and capacitive contributions can be estimated by determining k_1 and k_2 .

4.2.7 Estimation of Zn²⁺ transference number

The Zn²⁺ transference number was evaluated in symmetrical Zn battery using EIS before and after the CA test, and calculated by the following equation:

$$T = \frac{I_S(\Delta V - I_0 R_0)}{I_0(\Delta V - I_S R_S)}$$

Where ΔV is the voltage polarisation applied and the applied voltage polarisation is 5 mV, I_s and R_s are the steady state current and resistance, respectively, and I_0 and R_0 are the initial current and resistance, respectively.

4.3 Results and discussion

4.3.1 Electrolyte characterisation

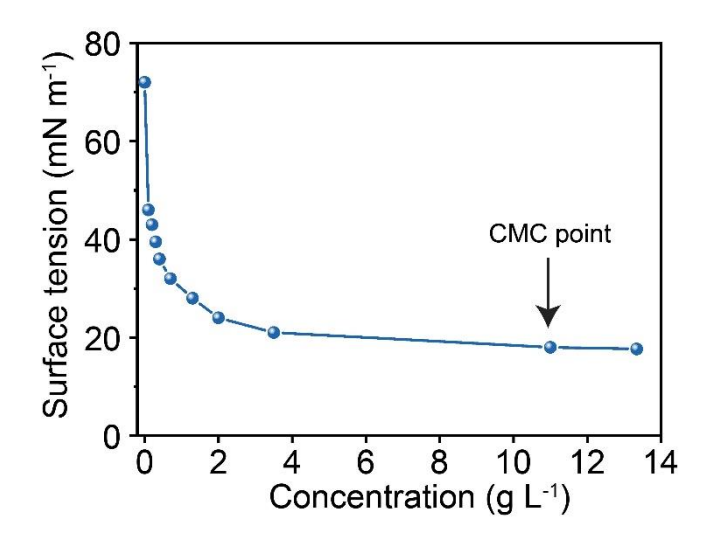


Figure 4.2 Surface tension curve of the PFOA electrolytes.

Depending on their hydrophobic tail, surfactants can be categorised into fluorinated surfactants (e.g., PFOA, perfluorooctanesulfonic acid (PFOS)) and non-fluorinated surfactants (e.g., SDS, tetrabutylammonium sulfate (TBA)). Fluorinated surfactants, particularly perfluorinated surfactants, are more effective due to the strong electronegative C-F bonds in their hydrophobic tails. These bonds contribute to a lower required amount of additive and the efficient spreading of surfactant molecules in the electrolyte and at interfaces, even at low concentrations. The increasing length of the hydrophobic perfluoro tail enhances the effectiveness of fluorinated surfactants. However, the solubility of fluorinated surfactants in AZIBs electrolytes also need to be considered when screening the appropriate tail length for perfluorinated surfactant

candidates. C8 fluorinated surfactants (eight-carbon fluorinated compounds) outperform C4 and C6 fluorinated surfactants owing to their balance of solubility and effectiveness in practical (e.g., non-stick cookware and waterproof fabrics), so the perfluorooctyl group was chosen as the hydrophobic tail for the target molecule. Considering the fact that AZIBs electrolytes are generally mildly acidic, PFOA with carboxylic acid group was chosen as the electrolyte additive used in this work. In addition, due to the absence of strong electrostatic or hydrogen bonding, the intermolecular forces between PFOA and water molecules are significantly weaker than those between water molecules. Consequently, even a minute amount of PFOA additive can reduce the electrolyte's surface tension from 72 mN m⁻¹ to around 20 mN m⁻¹. It is worth note that even a minute amount of PFOA (0.25 mM) is capable of reducing the surface tension to 30 mN m⁻¹. This substantial reduction in surface tension leads to enhanced wettability on both the zinc anode and cathode parts, ensuring that the electrolyte can spread more uniformly and access the entire surface area more effectively.

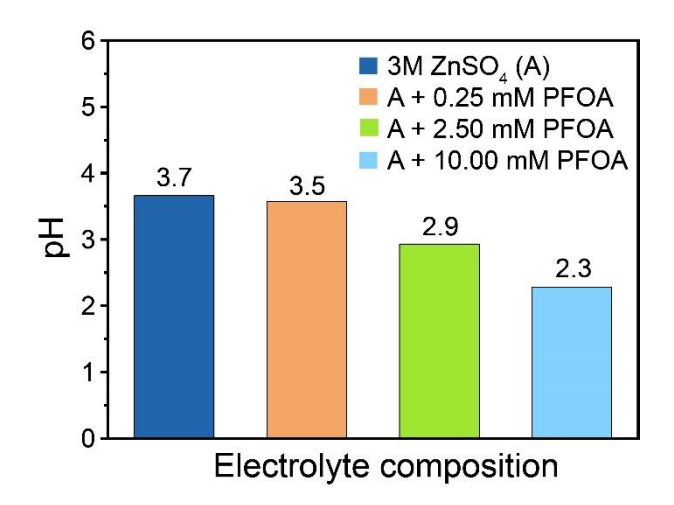


Figure 4.3 pH values of 3 M ZnSO₄ electrolytes with varying PFOA addition amounts.

The pH value of the electrolyte has a significant effect on water-related side reactions and the dissolution of cathode materials. As an acidic additive, PFOA influence the pH value of the pristine electrolyte (3 M ZnSO₄) electrolyte. As shown in **Figure 4.3**, PFOA can reduce the electrolyte pH value from 3.7 to 2.3 depending on the additive concentration. A concentration of 0.25 mM PFOA added to the pristine electrolyte balances the electrolyte surface tension (30 mN m⁻¹, **Figure 4.2**) and pH value (3.5, **Figure 4.3**). This concentration was selected for experiments in Chapter 4, referred to as PFOA electrolyte in discussions, and labelled as PFOA in the figures. The PFOA electrolyte additive provides significant advantages due to its low usage requirements and cost-effectiveness.

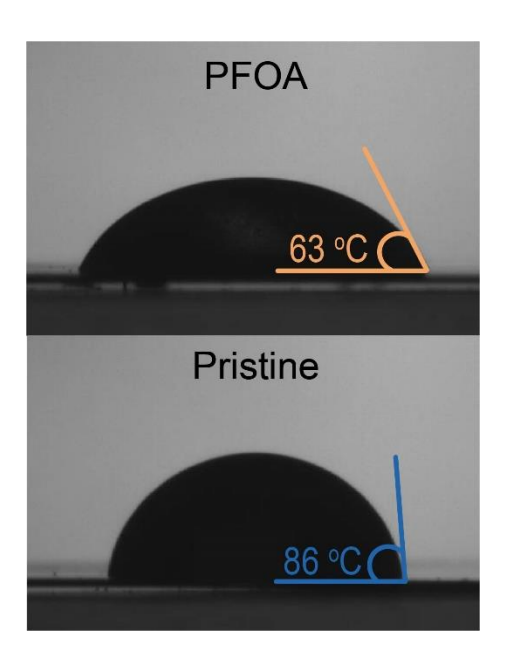


Figure 4.4 Contact angles measurements on Zn anodes with different electrolytes.

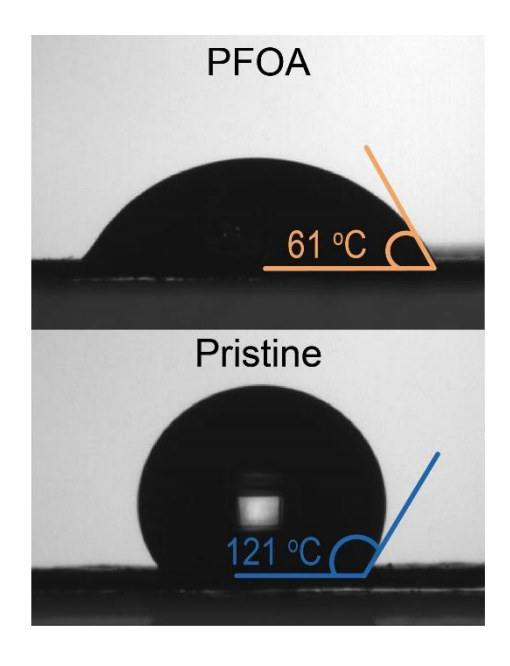


Figure 4.5 Contact angles measurements on Na_{0.65}Mn₂O₄ with different electrolytes.

Different from the SEI/CEI method, which normally focus on a single electrode, PFOA electrolyte can improve wettability on both electrodes due to its surfactant properties. Contact angle measurements were performed to characterise the wettability on both the zinc anode and the Na_{0.65}Mn₂O₄ cathode. As shown in **Figure 4.5**, compared to the relatively hydrophobic nature of the pristine 3 M ZnSO₄ electrolytes on the Zn anode (83°), the lower contact angle PFOA electrolyte have an obviously lower contact angle (63°). This indicates that the PFOA additive greatly enhances the electrolyte's wettability on the zinc anode. This enhancement allows Zn²⁺ ions in the electrolyte with PFOA to more uniformly reach the entire zinc anode

surface, which minimising the concentration difference that led to the dendrite formation. Additionally, the improved wettability of the electrolytes with PFOA additive on the cathode material was investigated (**Figure 4.5**). The PFOA electrolyte shows a significantly lower contact angle compared to the pristine electrolyte on Na_{0.65}Mn₂O₄, which facilitates more efficient ion access to the cathode material. These results confirm that one of the benefits of PFOA additives is that they can effectively enhance wettability on both the anode and cathode due to their surfactant properties.

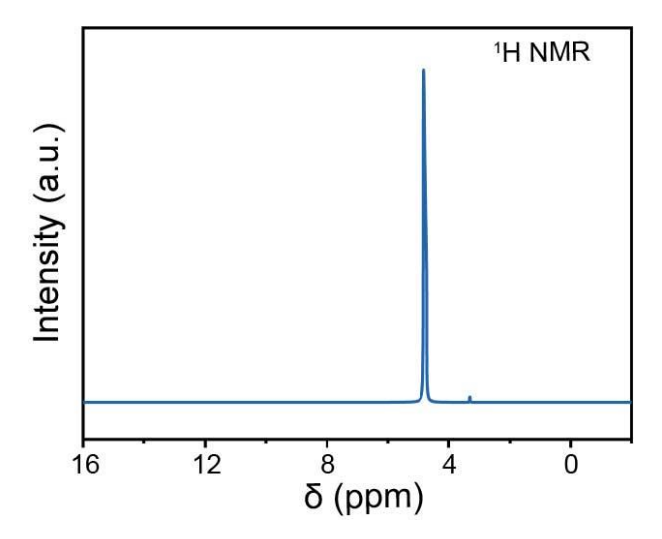


Figure 4.6 ¹H NMR spectrum of the PFOA electrolyte.

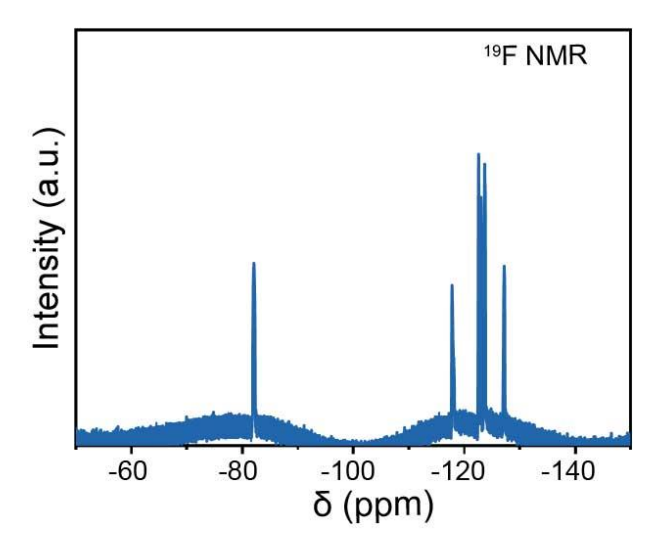


Figure 4.7 ¹⁹F NMR spectrum of the PFOA electrolyte.

The chemical environment of fluorine species in the PFOA electrolyte was investigated by ¹⁹F NMR. As shown in **Figure 4.7**, the peak around 82 ppm corresponds to the fluorine atoms in the terminal trifluoromethyl CF₃ group in the PFOA molecule. The CF₂ group are found to

resonate in the range from 119 ppm to 127 ppm, with the peak at 127 ppm corresponds to the CF₂ group adjacent to the CF₃ group.

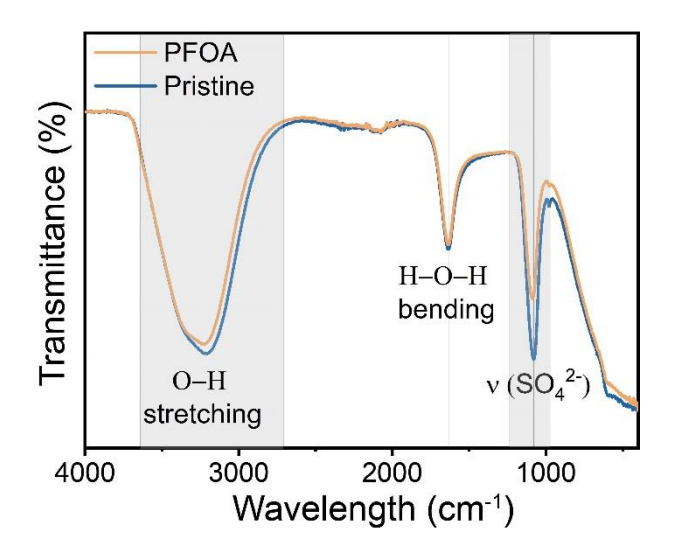


Figure 4.8 ATR-FTIR spectra of different electrolytes.

FTIR spectra were performed to examine the environmental changes in the electrolyte after the addition of PFOA (**Figure 4.8**). The intensity of the SO_4^{2-} broad band peak at 1,085 cm⁻¹ decreases after PFOA was added, illustrating that PFOA interacts with sulfate anions and limits their migration in the electrolyte. This interaction also facilitates the rapid migration of Zn^{2+} ions in the electrolyte.

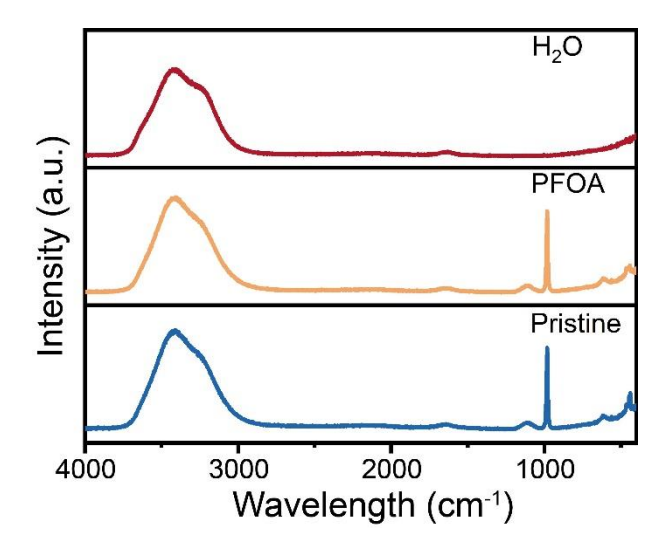


Figure 4.9 Raman spectra of different electrolytes.

4.3.2 Anode characterisation

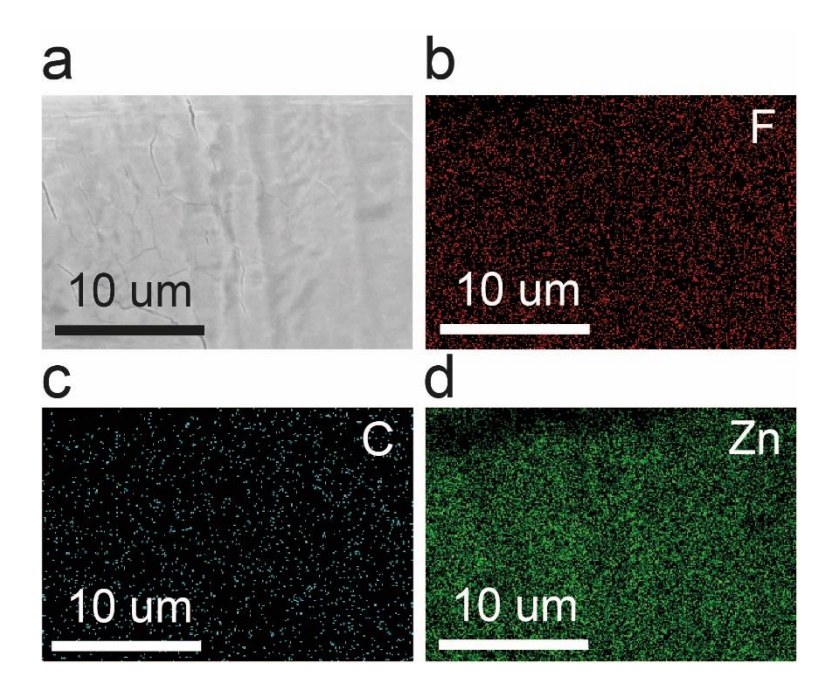


Figure 4.10 Microscopy characterisation of zinc anodes after immersion experiment in the PFOA electrolyte: (a) SEM; EDS mapping images: (b) F; (c) C; (d) Zn.

The EDS mapping results (**Figure 4.10**) show an even distribution of C and F signals, confirming uniform coverage of PFOA molecule coverage on the zinc anode surface. The PFOA surfactant's adsorption property can be further applied to complex surface architectures, such as 3D electrodes.

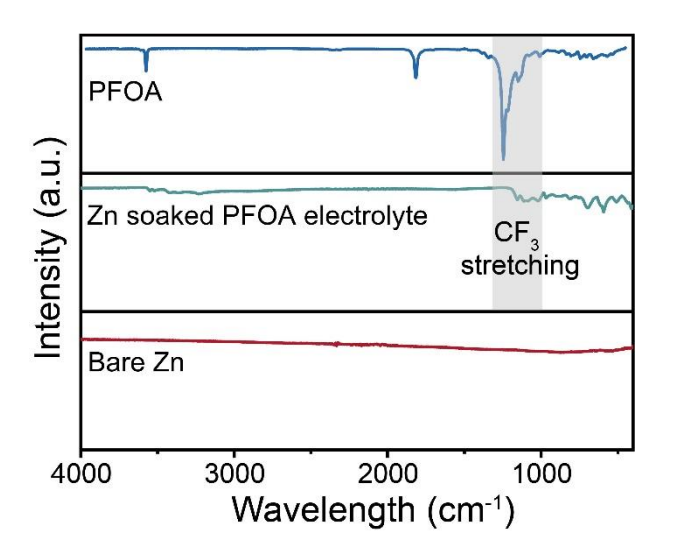


Figure 4.11 FTIR spectra of zinc anodes soaked in the PFOA electrolyte.

FTIR measurements were performed to further understand the surface chemical environment of the PFOA adsorption layer. As shown in **Figure 4.11**, after immersion in PFOA electrolyte,

the zinc anode displays C-F stretching in the range from 1,000 to 1,400 cm⁻¹ in the FTIR spectrum, attributed to the adsorption of the PFOA fluorocarbon tail.

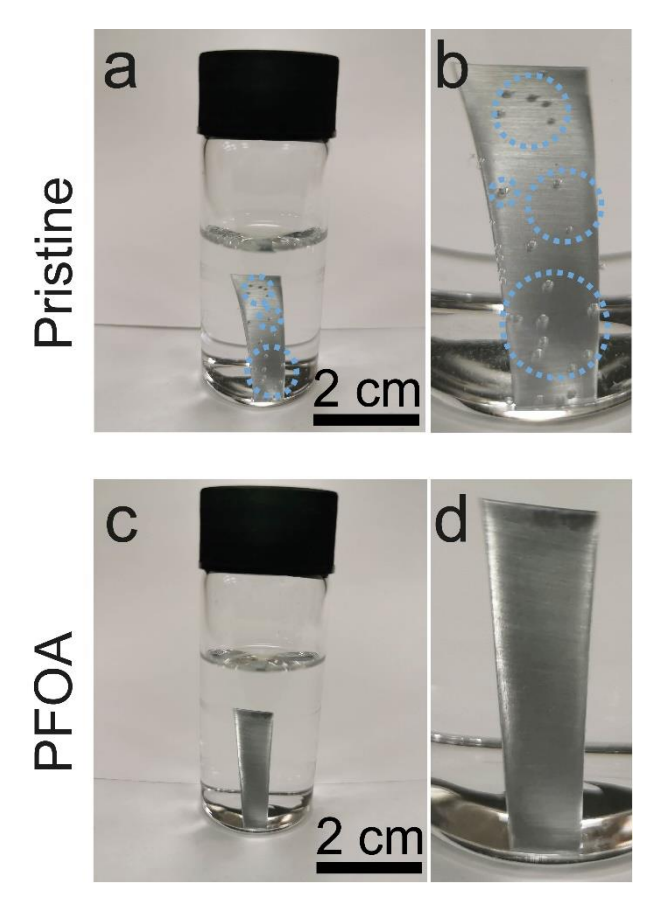


Figure 4.12 Digital images of zinc anodes after immersion experiment: (a,b) in the pristine electrolyte and (c, d) in the PFOA electrolyte.

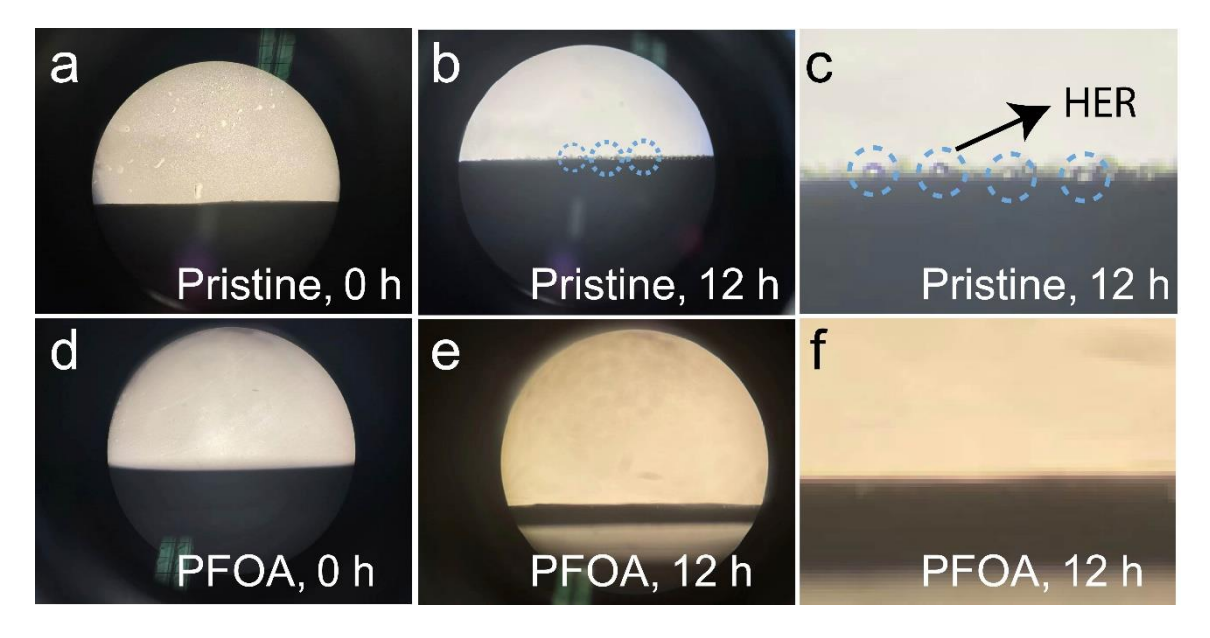


Figure 4.13 Optical microscopy observations of zinc anodes immersed in the pristine electrolyte (a-c) and the PFOA electrolyte (d-f).

PFOA surfactant tends to adsorb onto the electrode, which forms a self-adjusting adsorption layer with hydrophobic carbon-fluorine chain that can regulate the water-related side reactions at the electrode/electrolyte interface. To directly illustrate the anti-corrosion effect of the PFOA electrolyte, zinc anode immersion experiments were conducted (**Figure 4.12** and **Figure 4.13**). Obvious hydrogen bubbles were observed after immersing the zinc anode in pristine electrolyte for 12 hours, indicating that the mildly acidic environment of 3 M ZnSO₄ corrodes the zinc anode through side reactions such as HER. In contrast, no hydrogen bubbles were spotted on the zinc anode in the PFOA electrolyte, indicating that H₂O penetration was suppressed by the PFOA adsorption layer with its carbon-fluorine chain.

4.3.3 Ex-situ characterisation

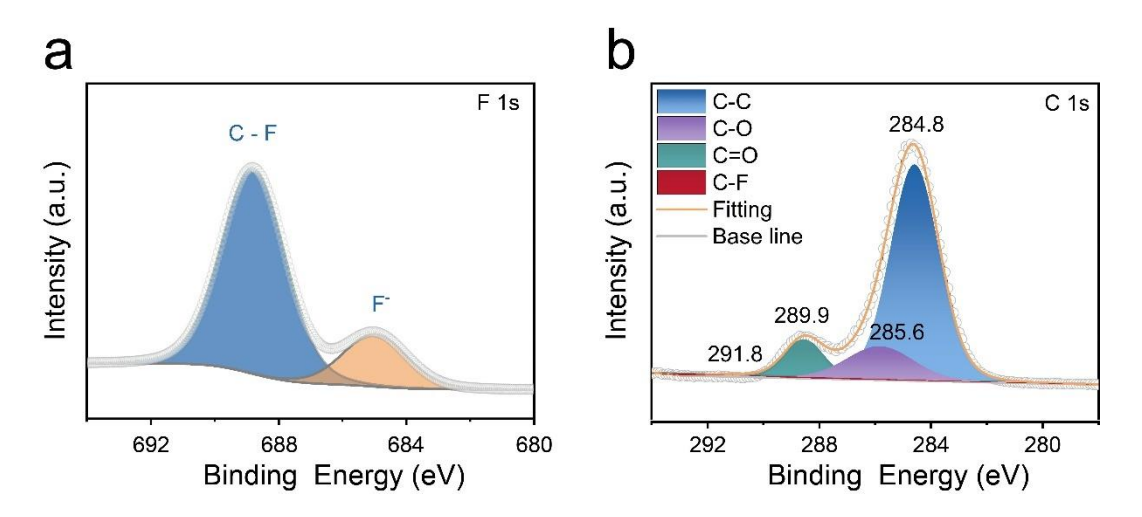


Figure 4.14 XPS analysis of the anodes cycled in PFOA electrolytes: (a) F 1s; (b) C 1s.

XPS was used to verify the adsorption behaviour of PFOA on the zinc anode surface. The F 1s XPS spectrum presented in **Figure 4.14** shows the presence of -CF₂ (688.9 eV). It is noted that there is no additional peak corresponding to ZnF₂, indicating that the PFOA surfactant follows a non-sacrificial mechanism and the composition of the PFOA adsorption layer remains stable on the zinc surface throughout cycling.

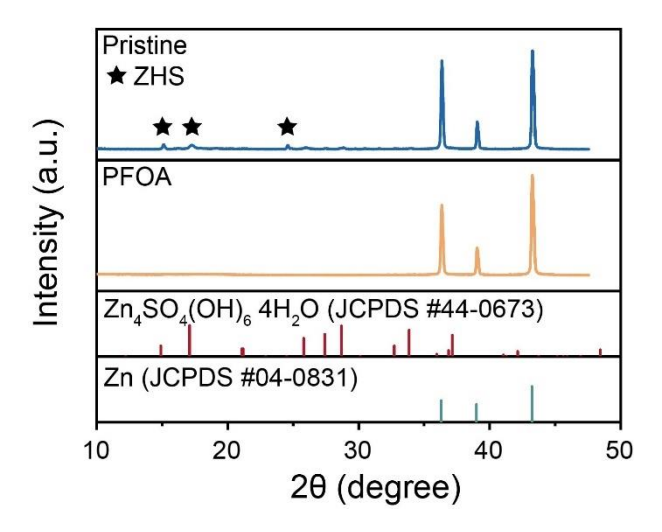


Figure 4.15 Ex-situ XRD profiles of the anodes after cycling for 50 cycles at 1 mA cm⁻².

The highly reversible Zn plating and stripping voltage plateau is due to the reduced water-related side reactions on the Zn anode. To verify this hypothesis, *ex-situ* XRD analyses were performed on the disassembled Zn anodes from symmetric cells cycled in both electrolytes. The XRD results in the pristine electrolyte (**Figure 4.15**) show peaks at 14.9°, 17.1°, and 25.8°,

corresponding to the aggregation of hydrated zinc hydroxide sulfate Zn₄SO₄(OH)₆·4H₂O on the zinc anode (PDF #44-0673). This indicates that water-related side reactions in the pristine electrolyte remain unregulated. In contrast, the Zn anode in the PFOA electrolyte shows a clear XRD pattern of Zn without obvious byproduct peaks, demonstrating that zinc deposition in the PFOA electrolyte is highly reversible and the side reactions are suppressed due to the adsorption layer on the Zn anode.

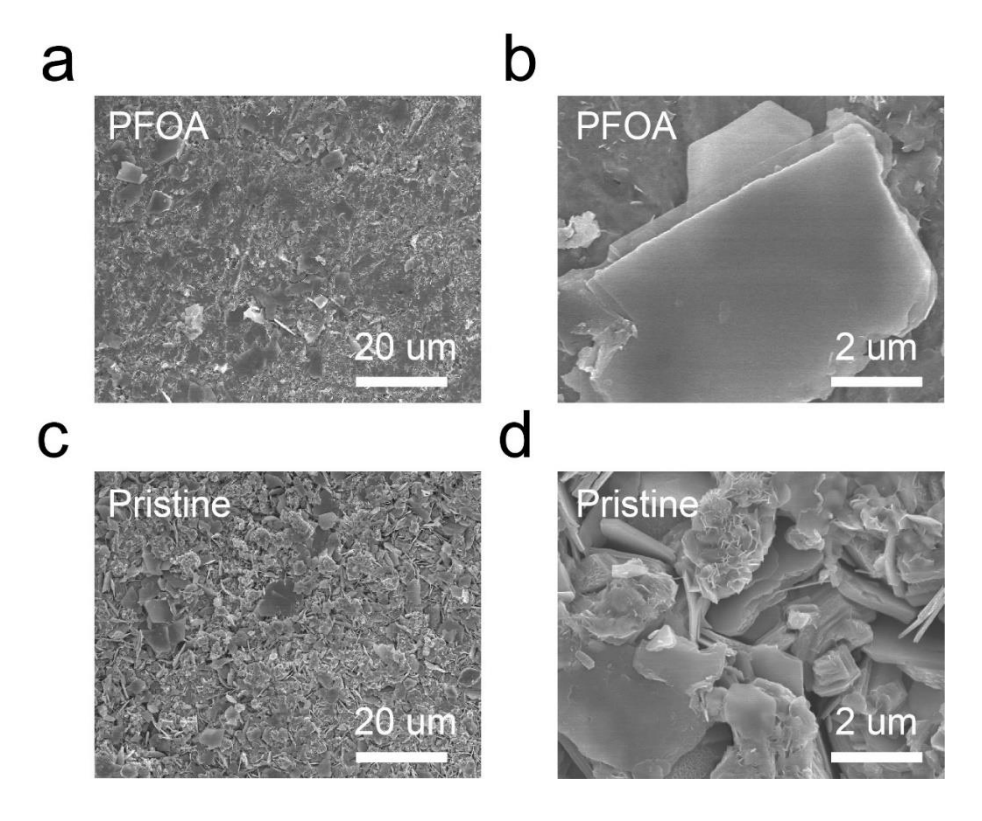


Figure 4.16 *Ex-situ* SEM profiles of the anodes after cycling: (a,b) in PFOA electrolyte; (c,d) in pristine electrolyte.

To directly illustrate the effects of PFOA additive on the zinc deposition process, SEM characterisation was performed to show the morphological evolution of the zinc anodes after cycling in different electrolytes. **Figure 4.16** shows that the anode is covered by 'flower-like' aggregates in the pristine electrolyte, indicating that zinc undergoes corrosion due to water-related side reactions, which is consistent with the *ex-situ* XRD results. In contrast, the Zn anode retains a smooth, dendrite-free surface after cycling in the PFOA electrolyte, confirming that the PFOA electrolyte can inhibit side product formation and promotes uniform Zn deposition. This contributes to the long-term stability of AZIBs.

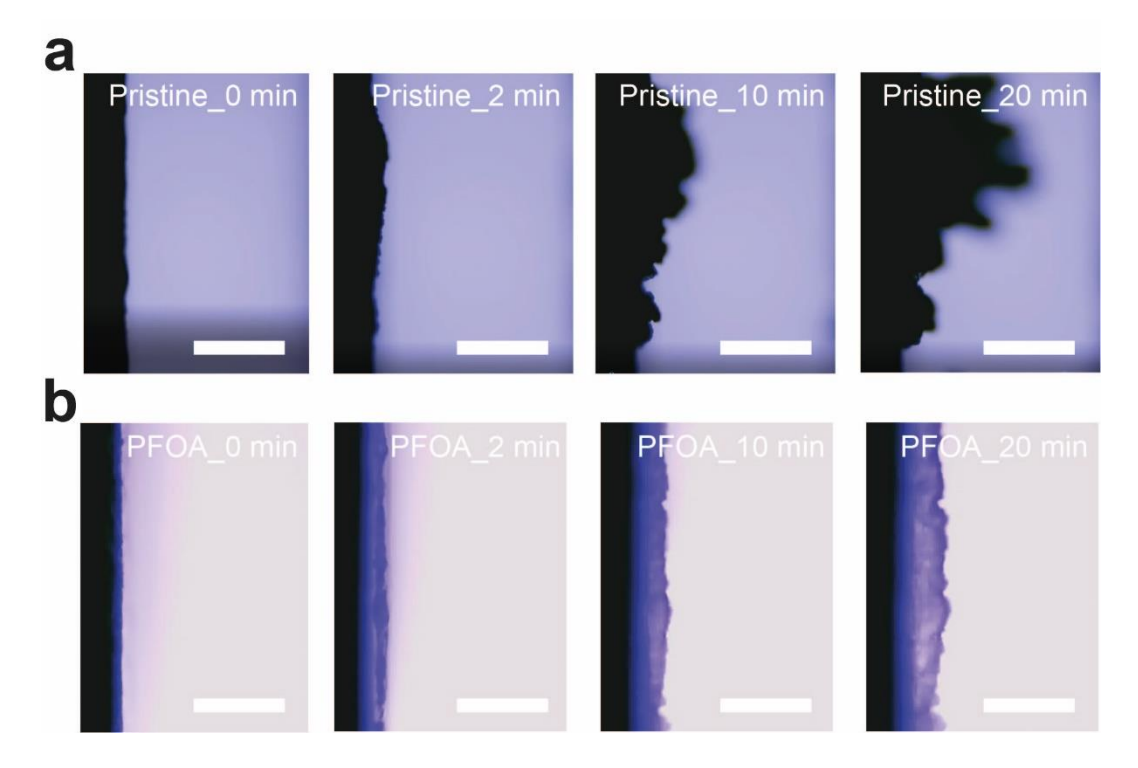


Figure 4.17 *In-situ* optical microscopy of the zinc symmetric cells cycled in different electrolytes: (a) Pristine electrolyte; (b) PFOA electrolyte. Scale bar: 50 μm.

To directly monitor the zinc deposition process in different electrolytes, *in-situ* optical microscopy observations (**Figure 4.17**) were conducted in zinc symmetric cells under a current density of 5 mA cm⁻². In the pristine electrolyte, zinc dendrites began forming on the zinc anode within two minutes. With increasing deposition time, the zinc exhibited a highly dendritic and mossy morphology, which can further penetrate the separator, potentially leading to battery collapse. In contrast, a homogeneous zinc deposition process was achieved in the PFOA electrolyte, confirming the effective regulation of the zinc deposition process by the PFOA adsorption layer. This observation is consistent with the results of the corrosion experiments.

4.4.4 Electrochemical characterisation

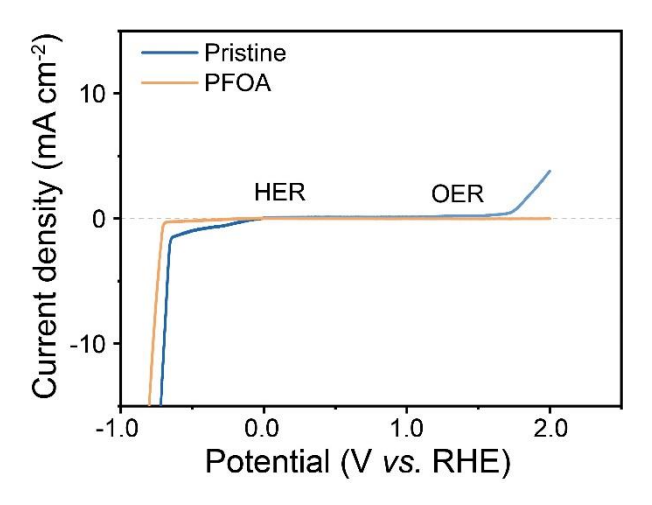


Figure 4.18 LSV scans of different electrolytes.

The electrochemical stability window of the electrolytes was investigated using linear sweep voltammetry (LSV). The addition of PFOA surfactant to the electrolyte can affect the electrolyte's working window due to the electron-withdrawing polyfluoroalkyl groups, which reduce electron density in molecules *via* carbon-fluorine bonds. As a result, the water-related side reactions, such as HER and OER, were suppressed by the PFOA adsorption layer. As shown in **Figure 4.18**, anodic and cathodic scans were performed with Ti electrodes. In the polarisation curves during the cathodic scans at a scan rate of 10 mV s⁻¹, the onset potential of the HER was suppressed in the electrolyte with PFOA additive (-0.69 V *vs.* RHE), which is more positive than in the pristine electrolyte (-0.64 V *vs.* RHE). For the OER, the onset potential shifted from 1.7 V to 2.1 V. These results are in line with the immersion experiment results, demonstrating that the PFOA adsorption layer effectively regulates water-related side reactions in AZIBs, both on the anode and the cathode, thereby benefiting anode anti-corrosion and cathode stability.

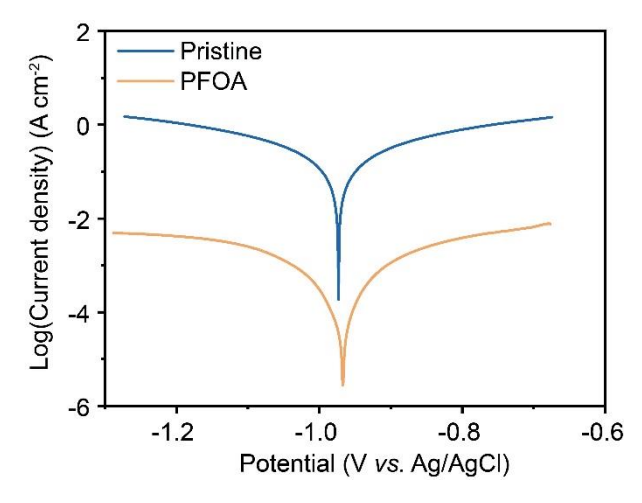


Figure 4.19 Linear polarisation curves of Zn foils in different electrolytes.

Corrosion resistance is a crucial parameter for evaluating interface stability between the electrode and electrolyte. As shown in **Figure 4.19**, the corrosion current in the PFOA electrolyte is lower than that of pristine electrolyte, indicating reduced corrosion reactions, including HER and OER, have occurred in the presence of PFOA adsorption layer. Additionally, corrosion occurs at a more positive potential with the PFOA additive, demonstrating that the PFOA adsorption layer serves as a protection layer for the zinc anode.

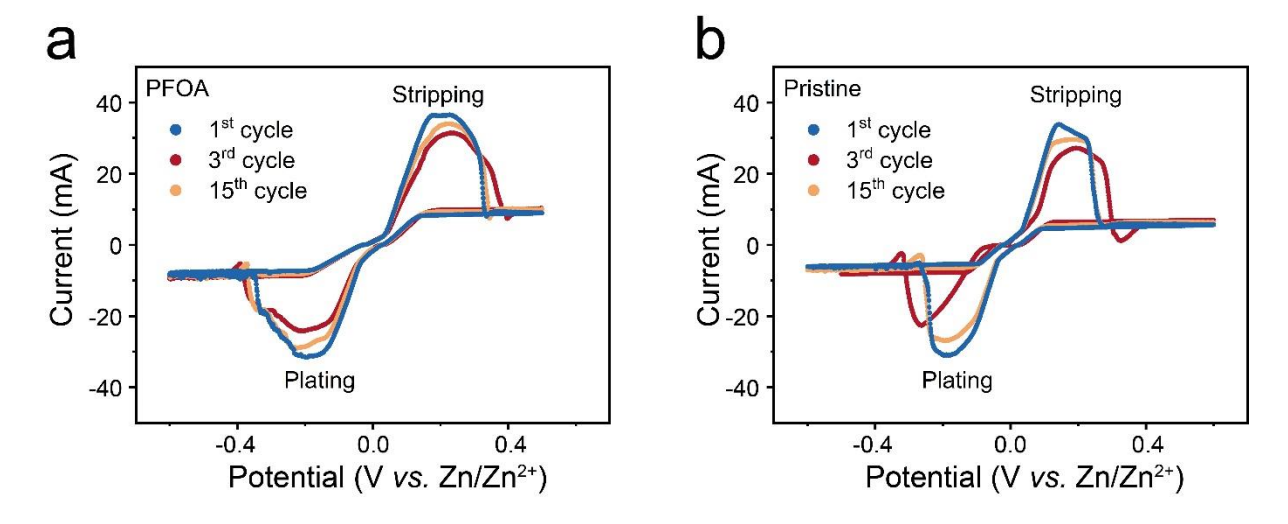


Figure 4.20 CV curves of Zn symmetric cells in different electrolytes under 1 mV $\rm s^{\text{--}1}$ scan rate.

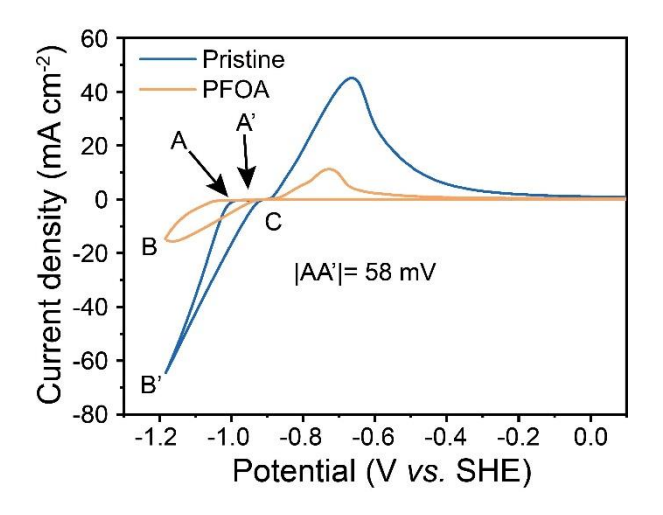


Figure 4.21 Zn plating and stripping CV curves in Zn||Ti cells.

To further investigate the initial nucleation behaviour at the electrode/electrolyte in different electrolytes, CV measurements were performed in a two-electrode configuration. Ti foil was used as the working electrode, when Zn foil serving as both the counter and reference electrodes. As the potential sweep moved towards the positive side, a crossover characteristic associated with nucleation processes was observed (**Figure 4.21**). Point A represents the potential at which Zn^{2+} ion plating begins, and point B represents the crossover potential. The gap between the plating point (A) and crossover point (B) indicates the nucleation overpotential (NOP). The difference in NOP illustrates the extent of zinc plating polarisation and the effect of the additive in the electrolyte. According to previous research, the relationship between the critical Zn nucleus radius (r_{crit}) and NOP follows the equation below:

$$r_{crit} = 2\frac{\gamma V_m}{F|\eta|}$$

Where γ is the surface energy of the Zn-electrolyte interface, V_m is the molar volume of Zn, F is Faraday's constant, and η is the NOP. It is known that Zn deposition proceeds more orderly with a higher NOP value. Compared to the pristine electrolyte, the electrolyte with PFOA additive increases the NOP value by 58 mV, the increased NOP value indicates that Zn nuclei formation in the PFOA electrolyte is more denser and finer, while the nuclei in the pristine electrolyte follows the 'tip effect' to aggregate into larger nuclei for initial dendrite. This result shows that the PFOA electrolyte guides a uniform Zn²⁺ nucleation process.

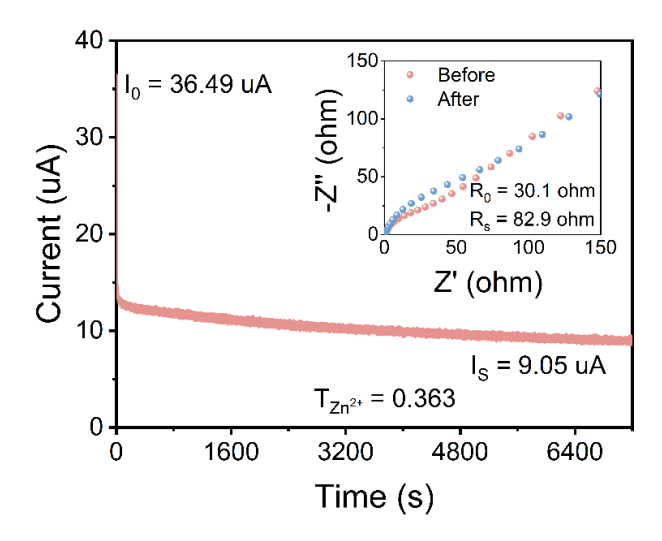


Figure 4.22 Ion-transport properties of pristine electrolyte (3 M ZnSO₄).

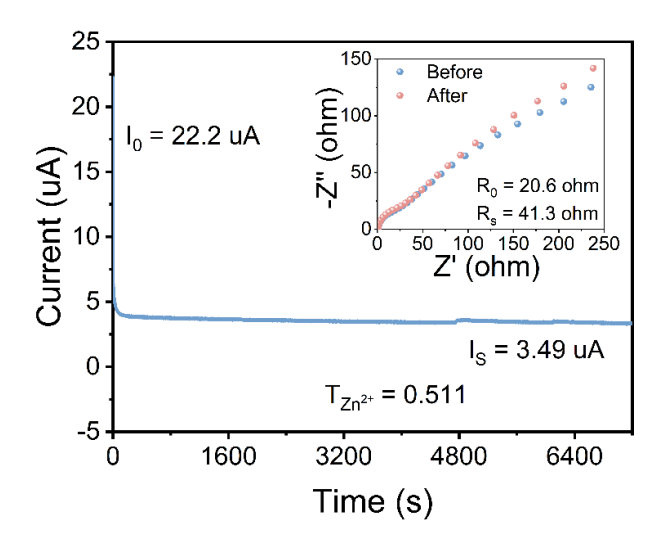


Figure 4.23 Ion transport properties of PFOA electrolyte (3 M ZnSO₄ 0.25 mM PFOA).

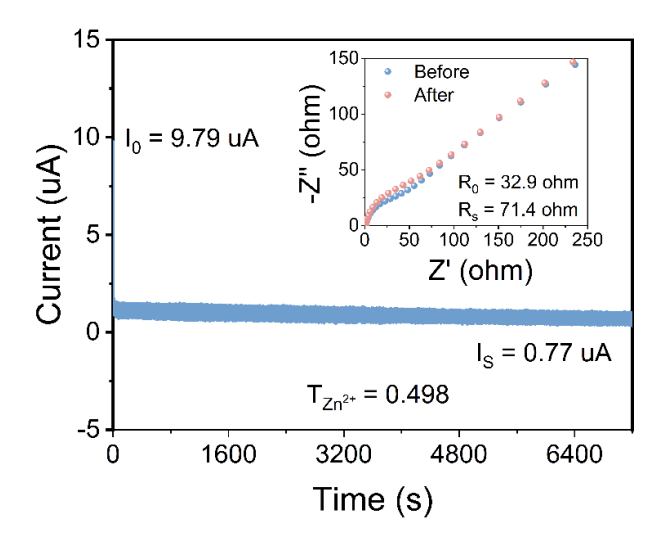


Figure 4.24 Ion-transport properties of electrolyte with PFOA additive (3 M ZnSO₄ 10 mM PFOA).

The nucleation process can also be monitored from the current response during CA testing in different electrolytes. As shown in **Figure 4.22**, in the pristine electrolyte, the current response continuously decreases during cycling, indicating a combination of 2D and 3D Zn²⁺ diffusion and deposition in the pristine electrolyte, which further leads to the dendrite formation. In contrast, the current response in the PFOA electrolyte stabilises within 50 seconds and remains steady throughout the testing (**Figure 4.23**). This illustrates that the PFOA adsorption layer could quickly form during the zinc deposition process, guiding the Zn²⁺ ions to deposit uniformly on the zinc anode.

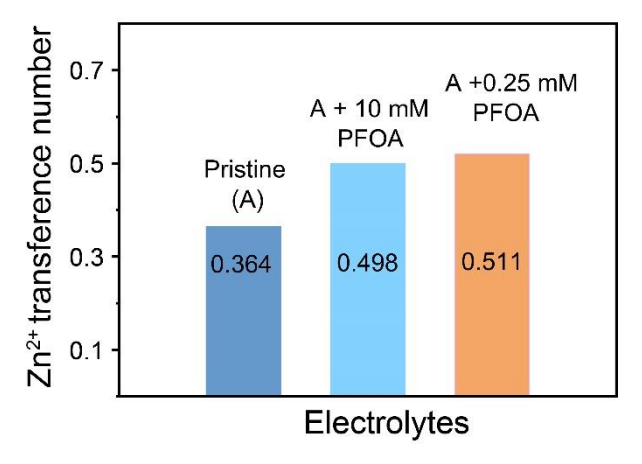


Figure 4.25 Zn²⁺ transference number in different electrolytes.

Difference in zinc ion diffusion and migration across electrolytes were further studied by analysing the Zn²⁺ transference number. As shown in **Figure 4.25**. The PFOA electrolyte exhibited a higher zinc transference number of 0.511 compared to 0.364 for the pristine electrolyte. These results, combined with the FTIR measurement and corrosion resistance results, illustrate that the PFOA additive can regulates the Zn²⁺ ions transfer and deposition in the electrolyte and while suppressing water-related sides reactions such as HER and OER. This improvement on ion transport can result in more efficient battery performance and an excellent lifespan. The solubility of PFOA in water is 9.5 g L⁻¹ and about 22 mM. However, in the 3 M ZnSO₄ electrolyte, the solution became unclear when the PFOA additive concentration exceeds 10 mM. Thus, the upper concentration limit for PFOA is 10 mM. In addition, the Zn²⁺ transference number results indicate that a concentration of 0.25 mM provides a high transference number environment of 0.511. Considering the balance of additive acidity, Zn²⁺ transference number and resulting surface tension, 0.25 mM was selected as the optimal concentration for PFOA additive in this work.

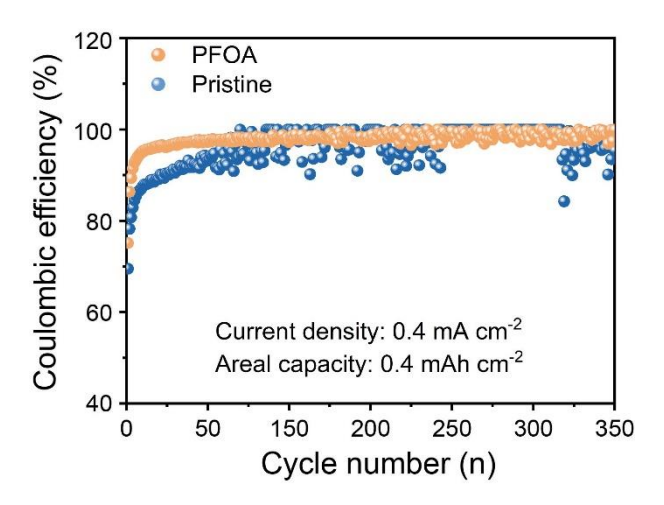


Figure 4.26 CE in different electrolytes using Cu||Zn cells.

The CE of zinc deposition in different electrolytes was studied *via* Cu||Zn cell testing. A certain amount of zinc was first deposited on the copper foil and then reversibly charged and discharged at a fixed current density and capacity (0.4 mA cm⁻², 0.4 mAh cm⁻²). As shown in **Figure 4.26**, the initial CE in the pristine electrolyte is approximately 70%, and the average CE is only 96%. This indicates significant side reactions occurs during the zinc deposition process. These side reactions not only lead to the formation of side-product on the zinc anode and are primarily attributed to water-related reactions, such as HER and OER, that impact the electrolyte, resulting in an unstable zinc deposition process in the pristine electrolyte. In contrast, the CE in the PFOA electrolyte is significantly higher at 98% compared to the pristine electrolyte. Additionally, the CE remains stable over 350 cycles in the PFOA electrolyte, indicating that the zinc deposition process in the PFOA electrolyte is highly reversible.

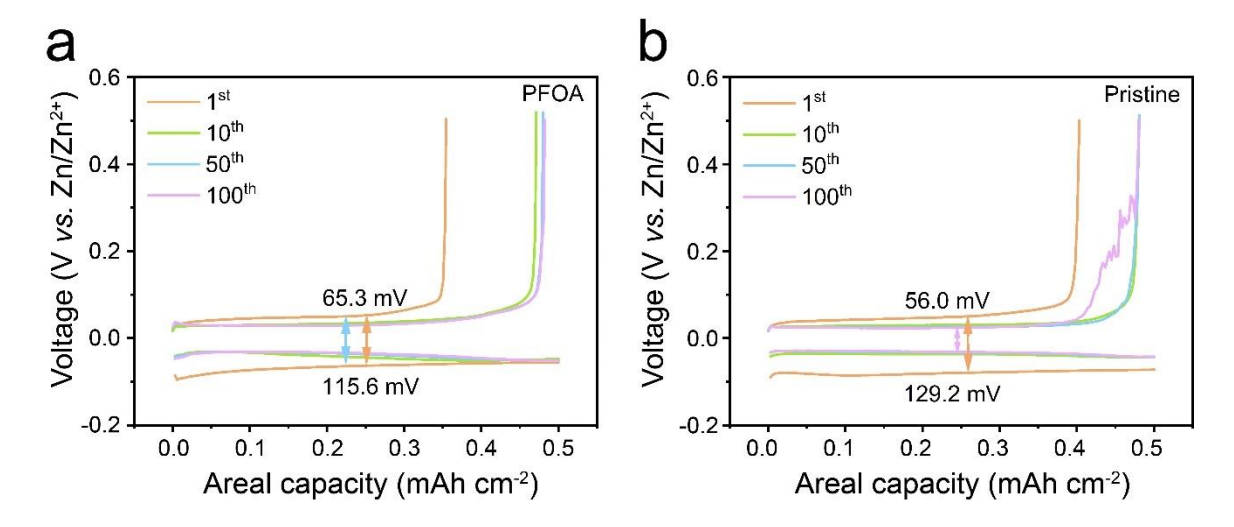


Figure 4.27 Voltage-capacity curves using Cu||Zn cells in different electrolytes: (a) PFOA electrolyte; (b) Pristine electrolyte.

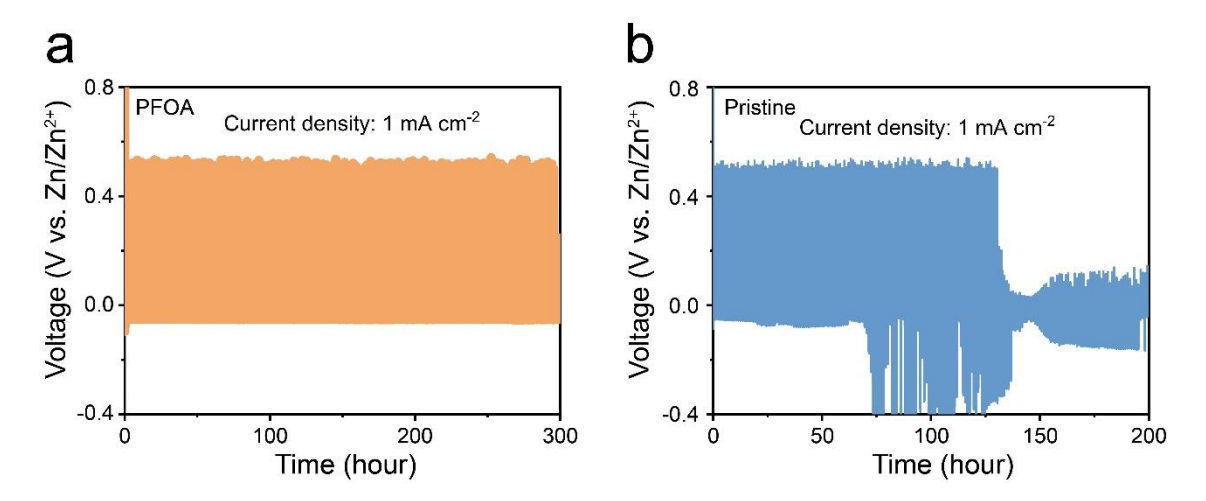


Figure 4.28 Voltage-time curves of zinc plating and stripping on copper substrates in different electrolytes: (a) PFOA electrolyte; (b) Pristine electrolyte.

Further analysis of the voltage-capacity curves of Cu||Zn cells reveals a clear difference in the deposition process. As shown in **Figure 4.27a**, the deposition plateau remains highly stable after 50 cycles in the PFOA electrolyte, indicating that the formation of the PFOA adsorption layer effectively regulate the zinc deposition process. Additionally, the consistent plateau suggests that the PFOA additive in the electrolyte is self-adaptive and can tolerate changes in morphology and thickness during Zn plating and stripping. In contrast, the voltage-capacity curve in the pristine electrolyte fluctuates after 100 cycles, indicating that the zinc deposition process is not reversible due to the accumulation of side-products in the pristine electrolyte. This highlights the effectiveness of PFOA electrolyte in enhancing the reversibility of the zinc deposition process, contributing to enhanced battery performance.

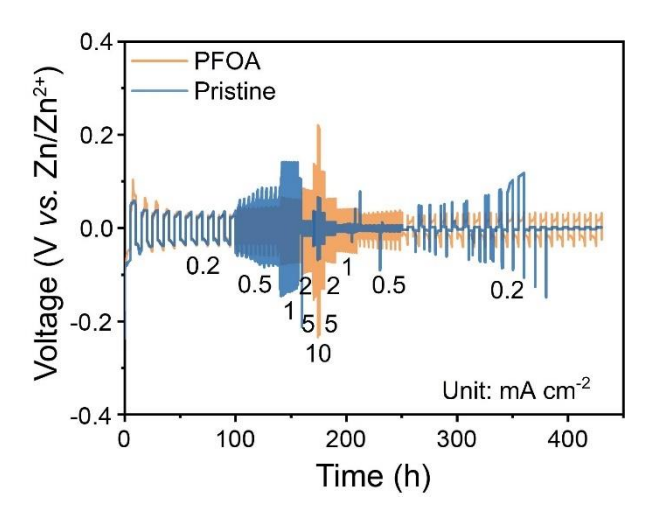


Figure 4.29 Rate performance of Zn symmetric cells measured at stepwise current densities of 0.2, 0.5, 1, 2, 5, 10, 5, 2, 1, 0.5, 0.2 mA cm⁻².

To further verify the tolerance and polarisation of the electrolytes under various current densities, Zn-Zn symmetric cells were assembled using different electrolytes under at stepwise current densities ranging from 0.2 to 10 mA cm⁻² and returning to 0.2 mA cm⁻². As shown in **Figure 4.29**, the Zn plating and stripping overpotentials are lower in the electrolyte with PFOA additive than the overpotentials in the pristine electrolyte, especially under the high current density of 10 mA cm⁻². Additionally, the PFOA electrolyte operates with a steady voltage, while the pristine electrolyte exhibited micro short-circuits in the rate performance test. This indicates that the enhanced Zn transfer kinetics in the PFOA electrolyte with PFOA additive make it capable of tolerating zinc deposition under high current densities.

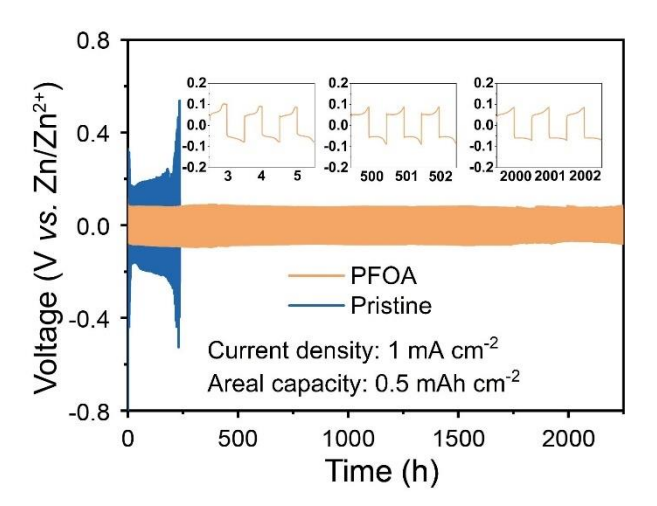


Figure 4.30 Long-term cycling using the Zn symmetric cell in different electrolytes under 1 mA cm⁻².

An ultralong lifespan of symmetric cells can be achieved with the PFOA electrolyte. As shown in **Figure 4.30**, Zn symmetric cells operate steadily for 2,200 hours at 1 mA cm⁻², in contrast to the failure of symmetric cells in the pristine electrolyte after 180 hours. The electrolyte with PFOA additive maintains a low voltage hysteresis during long-term cycling, indicating that the PFOA additive can facilitate the zinc deposition process. Indeed, the zinc reversible stripping/plating curves using symmetric zinc cell (inset in **Figure 4.30**) align with the high CE of Cu||Zn cells, confirming the highly reversible zinc deposition process in the PFOA electrolyte.

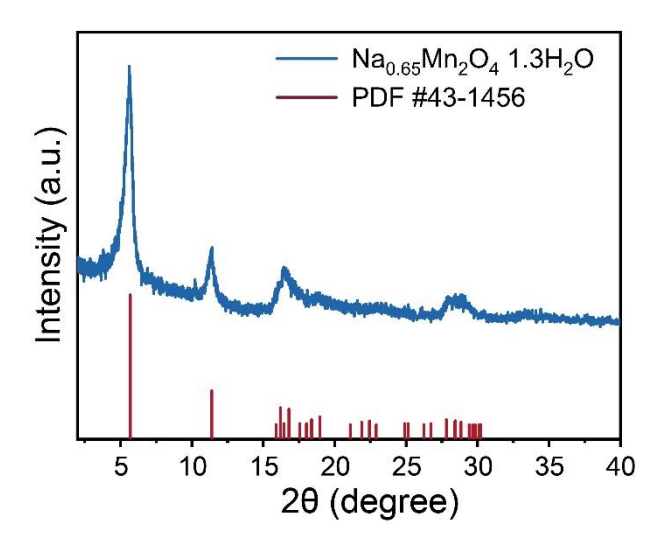


Figure 4.31 XRD profile of Na_{0.65}Mn₂O₄.

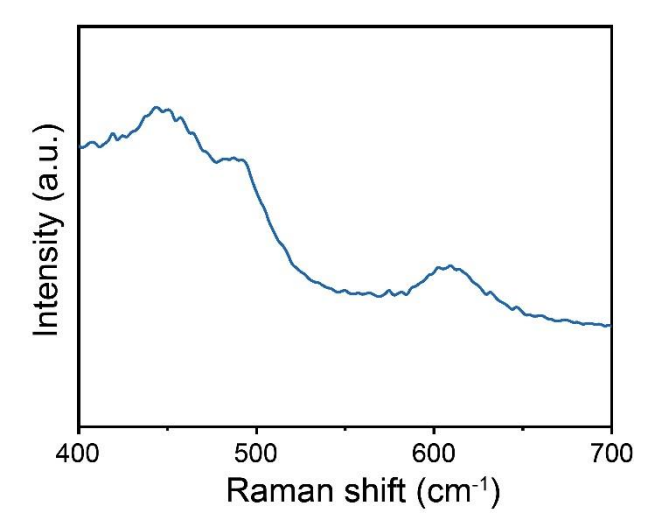


Figure 4.32 Raman curve of Na_{0.65}Mn₂O₄ self-standing electrode mixed with PTFE.

To further study the capability of PFOA electrolyte with AZIBs cathode, Na_{0.65}Mn₂O₄ was synthesised and used as the cathode material in Chapter 4. Further *ex-situ* and *in-situ* characterisations were performed using self-standing Na_{0.65}Mn₂O₄ electrodes by mixing PTFE, Na_{0.65}Mn₂O₄ and Super P with NMP and rolling mixture into foils. The as-prepared electrode has a high loading amount of 10-15 mg cm⁻², which is suitable for *ex-situ* testing. This fabrication method offers a higher signal-to-noise ratio compared to the slurry coating method, enabling more reliable characterisation of structure change in the cathode material.

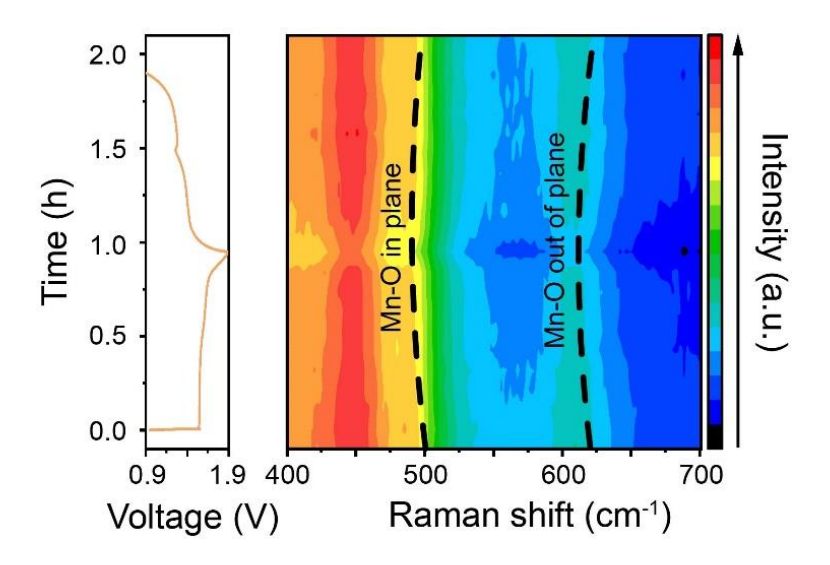


Figure 4.33 *In-situ* Raman spectra of Na_{0.65}Mn₂O₄ cathode cycled in the PFOA electrolyte.

To further investigate the cathode material structural changes during charge and discharge in different electrolytes, *in-situ* Raman spectroscopy was performed using a 532 nm laser (**Figure 4.33**). Three characteristic Raman peaks were observed between 400 and 700 cm⁻¹ before cycling: two in-plane Mn-O stretching vibrations within the octahedral layers between 450 and 500 cm⁻¹ and an out-of-plane Mn-O vibration perpendicular to the layers around 630 cm⁻¹. No additional peaks were observed during cycling, and the three prominent peaks remained, indicating that the Na_{0.65}Mn₂O₄ crystal structure and Mn-O bonds were stable in the PFOA electrolyte. During the charge process, peaks near 500 cm⁻¹ and 630 cm⁻¹ exhibited a red shift, attributed to the contraction among the [MnO₆] interlayer spacing due to reduced interlayer repulsion of the [MnO₆] octahedra, showing the deintercalation process of Zn²⁺ in the cathode material. These peaks reverted to their original positions after discharge, indicating the reversible cathode material interlayer spacing changes in the PFOA electrolyte.

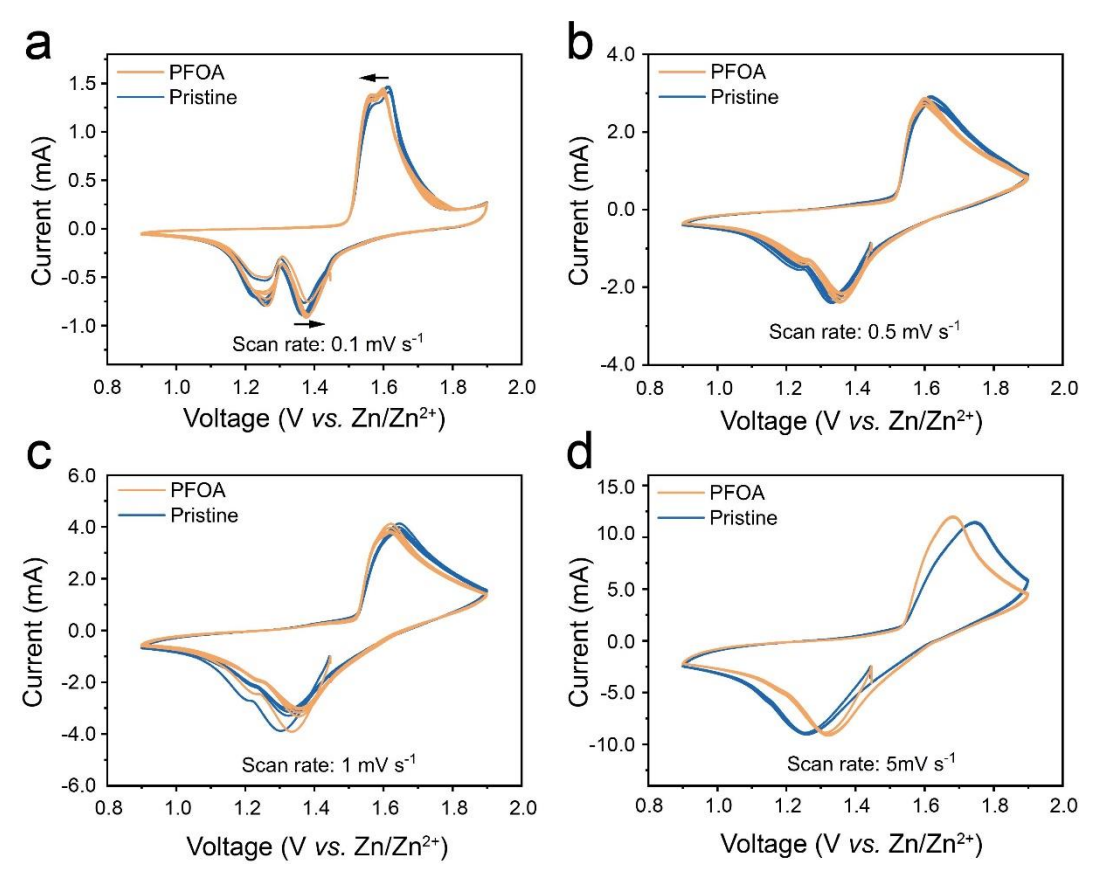


Figure 4.34 CV curves of $Na_{0.65}Mn_2O_4||Zn|$ cells under different scan rate: (a) 0.1 mV s⁻¹; (b) 0.5 mV s⁻¹; (a) 1 mV s⁻¹; (d) 5 mV s⁻¹.

CV measurements on Na_{0.65}Mn₂O₄||Zn cells were performed under various current scan rate to study the dynamic change. The full cells were tested with the addition of 0.2 M MnSO₄ to supress the dissolution of the manganese oxide. **Figure 4.34** shows the typical redox peaks of the Na_{0.65}Mn₂O₄ cathode material in AZIBs, indicating that the PFOA molecule has no adverse effects on the cathode materials. PFOA electrolyte shows a reduction on the polarisation of the redox peaks compared to the pristine electrolyte, demonstrating that ion transport is enhanced by PFOA additives, this is attributed to the enhanced zinc transference number and ions accessibility of PFOA electrolyte.

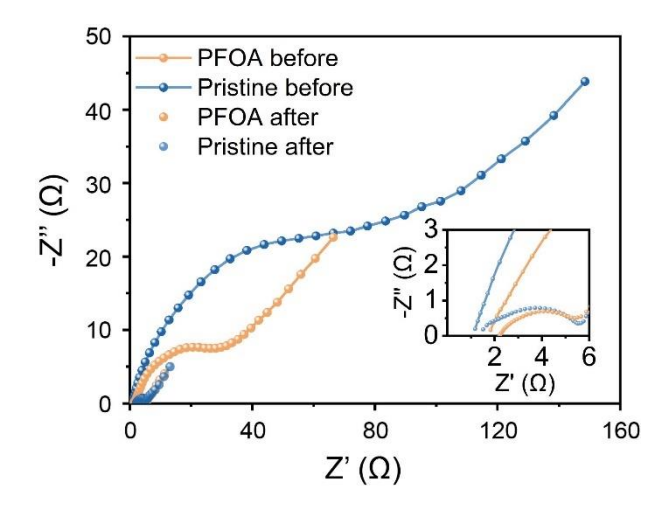


Figure 4.35 EIS profiles of Na_{0.65}Mn₂O₄||Zn cells with different electrolytes.

EIS was conducted to investigate the kinetic differences in various electrolytes (**Figure 4.35**). The charge transfer resistance (R_{ct}) decreased from 45.87 Ω to 25.15 Ω , aligning with the enhanced desolvation process of hydrated Zn^{2+} and the reduced polarisation observed in the CV curves. The reduced semi-circle size in the PFOA electrolyte compared to the pristine electrolyte indicates improved charge transfer capabilities, which consistent with the high transference number observed in the PFOA electrolyte. These results demonstrate that PFOA additive significantly enhances charge transfer dynamics in the electrolyte.

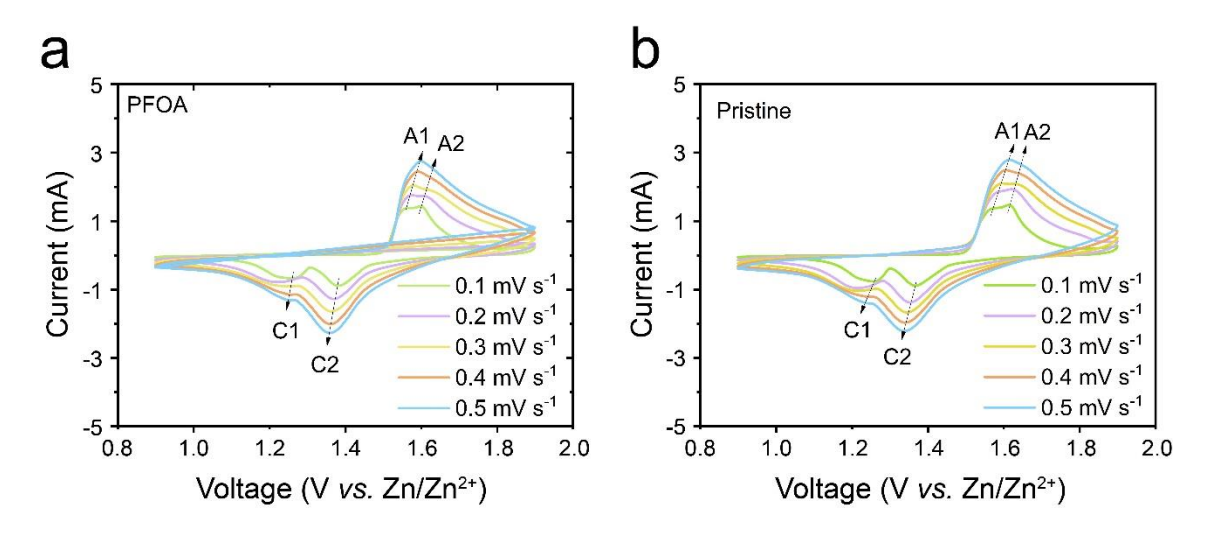


Figure 4.36 CV plots of $Na_{0.65}Mn_2O_4||Zn$ at scan rates of 0.1 to 0.5 mV s⁻¹: (a) in 3 M ZnSO₄ 0.2 M MnSO₄ 0.25 mM PFOA, (b) in 3 M ZnSO₄ 0.2 M MnSO₄.

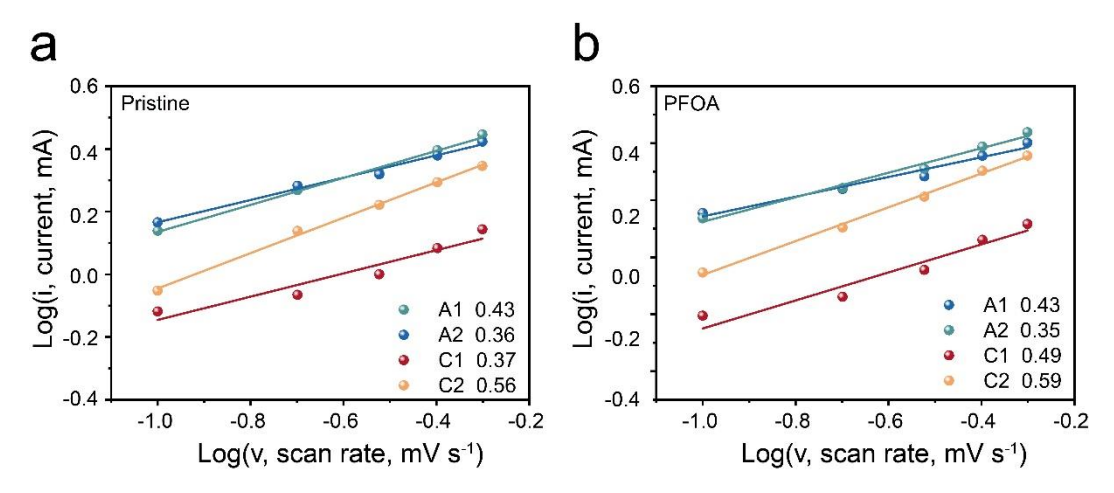


Figure 4.37 Fitting results of b value in different electrolytes: (a) Pristine electrolyte; (b) PFOA electrolyte.

CV curves were analysed through b-value fitting to distinguish differences in the charge storage process in different electrolytes. Diffusion-capacitive analysis was conducted in log(i)-log (v) plots regarding the peaks shown in CV curves. The fitting b-values for the anodic/cathodic peaks in the PFOA electrolyte were 0.43/0.35/0.49/0.59, which is slightly higher than those in the pristine electrolyte 0.43/0.36/0.37/0.56. These differences demonstrate that the PFOA electrolyte can facilitates ion transfer in the cathode material, especially around the 1.3 V discharge plateau.

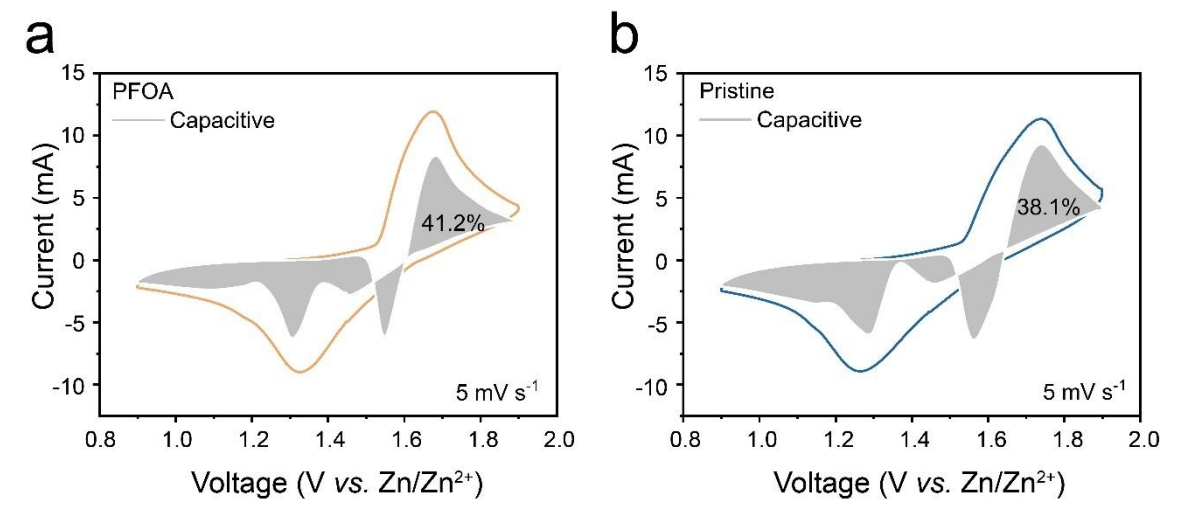


Figure 4.38 Capacitive contribution (grey region) to the electrochemical response current at 5 mV s⁻¹: (a) PFOA electrolyte; (b) Pristine electrolyte.

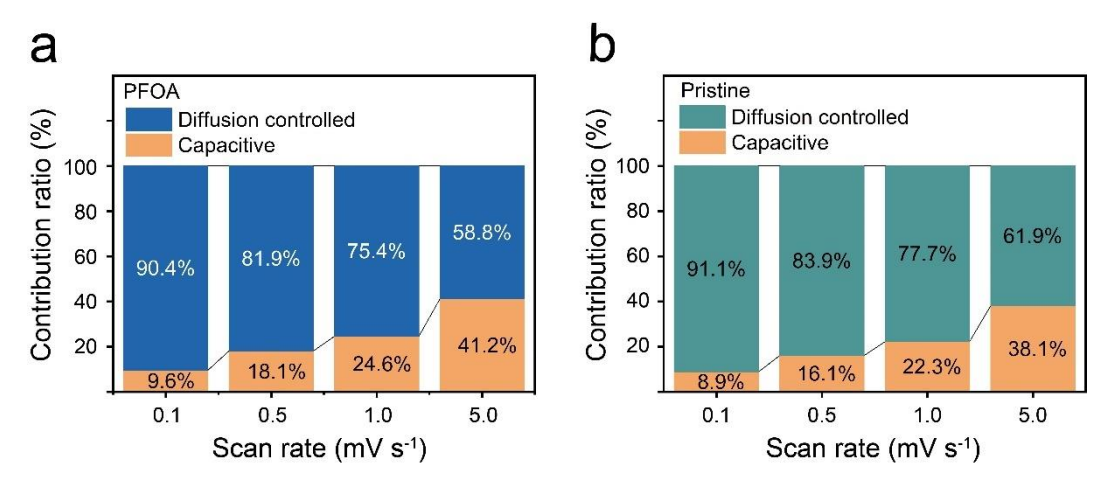


Figure 4.39 Capacitive contribution in the PFOA electrolytes (a) and pristine electrolytes (b).

The capacitive contribution to the charge storage mechanism was studied and compared between the PFOA electrolyte and pristine electrolyte (**Figure 4.39**). The results show that the electrolyte with PFOA has a higher proportion of capacitive contribution at different scan rates. These results demonstrate the effectiveness of the PFOA electrolyte in enhancing the surface-controlled processes, leading to improved ion transfer.

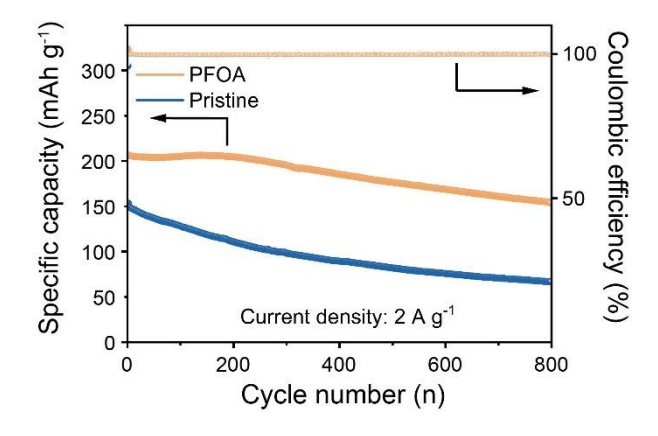


Figure 4.40 Na_{0.65}Mn₂O₄||Zn GCD testing with different electrolytes.

The long-term durability of batteries in different electrolytes was evaluated. As shown in **Figure 4.40**, under the same current density, the Na_{0.65}Mn₂O₄ specific capacity faded from 150 mAh g⁻¹ to 66 mAh g⁻¹ after 800 cycles in the pristine electrolyte, resulting in a 43% capacity retention ratio. This capacity decay is primarily attributed to severe side reactions and uncontrolled dendritic Zn growth during cycling. In comparison, the electrolyte with PFOA additive exhibited a 26% capacity decay after 800 cycles at 2 A g⁻¹, with a specific capacity remaining at 203 mAh g⁻¹, owing to superior Zn reversibility.

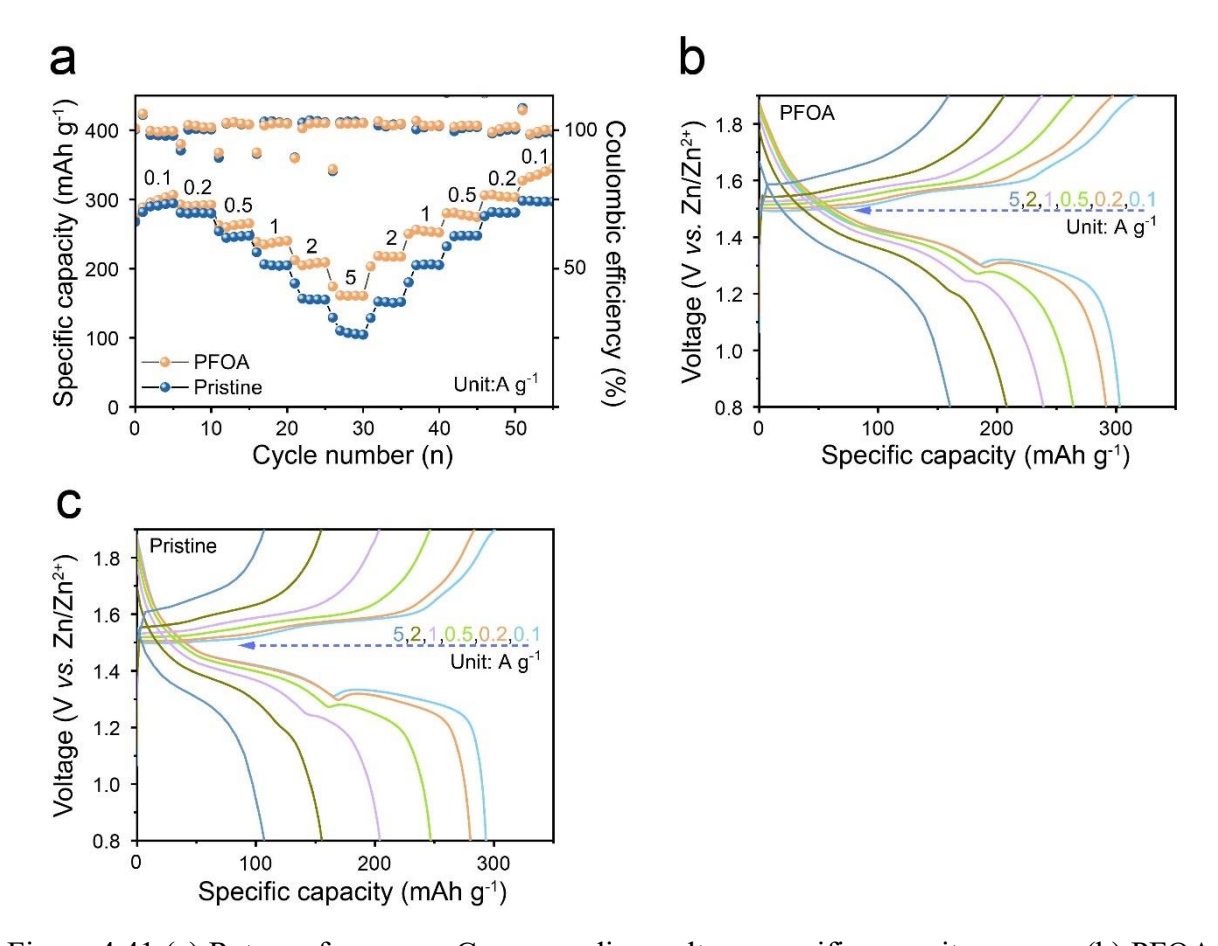


Figure 4.41 (a) Rate performance; Corresponding voltage-specific capacity curves: (b) PFOA electrolyte; (c) Pristine electrolyte.

Figure 4.41a illustrates the rate performance of AZIBs using different electrolytes. The current density was sequentially increased from 0.1 to 5 A g⁻¹ and then subsequently decreased to 0.1 A g⁻¹, with five cycles at each current density. Impressively, Na_{0.65}Mn₂O₄ cathode materials using the electrolyte with PFOA additive showed higher specific capacity under different current densities: 295, 290, 262, 236, 206, and 153 mAh g⁻¹ at 0.1, 0.2, 0.5, 1, 2, and 5 A g⁻¹, respectively, with capacity recovery and a corresponding CE exceeding 99 %. In comparison, the specific capacity in the pristine electrolyte was lower: 290, 279, 245, 204, 155, and 110 mAh g⁻¹ at the same current densities. The rate performance with the PFOA electrolyte was notably improved, especially at high current densities, representing a 39% increase from 110 mAh g⁻¹ to 153 mAh g⁻¹ (**Figure 4.41b**). These improved performances are attributed to the PFOA adsorption layer on both cathode and anode, which facilitates the Zn²⁺ ion transfer and mitigates water-related side reactions.

4.3.5 Molecular dynamics simulation

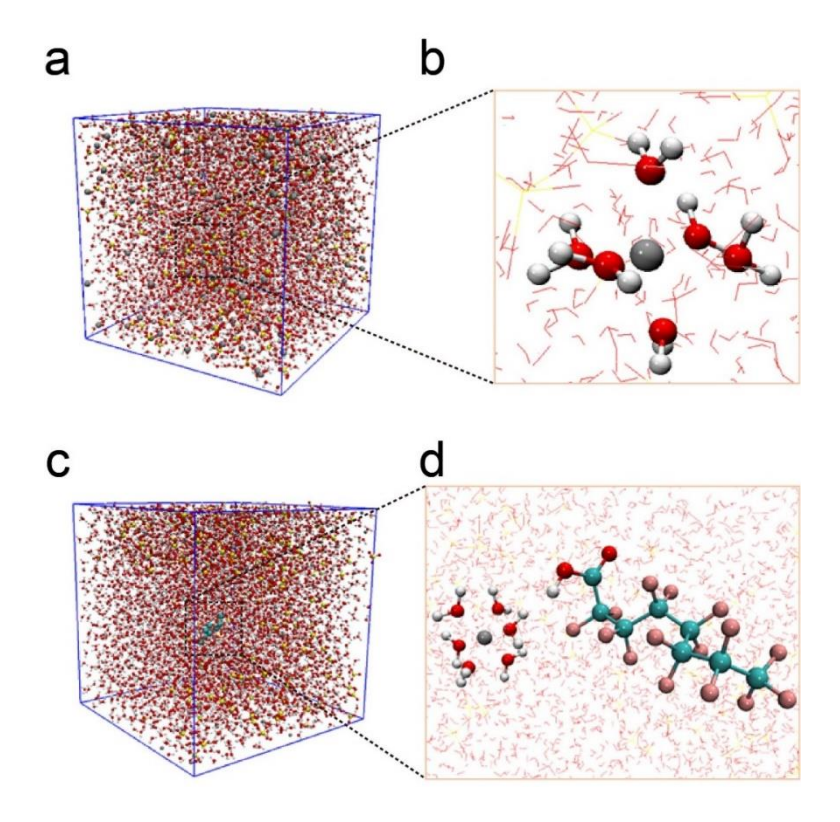


Figure 4.42 Molecular dynamic simulations: (a) Simulation model of the pristine electrolyte. (b) H_2O molecule distribution in the Zn^{2+} first hydration layer of the pristine electrolyte. (c) Simulation model of electrolyte with PFOA additive. (d) H_2O molecule distribution in the Zn^{2+} first hydration layer of the electrolyte with PFOA additive.

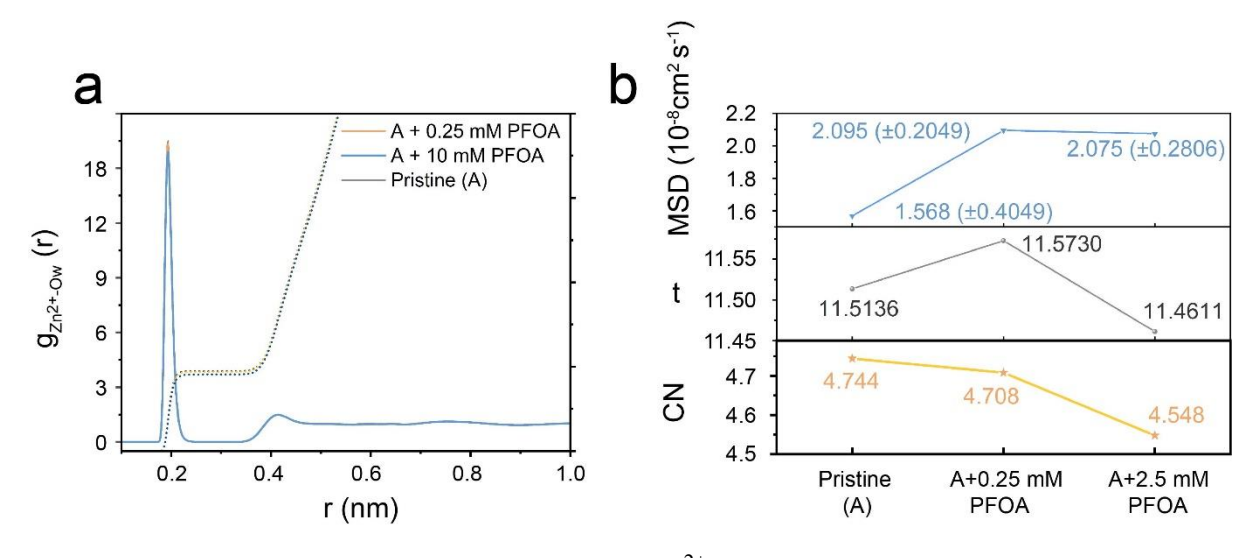


Figure 4.43 Radial distribution functions of (a) Zn^{2+} ions and (b) water molecule, where Ow represents the oxygen atoms in water molecules.

The computational simulations presented in this chapter were conducted in collaboration with Dr Zhuanfang Jing from the Qinghai Institute of Salt Lakes, Chinese Academy of Sciences. The related part was rewritten according to the results. MD calculations were performed using GROMACS 2019.3 to investigate the hydration and movement features of Zn^{2+} in electrolytes with and without PFOA additive at 298.15 K. Partial electric charge sets and Lennard-Jones parameters for the AMBER force field describing Zn^{2+} binding with water and SO_4^{2-} are shown in Table 1. Simulation results in **Figure 4.42** and **Figure 4.43** reveal that in the PFOA electrolyte, PFOA molecules occupy part of the Zn^{2+} solvation sheath, resulting in a PFOA anion-water composition of the Zn^{2+} solvation shell. A reduced coordination number of Zn^{2+} with water molecules was observed in comparison to the pristine zinc sulfate electrolyte. Furthermore, according to the τ value of MD, the formation of PFOA-water- Zn^{2+} aggregates facilitates the Zn^{2+} desolvation process more effectively than water- Zn^{2+} aggregates. Mean square displacement (MSD) results confirmed that Zn^{2+} exhibits enhanced ion mobility in the PFOA electrolyte than in pristine electrolyte, which could enhance the rate performance of AZIBs.

4.4 Conclusion

In this chapter, ultralow concentrations of a fluorinated surfactant additive were introduced into the electrolyte to improve the reversibility of the Zn plating process and overall battery performance. The electrolyte with PFOA additive optimises Zn plating nucleation by increasing nucleation overpotentials and enhancing Zn²⁺ migration by regulating sulfate anion. *In-situ* optical microscopy revealed uniform and dense Zn plating. The absorption layer of PFOA molecules on the electrode acts as a barrier, blocking excess SO₄²⁻ anions and H₂O molecules from reaching the zinc anode, thereby suppressing HER and OER side reactions and enlarging the working window of AZIBs.

MD simulations confirmed that PFOA molecules could occupy the Zn²⁺ solvation sheath, with results showing increased Zn²⁺ MSD with the addition of PFOA, proving the optimised Zn²⁺ desolvation process in the electrolyte with PFOA additives. Accordingly, the lifespan of Zn plating/stripping extended to 2,200 hours in the electrolyte with PFOA additive, with the working window increased to 2.1 V. The PFOA additive supports excellent rate performance under current densities from 0.2 mA cm⁻² to 10 mA cm⁻² with low overpotential change and high reversibility. An aqueous battery consisting of a Na_{0.65}Mn₂O₄ cathode and a Zn anode in the electrolyte with PFOA additive was assembled. The battery achieved excellent rate

performance with a specific capacity of 153 mAh g⁻¹ under 5 A g⁻¹ and excellent cycling stability at 2 A g⁻¹ with a high CE exceeding 97%. Furthermore, the interfacial wettability between the electrolyte and electrode improved, confirmed by reduced contact angles from 121° to 61° with the addition of PFOA molecules.

These findings indicate that PFOA surpass state-of-the-art electrolyte additives, boosting performance in both cathodes and anodes. The method of preparing electrolyte with PFOA additives is straightforward and cost-effective, providing a practical solution for the large-scale application of AZIBs with high stability and reversible Zn plating/stripping. This surfactant electrolyte strategy also opens opportunities for numerous cathode materials with high redox reaction potentials, such as Co²⁺/Co³⁺ and Fe³⁺/Fe²⁺, owing to the enlarged working potential window, and will advance the development of aqueous energy storage systems with enhanced energy density.

4.5 References

- [1] J. Xie, Y. C. Lu, Nat Commun 2020, 11, 2499.
- [2] C. Liu, X. Xie, B. Lu, J. Zhou, S. Liang, ACS Energy Lett. 2021, 6, 1015.
- [3] F. Wang, O. Borodin, T. Gao, X. Fan, W. Sun, F. Han, A. Faraone, J. A. Dura, K. Xu, C. Wang, *Nat Mater* **2018**, *17*, 543.
- [4] X. Feng, M. Ouyang, X. Liu, L. Lu, Y. Xia, X. He, Energy Storage Mater. 2018, 10, 246.
- [5] Z. Cao, P. Zhuang, X. Zhang, M. Ye, J. Shen, P. M. Ajayan, *Advanced Energy Materials* **2020**, *10*.
- [6] D. Li, L. Cao, T. Deng, S. Liu, C. Wang, Angew. Chem. Int. Ed. 2021, 60, 13035.
- [7] T. Zhang, Y. Tang, S. Guo, X. Cao, A. Pan, G. Fang, J. Zhou, S. Liang, *Energy Environ. Sci.* **2020**, *13*, 4625.
- [8] K. Wu, J. Huang, J. Yi, X. Liu, Y. Liu, Y. Wang, J. Zhang, Y. Xia, *Adv. Energy Mater.* **2020**, *10*.
- [9] Z. Hou, X. Zhang, X. Li, Y. Zhu, J. Liang, Y. Qian, J. Mater. Chem. A 2017, 5, 730.
- [10] A. Bayaguud, X. Luo, Y. Fu, C. Zhu, ACS Energy Letters 2020, 5, 3012.
- [11] H. Lu, X. Zhang, M. Luo, K. Cao, Y. Lu, B. B. Xu, H. Pan, K. Tao, Y. Jiang, *Adv. Funct. Mater.* **2021**, *31*.
- [12] X. Guo, Z. Zhang, J. Li, N. Luo, G.-L. Chai, T. S. Miller, F. Lai, P. Shearing, D. J. L. Brett, D. Han, Z. Weng, G. He, I. P. Parkin, *ACS Energy Lett.* **2021**, *6*, 395.
- [13] Y. Yang, C. Liu, Z. Lv, H. Yang, Y. Zhang, M. Ye, L. Chen, J. Zhao, C. C. Li, *Adv. Mater.* **2021**, *33*, e2007388.
- [14] M. Zhou, S. Guo, J. Li, X. Luo, Z. Liu, T. Zhang, X. Cao, M. Long, B. Lu, A. Pan, G. Fang, J. Zhou, S. Liang, *Adv. Mater.* **2021**, *33*, e2100187.
- [15] Q. Zhang, J. Luan, L. Fu, S. Wu, Y. Tang, X. Ji, H. Wang, *Angew. Chem. Int. Ed.* **2019**, *58*, 15841.
- [16] C. Y. Chen, K. Matsumoto, K. Kubota, R. Hagiwara, Q. Xu, Adv. Energy Mater. 2019, 9.
- [17] H. Qiu, X. Du, J. Zhao, Y. Wang, J. Ju, Z. Chen, Z. Hu, D. Yan, X. Zhou, G. Cui, *Nat Commun* **2019**, *10*, 5374.
- [18] S. Guo, L. Qin, T. Zhang, M. Zhou, J. Zhou, G. Fang, S. Liang, *Energy Storage Mater.* **2021**, *34*, 545.

[19] H. Dong, J. Li, S. Zhao, F. Zhao, S. Xiong, D. J. L. Brett, G. He, I. P. Parkin, *J. Mater. Chem. A* **2020**, *8*, 22637.

Chapter 5: Highly Stable Manganese Oxide Cathode Material Enabled by Grotthuss Topochemistry for Aqueous Zinc Ion Batteries

5.1 Introduction

Driven by practical demands for safety and cost-effectiveness, AZIBs have attracted significant attention in recent years. Manganese dioxide (MnO₂) has been extensively researched due to its relatively high discharge plateau and long lifespan. However, the development of manganese oxide cathode materials is challenged by their restricted cycle lifespan at low current densities. This limitation arises from the divalency of the Zn^{2+} ions, where strong electrostatic interactions between Zn^{2+} cations and host frameworks hinder transport. The elevated desolvation energy of Zn^{2+} at the electrode–electrolyte interface compared to monovalent ions, adds additional energy penalties to its intercalation into manganese oxide. Furthermore, the strong electrostatic repulsion between the charge carrier and manganese oxide during intercalation and deintercalation limits ion transfer in AZIBs. Thus, enhancing the kinetics of charge carriers within manganese oxide materials is a crucial focus of AZIBs cathode research.

Previous studies have suggested that the Grotthuss mechanism represents an efficient proton conductivity process, facilitating collective, chain-like proton transfer in which the net charge moves faster than the individual protons. The Grotthuss mechanism provides efficient proton transport by eliminating the need for entire molecule mobility. Combining defect engineering with the Grotthuss mechanism could significantly enhance charge carrier kinetics (**Figure 5.1a**). Recent studies show that Grotthuss conduction occurs in defective Prussian blue analogues. In this mechanism, a hydrogen atom hops between hydrogen-bonded water molecules, causing a cascade of identical displacements along the hydrogen-bonding network. This motion is analogous to the motion observed in Newton's cradle (**Figure 5.1b**), with correlated local displacements leading to long-range proton transport. This allows for fast, efficient proton transfer without requiring a proton to traverse the entire structure solely. Continuous proton hopping within the host material induces periodic, temporary local structural changes in the lattice, altering the energy barriers for zinc ion intercalation and deintercalation and optimising diffusion pathways for zinc ions.

Manganese vacancies within the lattice provide low-energy pathways for proton hopping and create additional intercalation sites for both proton and Zn²⁺ ion, increasing battery capacity. Defect engineering effectively modifies the electronic structure of host materials and lowers energy barriers for charge carrier transfer. The most common cation vacancy in manganese oxides is the Mn vacancy. Density of states comparisons of manganese oxide with and without vacancies suggest that introducing Mn vacancies increases charge density at the Fermi level

and lowers surface energy barriers. In contrast to the uniform charge distribution in typical manganese oxide, electrons in defective manganese oxide congregate near the Mn vacancy. Defect-induced local structural modifications and charge redistribution facilitate charge transfer and accommodate volume changes during ion intercalation.

A strategic approach is needed to achieve the Grotthuss mechanism in manganese oxide-based AZIBs. This approach should focus on constructing a continuous hydrogen-bond network within the lattice to facilitate proton migration from the electrolyte to the cathode material's interlayer spaces and reducing the charge transfer energy barrier within the host cathode material *via* defect engineering. By effectively addressing these challenges, realising efficient AZIBs operation through the Grotthuss-like conduction mechanism can enhance energy storage performance.

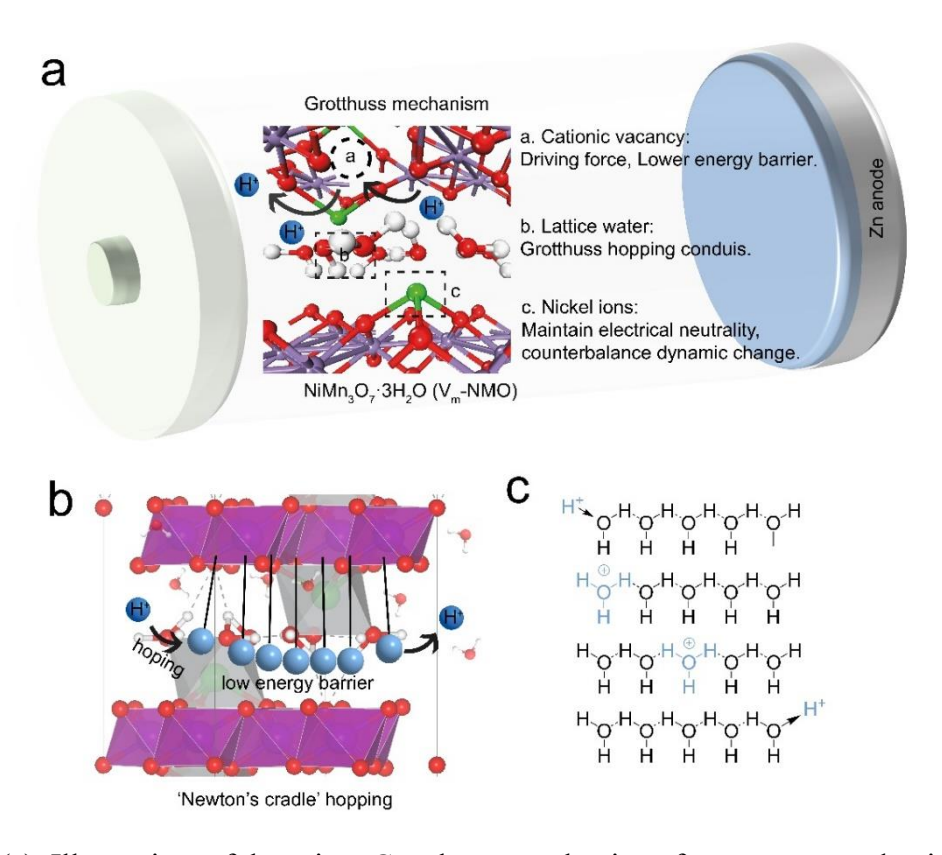


Figure 5.1 (a) Illustration of hopping Grotthuss mechanism for proton conductivity; (b) Newton's cradle illustration of proton hopping *via* Grotthuss mechanism in NiMn₃O₇ lattice; (c) Illustration of hydrated proton hopping *via* Grotthuss mechanism.

This chapter presents a novel strategy to enhance the rate performance and long-term cycling stability of AZIBs by leveraging the Grotthuss mechanism in manganese oxide. A facile hydrothermal synthesis process was employed to prepare Ernienickelite NiMn₃O₇. It found that specific peak intensity and lattice structure in NiMn₃O₇ could be tailored by altering synthesis

conditions, leading to the formation of vacancies in the lattice. For convenience, the resulting samples are referred to as V_m-NMO (with vacancy) and NMO (without vacancy). It was demonstrated that V_m-NMO can serve as highly reversible and high-capacity cathode materials for AZIBs. The prepared V_m-NMO cathode material, containing abundant cation vacancies, exhibits enhanced ion transfer and a high capacity of 318 mAh g⁻¹ at 200 mA g⁻¹, along with a stable capacity of 121 mAh g⁻¹ at 5 A g⁻¹ and 91% capacity retention after 4,000 cycles. The energy storage mechanism of the V_m-NMO cathode material was systematically investigated using synchrotron X-ray absorption spectroscopy and DFT simulations. In aqueous electrolytes, protons react with water molecules, forming hydronium ions (H₃O⁺). Numerous lattice water molecules within the host material create a continuous hydrogen bond network, facilitating the migration of water molecules from the electrolyte to the interlayer spaces in layered manganese oxides. Simulation results indicate that protons prefer to bond with O²⁻ ions on the Mn-O layer rather than remaining with water molecules. Proton transfer energy barrier calculations with and without Mn⁴⁺ vacancies, indicate that proton transfer is favoured in the presence of defects. Mn⁴⁺ vacancies facilitate proton hopping in V_m-NMO systems. Continuous proton hopping within the host material induces periodic, temporary local structural changes in the lattice, dynamically altering energy barriers for ion intercalation and deintercalation and optimising diffusion pathways for zinc ions. Moreover, the presence of manganese vacancies in the lattice serves as low-energy barrier pathways for proton hopping and additional sites for proton and zinc ion intercalation, increasing overall battery capacity. This dynamic behaviour underscores the potential of the Grotthuss-like mechanism on the Mn-O layer in V_m-NMO.

5.2 Experimental section

5.2.1 Chemicals

The following chemicals were used as received without further purification: Potassium permanganate (Sigma-Aldrich, ACS reagent, $\geq 99.0\%$), Manganese (II) nitrate tetrahydrate (Fisher Chemical, AR, $\geq 98.0\%$), Nickel (II) nitrate hexahydrate (Sigma-Aldrich, ACS reagent, $\geq 99.0\%$), Ammonium chloride (Sigma-Aldrich, ACS reagent, $\geq 95\%$), Zinc trifluoromethanesulfonate (Sigma-Aldrich, ACS reagent, $\geq 98\%$), Manganese bis(trifluoromethanesulfonate) (Sigma-Aldrich, ACS reagent, $\geq 98\%$), PVDF (Sigma-Aldrich, average $M_w \sim 534,000$ by GPC, powder), and NMP (Sigma-Aldrich, ACS reagent, $\geq 99.0\%$).

5.2.2 Material synthesis

The cation-defective nickel manganese oxide (NiMn₃O₇) cathode material (V_m-NMO) was synthesised following established literature procedures. Aqueous KMnO₄ solution (0.04 M, 18 mL), aqueous NH₄Cl solution (0.04 M, 18 mL), and aqueous Ni(NO₃)₂ solution (1 M, 4 mL) were added sequentially and vigorously stirred for 25 minutes. The resulting mixture was transferred into an autoclave and heated at 200°C for 24 hours. The precursor was collected, washed three times with deionised water and once with ethanol, and then dried in an oven at 60°C overnight.

5.2.3 Material characterisation

XRD patterns were obtained using a STOE SEIFERT diffractometer, covering an angular range of $2^{\circ} < 2\theta < 40^{\circ}$ with Mo X-ray radiation. The morphology and chemical states of the synthesised materials were analysed using SEM (JEOL 7600F), TEM (JEOL JEM-2100 and ARM200F), and XPS (Thermo Scientific K-alpha), respectively. XPS data processing was conducted using CasaXPS software, calibrated using the adventitious carbon binding energy at 284.8 eV. Raman and FTIR spectra were obtained using a Renishaw Raman microscope (laser wavelength of 514.5 nm) and ATR-FTIR (Bruker, platinum-ATR). Thermogravimetric analysis (TGA) was conducted using a PerkinElmer TGA 4000 System to record mass changes during annealing. The mass of the active materials was measured accurately with an Ohaus analytical balance ($\delta = 0.01$ mg). Crystallographic structures were simulated using VESTA software with standard ICSD CIF documents.

The Mn, Ni, and Zn K-edge X-ray Absorption Spectra of electrode plates were collected at B18 beamline at Diamond Light Source. The monochromatic beam, ranging from 6.35 keV to 10.55 keV ($k_{max} = 16$), was delivered through a bending magnet and a platinum-coated silicon (111) double crystal monochromator. The beam size at the sample was approximately $1.0 \times 1.0 \text{ mm}^2$ (vertical x horizontal) with a photon flux of $\sim 10^{11} \text{ ph/s}$ (no attenuation). XAFS spectra were collected in transmission mode, with ionisation chambers monitoring the intensity of the incident beam (I_0) and the transmitted beam (I_t). The sample, comprising electrode carbon paper (D: 8 mm), was cut into four pieces, stacked, sealed with Kapton tape, and mounted on the sample rack. XAFS measurements were performed at room temperature, with each sample was measured twice, and the data were merged to enhance the signal-to-noise ratio. Mn, Ni, and Zn metal foils served as energy calibration references.

The NEXAFS experiment was conducted at the B07-B beamline of Diamond Light Source (UK). NEXAFS measurements of O K-edge, Mn L-edge, and Ni L-edge were conducted in total electron yield (TEY) mode in the ES-2 end station for Ambient Pressure NEXAFS. The pristine, charged, and discharged electrodes, along with Mn₂O₃ and MnO₂ powder references, were dispersed onto carbon tape to ensure good conductivity. Samples were illuminated by an incident beam produced by a bending magnet and directed through plane grating monochromator, with a spot size of approximately 200 μm x 200 μm. The specimen chamber pressure was maintained at 1 x 10⁻⁷ mbar. Three repetitions of the NEXAFS spectrum were collected and merged for each edge to enhance the signal-to-noise ratio, with energy resolution set to 0.1 eV for each repetition. Energy shifts of O K-edge, Mn L-edge, and Ni L-edge were calibrated against standard Mn₂O₃ and NiO spectra. NEXAFS spectra were normalised relative to the incident beam intensity, and X-ray Absorption Spectroscopy data processing and analysis were conducted using Demeter software package.

5.2.4 Electrochemical measurements

The electrochemical performance of NiMn₃O₇ was evaluated by assembling the material into coin cells. The cathode slurry was prepared by mixing 70 wt% of the synthesised NiMn₃O₇, 20 wt% of Carbon black Super-P, and 10 wt% of PVDF in NMP solvent. This slurry was then deposited onto carbon paper and vacuum-dried at 80°C for 8 hours to form the cathode. The cathode was paired with a zinc plate anode of 500 µm thickness, forming a complete coin cell configuration with a 3 M Zn(OTf)₂ and 0.2 M Mn(OTf)₂ electrolyte, with Whatman[®] GF/A

glass fibre as the separator. The electrode discs, with a diameter of 1.4 cm, had a loading mass between 1.0 and 2.5 mg cm⁻².

All battery performance tests were conducted using the Neware battery testing system. CV curves were recorded within a voltage range of 0.9 - 1.9 V (vs. Zn²⁺/Zn). Additional electrochemical analyses, including CV and EIS, were performed using a BioLogic VMP3 potentiostat.

5.2.5 Estimation of capacitive and diffusion-controlled contributions

To quantitatively distinguish the capacitive and diffusion-controlled contributions to the current, CV curves were recorded at various sweep rates. Typically, the relationship between the measured peak current (i) and the sweep rate (ν) in a CV scan follows the power law:

$$i = av^b$$

$$\log(i) = \log(a) + b \times \log(v)$$

The b-value can be determined by fitting the slope of log(i) versus log(v). A b-value of 0.5 indicates diffusion-controlled behaviour, whereas a b-value of 1.0 signifies capacitive behaviour. To further distinguish between the capacitive and diffusion-controlled contributions, quantitatively assume that the current (i) comprises both processes:

$$i = k_1 v + k_2 v^{\frac{1}{2}}$$

 k_1 can be used to estimate capacitive and diffusion-controlled contributions.

5.2.6 Detailed information on galvanostatic intermittent titration technique

GITT was employed to establish the thermodynamic voltage-composition relationship, consistent with the equilibrium phase diagram. The diffusion coefficients of Zn²⁺ ions were evaluated from the GITT data. In the GITT process, the transient voltage induced by a current pulse is studied as a function of time. GITT testing involved 15 cycles of charge/discharge at 0.1 A g⁻¹ to reach a stable state. Subsequently, a galvanostatic pulse of 30 mA g⁻¹ was applied to the assembled coin cell for 20 minutes, followed by a 2-hour relaxation period under open circuit conditions to achieve equilibrium (defined as < 2 mV h⁻¹). These steps were repeated until the batteries reached fully charged or discharged states. The diffusion coefficients of the charge carriers follow the equation:

$$D_{charge\ carriers} = \frac{4}{\pi} \left(\frac{n_M V_M}{S}\right)^2 \left[\frac{\Delta E_s}{\tau \left(\frac{dE_\tau}{d\sqrt{\tau}}\right)}\right]^2 \left(\tau \ll \frac{L^2}{D_{charge\ carriers}}\right)$$

Where τ represents the dwell time of the constant current pulse (20 minutes); S corresponds to the interface area between the cathode material and electrolyte (cm², referring to the geometric area of the electrode); n_M and V_M denote the moles of NiMn₃O₇ (mol) and the molar volume (cm³ mol⁻¹), respectively; ΔE_s and ΔE_τ are the shifts in steady-state voltage and the total cell voltage after applying a current pulse in a single-step GITT test, eliminating the i_R drop. L refers to the cathode thickness. When the variation of the cell voltage (ΔE_τ) shows a linear relationship with $\tau^{\wedge}(1/2)$, the equation can be simplified as follows:

$$D_{charge\ carriers} = \frac{4}{\pi\tau} \left(\frac{n_M V_M}{S}\right)^2 \left[\frac{\Delta E_s}{\Delta E_\tau}\right]^2$$

5.2.7 DFT computational details

All DFT calculations were performed using the Vienna Ab-initio Simulation Package (VASP)^[1, 2]. Projector augmented wave (PAW) method was employed with a plane-wave cut-off of 420 eV for the expansion of wave functions, ensuring bulk total energies converged within 10⁻⁵ eV^[3]. Structural optimisations used a convergence criterion of 0.01 eV/Å and the Perdew-Burke-Ernzerhof generalised gradient approximation (GGA) as the exchange-correlation functional^[4, 5]. A gamma-centred 4 x 4 x1 Monkhurst-Pack (MP) grid was used.

The ideal NiMn₂O₃ (100) models, comprising three NiMn₃O₇ layers with water molecules in between, were derived from optimised unit cells with lattice parameters a = 7.552 Å (Exp.: 7.514 Å), b = 6.540 Å (Exp.: 6.507 Å), and c = 20.623 Å (Exp.: 20.520 Å). The two top NiMn₃O₇ layers and the interlayer water molecules were relaxed, while the bottom layers were fixed to simulate bulk structure. A vacuum of ~15 Å along the surface normal direction was introduced to eliminate spurious interactions with neighbouring image slabs. The dipole moment due to the presence of species was accounted for using the methods of Neugebauer et al^[6, 7]. Grimme's dispersion correction (DFT+D3) was employed to account for significant dispersion forces^[8].

Previous studies have shown that electron localisation in d-orbitals of Mn^{4+} and Ni^{2+} ions is accurately represented by Hubbard parameters (U_{eff}) of 4.0 eV and 5.3 eV, respectively^[9]. Therefore, research in this chapter utilised U_{eff} values of 4.0 eV and 5.3 eV for Mn^{4+} and Ni^{4+}

ions, respectively, and 0 eV for the p-orbitals of O^{2-} ions. The adsorption energies (E_{ad}) of protons on the NiMn₂O₃(100) surface were evaluated using the equation:

$$E_{ad} = E_{H/NMO} - E_{NMO} - E_H$$

where $E_{H/NM0}$ is the total energy of the proton adsorbed on the NiMn₂O₃ (100) surface,

 E_{NM0} is the total energy of the relaxed pristine NiMn₂O₃ (100) surface, and E_H is the total energy of a hydrogen atom in the gas phase. To obtain $E_{H/NM0}$, the adsorption of the H atom was considered on various sites on the NiMn₂O₃ (100) surface, with and without Mn⁴⁺ defects. This includes adsorption on water molecules present between the NiMn₂O₃ layers, on O atoms of the NiMn₂O₃ layer, and on Mn⁴⁺ ions. Atomic charges were calculated using Bader charge analysis as implemented by Henkelman and co-workers^[10]. The VESTA package was employed for visualisation of optimised structures and to measure interatomic distances, bond angles, and dihedral angles^[11, 12].

5.3 Results and discussion

5.3.1 Cathode materials characterisation

To identify an appropriate type of manganese oxide that could utilise the proton transfer to boost the performance of aqueous zinc ion batteries. This raises the primary research question: which types of manganese oxide is suitable for proton transfer? In general, the intercalation barrier of proton is the key point of this, as the proton radius in aqueous system is significantly larger than its pristine state due to the coordination of water molecules, resulting in sluggish transport that hinders continuous proton transfer. There are three key factors that need to be considered: First, the lattice parameter needs to be big enough for the charge carrier to intercalate; second, a desired parameter is that the lattice structure contains some low energy barrier sites to facilitate proton migration; third, the target material must be highly stable to withstand the dynamic changes associated with proton transfer. Based on these three factors, a specific structure, the maple-leaf-lattice (MLL) structure AMn₃O₇, has garnered significant research interest.

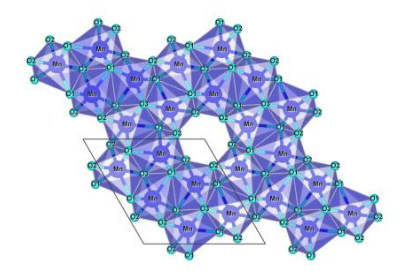


Figure 5.2 Illustration of the basic $Mn_{6/7}O_2$ unit of AMn_3O_7 MLL structure (A = Zn, Ni, Na etc.).

As shown in **Figure 5.2**, in AMn₃O₇, Mn atoms are octahedrally coordinated by six oxygen atoms in AMn₃O₇, forming MnO₆ octahedra that connect along common edges to create a two-dimensional layer. The Mn₃O₇ layer is formed by periodically removing one out of every seven Mn atoms in a triangular lattice, resulting in a MLL structure consisting of Mn⁴⁺ ions, with one Mn vacancy per seven-unit period in the AMn₃O₇ structure. The Mn₃O₇ layers are separated by a nonmagnetic block layer composed of Ni²⁺ ions located above and below the Mn-vacant sites of the Mn₃O₇ layer, as well as lattice water molecules. The Mn-Mn distance between the layers (6.8 Å) is much greater than the layer thickness (2.8 Å), providing ample room for ion diffusion within the crystal lattice and mitigating the strain associated with volume changes during ion intercalation and extraction. ^[13] In summary, the topochemistry structure of AMn₃O₇

satisfies the three theoretical criteria for an ideal cathode material, motivating its experimental synthesis.

A unique property of MLL materials is their pronounced sensitivity to synthesis conditions. To examine the impact of the synthesis parameters on the crystal structure, a series of experiments were conducted to investigate the impact of synthesis parameters, including pre-intercalated ions, additive concentrations, and synthesis temperature, on the crystal structure.

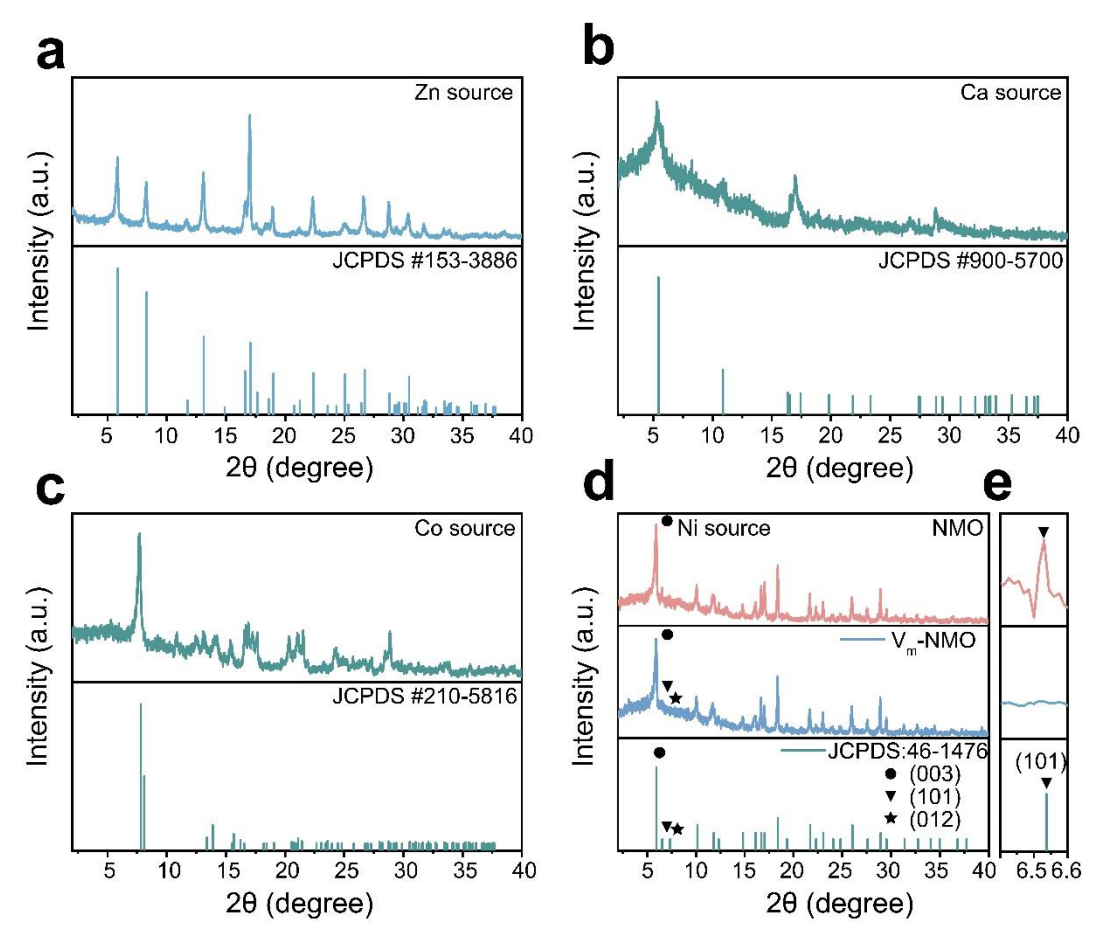


Figure 5.3 XRD characterisations of cathode materials with different pre-intercalated cations: (a) Zn²⁺; (b) Ca²⁺; (c) Co²⁺; (d) Ni²⁺; (e) Magnified Ni²⁺.

To synthesis AMn₃O₇, pre-intercalated ion act pillars supporting the interplanar spacing. After evaluating cost and the elemental abundance, Zn²⁺, Ca²⁺, Co²⁺ and Ni²⁺ were individually investigated as pre-intercalated ions. AMn₃O₇ nanoparticles were synthesised using a straightforward hydrothermal method,^[14] employing metal nitrates (Zn(NO₃)₂, Ca(NO₃)₂, Co(NO₃)₂ and Ni(NO₃)₂) as metal source. The resulting materials were characterised *via* XRD to determine their lattice structure. As shown in **Figure 5.3a**, using Zn²⁺ as the pre-intercalated ion leading to the formation of tetragonal MnO₂·H₂O_{0.15} (JCPDS: #153-3886). **Figure 5.3b** reveals a less ordered mixed phase when Ca²⁺ is used. The resulting XRD in **Figure 5.3c** shows

that Co forms a lattice structure similar to AMn₃O₇, but an additional peak around 12° indicates the presence of a mixed phase. Only pre-intercalated Ni²⁺ formed the targeting MLL AMn₃O₇ structure. The XRD pattern of the as-prepared nickel preintercalated manganese oxide (**Figure 5.3d**) matches well with Ernienickelite NiMn₃O₇·3H₂O (JCPDS: #46-1476), belonging to the hexagonal R(148)* space group with lattice constants a = 7.5293(4) Å and c = 20.752(1) Å.^[15] Additionally, structural defects and vacancies can modify the AMn₃O₇ pattern by altering the spacing between crystal planes. For simplicity, the cathode material with vacancies is referred to as V_m -NMO, and the material without vacancies is noted as NMO. The primary structural difference between V_m -NMO and NMO lies in the (101), (102) and (003) crystal planes. As shown in **Figure 5.3e**, the significant absence of (101) and (102) in the V_m -NMO lattice indicates changes in the crystal structure, which can be due to preferred orientation and preferred crystal growth during the synthesis. Furthermore, the intensity of the (003) lattice plane in V_m -NMO sample is significantly lower than in NMO, indicating disrupted long-range order and increased lattice disorder in V_m -NMO.

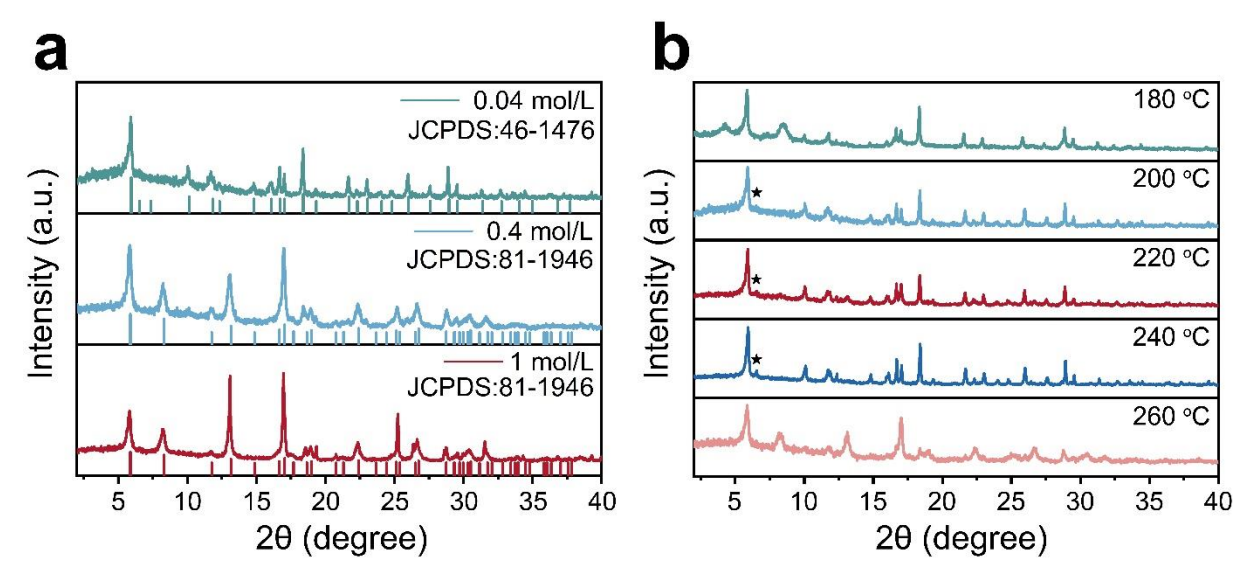


Figure 5.4 XRD characterisations of cathode materials synthesised under varying conditions: (a) NH₄Cl concentrations; (b) Temperatures.

Further synthesis experiments focused on tuning the lattice structure and lattice vacancies in NiMn₃O₇ by adjusting the synthesis additive concentration and the synthesis temperature. As shown in **Figure 5.4a**, the XRD characterisations on materials synthesised with different NH₄Cl concentrations indicate that the optimal NH₄Cl concentration for NiMn₃O₇ formation is 0.04 mol L⁻¹. NH₄Cl concentrations exceeding 0.4 mol L⁻¹ result in a phase transition from

NiMn₃O₇ to α-MnO₂. As shown in **Figure 5.4b**, XRD results on materials synthesised at different temperatures demonstrate that the formation of vacancies in NiMn₃O₇ is highly sensitive to temperature. Temperatures below 180°C lead to mixed-phase products. The optimised synthesis temperature for NiMn₃O₇ with vacancies is 200°C, evidenced by the absence of (101) and (102) lattice plane peak, and all other peaks match well with the JCPDS: #46-1476, the V_m-NMO sample is synthesised at 200°C. Lattice vacancies start to disappear when the synthesis temperature increases to 220°C, as indicated by the increased intensity of the (101) and (102) lattice peaks. The lattice plane became mature, and the lattice vacancies disappear when the synthesis temperature increased to 240°C, which is evidenced by the further increased intensity of (101) and (102) peaks. The NMO sample is synthesised at 240°C. Further temperature above 260°C cause a phase transition from NiMn₃O₇ to NiMn₂O₄. These results indicate that the (101) and (102) peaks act as indicators for lattice vacancies in NiMn₃O₇. The optimised conditions for the maple-leaf lattice structure AMn₃O₇ with lattice vacancies are Ni²⁺ pre-intercalation, 0.04 mol L⁻¹ NH₄Cl additive concentration, and 200°C synthesis temperature. In Chapter 5, to further investigate the lattice vacancies and relevant mechanism, V_m-NMO was chosen to represent NiMn₃O₇ sample with lattice vacancies, while NMO synthesised at a higher temperature of 240°C was used to represent NiMn₃O₇ materials without lattice vacancies. These changes in the lattice can further lead to differences in the physical and chemical properties of V_m-NMO and NMO.

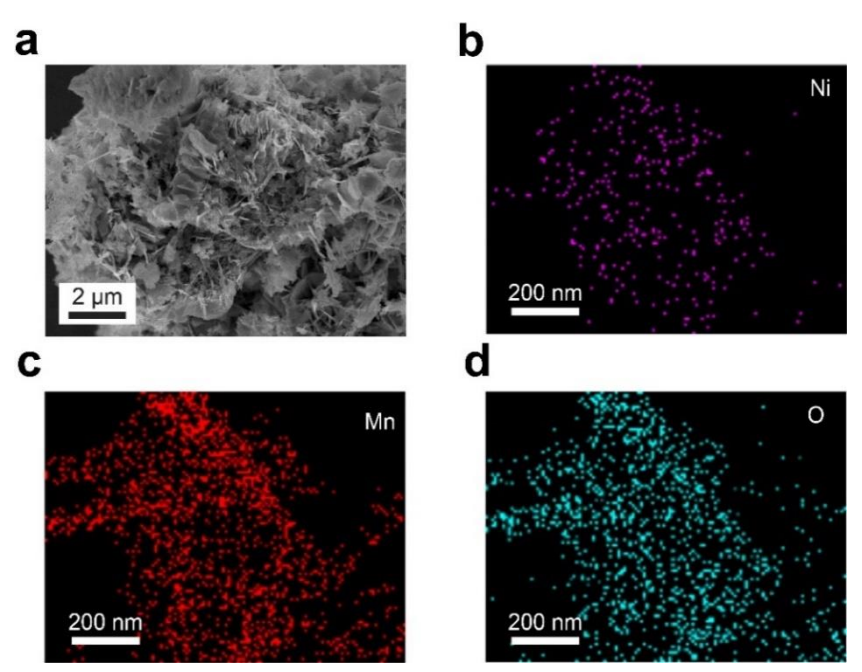


Figure 5.5 Microscopy characterisations for V_m-NMO: (a) SEM image for V_m-NMO; (b) EDS mapping images of V_m-NMO: (b) Ni; (c) Mn; (d) O.

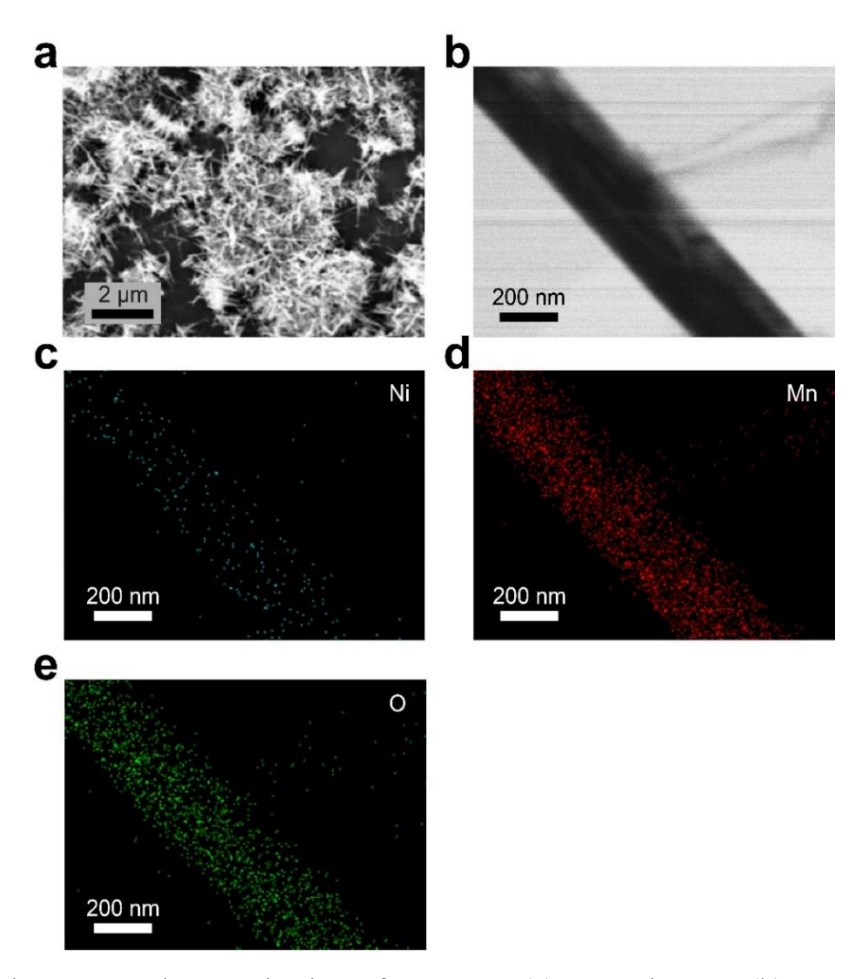


Figure 5.6 Microscopy characterisations for NMO: (a) SEM image; (b) TEM image. EDS mapping images: (c) Ni; (d) Mn; and (e) O.

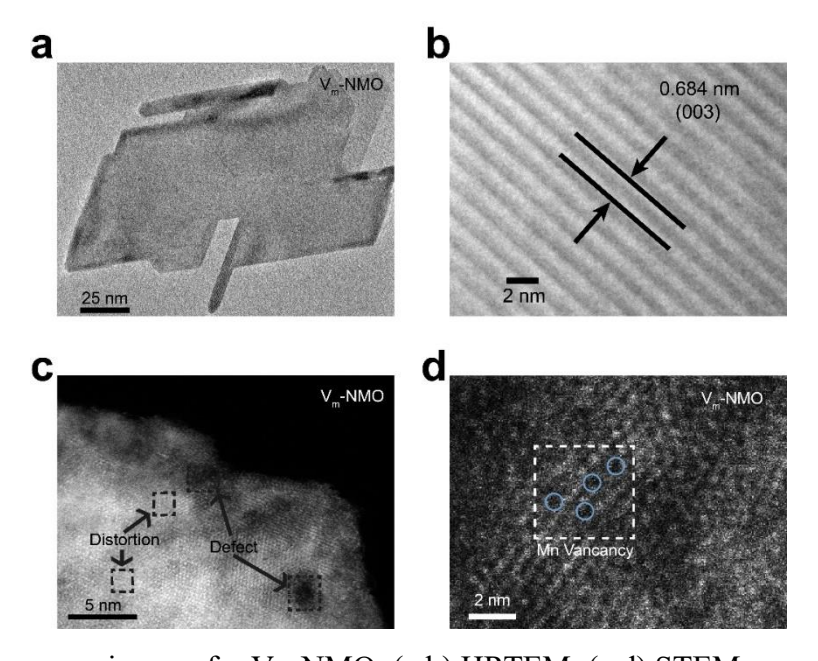


Figure 5.7 Microscopy images for V_m-NMO: (a,b) HRTEM; (c,d) STEM.

Scanning electron microscope (SEM) was used to analyse the morphology of V_m-NMO, revealing a homogeneous three-dimensional flower-like particle structure composed of nanoplates, as shown in **Figure 5.5a**. The elemental mapping results demonstrated that Ni, Mn, and O are uniformly distributed across V_m-NMO nanoplates (Figure 5.5 b-d) In contrast, the morphology of NMO displayed a cactus-like particles structure composed of nanorod (Figure 5.6b). The elemental mapping results demonstrated that Ni, Mn, and O are uniformly distributed across NMO nanorods (Figure 5.6 c-e). V_m-NMO nanoplates exhibited an average length of approximately 150 nm, as observed through TEM (Figure 5.7a). An inter-layer distance of 0.68 nm in the V_m-NMO was illustrated by high-resolution transmission electron microscopy (HRTEM) (Figure **5.7b**), which corresponds to the (003) lattice plane in V_m-NMO. This lattice space result is consistent with relevant XRD findings. The inter-layer distance of 6.8 Å provide a sufficient channel for the hydrated zinc-ions to transfer in the NiMn₃O₇. STEM images provide atomic-level insights into lattice distortion and defects within V_m-NMO lattice. As shown in **Figure 5.7d**, atomic-resolution STEM images of V_m-NMO show direct evidence of atomically scattered Mn vacancies distributed throughout the V_m-NMO nanoplate, which is in line with the XRD results. These comprehensive characterisation confirm that the lattice vacancies in the V_m-NMO material, highlight that these vacancies can be effectively tuned by optimising the synthesis parameters.

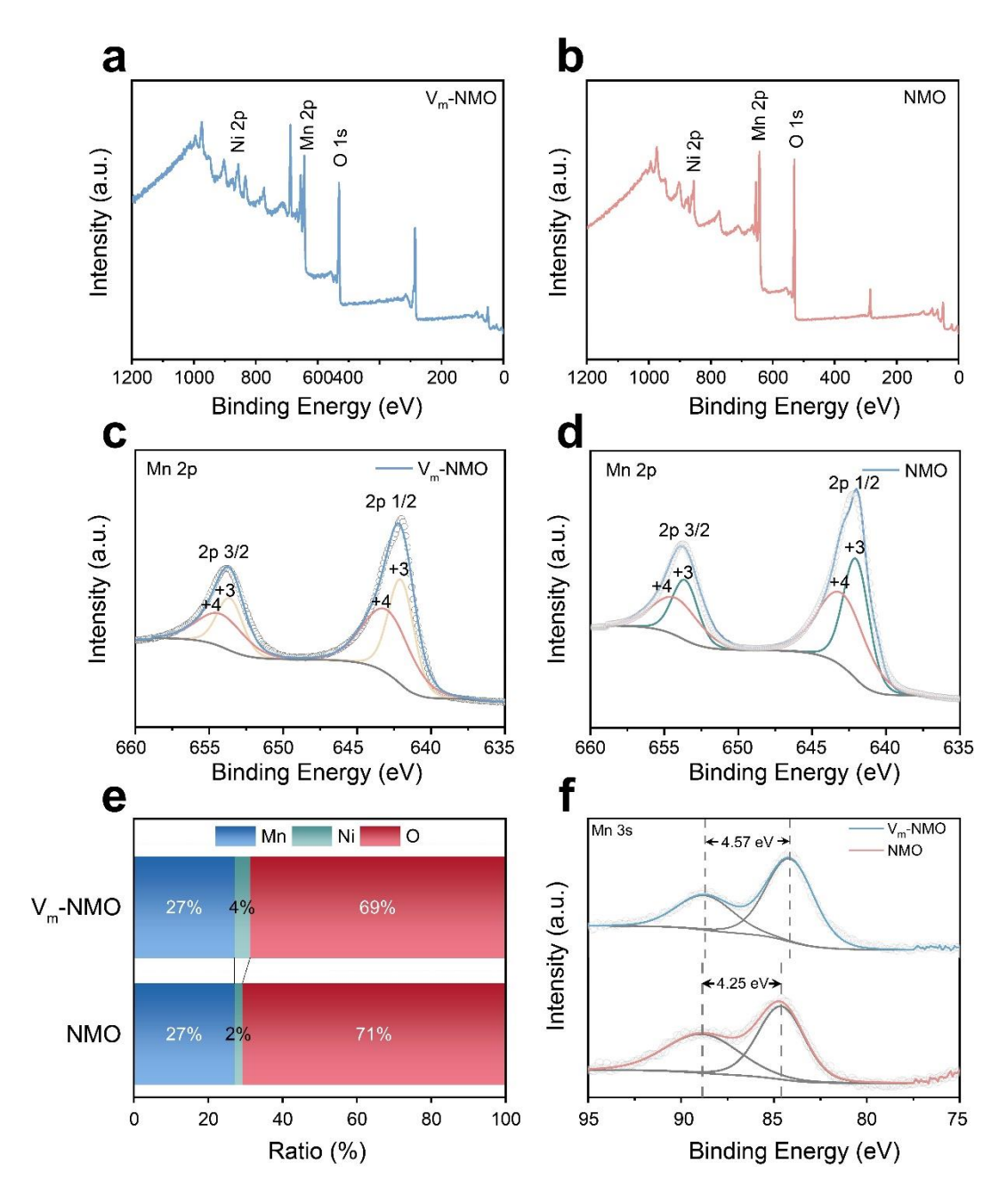


Figure 5.8 XPS spectra of cathode materials: (a) V_m-NMO XPS survey; (b) NMO XPS survey; (c) V_m-NMO Mn 2p; (d) NMO Mn 2p; (e) Elemental ratio; (f) Mn 3s.

The existence of vacancies in the lattice structure has a significant influence on the chemical valence and coordination environment of the cathode materials. The valence of the as-prepared cathode materials was investigated by XPS. As shown in **Fig. 5.8c** and **Figure 5.8d**, the Mn 2p XPS profiles exhibit two distinct peaks in both V_m -NMO and NMO materials, illustrating the co-existence of Mn^{3+} and Mn^{4+} . Additionally, the Ni/Mn ratio in V_m -NMO is higher than that in the NMO material. As shown in **Figure 5.8e**, the normalised ratios of Ni, Mn, and O in V_m -NMO is about 4:27:69, while the ratio in NMO is 2:27:71, indicating that V_m -NMO have a

higher nickel content. This difference is attributed to the presence of cation vacancies in V_m-NMO^[16, 17]. In the crystal structure, cation vacancies create local geometrical distortions and changes in the coordination of neighbouring atoms, leading to an altered distribution of cations within the material. Ni and Mn have similar ionic radii, making Ni a suitable substitute for Mn in the crystal lattice.^[18, 19] These nickel ions have two roles: first, nickel ions serve as pillars to support the lattice structure, second is that these nickel ions could accommodate the dynamic changes during cycling.^[20]

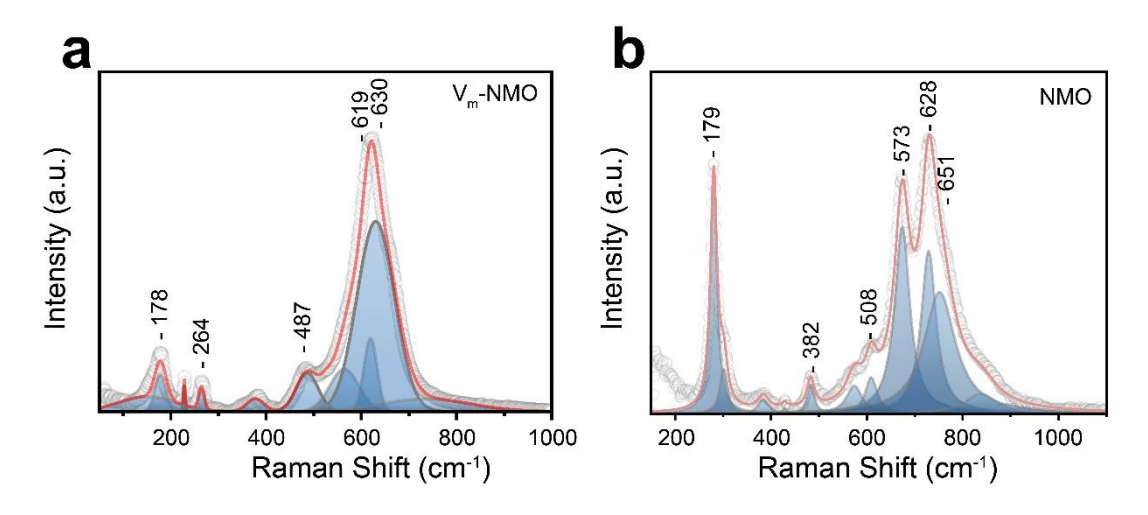


Figure 5.9 Raman spectra of cathode materials: (a) V_m-NMO; (b) NMO.

The existence of vacancies in the NiMn₃O₇ structure can have an impact on the arrangement of these octahedra and how they connect to each other in the crystal structure. As the [MnO₆] octahedral structure is the fundamental building block in the chemistry of manganese oxides. Raman spectroscopy was utilised to examine the intricate structural distinctions between V_m-NMO and NMO, employing an excitation wavelength of 532 nm. The Raman profile of V_m-NMO exhibits three distinct bands in the range of 450 - 700 cm⁻¹ (**Figure 5.9a**): Raman peaks features at ~490 and ~620-640 cm⁻¹ assigned to out-of-plane Mn-O vibrations perpendicular to the layers and Raman peak around 570 cm⁻¹ correspond to in-plane Mn-O stretching vibration along with the octahedral layers in V_m-NMO. Raman features of NMO with different vibrational modes were shown in **Figure 5.9b**. A dominant in-plane Mn-O stretching vibration was observed at 571 cm⁻¹, and an out-of-plane Mn-O vibration was found at 621 cm⁻¹. These Raman results on in-plane and out-of-plane bands changes indicate that the vacancies in V_m-NMO could lead to the changes in the coordination states of octahedral Mn cations and structural distortions of the related Mn-O environments.^[21-23]

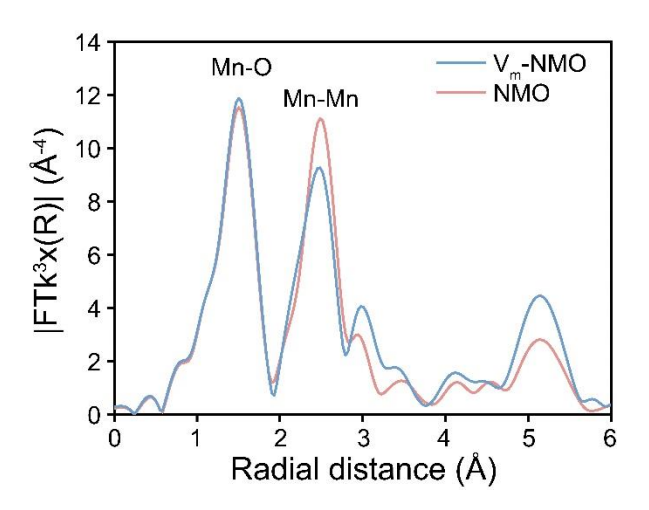


Figure 5.10 XAFS fitting on the Mn-Mn coordination numbers.

The comprehensive analysis of the coordination states differences between V_m -NMO and NMO was investigated by X-ray absorption fine structure analysis. The k^3 -weighted Fourier transform of the extended X-ray absorption fine structure (EXAFS) can provide information about the local atomic environment surrounding Mn atoms. ^[24] The Mn K-edge EXAFS spectrum of the as-prepared materials showed two peaks located at 1.5 Å and 2.5 Å, corresponding to the Mn-O (the six coordinated oxygen atoms coordinated to the nearest manganese atom) and Mn-Mn (the six manganese atom coordinated *via* edge-sharing through oxygen atom within [MnO₆] octahedral slab) shells, respectively. The position and intensity of these peaks provide information about the Mn-O and Mn-Mn bond length and coordination number in the NiMn₃O₇ material (**Figure 5.10**). A reduction in ratio of Mn-Mn/Mn-O peak intensity was observed in the V_m -NMO sample, suggesting a reduction in the coordination number of Mn cations in the V_m -NMO material. This reduction supports the presence of Mn vacancies in V_m -NMO^[25, 26]

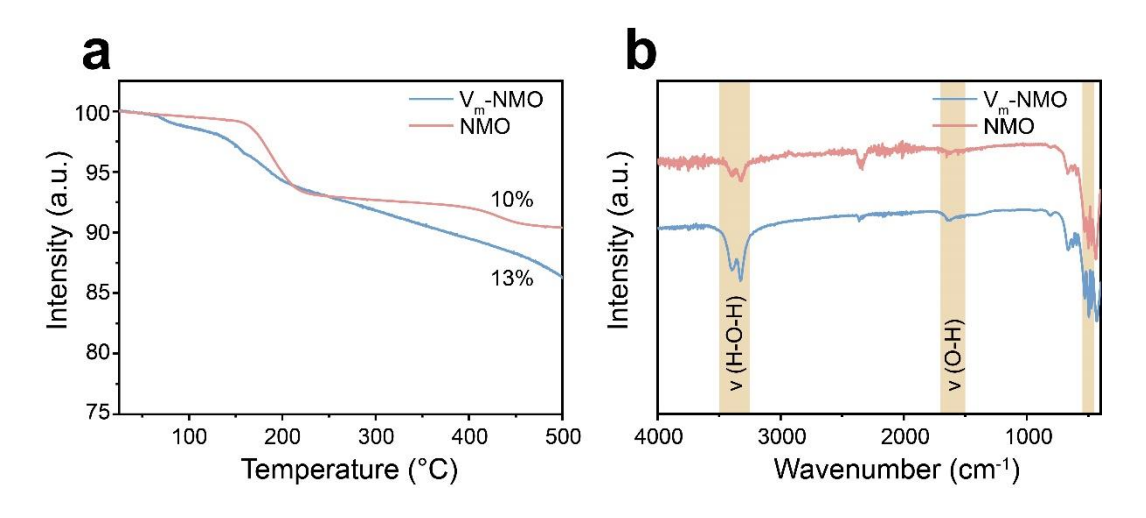


Figure 5.11 (a) TGA analysis of cathode materials; (b) FTIR spectra of cathode materials.

Another important characteristic of the NiMn₃O₇ layered material is the presence of the crystal lattice water. Previous research indicates that the lattice water molecules are located in the interlayer spaces of layered manganese oxide [27-30]. The crystal water content in the cathode materials was confirmed by TGA, the samples were preheated at 100 degree to get rid of the adsorbed water. Figure 5.11a shows that V_m-NMO contains 13% lattice water, consistent with the chemical formula NiMn₃O₇·3H₂O. In comparison, NMO lost 10% of weight during TGA testing. TGA results indicate that V_m-NMO has a higher crystal water content, which could contribute to building a continuous hydrogen bond network and screening the electrostatic interaction between charge carriers and the host framework.^[31] Further investigation on the chemical environment and the water vibrational information in the as-prepared materials were performed by Fourier transform infrared spectroscopy (FTIR) measurements. As shown Figure 5.11b, A series of absorption peaks appears in both samples, these can be assigned to different metal oxide vibration modes: Mn-O (530-570 cm⁻¹, 600-620 cm⁻¹), Ni-O (480-490 cm⁻¹), and the vibration of O-H, H-O-H (3,200-3,400 cm⁻¹) in crystal water, respectively. [32-34] The intensity of the water vibration signals in V_m-NMO is stronger than that in NMO, indicating that V_m-NMO contains more lattice water, which match the TGA results. The rich lattice water content can build up continuous H-bond network, which can contribute to the electrode wettability and ion migration from the electrolyte into the cathode material interlayer space.[35]

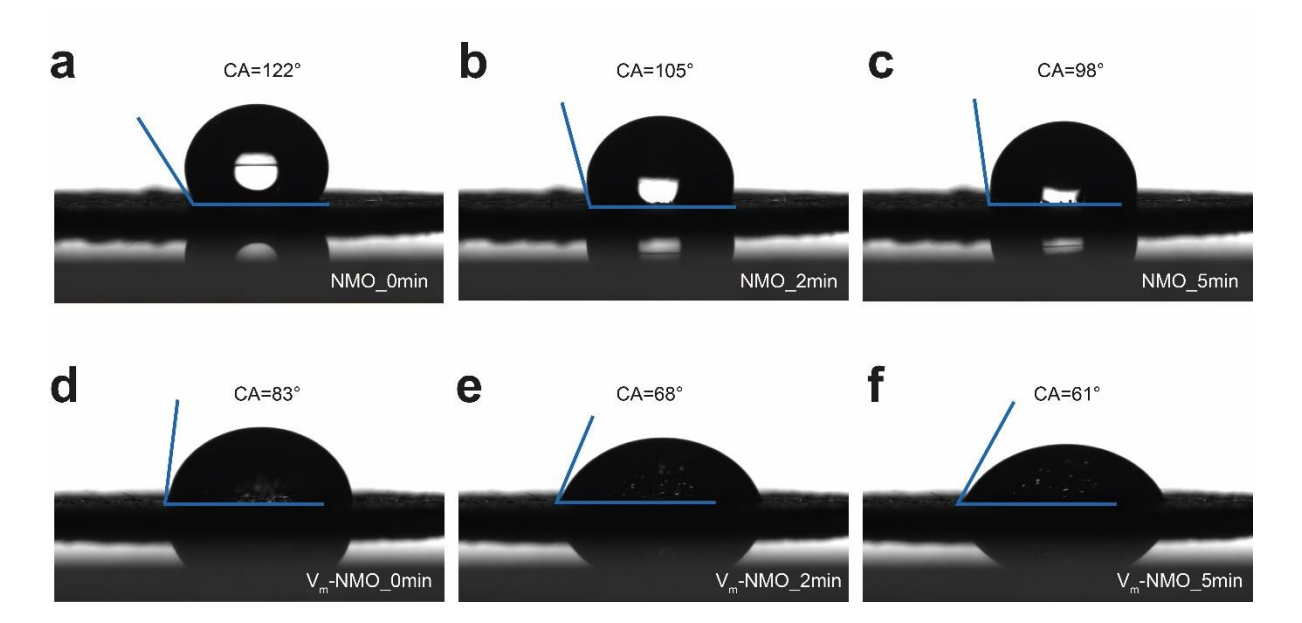


Figure 5.12 Contact angle measurements of 3 M $Zn(OTf)_2$ electrolyte on cathodes: (a-c) NMO; (d-f) V_m -NMO.

The wettability of an electrolyte on different cathode materials is directly illustrated by the contact angle measurement. As shown in **Figure 5.12a**, initial contact angle of the V_m-NMO is 83°, which is significantly smaller than the contact angle of NMO (122°, **Figure 5.12d**). Additionally, V_m-NMO appears to absorb the aqueous electrolyte more efficiently, with the contact angle of V_m-NMO reducing to 68° after 2 minutes (**Figure 5.12e**), while the contact angle for NMO remains around 105° in NMO (**Figure 5.12b**). These results demonstrate that V_m-NMO has improved wettability and enhanced ion accessibility compared to NMO in aqueous electrolytes.

These characterisations demonstrate that compared with NMO, V_m-NMO has a richer lattice water content, higher Ni²⁺ content and certain content of cation vacancies, these properties lead to increased electrolyte/cathode wettability and ion accessibility, contributing to the improved ion transfer mechanism in NiMn₃O₇.

5.3.2 DFT simulation on proton transfer

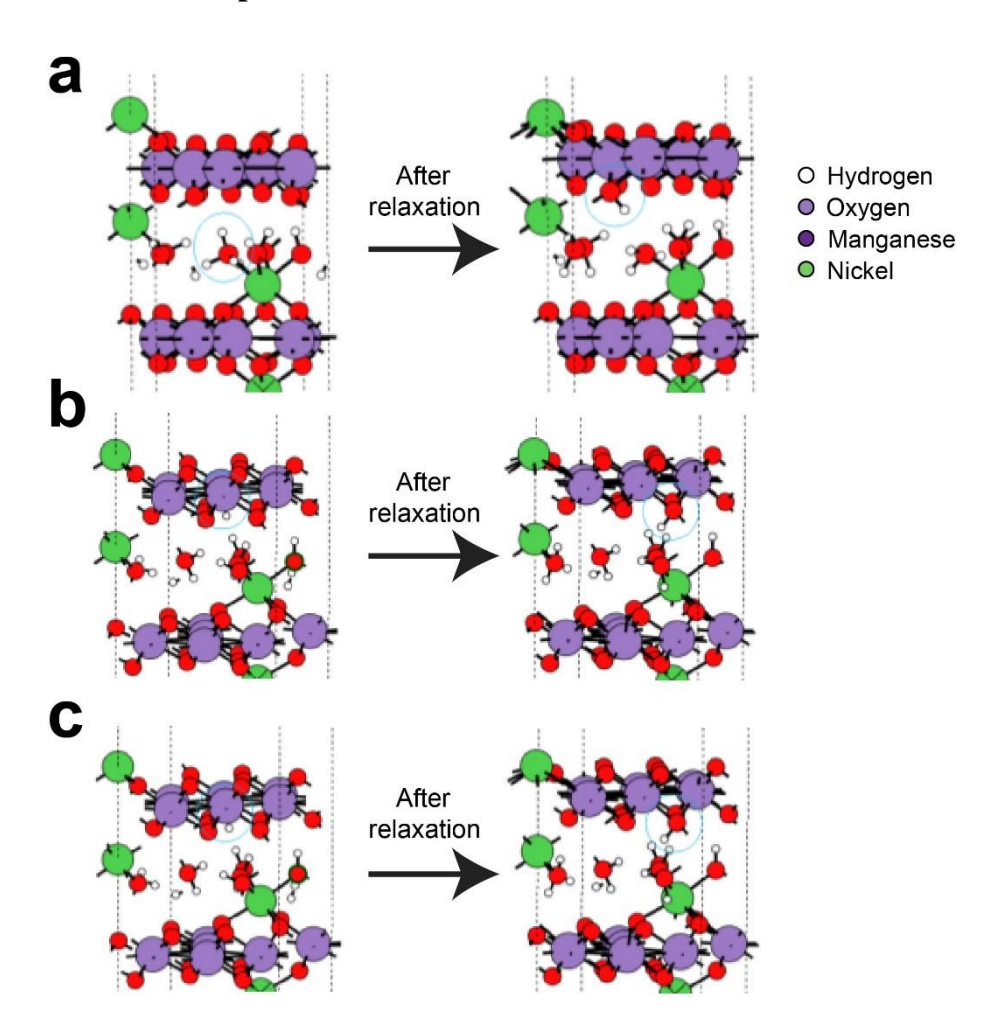


Figure 5.13 Adsorption of proton (a) on inter-layer water molecules; (b) on the Mn^{4+} ion; (c) on the O^{2-} ions of the NiMn₃O₇ layer.

The computational simulation reported in this chapter were conducted in collaboration with Dr. Arunabhiram Chutia from the School of Chemistry, University of Lincoln. The related part was rewritten according to the results. To further gain further insight into the charge transfer mechanism in NiMn₃O₇ system with and without cationic (Mn⁴⁺) vacancies, DFT based quantum chemical calculations were performed using the Vienna Ab initio Simulation Package (VASP).^[36,37] The adsorption of a proton was carried out around an Mn⁴⁺ defect, i.e., (i) on an O²⁻ ion next to the defect site (**Figure 5.13a**), (ii) on another O²⁻ ion away from the defect site (**Figure 5.13b**)and (iii) on the defect site (**Figure 5.13c**). The relaxed structures showed that in the first and second cases, the proton remained bonded to the O²⁻ ions, but in the third case, as expected, the proton migrated to a nearby O²⁻ ion close to the defect site.

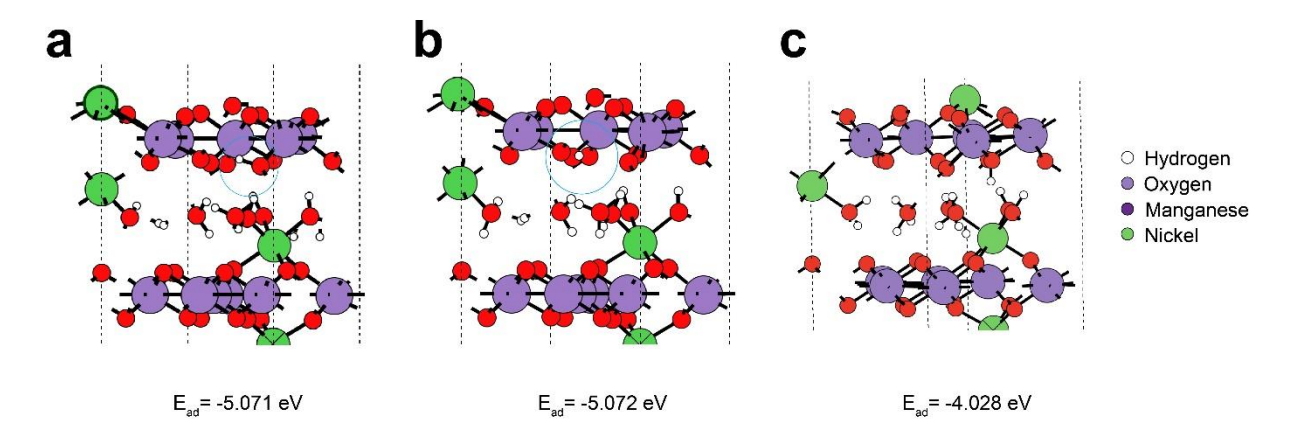


Figure 5.14 DFT simulation of proton adsorption sites in NiMn₃O₇ with and without Mn⁴⁺ vacancies.

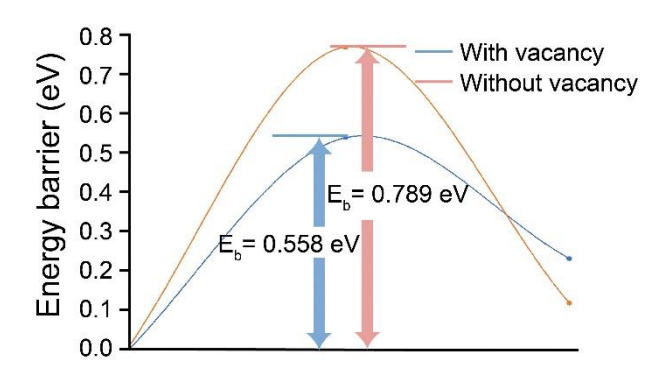


Figure 5.15 DFT simulation of the migration energy barrier of NiMn₃O₇ lattice with and without vacancies.

The computational adsorption energies of protons in pristine NiMn₃O₇ models without Mn⁴⁺ vacancies range from -2.97 eV to -3.07 eV. In the models with Mn⁴⁺ vacancies, the range is -4.03 eV to -5.07 eV (**Figure 5.14**). These results suggest that protons exhibit greater stability

in V_m -NMO systems due to the presence of cationic vacancies. The Bader charges of -1.13 eV and -1.21 eV on the O^2 -, respectively for NiMn₃O₇ systems without and with Mn⁴⁺ respectively indicate that this may be due to relatively larger charge localisation in the defective model. Additionally, within the NiMn₃O₇ system with Mn⁴⁺ defect, it found that when protons are adsorbed on the O^2 - ions close to the defect site, they are \sim -1.04 eV more stable than when they are slightly further away. This difference indicates that the protons could easily hop to a site closer to the defect site. As shown in **Figure 5.15**, the calculated energy barriers for proton hopping between two consecutive O^2 - ions in the absence (i.e., 0.79 eV) and presence (i.e., 0.56 eV) further support these findings. In conclusion, DFT calculations demonstrate that Mn⁴⁺ vacancies serve as a driving force for the Grotthuss-like proton hopping in NiMn₃O₇.

5.3.3 Ex-situ characterisation

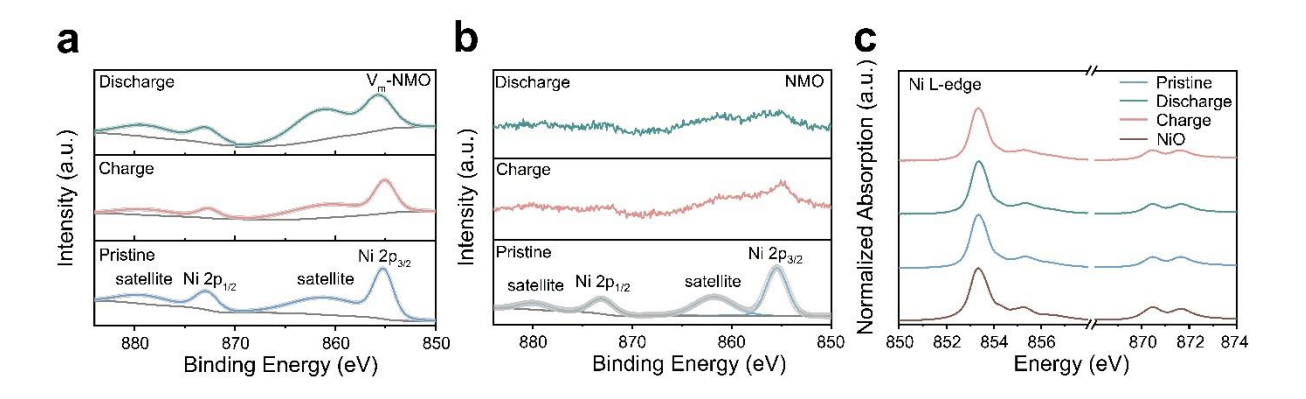


Figure 5.16 *Ex-situ* Ni 2p characterisation of cathode materials: (a) V_m-NMO; (b) NMO; (c) NEXAFS profiles of Ni L-edge of cathode materials in different states.

The octahedral layers in NiMn₃O₇ are separated by tetrahedral voids occupied by nickel cations. [13, 38] The dynamic behaviour of nickel ions was further investigated by *ex-situ* Ni 2p XPS and *ex-situ* Ni L-edge NEXAFS characterisation. **Figure 5.16a** demonstrates a persistent Ni 2p signal in various states, confirming the stability of nickel atoms in the cathode material. This indicates that the nickel atoms remain in the V_m-NMO lattice during charging and discharging cycles, with interlayer nickel ions compensating for the charge imbalance caused by cation vacancies and contributing to cycling stability. In contrast, the Ni 2p XPS intensity of the cycled NMO electrode decreased, indicating nickel deintercalation occurs in the NMO electrodes upon cycling (**Figure 5.16b**). Ni L-edge NEXAFS spectroscopy provides valuable information about the oxidation state of Ni and the coordination environment of Ni atoms in the cathode materials. The peak A (853 eV) and peak B (855 eV) are attributed to transitions

from Ni 2p 3/2 core level to the unoccupied 3d orbitals and unoccupied 4p orbitals, respectively. The intensity of these two peaks depends on the oxidation state of the Ni ions and is sensitive to changes in the local coordination environment of the Ni atoms. The multiple peaks in **Figure 5.16c** illustrate the high spin Ni²⁺ electronic structure and its octahedral coordination structure. The intensity and peak position for Ni²⁺ remain stable in the charging and discharging states, indicating that Ni²⁺ is electrochemically stable in the V_m-NMO lattice. The nickel stability difference between V_m-NMO and NMO in the *ex-situ* characterisation indicates that nickel ions are not just pre-intercalated pillar ions, they also facilitate the ongoing mobility of hydrated protons by counterbalancing the periodic dynamic changes caused by Grotthuss proton migration and preserving the system's electrical neutrality.

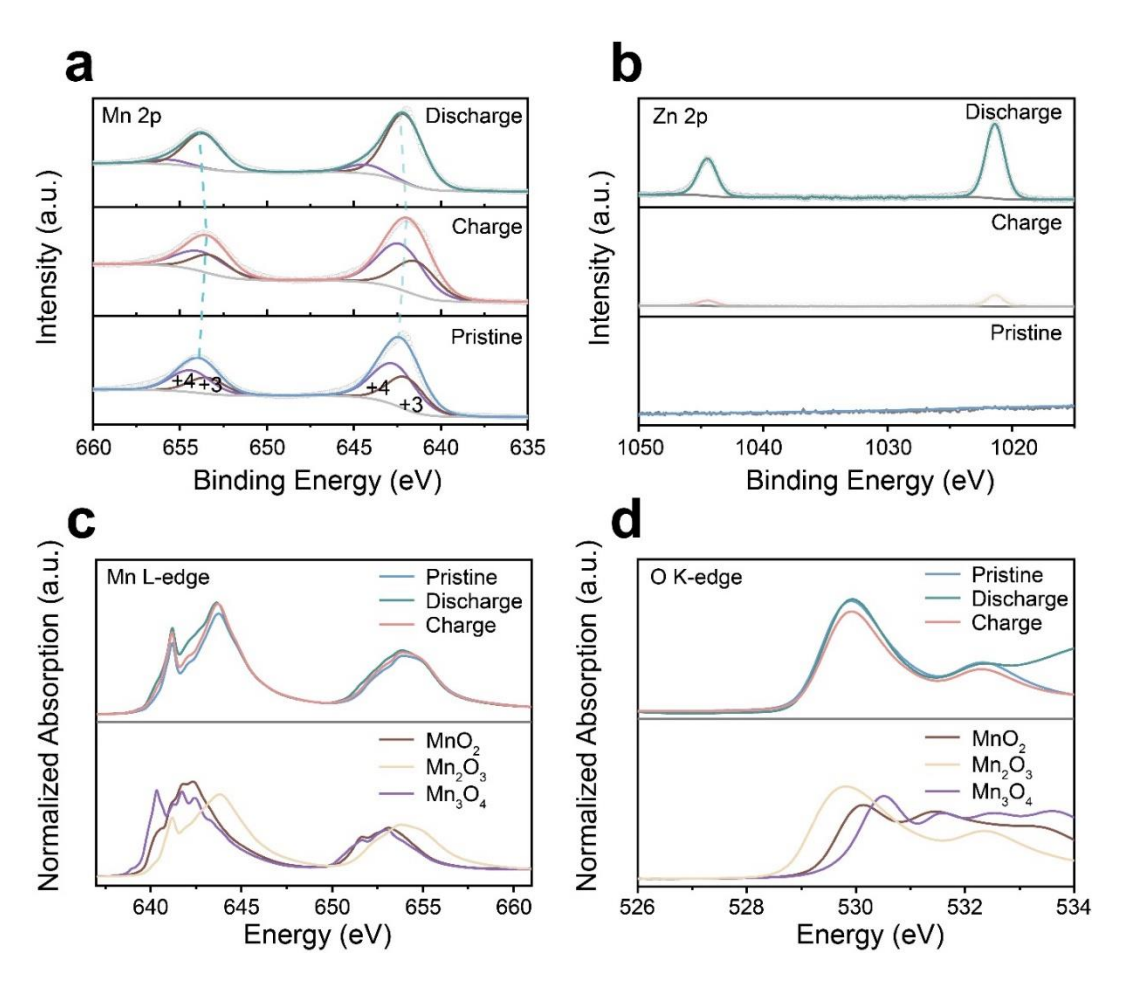


Figure 5.17 *Ex-situ* characterisation of V_m-NMO. *Ex-situ* XPS profiles of V_m-NMO: (a) Mn 2p; (b) Zn 2p; (c) *Ex-situ* Mn L_{3,2}-edge NEXAFS profiles; (d) *Ex-situ* O K-edge NEXAFS profiles.

Ex-situ XPS tests were conducted to uncover the valence changes during charging and discharging.^[39] Figure 5.17a illustrates the typical manganese valence transitions observed in AZIBs. The Mn 2p spectra fitting results, featuring two deconvoluted peaks, indicate the

coexistence of Mn valence states. [40] In the discharging state, the manganese valence peak position undergoes a negative shift, signifying the reduction of manganese oxide compared to the pristine state due to charge carrier intercalation. During the charging process, Mn 2p peaks shift positively toward the pristine position, indicating reversible valence changes^[41-45]. Zn 2p peaks in Figure 5.17b reveal the reversible intercalation/deintercalation of zinc ions in the V_m-NMO cathode material. The reversible zinc ion intercalation also confirms that zinc ion transport is not influenced by the Grotthuss mechanism, and its intercalation behaviour differs from the proton hopping. To better understand the Mn element in the V_m-NMO cathode material during cycling, Mn L-edge Near Edge X-ray Absorption Fine Structure (NEXAFS) spectra provided insights into the local bonding environment of manganese atoms in the cathode material. The pristine state spectrum exhibits multiple peaks corresponding to different electronic transitions and variations in the coordination environment with oxygen atoms, namely A (638-639 eV, 2p-3d, octahedral), B (641-642 eV, 2p-3d, tetrahedral), C (643-644 eV, 2p-3d, mixed octahedral and tetrahedral sites). [46] This indicates that the Mn ions in V_m-NMO can occupy both octahedral and tetrahedral sites, particularly those situated at the edge or corner sites of MnO₆ octahedral units. The crystal structure of V_m-NMO comprises edgesharing MnO₆ octahedra layers interconnected by sharing corners with other octahedra. **Figure** 5.17c of Mn L_{3,2}-edge NEXAFS reveals that the shape of V_m-NMO in the charging and pristine state resembles MnO₂(IV), verifying that pristine valence is close to +4 and Mn valence can be reduced to pristine in the charging state. The systematic shift of the L₃ leading edge position and gravity centre of the L₃/L₂ edge towards lower energies is observable in the fully discharging state, indicating that the Mn oxidation state in the discharging state is lower than in the pristine state and the fully charging state. Additionally, the Mn L-edge intensity between 641-642 eV increased in the discharging state, the similarity in the peak shape to Mn³⁺, indicating a reduction to a valence close to Mn(III) in the discharged state after zinc ion intercalation. Moreover, O K-edge NEXAFS spectra, determined by the hybridisation of O 2p and Mn 3d states, lead to electron transitions from ligand O 1s orbitals to unoccupied transition metal 3d orbitals. In Figure 5.17d, the O K-edge spectra include several distinct peaks around 529 eV and 532 eV. In the pristine and fully charging state, two absorption peaks can be identified due to the Mn(IV) with a $3d^3 (t_{2g}^3 e_g^0)$ configuration, while a lower energy peak belongs to spin-down t_{2g} and spin-up e_g transitions, and a higher energy peak originate from the spin-down e_g transitions. In the fully discharged state, the peak intensity increases with a

broad absorption peak identifiable between 530-531 eV, caused by the Mn(III) content with a $3d^4(t_{2g}^3e_g^1)$ configuration.

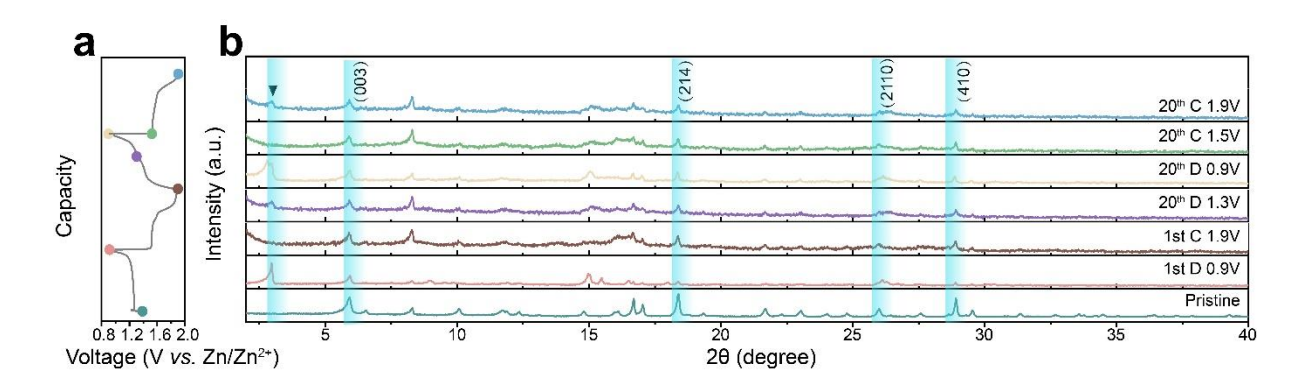


Figure 5.18 Ex-situ XRD characterisation of the V_m-NMO cathode material.

The lattice structure changes were further illustrated by *ex-situ* XRD, **Figure 5.18** shows the characteristic peaks associated with the discharging process of the V_m-NMO electrode. The appearance and disappearance of the zinc hydroxide trifluoromethyl sulfonate peak at a low angle (around 2.7°) indicate proton intercalation during the discharging process^[47, 48]. Consistent with numerous manganese-based materials studies, zinc hydroxide trifluoromethyl sulfonate forms through the integration of OH, Zn(CF₃SO₃)₂, and H₂O in the electrolyte resulting from proton transfer to the V_m-NMO electrode.^[49, 50] The characteristic peaks disappear in the subsequent charging phase, implying that the phase transfer of V_m-NMO during charging and discharging process is reversible. The formation and disappearance of XRD characteristic peaks highlight reversible proton transfer during the discharging process. Additionally, the characteristic XRD peaks (003), (214) and (2110) exhibit highly reversibility during the *ex-situ* XRD characterisation, demonstrating the reversibility of V_m-NMO material.

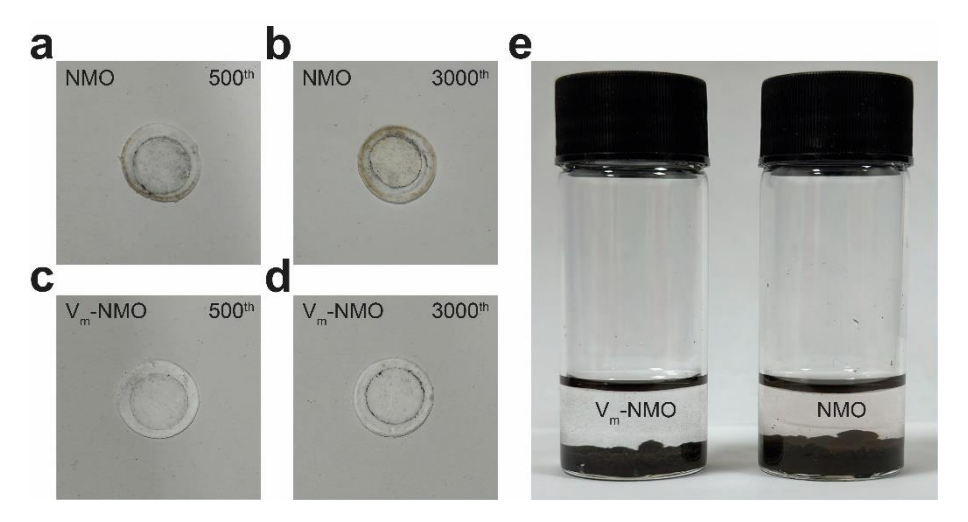


Figure 5.19 Digital images: (a-d) Unfolded separators after cycling; (e) V_m-NMO and NMO materials immersed in electrolyte for seven days.

To directly compare the Mn dissolution and the stability between V_m-NMO and NMO cathode materials. The optical microscopy of the separators was conducted after the cathode materials V_m-NMO and NMO were cycled in coin-cells under 2 A g⁻¹. These images highlight the extent of Mn dissolution from the cathode material during cycling (**Figure 5.19 a-d**). The NMO cathode material shows obvious dissolution at 500 cycles and the dissolution spreads across the entire separator after 3,000 cycles. In contrast, the V_m-NMO material shows significantly less dissolution, which indicates the stability of V_m-NMO. Immersion experiments were conducted to evaluate the stability of cathode materials in an aqueous environment. Optical microscopy revealed clear differences between the two materials; the V_m-NMO materials maintain stability, and the electrolyte stays clear and transparent, confirming the chemical stability of V_m-NMO in the electrolyte (**Figure 5.19e**). In contrast, NMO material shows a light brown colour after immersion in the electrolyte, indicating the dissolution of the NMO cathode material into the electrolyte.

5.3.4 Electrochemical characterisation

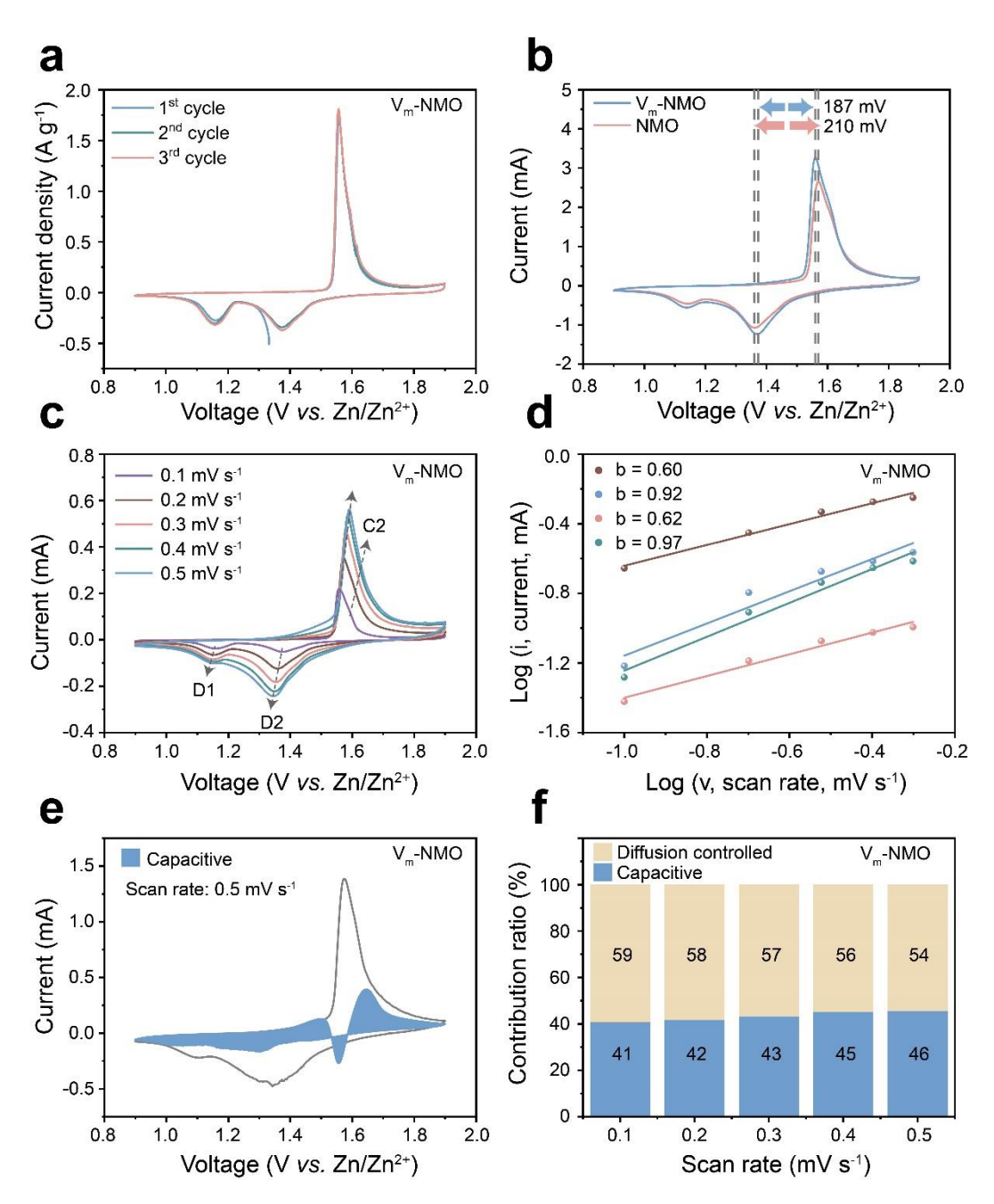


Figure 5.20 Electrochemical analysis of the cathode materials: (a) Initial three cycles of V_m -NMO CV curves after activation; (b) CV comparison of V_m -NMO and NMO; (c,d) b value fitting for V_m -NMO; (e) Capacitive contribution under 0.5 mV s⁻¹ scan rate for V_m -NMO; (f) Capacitive contribution ratio for V_m -NMO.

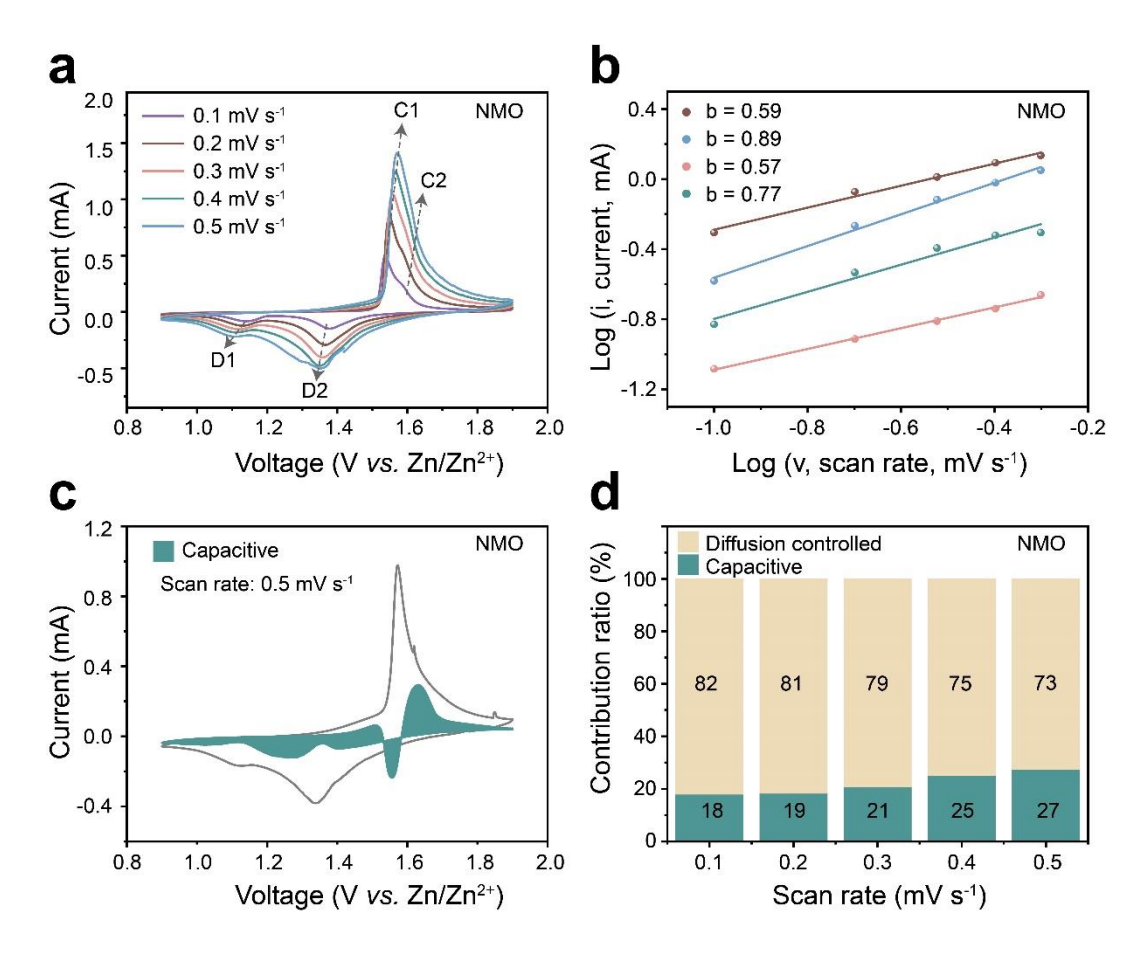


Figure 5.21 Electrochemical analysis of NMO: (a,b) b value fitting for NMO; (c) Capacitive contribution under 0.5 mV s⁻¹ scan rate for NMO; (d) Capacitive contribution ratio for NMO.

To systematically study the ion transport mechanism, the as-prepared cathode materials were investigated using CV curves in Swagelok cells with zinc metals as the anode. After activation, the V_m-NMO CV curves overlap, and the redox peaks positions are stable (**Figure 5.20a**), indicating that V_m-NMO material is highly electrochemically reversible, which is in line with the *ex-situ* XRD and *ex-situ* XPS results. The CV curves of V_m-NMO and NMO both reveal two pairs of redox peaks, corresponding to H⁺/Zn²⁺ intercalation/deintercalation. For NMO, the two redox peaks pairs are located at 1.12 V/1.63 V and 1.35 V/1.57 V, with a polarisation of 210 mV. In contrast, the V_m-NMO cathode material exhibits reduced redox reaction polarisation (187 mV), implying enhanced ion transport in the V_m-NMO material. In **Figure 5.20d**, the b values of V_m-NMO are 0.60, 0.92, 0.62, and 0.97, indicating an enhanced capacitive behaviour that could contribute to faster ion storage kinetics. In comparison, the b values of NMO (**Figure 5.21b**) are obviously lower than those of V_m-NMO, capacitive contribution ratios were revealed under different scan rates. The capacitive behaviour

contributes to 41% of overall storage at a scan rate of 0.1 mV s⁻¹, and this ratio gradually increases to 46% as the scan rate rises to 0.5 mV s⁻¹. In contrast, NMO exhibits only 18% capacitive behaviour at a scan rate of 0.1 mV s⁻¹. This difference between V_m-NMO and NMO aligns with the b value fitting results. More importantly, the redox peaks around 1.0 V, which belongs to the proton intercalation into the material during discharge. As shown in Figure **5.20e** and **Figure 5.20c**, the capacitive behaviour area in V_m-NMO around 1.0 V is significantly larger than that in NMO, this area is primarily contribute to the difference in capacitive ratios (Figure 5.20f). Diffusion control ion transport has a considerable ratio in both NMO and V_m-NMO cathode materials, which are primarily due to the ion transport of zinc ion. This indicates that zinc ion transport via diffusion co-exists with the Grotthuss mechanism. Additionally, proton hopping in V_m-NMO is less affected by increases in scanning rate during CV testing. This is due to the short ranged displacive motion of proton hopping between two adjacent hydrogen atoms is significantly more rapid than the long-range zinc ion diffusion, resulting in a reduced delay in response to changes in scanning rate. In contrast, for NMO cathode material, the capacitive control ratio is increased with the scanning rate, which indicates that diffusion behaviour dominates the ion transport in NMO cathode materials. These results indicate that an improved fast charge transfer is attributed to the fast displacive hydrated proton hopping in V_m-NMO, which is in line with the DFT simulation result that V_m-NMO have a favoured environment for proton transfer.

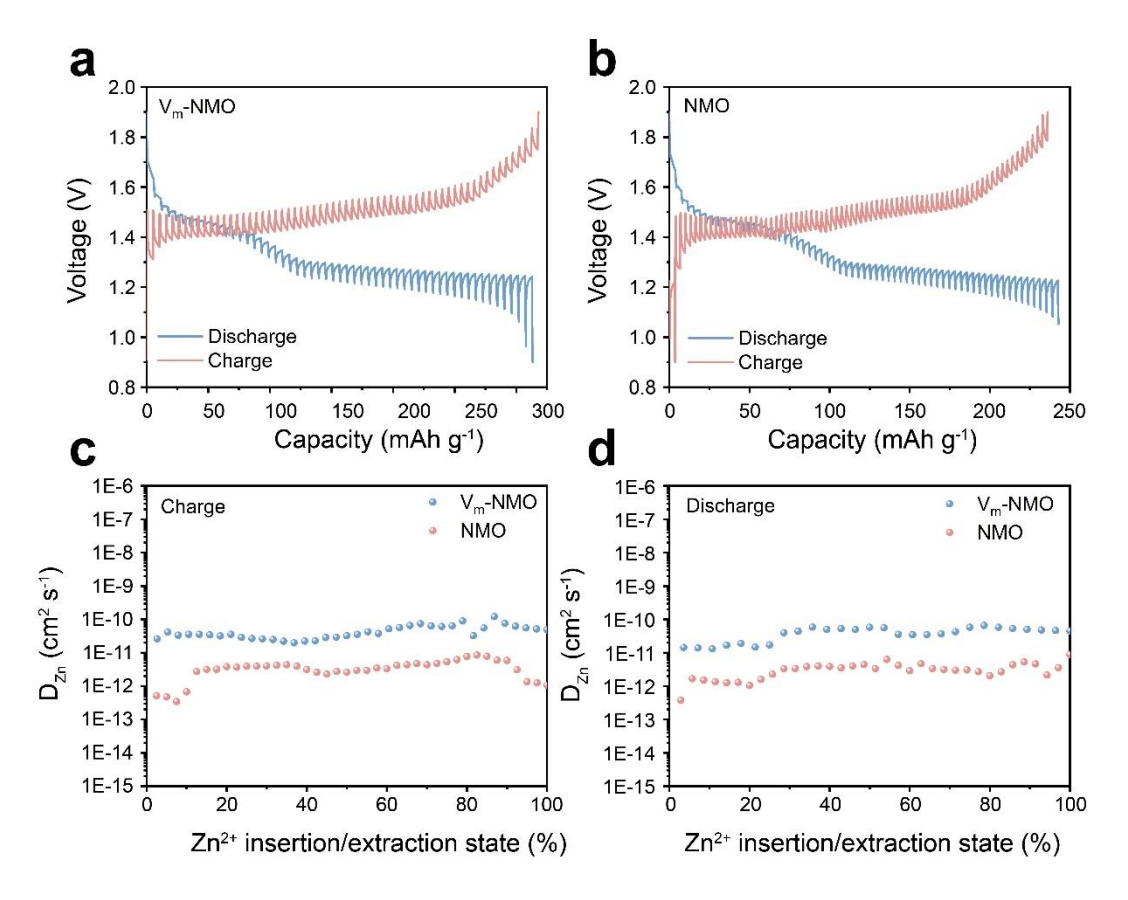


Figure 5.22 GITT testing profiles: (a) V_m-NMO; (b) NMO; Corresponding diffusion coefficient analysis: (c) Charge; (d) Discharge.

To further investigate the ion transport difference between V_m -NMO and NMO, GITT was employed to estimate the diffusion coefficient of Zn^{2+} (D_{Zn}^{2+}) with a rest time of 20 minutes. **Figure 5.22c** illustrates the NMO electrode exhibits a low D_{Zn}^{2+} (10^{-11} to 10^{-12} cm² s⁻¹) at the charge and discharge plateaus and a larger overpotential, indicating the sluggish charge/discharge mobility. In contrast, the average D_{Zn}^{2+} values of V_m -NMO are approximately 10^{-10} to 10^{-11} cm² s⁻¹, respectively. This Zn diffusivity is comparable to the Li diffusion coefficient (typically 10^{-10} cm s⁻¹) reported in the literature.

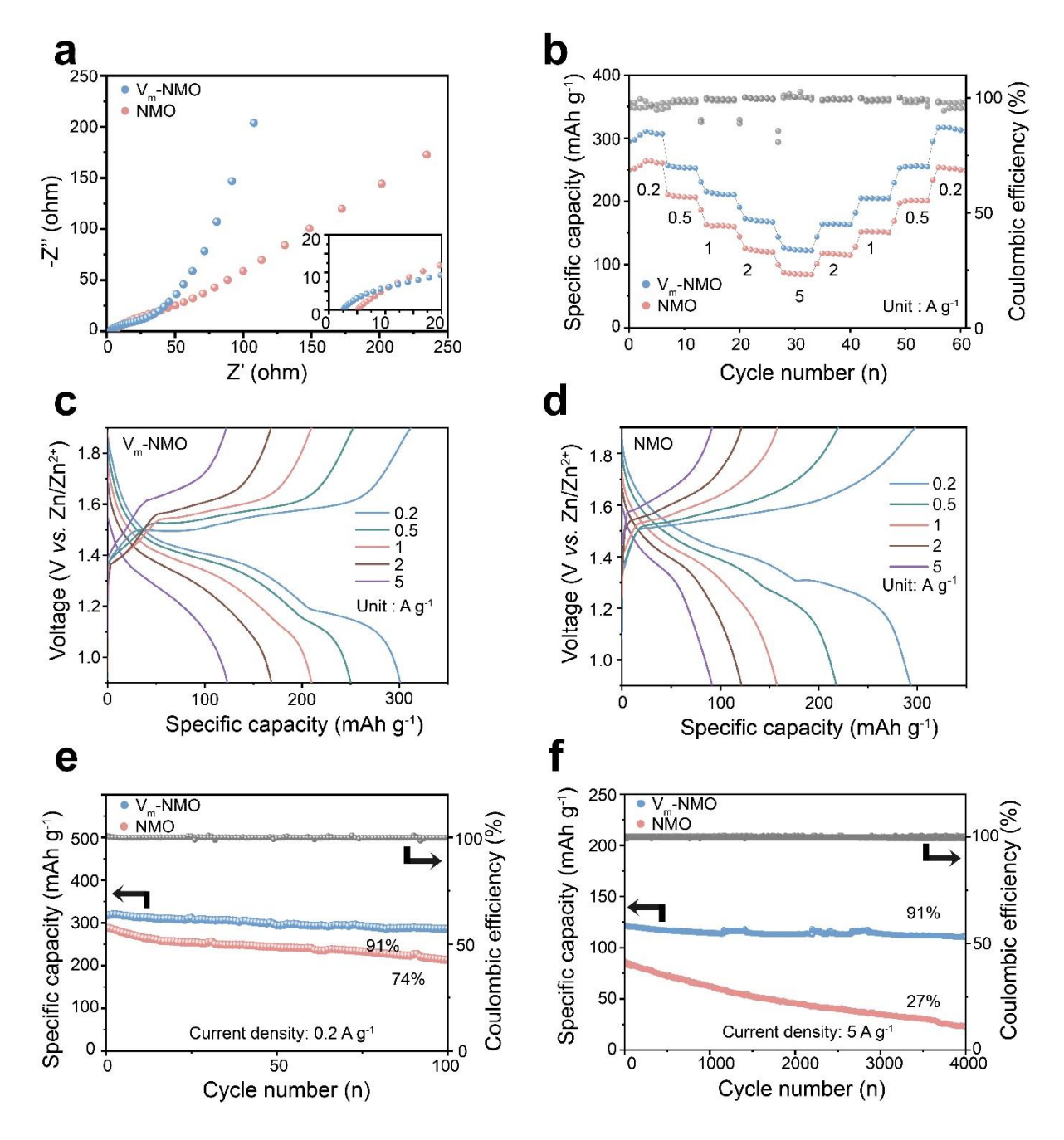


Figure 5.23 Electrochemical performances of as-prepared $Zn||V_m$ -NMO and Zn||NMO batteries. (a) EIS profiles of V_m -NMO and NMO; (b) Rate performance; Voltage-specific capacity profiles of cathode materials: (c) V_m -NMO; (d) NMO; (e) Cycling performance of V_m -NMO and NMO at 0.2 A g^{-1} ; (f) Cycling performance of $Zn||V_m$ -NMO and Zn||NMO batteries at 5 A g^{-1} .

EIS also contributes to revealing the electrochemical dynamics difference between V_m -NMO and NMO cathode materials (**Figure 5.23a**). The charge transfer resistance of V_m -NMO (43 Ω) is significantly lower than NMO (75 Ω), illustrating that manganese vacancies with a continuous hydrogen bond network within the V_m -NMO lattice could enhance charge transfer

in the system, which is in line with the GITT testing results. The rate performance of the cathode materials was tested under current densities ranging from 0.2 to 5 A g⁻¹, with eight cycles at each current density, as illustrated in **Figure 5.23b**. As the current density increases stepwise, the corresponding specific capacities of V_m-NMO were retained at 254, 215, 173 and 121 mAh g⁻¹ at 0.5, 1, 2 and 5 A g⁻¹, respectively. After the current density returns to 0.2 A g⁻¹ 1, the specific capacity recovers, demonstrating stable charge/discharge performance under different current densities. The galvanostatic charge-discharge curves of V_m-NMO and NMO cathode materials are illustrated in Figure 5.23c and Figure 5.23d, noticeable charge and discharge plateaus could be observed in V_m-NMO, with a high specific capacity of 318 mAh g⁻¹ achieved at 0.2 A g⁻¹. The V_m-NMO cathode material possesses substantial cycling performance (91% over one hundred cycles). Moreover, the specific capacity retains 38% of its original value after the current density is increased 25-fold to 5 A g-1. The remarkable rate performance enables V_m-NMO to maintain stably under high current densities, with a capacity retention of 91% over 4,000 cycles (Fig. 5.23f). In contrast, the rate performance of NMO under identical conditions is lower than that of V_m-NMO, indicating superior ion transport in the V_m-NMO cathode material, which matches the analysis on b-value and capacitive-diffusion contribution results.

5.4 Conclusion

In summary, this chapter demonstrates the synergistic collaboration between vacancies, lattice water and nickel ions on enhancing the hydrated protons hopping for high-performance zinc ion battery cathodes. Energy barrier calculations for proton transfer with and without Mn⁴⁺ vacancies indicate that proton transfer is favoured in the presence of defects. Mn⁴⁺ vacancies act as the driving force for proton hopping in the V_m-NMO systems. Additionally, the presence of lattice water molecules within the host material facilitates the migration of hydrated protons from the electrolyte to the interlayer spaces in the lattice. The simulation results indicate that protons prefer to bond with O²⁻ ions on the Mn-O layer rather than staying with water molecules. The continuous hopping of protons within the host material induces periodic, temporary local structural changes in the lattice. This dynamic behaviour alters the energy barriers for ion intercalation and deintercalation, thereby optimising their diffusion pathways. Moreover, the presence of manganese vacancies in the lattice serves as additional sites for hydrated proton and zinc ion intercalation, resulting in an increased capacity. The nickel ions increase the stability by preserving the system's electrical neutrality. The as-prepared V_m-NMO cathode

material exhibits enhanced ion transfer and a high specific capacity of 318 mAh g⁻¹ at 200 mA g⁻¹. Furthermore, it demonstrates excellent rate performances, and remarkable cycling stability, with a capacity retention of 91% over 4,000 cycles. Overall, this chapter provides insights into the utilisation of the Grotthuss mechanism and manganese oxide's distinct characteristics for the advancement of energy storage technologies. These findings highlight the potential of utilising the Grotthuss mechanism to develop high-performance energy storage materials.

5.5 References

- [1] G. Kresse, J. Non-Cryst. Solids 1995, 192-193, 222.
- [2] L. Bengtsson, Phys. Rev. B: Condens. Matter 1999, 59, 12301.
- [3] P. E. Blöchl, Phys. Rev. B: Condens. Matter 1994, 50, 17953.
- [4] J. P. Perdew, A. Ruzsinszky, G. I. Csonka, O. A. Vydrov, G. E. Scuseria, L. A. Constantin, X. Zhou, K. Burke, *Phys. Rev. Lett.* **2008**, *100*, 136406.
- [5] W. P. Davey, *Phys. Rev.* **1925**, *25*, 753.
- [6] J. Neugebauer, M. Scheffler, Phys. Rev. B: Condens. Matter 1992, 46, 16067.
- [7] S. Grimme, J. Antony, S. Ehrlich, H. Krieg, *J. Chem. Phys* **2010**, *132*.
- [8] A. M. Ferrari, C. Pisani, F. Cinquini, L. Giordano, G. Pacchioni, J. Chem. Phys 2007, 127.
- [9] C. Franchini, R. Podloucky, J. Paier, M. Marsman, G. Kresse, *Phys. Rev. B: Condens. Matter* **2007**, *75*, 195128.
- [10] W. Tang, E. Sanville, G. Henkelman, J. Phys.: Condens. Matter 2009, 21, 084204.
- [11] K. Momma, F. Izumi, J. Appl. Crystallogr. 2008, 41, 653.
- [12] K. Momma, F. Izumi, J. Appl. Crystallogr. 2011, 44, 1272.
- [13] Y. Haraguchi, A. Matsuo, K. Kindo, Z. Hiroi, *Phys. Rev. B: Condens. Matter* **2018**, *98*, 064412.
- [14] Y. Zhang, H. Zhang, L. Fang, J. Deng, Y. Wang, *Electrochim. Acta* **2017**, *245*, 32.
- [15] F. Putzolu, G. Balassone, M. Boni, M. Maczurad, N. Mondillo, J. Najorka, F. Pirajno, *Ore Geol. Rev.* **2018**, *97*, 21.
- [16] Y. Li, Y. Lu, X. Jiang, L. Lu, J. Qin, D. Yang, J.-L. Chen, L. Zhang, D. Wang, A. Lei, *Energy Storage Mater.* **2023**, *54*, 553.
- [17] H. Qin, Y. Ye, J. Li, W. Jia, S. Zheng, X. Cao, G. Lin, L. Jiao, *Adv. Funct. Mater.* **2023**, *33*, 2209698.
- [18] S. Mazen, N. Abu-Elsaad, A. Nawara, *Phys. Solid State* **2020**, *62*, 1183.
- [19] C. Liang, F. Kong, R. C. Longo, C. Zhang, Y. Nie, Y. Zheng, K. Cho, *J. Mater. Chem. A* **2017**, *5*, 25303.
- [20] Z. Ma, X. M. Shi, S. i. Nishimura, S. Ko, M. Okubo, A. Yamada, *Adv. Mater.* **2022**, *34*, e2203335.

- [21] Z. M. Chan, D. A. Kitchaev, J. N. Weker, C. Schnedermann, K. Lim, G. Ceder, W. Tumas, M. F. Toney, D. G. Nocera, *PNAS* **2018**, *115*, E5261.
- [22] Y.-K. Hsu, Y.-C. Chen, Y.-G. Lin, L.-C. Chen, K.-H. Chen, Chem. Commun. 2011, 47, 1252.
- [23] D. Chen, D. Ding, X. Li, G. H. Waller, X. Xiong, M. A. El-Sayed, M. Liu, *Chem. Mater.* **2015**, *27*, 6608.
- [24] P. Bhobe, K. Priolkar, P. Sarode, *Phys. Rev. B: Condens. Matter* **2006**, 74, 224425.
- [25] T. Ressler, S. L. Brock, J. Wong, S. L. Suib, J. Phys. Chem. B 1999, 103, 6407.
- [26] F. Wang, J. Deng, S. Impeng, Y. Shen, T. Yan, G. Chen, L. Shi, D. Zhang, *Chem. Eng. J.* **2020**, *396*, 125192.
- [27] X. Jia, C. Liu, Z. G. Neale, J. Yang, G. Cao, Chemical Reviews 2020, 120, 7795.
- [28] K. W. Nam, H. Kim, J. H. Choi, J. W. Choi, *Energy & Environmental Science* **2019**, *12*, 1999.
- [29] D. Yuan, X. Li, H. Yao, Y. Li, X. Zhu, J. Zhao, H. Zhang, Y. Zhang, E. T. J. Jie, Y. Cai, M. Srinivasan, *Adv. Sci.* **2023**, *10*, 2206469.
- [30] C. Xia, J. Guo, Y. Lei, H. Liang, C. Zhao, H. N. Alshareef, *Adv. Mater.* **2018**, *30*, 1705580.
- [31] K. W. Nam, H. Kim, J. H. Choi, J. W. Choi, Energy Environ. Sci. 2019, 12, 1999.
- [32] L. Kang, M. Zhang, Z.-H. Liu, K. Ooi, Spectrochim. Acta, Part A 2007, 67, 864.
- [33] X. Xie, J. Li, Z. Xing, B. Lu, S. Liang, J. Zhou, Natl. Sci. Rev. 2023, 10, nwac281.
- [34] R. Yi, X. Shi, Y. Tang, Y. Yang, P. Zhou, B. Lu, J. Zhou, Small Struct. 2023, 4, 2300020.
- [35] D. Kundu, B. D. Adams, V. Duffort, S. H. Vajargah, L. F. Nazar, *Nat. Energy* **2016**, *1*, 16119.
- [36] G. Kresse, J. Furthmüller, *Phys. Rev. B: Condens. Matter* **1996**, *54*, 11169.
- [37] G. Kresse, J. Hafner, *Phys. Rev. B: Condens. Matter* **1994**, *49*, 14251.
- [38] K. D. Kwon, G. Sposito, Advances in the Environmental Biogeochemistry of Manganese Oxides 2015, 51.
- [39] Y. Zhang, F. Wan, S. Huang, S. Wang, Z. Niu, J. Chen, *Nat. Commun.* **2020**, *11*, 2199.
- [40] M. Harada, F. Kotegawa, M. Kuwa, ACS Appl. Energy Mater. 2022, 5, 278.

- [41] Z. Zhong, J. Li, L. Li, X. Xi, Z. Luo, G. Fang, S. Liang, X. Wang, *Energy Storage Mater.* **2022**, *46*, 165.
- [42] D. Zhang, J. Cao, X. Zhang, N. Insin, S. Wang, J. Han, Y. Zhao, J. Qin, Y. Huang, *Adv. Funct. Mater.* **2021**, *31*, 2009412.
- [43] Y. Liu, Z. Qin, X. Yang, X. Sun, Adv. Funct. Mater. 2022, 32, 2106994.
- [44] G. Fang, C. Zhu, M. Chen, J. Zhou, B. Tang, X. Cao, X. Zheng, A. Pan, S. Liang, *Adv. Funct. Mater.* **2019**, *29*, 1808375.
- [45] Y. Ma, Y. Ma, T. Diemant, K. Cao, X. Liu, U. Kaiser, R. J. Behm, A. Varzi, S. Passerini, *Adv. Energy Mater.* **2021**, *11*, 2100962.
- [46] B. Ravel, M. Newville, *J. Synchrotron Radiat.* **2005**, *12*, 537.
- [47] Z. Song, L. Miao, L. Ruhlmann, Y. Lv, L. Li, L. Gan, M. Liu, *Angew. Chem. Int. Ed.* **2023**, *62*, e202219136.
- [48] S. Zheng, D. Shi, D. Yan, Q. Wang, T. Sun, T. Ma, L. Li, D. He, Z. Tao, J. Chen, *Angew. Chem. Int. Ed.* **2022**, *61*, e202117511.
- [49] P. Oberholzer, E. Tervoort, A. Bouzid, A. Pasquarello, D. Kundu, ACS Appl. Mater. Interfaces 2019, 11, 674.
- [50] L. Wang, K.-W. Huang, J. Chen, J. Zheng, Sci. Adv. 2019, 5, eaax4279.
- [51] Y. Tao, Y. Wei, Y. Liu, J. Wang, W. Qiao, L. Ling, D. Long, *Energy Environ. Sci.* **2016**, *9*, 3230.

Chapter 6: Summary and Perspectives

6.1 Summary

This section summarises the highlights of the innovations presented in Chapter 3, 4 and 5 from a general perspective. The limitations and related solution plans are also listed.

Chapter 3 introduces a sputtering process for zinc anode surface modification. The most notable achievement for this work is the rapid modification time of 10 seconds, which is estimated to save 25% in labour costs for the anode coating process, reducing the overall anode fabrication time from several hours to less than half an hour using the rapid sputtering method. This reduces the manufacturing time and labour costs of AZIBs. Additionally, the sputtering process avoids using wet chemistry solvents and reactants, reducing the total volatile organic compounds during electrode manufacturing and decreasing the time and raw material cost in the electrode during the drying and formation process. More importantly, this work provides an improved understanding of the most suitable surface functional group, combining experimental analysis and simulation tools. It proves that hydroxyl O dopants outperform other O functional group in enhancing interface wettability for AZIBs. Pyrrolic N introduces local variations in the charge distribution, showing that nitrogen dopants play a crucial role in shaping the distribution of the electric field by giving rise to surface dipoles. As a result, long-term stability of the zinc anode was achieved by applying the sputtering layer.

Some limitations also exist for Chapter 3 work. First and foremost, the size of the sputtering layer is limited to the sputtering chamber size, which support a maximum 10 cm x 10 cm uniform deposition. This size is sufficient to fabricate pouch cell, however, for the ambitious goal of developing Ah level cell, the sputtering chamber needs to be redesigned to accommodate larger sputtering area. Second, the sputtering efficiency decreases with distance from the centre, which means a longer sputtering time will be needed to evenly cover a large surface (more than 20 cm x 20 cm), which needs a further optimisation of the sputtering chamber. Third, the chemical environment of the sputtering species is limited to carbon, nitrogen and oxygen in this chapter. However, the research is relatively initial considering the potential of other elements. For example, on the ongoing following up research on fluorination plasma strategy for zinc anode, it is shown that the fluorine element not only contributes to the hydrated Zn²⁺ dehydration process during zinc deposition, but also exhibits zincophilicity which can guide uniform Zn deposition. Lastly, the oxygen and nitrogen dopant composition optimisation results may only work for aqueous electrolyte, while the interface mechanism for organic electrolytes show significant differences. For example, hydroxyl oxygen dopants may not enhance wettability in a non-aqueous PC electrolyte. In summary, the rapid sputtering is effective not only in building zinc anode protection layer but also capable to achieve a uniform coating layer in relevant fields (e.g., electro catalysis). The current pain point of the sputtering method is the uncertainty of scalability in considering the 'spray boundary effect', while the deposited material from the sputtering target is not uniformly distributed across the boundary, this issues can be dealt with in the cost of cutting the boundary area and utilising only the centre area. In large-scale applications, there are two methods to maintain a uniform sputtering surface by utilising robots and programmed sputtering paths. The first method is feathering, where the robot with a sputtering gun overlaps the edges of each sputtering pass to ensure the sputtering layers blend smoothly and evenly. A common practice in the industry is to have a 50% overlap between successive passes of the sputtering gun, with half of each new sputtering path covering the edge of the previous one, ensuring a uniform distribution of sputtering and consistent thickness across the entire surface. The second method is to follow cross-hatch patterns, where the sputtering gun moves first horizontally and then vertically across the surface, ensuring a uniform distribution and coverage, particularly on complex or flexible electrode materials.

Chapter 4 reports that a minute amount of PFOA electrolyte benefit both the cathode and anode parts. First, the C-F chain forms self-adjusting adsorption layer on both anode and cathode. As a result, the actively of free water molecules around the interface is limited, and a broader range of working window is achieved, which could tolerate more redox pairs. Second, the concentration of the PFOA additives is 0.25 mM. This additive concentration is only 10% or 1% of other reported additives, which significantly lower the cost and the overall weight of the battery pack. Third, the surface tension of the battery is significantly reduced due to the fluorine surfactant, leading to enhanced electrolyte wettability and diffusion on the zinc anode, resulting in improved ion transfer. Fourth, the lower surface tension of the PFOA electrolyte also contributes to the escape of trapped gas from HER or OER side reactions, which helps to maintain the battery stability.

It is worth noting that there are some limitations in Chapter 4 work: First, the toxicity of the fluorinated surfactants should be considered, as the super stability of PFOA also means that it takes a long time to decompose. Second, the solubility of PFOA is relatively low due to the C8 C-F chain, thus it may not work for some highly concentrated electrolyte such as ZnCl₂. Third, the mechanism is not completely understood. For example, it is unclear whether PFOA works solely as an adsorption layer or PFOA-related SEI also formed during cycling. According to previous reports, fluorine species can decompose and react with Zn to form a ZnF₂ layer. However, the expected 522 cm⁻¹ ZnF₂ signal did not appear in this work after repeated Raman testing. There are two reasons for this: one explanation is that PFOA is nonreactive during

cycling due to the highly stability of C-F bond, meaning there is no reaction between PFOA and Zn metal; another explanation is that reaction between PFOA and Zn metal happens but the amount of formed ZnF2 is out of the limit of detection of Raman device due to the minute amount of the electrolyte additive. From the experimental data and previous research on the high stability of PFOA, indicating that PFOA does not decompose even under a high temperature around 400°C. The first explanation is more plausible. Forth, due to the computational resource limitations, the time scale for the simulation process is ns (10⁻⁹), which is obviously lower than the real word parameters. The simulation model is performed in a "simulation box", which consists of a periodic cubic box with lengths of 5.2 nm containing 4051 water molecules, 230 ZnSO₄ and 1 or 5 PFOA molecules. This raises the questions of how one molecule interacts with its surrounding molecules to achieve a difference in electrochemical. This is also a general question for existing research regarding the simulations size scale and timescale. The pain point of the C8 PFOA surfactant, or the general application of fluorinated surfactant, is the concern over its toxicity and potential regulation by authorities. Considering the fact that C8 related industry is still widely used in civilian product including the well-known Gore-tex® membrane, fluorinated surfactant is allowed in some fields, but its toxicity need to mitigated in the chemistry way. The toxicity and the half-life of the fluorinated surfactant is dominated by their fluorine-carbon chain length, while the estimated half-life of C8 chain is three-year in human and even longer in environment. Specific modification strategy is to replace C8 chain with shorter hydrophobic groups including C4 or C6 perfluorinated chain. The cost of this strategy is the reduction of the surfactant effectiveness on surface tension, which can be mitigated by slightly increasing the C4/C6 additive dose amount. Another more innovative method to replace PFOA surfactants is to directly fluorinated the zinc anode by plasma fluorination treatment, which utilise biologically inert PTFE as the fluorine source to build the CF₂ block on the zinc anode surface.

Chapter 5 reports on hydronium hopping *via* the Grotthuss mechanism in manganese oxide. First, the prepared maple-leaf structure NiMn₃O₇·3H₂O achieved a specific capacity close to the theoretical value after lattice optimisation synthesis. The detailed influence of synthesis parameter on nickel manganese oxide vacancies and phase changes was investigated *via* parallel experiments with controlled variables such as temperature and synthesis additive concentrations. Second, advanced characterisation combined with simulation method provides an atomic level understanding of the Grotthuss mechanism in zinc ion batteries, which is based on the synergistic collaboration between manganese vacancies, the lattice water and nickel ions.

Third, the hydronium hopping provides a unique water-related mechanism for the design of AZIBs, which is different from the traditional Zn²⁺/H⁺ intercalation/deintercalation mechanism. In the meantime, there are several limitations for Chapter 5 work: 1. As the hydronium hopping through Grotthuss mechanism is driven by the presence of vacancies. This mechanism may be limited to materials with vacancies and lattice water. 2. The targeted lattice structure is highly sensitive to synthesis parameters. For example, a higher NH₄Cl additive concentration could lead to lattice change and further increase could lead to a phase change. The metal source anion has an impact on the purity of the product. The temperature has impact on the preference growth of lattice face. These factors raise research interest on structure control but may become obstacle for further scaling up or commercialisation. 3. A direct and precise evaluation of the specific contribution of hydronium and zinc ions to the total capacity is still unclear for this work. Changes on the b value and diffusion/capacitive charge transfer behaviour around the redox peak positions are used as indicators to monitor the hydronium transfer mechanism. However, this estimation value may not be suitable for investigating the transfer mechanism of hydronium hopping, as it differs from the traditional diffusion/capacitive method, where a hydrogen atom jumps between adjacent hydrogen-bonded water molecules, displacing an existing hydrogen atom. 4. Carbon paper is used as current collector for this work and the cell is limited to coin-cell and Swagelok cell, the loading amount is relatively lower that commercial lithium-ion batteries. These limitations indicate that the research project still has numerous challenges to be further investigated.

6.2 Challenges

AZIBs benefit from the aqueous electrolyte, which is regarded as a safe, abundant and environmentally friendly component. In practice, water also brings significant disadvantage to the electrochemical system. This is because the relatively reactive in physical and chemical properties of water molecules. For example, water molecules can undergo ionisation and splitting in a mild acid environment such as ZnSO₄ electrolyte. This results in the formation of H⁺, OH⁻, H₂ and O₂ within the AZIBs system. This further leads to battery swelling and side products formation such as MnOOH, Zn(OH)₂SO₄. These byproducts generated at the interface could slow down mass transfer and charge transfer once formed, and this problem becomes more serious in long-term cycling under high current density. Besides, the generation of oxygen and hydrogen gas from uncontrolled wate splitting also further raises the safety concern of batteries explosion.

The following challenges related to water can be simplified into a question: which is better, more or less water? Excessive water molecules are regarded as free water molecules at the electrolyte/electrode interface. At the cathode part, some materials such as Prussian blue undergoes serious capacity degradation due to their solubility in water and can partly dissolve into the electrolyte, as evidenced by the colour changes of the electrolyte. Manganese oxide also face this issue due to the Jahn-teller effect which generate soluble Mn²⁺ ions. The situation with vanadium oxide situation is even worse. This drives researchers to reduce the amount of water molecules in AZIBs electrolyte, one example is the use of a concentrated electrolyte strategy, such as Zn(OTf)₂, Zn(TFSI)₂ and ZnCl₂ electrolytes. These electrolytes could also be regarded as 'water in salt' electrolyte, in which the concentration of zinc salt outnumbers the water molecules, thus limiting the water-related reactions due to the lack of free water molecules. However, these types of electrolytes are expensive, significantly increasing the cost of AZIBs.

Another challenge is related to the existing mechanism, which has some points of contradiction. For example, the role of Mn²⁺ in the electrolyte is unclear. The general opinion is that Mn²⁺ as an inhibitor for the dissolution of manganese oxide. However, Mn²⁺ ions can also convert into MnO₂ within the working window of AZIBs, resulting in deposited MnO₂ mixing with the pristine cathode material during cycling. This makes the precise evaluation of MnO₂ cathode active materials' weight and specific capacity more complex. Since these Mn²⁺ are normally not accounted in the weight of the cathode material in calculation, it results in reported specific capacities being higher than the practical ones. Additionally, the MnO₂ deposited from the electrolyte additive typically lacks the desired lattice parameters and stability, potentially blocking the transfer of zinc ions from the electrolyte into the electrode. The stability of cathode materials needs to be further improved by methods other than the use of transferable additive salt.

6.3 Perspectives

6.3.1. Enlarging working window for aqueous electrolyte

Enlarging the working window of zinc-ion battery electrolytes is a promising topic to tolerate more redox reactions for further energy density improvement. Non-sacrificial adsorption layers and sacrificial-type electrolytes/electrolyte additives are suitable strategies for this research direction. Fluorine compounds are central to these strategies because of their high electronegativity, which can mitigate water-splitting side reactions. These compounds also offer a rich library for building up CEI/SEI from in-situ decomposition at the electrolyte/electrode interface. Fluorinated surfactants are highlighted here because their dual effect on both SEI in-situ formation and their preferential orientation on interfaces to build a water-shielding adsorption layer. From the aspect of device innovation, the challenge in water's 1.23 V narrow electrochemical stability window of AZIBs can be further increased by separating the anolyte and catholyte using ion-selective membranes, including cation-exchange membranes (CEM), anion-exchange membranes (AEM). In theoretically, CEM can mitigate the HER by reducing the migration of OH⁻ to the cathode. AEM can reduce the chance of OER by reducing the transport of hydronium through the membrane. For AZIBs, CEM is fit for the specific demand of enlarging the working window because it allows for high voltage, which primarily causes the OER reactions. The selection of CEM should consider the acidity environment of AZIBs and the membrane selectively of Zn²⁺ rather than H⁺. Thus Nafion[®] membranes are less promising on this topic because it is designed for proton migration which could lead to serious HER reaction on zinc anode during cycling. The proposed membrane material are sulfated polyether ether ketone membranes and polybenzimidazole membranes with specific modification structure to hinder the proton migration and still allows the migration of zinc ions, for example, thickener membrane have a more significant influence on proton migration than Zn²⁺, or, fixed negative charge groups which follow the Donnan exclusion effect to selective large Zn²⁺ ions and blocks the small proton migration thorough CEM membranes.

6.3.2. Increasing specific capacity

The specific capacity of cathode materials for AZIBs needs further improvement, and there are several potential opportunities.

First, defect engineering can be employed by using oxygen vacancies and cationic vacancies in the lattice. As highlighted in Chapter 5, cationic vacancies (Mn vacancies) can not only act as additional active sites for charge carriers intercalation/deintercalation, providing additional capacity, but also mitigate the charge transfer energy barrier, serving as a transfer driving force. To achieve this goal, the theoretical exploration can be focus on investigating cathode materials with periodic lattice vacancies. The key point is the geometrically frustrated lattice structure. For example, compared with triangular lattice, The 1/7 depleted MLL and 1/4 depleted Kagome lattice can theoretically serve as intercalation sites in the AZIBs. However, proper modification on these two kinds of materials need to be considered. First is the structural stability, the geometrical frustration in these MLL and Kagome lattice undergoes lattice breathing at depletion sites during cycling, to handle the intercalation stresses. Design Fluorine doping experiment for these two kinds of lattice can forms strong ionic bonds with transition metals in the lattice, thus maintaining geometrical frustration and keeping depletion sites stable during AZIBs cycling. These theoretical exploration will be benefiting from the collaboration with experts on crystallography and physics in combining with proper synchrotron exploration on the materials coordination environment. The precise synthesis of these two kinds of materials with certain type of vacancies can be achieved via hydrothermal synthesis method and monitoring the XRD peak changes with adjusting synthesis condition. Introducing two electron transition redox pairs is another fundamental aspect to increase the specific capacity of zinc ion battery. Theoretically, two-electrons redox pairs such as Mn²⁺/Mn⁴⁺ and Sn²⁺/Sn⁴⁺ can contribute significantly higher capacities compared to Mn³⁺/Mn⁴⁺. These redox pairs enable the participation of two electrons in the charge transfer process, effectively doubling the theoretical capacity relative to single-electron redox pair. The challenge is to achieve these redox reaction in zinc ion batteries' narrow working window. Through a joint experimental design with Perspective 6.3.1 to broadening the working window or optimise the redox peak potential by replacing metal oxide based cathode materials with metal sulphide-based cathode material. For example, in manganese oxide, changing the redox pair from Mn³⁺/Mn⁴⁺ to Mn²⁺/Mn⁴⁺ could theoretically double the specific capacity of Mn-based cathodes from 308 mAh g⁻¹ to 616 mAh g⁻¹. In experimental design, to achieve this goal, proper electrolyte additive needs to be investigated to maintain a stable and reversible electrolyte environment, such as catalysis additives or pH buffers (e.g., H₂PO₄⁻/HPO₄²- pair).

6.3.3. Increasing loading amount of active materials

High loading amount is one of the main objectives of AZIBs. Currently the loading amount is lower than 5 mg cm⁻². Increasing the loading amount to over 15-20 mg cm⁻² could meet the needs for grid energy storage, which is one of the target application fields for AZIBs. Therefore, electrodes with higher loading amounts represent a promising research topic not only for AZIBs but also for other batteries technologies.

Additionally, the current composition of the cathode part is typically 7: 2: 1 (active material: PVDF: Carbon P), where the active material accounts for only 70% of the total weight of the cathode composition, which falls far behind lithium-ion batteries (over 90%). Further increasing the active material ratio is in high demand. In theory, investigating self-stand active materials and binding-free strategies can further increase the mass loading from 2 mg cm⁻² to 20 mg/cm⁻² and the active material ratio from 70% to 95%. For the self-standing strategy, the experimental design involves synthesising the active materials with a conductive matrix, specifically using a co-precipitation method to integrate carbon nanotubes with cathode materials or utilising porous carbon materials such as carbon foam to growth the cathode materials in-situ within the porous structure. Utilising multiple types of carbon materials can further increase the internal connectivity and electrical conductivity of the porous self-standing electrode, such as introducing carbon nanotubes or carbon nanofibers during the preparation stage of the foam structure, which also enhances the mechanical strength of the self-standing carbon foam. This research could benefit from the collaboration with experts in carbon materials synthesis or lignocellulosic materials, which are eco-friendly and cost effective. The complexity of battery chemistry is fundamentally grounded in the simple principles of physics (e.g., crystallography and physical chemistry). By applying this knowledge, a more advanced electrochemical world could be achieved.

Publication list

- (1) **F. Zhao**, J, Li. A. Chutia, L. Liu, L. Kang, F. Lai, H. Dong, X. Gao, Y. Tan, T. Liu, I. Parkin*, G. He*, Highly stable manganese oxide cathode material enabled by Grotthuss topochemistry for aqueous zinc ion batteries, *Energy Environ. Sci.*, **2024**, 17, 1497-1508. DOI: 10.1039/D3EE04161A
- (2) **F. Zhao,** J. Feng, H. Dong, R. Chen, T. Munshi, I. Scowen, S. Guan, Y. Miao, T. Liu, I. P. Parkin*, G. He*, Ultrathin protection layer via rapid plasma strategy for stable aqueous zinc ion batteries, *Adv. Funct. Mater.*, **2024**, 202409400.
- (3) **F. Zhao**, Z. Jing, X. Guo, J. Li, H. Dong, Y. Tan, L. Liu, Y. Zhou, R. Owen, P. Shearing, D. Brett, G. He*, I. P. Parkin*, Trace amounts of fluorinated surfactant additives enable high performance zinc-ion batteries, *Energy Storage Mater.*, **2022**, 53, 638-645.
- (4) H. Dong, J. Li, J Guo, F. Lai, **F. Zhao**, Y. Jiao, Y. Liu, D. J.L. Brett, T. Liu, G. He*, I. P. Parkin*, Insights on flexible zinc-ion batteries from lab research to commercialisation, *Adv. Mater.*, **2021**, 33, 2007548.
- (5) H. Dong, J. Li, S. Zhao, F. Zhao, S. Xiong, D. Brett, G. He* and I.P. Parkin*, An antiaging polymer electrolyte for flexible rechargeable zinc-ion batteries. *J. Mater. Chem. A*, **2020**, 8, 22736-22644.
- (6) J. Li, N. Luo, L. Kang, **F. Zhao**, Y. Jiao, T. Macdonald, M, Wang, I. P. Parkin, P. Shearing, D. Brett, G. Chai*, G. He*, Hydrogen-bond reinforced superstructural manganese oxide as the cathode for ultra-stable aqueous zinc ion batteries, *Adv. Energy Mater.*, **2022**, 202201840.
- (6) H. Dong, R. Liu, X. Hu, **F. Zhao**, L. Kang, L. Liu, J. Li, Y. Tan, Y. Zhou, D. Brett, G. He*, I. P. Parkin*, Cathode-electrolyte interface modification by binder engineering for high-performance aqueous zinc-ion batteries, *Adv. Sci.*, **2022**, 202205084.
- (7) X. Gao, C. Zhang, Y. Dai, S. Zhao, X. Hu, **F. Zhao**, W. Zhang, R. Chen, W. Zong, Z. Du, H. Dong, Y. Liu, H. He, J. Li, I. P. Parkin, G. He*, C.J. Carmalt, Three-dimensional manganese oxide@carbon networks as free-standing, high-loading cathodes for high-performance zin-ion batteries, *Small Structures*, **2023**, 2200316.
- (8) Y. Tan, R. Xie, S. Zhao, X. Lu, L. Liu, **F. Zhao**, C. Li, H. Jiang, G. Chai, D. Brett, P. Shearing, G. He*, I. P. Parkin*, Facile fabrication of robust hydrogen evolution electrodes under high current densities via Pt@Cu interactions, *Adv. Funct. Mater.*, **2021**, 202105579.
- (9) Y. Tan, J. Feng, L. Kang, L. Liu, **F. Zhao**, S. Zhao, D. Brett, P. Shearing, G. He*, I. P. Parkin*, Hybrid Ni2P/CoP nanosheets as efficient and robust electrocatalysts for domestic wastewater splitting, *Energy Environ. Mater.*, **2022**, 0, 1-10.

Manuscript in preparation

(1) **Zhao, F.** et al., 3D porous zincophilic-hydrophobic layer for high reversible zinc anode enabled by plasma fluorination treatment

Academic activities

- 1. Oral presentation. 30th SCI-CSCST Conference, London, UK, Sep 2023.
- 2. Oral presentation. ECS chapter annual event, London, UK, Feb 2024.
- 3. Oral presentation. 2024 DMUGM Conference, Abingdon, UK, April 2024.